The Gas Phase Reactivity of Doubly–Charged Ions with Neutral Species

A thesis submitted for the degree of Doctor of Philosophy

by

Jessica Frances Lockyear

Department of Chemistry, UCL

2011

I, Jessica Frances Lockyear confirm that the work presented in this thesis is my own. Where information has been derived from other sources, I confirm that this has been indicated in the thesis.

Signed,

Abstract

Doubly charged atomic and molecular species (dications) are potentially influential reactants in many environments, including our Earth's own ionosphere and ionospheres of planets and moons such as Mars and Titan. However, the dication chemistry of these energized environments is far from understood. This thesis attempts to experimentally and theoretically characterize some dicationic reactions that could occur in such environments. Moreover, astro–chemists have pondered for decades how the polycyclic aromatic hydrocarbons and long chain alkynes thought to exist in the interstellar medium are synthesized. Reactions of dications with neutral molecules have been proposed as one possible mechanism for the formation of these large molecules. In this context, it is important to undertake a systematic experimental study of the reactions of dications with neutrals to discover the products that might be formed. Dication–neutral reaction dynamics are also not fully understood and are often surprising, meriting further study.

A position–sensitive coincidence time–of–flight mass spectrometer has been used to probe the reactions of dications, including Ar^{2+}, N_2^{2+}, $C_2H_2^{2+}$, SF_4^{2+} and O_2^{2+}, with a variety of neutrals. The experiment exploits the fact that dication reactions often result in a pair of product monocations. These pairs of charged products are detected in coincidence, on an event–by–event basis, allowing the reaction channels to be characterised. The position–sensitive detection provides data from which the reaction dynamics and energetics can be determined. One might anticipate that dication–neutral interactions would predominantly result in electron–transfer at large interspecies separation. However, this thesis presents results proving that the chemistry can be far more diverse, with bond–formation between the reactants competing favourably with the more dominant electron–transfer process.

Acknowledgments

I would like to express my gratitude to the following people who have made completion of this PhD possible. First and foremost, my supervisor Professor Steve Price, who has been of great support on matters both personal and science related.

Secondly, I am especially grateful to Dr. Mike Parkes, who has taught me so much and has been interminably patient. Members of the Price group and my many friends in the Chemistry Department, particularly Kevin Douglas who has made me laugh so much over the years. Thanks to members of the technical support staff for patience with me when I wasn't quite sure what I was after!

Thank you to all the other friends who have been so supportive including Helen, Hannah, Kev, Tom and particularly Sol. To my parents for their belief and encouragement and lastly my amazing sister Harriet, I am eternally grateful.

List of Publications as a Result of Studies Reported in this Thesis

D. Ascenzi, P.Tosi, J. Roithová, C. L. Ricketts, D. Schröder, J. F. Lockyear, M. A. Parkes and S. D. Price, **Generation of the organo-rare gas dications HCCRg(2+) (Rg = Ar and Kr) in the reaction of acetylene dications with rare gases**, *Physical Chemistry Chemical Physics (2008)*, Vol. 10, Issue 47, Pages 7121-7128.

M. A. Parkes, J. F. Lockyear and S. D. Price, **Electron-transfer and chemical reactivity following collisions of Ar^{2+} with C_2H_2**, *International Journal of Mass Spectrometry (2009)*, Vol. 280, Issue 1-3, Pages 85-92.

J. F. Lockyear, M. A. Parkes, S. D. Price, **Single-electron transfer between $Ar^{2+}(^3P, ^1D)$ and He at low collision energies**, *Journal of Physics B – Atomic, Molecular and Optical Physics (2009)*, Vol. 42, Issue 14, Article Number 145201.

J. F. Lockyear, C. L. Ricketts, M. A. Parkes and S. D. Price, **The formation of NH^+ following the reaction of N_2^{2+} with H_2**, Chemical Science (2011), Vol. 2, Issue 1, Pages 150-156.

J. F. Lockyear, M. A. Parkes and S. D. Price, **Fast and Efficient Fluorination of Small Molecules by SF_4^{2+}**, *Angewandte Chemie – International Edition (2011)*, Vol. 50, Issue 6, Pages 1322-1324.

Table of Acronyms

DIE – Double Ionisation Energy

EI – Electron Ionisation

CS – Charge Stripping

DCT – Double Charge Transfer

VUV – Vacuum Ultra Violet

TA – Terrestrial Atmosphere

INMS – Ion–Neutral Mass Spectrometer

ISM – Interstellar Medium

PAH – Polycyclic Aromatic Hydrocarbon

SET – Single Electron Transfer

DET – Double Electron Transfer

CID – Collision–Induced Dissociation

PT – Proton Transfer

TES – Translational Energy Spectroscopy

SIFT – Selected–Ion–Flow–tube

TOF – Time–of–Flight

LZRW – Landau–Zener Reaction Window

PEC – Potential Energy Curve

PES – Potential Energy Surface

PSCO – Position–Sensitive Coincidence

MS – Mass Spectrometer

PSD – Position Sensitive Detector

MCPs – Micro–Channel Plates

FWHM – Full–Width at Half–Maximum

KE – Kinetic Energy

TDC – Time–to–Digital Converter

LAB – Laboratory

CM – Centre–of–Mass

E_{CM} – Centre–of–Mass Collision Energy

KER – Kinetic Energy Release

Rg – Rare Gas

Table of Contents

Chapter 3: Ar^{2+} + He 103

Chapter 4: N_2^{2+} + H_2 121

Table of Figures

Chapter 1: Introduction

Chapter 2: Experimental Methodology and Data Processing

Chapter 3: Ar^{2+} + He

Chapter 4: $N_2^{2+} + H_2$

Chapter 5: Reactivity of SF_4^{2+} with Neutrals

Chapter 6: $C_2H_2^{2+}$ + Ar and Ar^{2+} + C_2H_2

Chapter 7: The Oxygen Dication Part I – Reactions of O_2^{2+} with Small Neutral Organic Molecules

Chapter 8: The Oxygen Dication Part II – Selected Reactions of O_2^{2+} with Neutral Species

Appendix

Table of Tables

Chapter 1: Introduction

Chapter 3: Ar^{2+} + He

Chapter 4: N_2^{2+} + H_2

Chapter 5: Reactivity of SF_4^{2+} with Neutrals

Chapter 6: $C_2H_2^{2+}$ + Ar and Ar^{2+} + C_2H_2

Chapter 7: The Oxygen Dication Part I – Reactions of O_2^{2+} with Small Neutral Organic Molecules

Chapter 8: The Oxygen Dication Part II – Selected Reactions of O_2^{2+} with Neutral Species

Chapter 1: Introduction

1.1 Doubly Charged Ions

Removal of two electrons from an atom or molecule generates a di–positively charged species, a dication. The first dicationic molecule detected in the gas phase was the CO^{2+} ion, which was observed in 1930 by Conrad employing a magnetic sector mass spectrometer[1]. In the following decades, dications have been the subject of increasing interest, as gradually more is understood about their properties and reactions.

The discovery of the CO^{2+} dication in 1930 was rapidly followed by measurements of the double ionisation energy (DIE) of CO and other small molecules such as NO, N_2 and O_2[2–4]. However, as noted by Vaughan, there is an inherent difficulty in measuring the DIE of homonuclear diatomics using mass–spectrometric techniques because the dication has the same mass–to–charge ratio (m/z) as the associated atomic monocation[2]. It is for this reason that, in 1931, Vaughan could not suggest a DIE for N_2, and only with the development of more sophisticated techniques could accurate DIEs of molecules such as N_2 or O_2 be determined. The first theoretical prediction of a stable dicationic species was made by Pauling in 1933[5]. Pauling predicted that the He_2^{++} dicationic dimer should be metastable with a potential well 1.4 eV in depth, which supports four vibrational levels. In fact, the predicted equilibrium bond–distance of 0.75 Å for the dicationic dimer He_2^{++} is shorter than that of the monocationic dimer He_2^{+} (1.09 Å)[5].

A schematic of the potential energy curve of a diatomic dication is shown in Figure 1. At significant interspecies separation, the Coulomb repulsion between the charges dominates. However, as originally noted by Pauling with reference to the He_2^{++} dicationic dimer, the resonance interaction of the electrons becomes important with decreasing interspecies separation causing the force to become attractive, leading to formation of a bound doubly charged molecule[5]. In general, the asymptote for an infinitely separated dication and neutral, A^{2+} + B, lies higher in energy than that of a monocation and monocation, $A^{+} + B^{+}$. The interaction between A^{2+} and B is dominated by polarisation attraction that varies according to Equation (1.1), in atomic units.

$$V = -\frac{Z^2 e^2 \alpha}{2r^4} \qquad (1.1)$$

This dication–neutral interaction potential undergoes an avoided crossing with the potential for the monocation–monocation interaction, creating a potential energy barrier to dissociation of the dicationic molecule, Figure 1. The height of this barrier, coupled with the depth of the potential well essentially defines the lifetime of the molecule. For the vast majority of molecular dications the potential minimum lies higher in energy than the asymptote for the charge-separated fragments, Figure 1, as such these species are thermodynamically unstable, or metastable[6]. Several instances of thermodynamically stable dications are known, but these are generally "exotic" species such as $XeHe^{2+}$ or UO^{2+}[6].

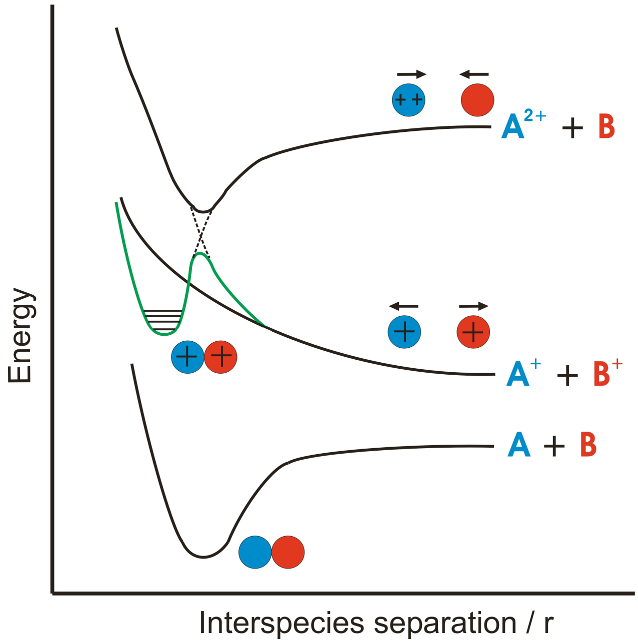

Figure 1.1 A schematic diagram showing the potential energy curves for a neutral diatomic, a molecular dication and the polarisation attraction between the dicationic and neutral fragments.

One might expect the Coulomb repulsion between the charges to result in rapid dissociation of molecular dications; however, many molecular dications have been shown to have significant lifetimes. Indeed, the fact that molecular dications can be detected with conventional mass spectrometry means that their lifetimes must be at least several microseconds in order that they can travel between the ionisation source and the detector[7]. Dications that are formed in vibrational levels near the top of the potential well can tunnel through the barrier, thus the lifetime of the isolated dication depends on the vibrational distribution formed in the ionisation process. Ion–storage ring experiments have been employed to try and measure the lifetime of several isolated dications and N_2^{2+}, CO^{2+}, CO_2^{2+}, CS_2^{2+} and SH^{2+} have all been found to survive for several seconds[8,9]. Essentially, these dications are infinitely long–lived and it is only *via* interactions with residual gases that they are destroyed[10]. One of the major fragmentation pathways for molecular dications is *via* a curve crossing to a dissociative state, termed pre–dissociation. The probability of pre–dissociation is more significant for excited electronic states of dications than for the ground state, thus fewer excited electronic states have significant lifetimes.

1.1.1 Ion Formation

Dications, both atomic and molecular, can be formed in several ways. Electron ionisation (EI) has been employed for creation of multiply charged ions for many decades. Dications formed by EI can either be formed directly or in a step–wise manner *via* a monocationic intermediate. Photoionisation can also be employed for the formation of dications[11], again in a direct or stepwise manner. Yields of dications formed by EI or photoionisation in a direct manner are low, in comparison with yields for single ionisation, due to the need for electron–correlation to allow the ejection of two electrons. Impact of a single electron or photon upon an atom or molecule is less likely to cause the ejection of two electrons since electron–correlation is generally small. Another disadvantage of direct EI or photoionisation is that the Franck–Condon overlap between the neutral and dicationic states is often poor. In some cases, the geometry change between the neutral and the dication is so great that formation of the dication *via* vertical ionisation is impossible, for example CH_4^{2+}[12,13]. Since 1990, electro–spray ionisation (ESI) has been useful as a "soft" ionisation technique that limits fragmentation of the dication[14,15]. ESI has been used to generate some interesting doubly–charged species in the gas phase such as $Co(H_2O)_4^{2+}$[14]. However, ESI is generally used to generate large molecular dications (>10 atoms), in particular from organic species. Thus, given that the experiments presented in this thesis involve small molecular dications, ESI would provide limited benefits to our experiments. In addition to those methods described above, "collisional" procedures can also be used to generate dications, specifically *via* charge–stripping (CS)[16] or double–charge–transfer (DCT)[17].

1.2 Astrochemical Role of Dications

Dication reactions are thought to play an important role in the chemistry of various energised media[18]. As described in section 1.1.1, dications can be formed by EI, photoionisation or in collisions with other high–energy particles. The levels of high–energy vacuum ultra–violet (VUV) radiation and cosmic rays present in interstellar regions and planetary and lunar ionospheres mean that the density of dicationic species is expected to be reasonably high compared to the monocation density, around 50% of the equivalent monocation in some cases[19-21]. Moreover, in these environments, the number densities of gas molecules are very low: around 10^2 cm^{-3} in diffuse interstellar (IS) clouds, around 10^4–10^6 cm^{-3} in dense IS clouds and around 10^8 cm^{-3} in the terrestrial thermosphere. In contrast, the number density of gas molecules in the lower terrestrial atmosphere (TA) is approximately 10^{14}–10^{19} cm^{-3}[19]. Such low pressures allow for sequential ionisation to a dicationic state *via* the formation of an intermediate monocation. In dense environments, such as the lower TA, these monocations would very swiftly undergo collisions that de–excite the species.

Rocket–mounted mass spectrometers launched in the 1960s discovered, contrary to popular belief, that the cationic species abundant in the upper TA were not simply those derived from the most abundant neutral species such as N_2 and O_2[19]. In fact, the upper TA is rich in species such as NO^+, implying the occurrence of a range of gas–phase ion chemistry[22,23]. Over the following decades, this ionospheric chemistry has been of great interest to chemists[19]. The planets, and several moons and comets, in our Solar System possess a gaseous atmosphere and therefore an associated ionosphere. Consequently it is extremely valuable to develop a comprehensive understanding of the dication–neutral reactivity that could occur in these environments. A summary of the most significant atmospheres where dications have been predicted to exist will be given in the next sections.

1.2.1 Saturn's Moon Titan

Titan is the only moon in our Solar system to have a fully developed atmosphere, which is in fact 1.19 times as massive as Earth's. The chemistry of Titan's atmosphere has been described as "the richest ... in the Solar System"[24]. Titan's atmosphere is composed of approximately 98.4 % N_2, with the remaining 1.6 % largely comprising CH_4 and H_2. However, it is the trace species in Titan's atmosphere that are the most fascinating. A host of organic species make up a distinctive "haze" around Titan that has been photographed by both Voyager 1 and the Cassini–Huygens probe (Figure 1.2). Measurements taken by the Huygens probe on board the Cassini spacecraft, and their subsequent modelling, have revealed a highly complex ionospheric composition, both on the day–side and the night–side of Titan[24–27]. Around 50 ions have been detected at or above threshold by the Ion–Neutral Mass–Spectrometer (INMS) on the Huygens probe meaning that Titan has the most compositionally complex ionosphere in the Solar System[28]. These observations indicate that molecular growth starts in the upper atmosphere of Titan, rather than at lower levels, and results in large positively and negatively charged ions, which are probably the precursors for even larger molecules and eventually aerosols[24–27]. Such a rich organic chemistry has led many to propose that the conditions on Titan are similar to those on a prebiotic Earth and as such great attention has been paid to increasing understanding of Titan and its atmosphere. Successful attempts to replicate the general themes of this molecular synthesis in the laboratory have recently been reported[29–31].

Figure 1.2 Image of the organic "haze" around Titan. Image was obtained by the Cassini Orbiter wide angle camera using red, green and blue spectral filters[32].

Titan's organic haze is composed of small species such as C_2H_2, nitriles such as HCN, NCCN, NCCCN and NCCCCN[28,33], many larger organic molecules and aerosols. A surprising number of highly unsaturated long chain hydrocarbons have been detected or proposed[34]. The mechanisms behind the formation of such species have not all been discovered and it has been proposed that dication–neutral reactions could play an important role in the synthesis of long–chain poly–unsaturated hydrocarbons on Titan and elsewhere[35]. Indeed, Roithová and Schröder have shown that the reaction of $C_7H_6^{2+}$ with C_2H_2 forms $C_9H_n^{2+}$, thereby increasing the carbon chain length by two[36]. Further investigation of similar hydrocarbon dications $C_mH_n^{2+}$ (m = 6, 8, 12, 14) suggests that the coupling reaction with acetylene is a general property of these medium–sized dications[36].

Recent investigations have concluded that to improve the agreement between models and observations of Titan's ionospheric ion abundances, beyond the current factors of 2–3, requires a more detailed knowledge of the ion/neutral chemistry[27]. Some of the dication–neutral reactions investigated in this thesis could indeed go some way to revealing the intricacies of the ionospheric chemistry of Titan, and also other planetary bodies.

1.2.2 Mars

The carbon dioxide dication CO_2^{2+} has been predicted by Witasse *et al* to be a minor constituent of the atmosphere of Mars[37]. The altitudes at which the CO_2^{2+} is expected to be present range from 130 km to 230 km, but peaking at 155 km to 160 km, as shown by the predicted concentrations in Figure 1.3.

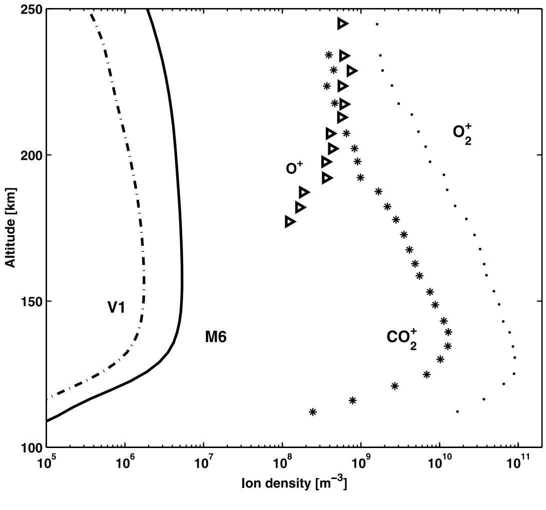

Figure 1.3 Predicted ion–density profiles for CO_2^{2+} using the geophysical conditions present at the time of the Viking 1 lander (V1) and Mariner 6 (M6) descents. Also shown are the ion densities of O^+ (triangles), O_2^+ (dots) and CO_2^+ (asterisks) recorded by the Viking 1 lander. From ref. [37].

The lifetime of the ground state of CO_2^{2+} has been measured as 4.2 seconds[8], though it may be even longer. Clearly, once formed by VUV radiation or impact from cosmic rays, these dications will likely survive long enough to undergo collisions with neutral atmospheric constituents or electrons. The Viking 1 mission detected only O^+, O_2^+ and CO_2^+ in the Martian atmosphere; the densities of these ions are also shown in Figure 1.3. Presumably, dications other than CO_2^{2+} may also be present, although in lower concentrations. Interactions of CO_2^{2+} and other dications with neutral species have the potential to influence the ionospheric chemistry of the "Red Planet".

1.2.3 Venus

Similarly to Mars, a layer of CO_2^{2+} has been predicted to exist in the ionosphere of Venus[38]. The three most abundant dications in the Venusian ionosphere are O^{2+}, CO_2^{2+} and N_2^{2+}. The O^{2+} dication was detected by the Pioneer Venus Orbiter[39]; whereas, the latter two molecular dications have not been experimentally identified but are predicted to exist. Gronoff *et al* have modelled the densities of these three dicationic species and the results are shown in Figure 1.4[38].

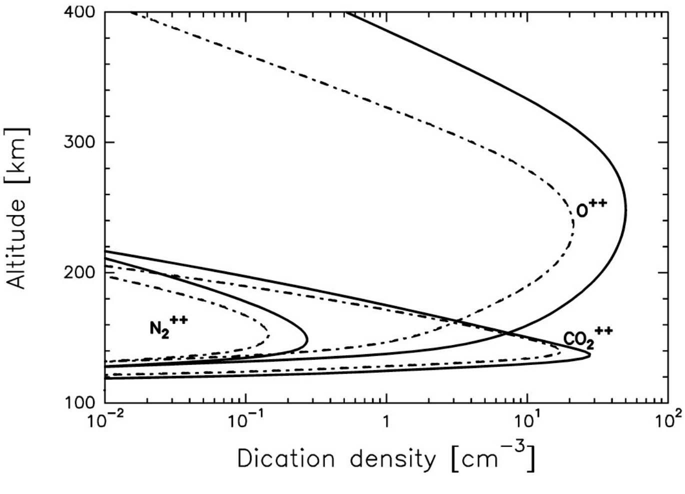

Figure 1.4 Predicted ion density profiles for the three most abundant dications in the Venusian ionosphere.

Gronoff *et al* predict that CO_2^{2+} has a significant density approaching 10^2 cm^{-3} but over a narrow altitude range peaking at around 140 km. The ion density of N_2^{2+} also peaks at around 140 km, but this dication is around half as abundant as CO_2^{2+}.

1.2.4 Earth

Earth's ionosphere is traditionally assigned as that part of the atmosphere at altitudes greater than around 60 km[40]. At altitudes of around 300 km, ionisation reaches its peak and several parts per thousand of the atoms and molecules are ionised. Therefore, around these altitudes, ions represent a significant fraction of the atmosphere. Observation of the O^{2+} line at 500.8 nm in the auroral spectrum by Vegard in the 1940s stimulated the interest in dications in the terrestrial ionosphere[41]. However, at this time the accompanying line at 496.0 nm was not observed and so the presence of O^{2+} was questioned[41]. Later, in the 1970s, Hoffman *et al* reported the detection of O^{2+} at m/z of eight with a mass–spectrometric probe on board the Explorer 31 satellite[42–45]. O^{2+} is believed to be formed by photoionisation of O^+ and may be destroyed by a variety of processes. According to the observations of Hoffman *et al,* and several theoretical models, the O^{2+} should reach a maximum concentration of around 10^2 cm^{-3} at altitudes of around 400 km[42,43,46–48].

In addition to O^{2+} ions, N^{2+} ions have been detected in the terrestrial magnetosphere[49]. The density of N^{2+} ions is certainly lower than O^{2+} ions. Assuming a direct correlation of the density of N^+ and O^+ with N^{2+} and O^{2+} respectively, then the density of N^{2+} should be around 1 % of that of O^{2+}[21,49]. More recent observations of the polar ionospheric composition have confirmed that O^{2+} and N^{2+} are present with significant densities. In particular O^{2+}, for which the ion flux in some observations reached 50 % of the O^+ flux[21].

Given the significant, and reproducible, signals detected due to O^{2+} and N^{2+} in the TA, it seems probable that O_2^{2+} and N_2^{2+} are also present. Indeed, it was suggested by Prasad and Furman that the presence of O_2^{2+} could account for the unexpectedly high auroral density of O^+[50]; detected fluxes are a factor of 50 higher than expected[51]. Detection of atomic dications such as O^{2+} and N^{2+} using mass–spectrometry is comparatively easy since they have an m/z that is not in the proximity or overlapping with other ions. Conversely, this is the principle difficulty when trying to detect homonuclear diatomic dications such as O_2^{2+} or N_2^{2+}. These diatomic dications will produce a peak in a mass–spectrum that is overlapping with the associated atomic monocation, O^+ or N^+ respectively. Thus, other detection methods need to be employed to prove the existence of O_2^{2+} and N_2^{2+} in the TA. It has been shown that fluorescence from N_2^{2+} can be experimentally detected[52,53]. Therefore, it has been predicted that fluorescence from N_2^{2+} should be observable from the TA[46].

Several theoretical models of the density profiles of O_2^{2+}, N_2^{2+} and O^{2+} have been devised; the first of these by Avakyan[54,55]. Avakyan predicted that dicationic densities should peak at altitudes between 100 km and 200 km. However, the experimentally detected peak in the O^{2+} density is around 400 km, thus outlining a need for more accurate models. Simon *et al* have also modelled the abundances of oxygen and nitrogen-based ions in the TA between 100 km and 500 km altitudes[46]. The resulting densities from the model of Simon *et al* are shown in Figure 1.5[46].

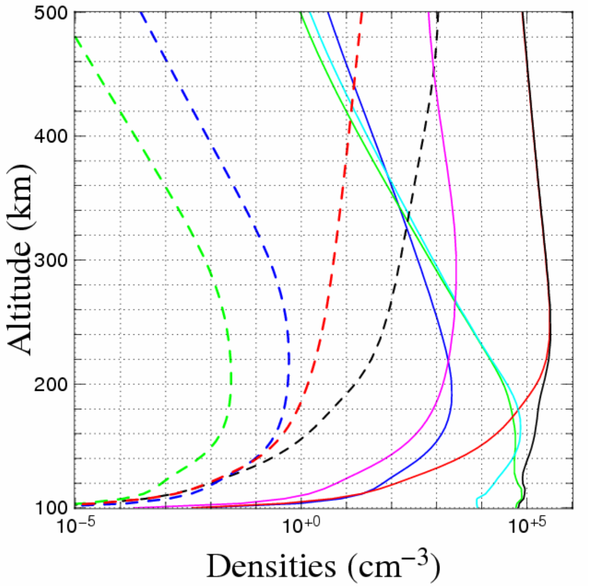

Figure 1.5 Density profiles predicted by Simon *et al* for the most abundant ionic species in the ionosphere[46]. The different lines represent N_2^+ (solid dark blue), O_2^+ (solid green), O^+ (solid red), N^+ (magenta), H^+ (dashed black), NO^+ (solid light blue), N_2^{2+} (dashed blue), O_2^{2+} (dashed green) and O^{2+} (dashed red). The black line represents the electron density.

It is interesting to note that despite the fact that O^{2+} is undoubtedly the most abundant atomic dication in the TA, Simon *et al* predict N_2^{2+} to be more abundant than O_2^{2+}. The reason for this is that molecular N_2 is much more abundant than molecular O_2 in these regions due to the efficient photolysis of O_2[40]. Simon *et al* predict that the three most abundant dications, O^{2+}, N_2^{2+} and O_2^{2+} will be destroyed by dissociative recombination and collisions with the three most abundant neutral species N_2, O_2 and O. Dication-monocation collisions will be negligible in frequency compared to dication-neutral collisions, compounded by the fact that these former two species will experience a Coulomb repulsion from each other. Evidently, dications such as O^{2+}, O_2^{2+} and N_2^{2+} are not negligible atmospheric components as they were once thought to be, and due to their high energy have the potential to effect a change in the chemical composition of the terrestrial atmosphere. Clearly, collisions of these dications with trace atmospheric constituents could also lead to some interesting chemistry. This thesis reports an extensive investigation into the reactivity of O_2^{2+} with small neutral species, thus creating a useful body of work from which to increase our understanding of Earth's atmosphere.

1.2.5 The Interstellar Medium

Over 140 molecules have been detected in the interstellar medium (ISM)[56]. In addition, many indications of neutral and ionic polycyclic aromatic hydrocarbons (PAHs) have been detected. The diffuse interstellar bands, which are broad spectroscopic absorption lines, are observed in the visible and near infra–red (near IR) regions of the ISM. Many of these diffuse bands have been suggested to be due to the presence of PAHs, fullerenes, polyenes and polyynes[57]. It is proposed that conditions in the interstellar medium are such that formation of PAH dications should readily occur[58]. There are two possible dissociation pathways for the nascent PAH dications, charge separation into two monocations or fragmentation into a dication and neutral partner(s). It has been found experimentally that the latter dissociation process dominates for medium to large PAHs in regions of interstellar space where the PAH ions are formed with little internal energy[59–61]. Such fragmentation yields dicationic products in conjunction with small neutral products such as H, H_2, C_2H_2, C_2H_3 and C_4H_2[59]. The interaction of these fragment species with other molecules may be involved in the synthesis of other large interstellar hydrocarbons such as the polyynes.

Neutral–neutral reactions are usually inhibited by an activation barrier and in general proceed very slowly at the low gas temperatures in the interstellar medium. These temperatures can be as low as 5 K in dense clouds and 100 – 200 K in diffuse clouds[19]. In contrast, ion–neutral reaction rates usually increase with decreasing temperature as, in general, they are not inhibited by activation barriers[19]. Moreover, the polarisation attraction between the reactants increases the likelihood of a collision. The increased collision rate, coupled with the lack of activation energy barrier for ion–neutral reactions, means that these reactions are readily invoked to explain interstellar chemistry. The polarisation attraction is in general stronger for dication–neutral interactions, compared with monocation–neutral reactions, and so the former should proceed very rapidly at low temperatures. In fact, most dication–neutral reactions are thought to occur at close to the collision rate. Often, dication–neutral interactions result in the formation of a pair of monocations with significant translational energy[62]. These nascent monocations may go on to react with neutrals at elevated collision energy resulting in different products compared to thermal ion–neutral interactions[62]. Thus, dications may directly or indirectly influence the chemistry of the interstellar medium.

1.3 Bimolecular Reactivity of Dications

Upon interaction of an atomic or molecular dication with a neutral, there are several reactive processes that may occur. The general forms of these processes are shown in Table 1.1 and will be described in the next sections.

Table 1.1 General forms of the seven types of reactivity that can occur following interactions of dications with neutrals.

Equation	Reaction Process	
$AB^{2+} + XY \rightarrow AB^{+} + XY^{+}$	Non–dissociative single electron–transfer	(1.2)
$AB^{2+} + XY \rightarrow AB^{+} + X^{+} + Y$	Dissociative single electron–transfer	(1.3)
$\rightarrow A^{+} + B + XY^{+}$		
$\rightarrow A^{+} + B + X^{+} + Y$		
$AB^{2+} + XY \rightarrow AB + XY^{2+}$	Non–dissociative double electron–transfer	(1.4)
$AB^{2+} + XY \rightarrow AB + X^{+} + Y^{+}$	Dissociative double electron–transfer	(1.5)
$AB^{2+} + XY \rightarrow AB^{2+} + X + Y$	Collision–induced dissociation	(1.6)
$\rightarrow A^{+} + B^{+} + XY$		
$\rightarrow A^{2+} + B + XY$		
$AB^{2+} + XY \rightarrow ABX^{+} + Y^{+}$	Charge–separating bond–formation	(1.7)
$AB^{2+} + XY \rightarrow ABX^{2+} + Y$	Bond–formation with maintenance of two–fold charge	(1.8)

1.3.1 Electron–Transfer

Following interaction of a dication and neutral, single electron–transfer (SET) can occur. SET can be classed as non–dissociative (Equation (1.2)) or dissociative (Equation (1.3)). In non–dissociative SET, the net effect is formation of two product monocations that are directly derived from the reactants, for example Equation (1.9)[63].

$$Ne^{2+} + Ar \rightarrow Ne^{+} + Ar^{+} \qquad (1.9)$$

In dissociative SET, either or both of the product monocations may fragment to form new secondary monocations and neutrals; this class of reaction yields at least three products. An example is shown in Equation (1.10)[64].

$$N_2^{2+} + O_2 \rightarrow N_2^{+} + O^{+} + O \qquad (1.10)$$

Early investigations of dication–neutral reactivity were carried out employing multi–sector mass–spectrometers at laboratory frame collision energies of several keV[65-67]. Results from these experiments showed large amounts of dissociative or non–dissociative SET occur. More recently, experiments have been devised that allow the study of dication–neutral reactions at low collision energies of a few eV or lower[68-71]. These experiments have also revealed significant levels of SET reactivity. Thus, SET is clearly a common outcome of dication–neutral interactions over a wide range of collision energies.

In addition to transfer of a single electron, double electron–transfer (DET) can also occur following dication–neutral collisions (Equations (1.4) and (1.5)). This transfer of the two electrons can occur in either a concerted or sequential manner. Again, DET can be non–dissociative or dissociative and examples are shown in Equations (1.11)[70] and (1.12)(see Chapter 8 for more details).

$$CO^{2+} + Xe \rightarrow CO + Xe^{2+} \qquad (1.11)$$

$$O_2^{2+} + CS_2 \rightarrow O_2 + CS^{+} + S^{+} \qquad (1.12)$$

1.3.2 Collision–Induced–Dissociation

The Equations labelled (1.6) represent collision–induced–dissociation (CID). CID occurs due to the inelastic nature of dication–neutral collisions. The collisional energy or vibrational, electronic or rotational energy can be transferred from one reactant to the other causing either or both of them to fragment. In general, the dication fragments due to promotion of the reactant into vibrational levels high in the potential well, allowing the dication to tunnel through the potential barrier, forming two monocations. Alternatively, the dication fragmentation can take the form of neutral–loss yielding a new dication and a neutral fragment. However, there is no traditional "chemical" reaction, specifically, no electrons, atoms or molecular fragments are transferred between the reactants. CID is very different to the related process of unimolecular dissociation, which requires no collision between the reactants. In unimolecular dissociation, the metastable dication merely falls apart to a pair of monocations or a new dication and neutral after a certain amount of time. More specifically, the dication tunnels through the potential barrier that prevents instantaneous dissociation, yielding two fragments, which generally occurs for dications formed in vibrational levels near the top of the potential well.

1.3.3 Bond–Forming

Possibly the most intriguing and surprising reactivity that can occur following dication–neutral interactions is the formation of new chemical bonds. As described in section 1.4.1, early experiments at collision energies of the order of keV showed mainly CID and SET reactivity. Thus, it was a surprising discovery that, when advances in techniques made it possible to study dication–neutral reactions at collision energies of a few eV, many dicationic collision–systems exhibit bond–forming reactivity[64,68,72–74]. The first discovery of a dication–neutral bond–forming reaction was following interactions of O_2^{2+} with NO, where NO_2^+ products were observed[75]. However, doubt has been cast on the accuracy of these results by experiments reported in this thesis (see Chapter 8 for more information). Nevertheless, stimulated by this first report, numerous discoveries of chemical reactions following dication–neutral interactions were subsequently made.

Some of the earliest examples of dication–neutral bond–forming chemistry in the gas–phase involved collisions of substituted metal dications[76,77]. For example, successive collisions of $NbCH_2^{2+}$ with CH_4 results in $NbC_6H_6^{2+}$ and $NbC_6H_8^{2+}$ products[78]. The first observations of bond–forming reactions of dications not involving metals were reported by Price *et al* in the early 1990s, examples of which can be seen in Equations (1.13) and (1.14)[73].

$$OCS^{2+} + D_2 \rightarrow DS^{+} + [D + C + O]^{+} \tag{1.13}$$

$$CF_3^{2+} + D_2 \rightarrow DCF_2^{+} + [F + D]^{+} \tag{1.14}$$

It has also been shown for collisions between certain dications and H_2/D_2 that proton–transfer (PT) can dominate the product ion yield, Equation (1.15)[79].

$$CHBr^{2+} + H_2 \rightarrow CBr^{+} + H_3^{+} \tag{1.15}$$

Recent experiments[80-84] have shown that these bond–forming reactions can occur v*ia* a direct process, which is generally the case for PT[85], or *via* formation of a long–lived complex between the reactants[81]. For the duration that the complex remains intact, molecular rearrangement can take place resulting in formation of new chemical bonds and then the complex subsequently fragments. The complex can fragment in such a way that yields two monocations (Equation (1.7)), or alternatively the complex can fragment *via* neutral loss to form a new dicationic species (Equation (1.8)). Many examples of the latter type of bond–forming reaction, yielding a new dication, have been found by Bassi *et al* and some examples are shown in Equations (1.16)[86], (1.17)[87], (1.18)[88] and (1.19)[89].

$$CO^{2+} + Ar \rightarrow ArC^{2+} + O \tag{1.16}$$

$$Ar^{2+} + N_2 \rightarrow ArN^{2+} + N \tag{1.17}$$

$$Ar^{2+} + CO_2 \rightarrow ArC^{2+} + O_2 \tag{1.18}$$

$$Ar^{2+} + O_2 \rightarrow ArO^{2+} + O \tag{1.19}$$

This list is by no means exhaustive and many more examples of bond–formation with maintenance of the two–fold charge are present in the literature. In conclusion, there are several mechanisms by which dications and neutrals react; SET, DET, CID and bond–forming chemistry can all occur. SET and DET cross–sections are generally fairly independent of collision energy, whereas cross–sections for CID and chemical reactivity can have a very sensitive dependence on the collision energy. Moreover, all of these reactive processes can proceed by a variety of mechanisms, specifically either directly or *via* formation of a complex. The position–sensitive coincidence technique used for the experiments reported in this thesis allows us to reveal the mechanism of each reaction channel detected. Further details regarding the elucidation of dicationic reaction dynamics will be given in Chapter 2.

1.4 Experiments and Techniques Employed to Probe Dication Properties and Reactions

In order to understand the reactivity of dications, it is first important to grasp dicationic properties. For the experiments described in this thesis it is often very useful to know the enthalpy of formation of the dicationic reactant. Then, the dication–neutral reaction energetics can be calculated and compared to experimental results. Often such comparisons can allow the electronic, and sometimes vibrational, states participating in the reaction to be determined. Therefore, a knowledge of dicationic enthalpies of formation is clearly desirable. In this section, some techniques used to probe dication properties will be described followed by a discussion of experimental methods used to investigate their reactivity.

1.4.1 Probing the Properties of Dications

Several collisional ionisation methodologies have been employed to study dications: electron ionisation (EI) threshold measurements, Auger spectroscopy, translational energy spectrometry (TES) and charge–transfer spectrometry. EI can be employed to determine the threshold double ionisation energy of atoms or neutrals simply by measurement of dication signal intensities as a function of the ionising electron energy[90–94]. A step in the ionisation cross–section should be seen at the threshold for formation of the doubly charged ion. Auger spectroscopy can be used in conjunction with EI, or photoionisation, to gain information about the energies of the electronic states of a dication. Auger spectroscopy is particularly useful when the Auger electron is detected in coincidence with the nascent dication[95-101]. TES involves the collision of a high–energy ion with a neutral in a collision cell followed by precise measurement of the translational energy loss (or gain) of the fast ion as a result of the collision. The loss or gain of translational energy allows the electronic and vibrational states of the ion to be determined. In modified TES experiments, the ionising energy can be varied whilst monitoring the product peak heights, which also yields detailed information about the electronic states of the dication[102-105]. Very similar to TES, double charge-transfer spectrometry involves the interaction of a fast moving monocation with a neutral species. Upon collision, two electrons are transferred from the neutral to the monocation, forming a dication (from the neutral precursor) and an anion (from the monocationic precursor). The translational energy loss of the nascent anion from that of the original monocation is measured, thereby yielding information about the ionisation energy of the neutral collision partner[13,106-110].

Excited electronic states of some molecular dications fluoresce. Simple optical spectroscopic detection of this fluorescent light can allow for the characterisation of the electronic states of dications. In 1958 Carroll observed the fluorescence from N_2^{2+} and obtained a rotationally resolved spectrum of the $^1\Sigma_u^+$-$X^1\Sigma_g^+$ transition[52]. Cossart *et al*, who detected additional fluorescent bands of the N_2^{2+} dication, later confirmed this assignment[111]. However, it has recently become clear that few dicationic states have lifetimes that allow the detection of their fluorescence. For example, Pettersson *et al* predicted that the spectroscopic observation of the $A^2\Pi$-$X^2\Sigma^+$ band of NO^{2+} should be possible by photofragmentation spectroscopy[32]. However, the NO^{2+} $A^2\Pi$-$X^2\Sigma^+$ band was not observed in their experiments. This lack of observation of the band prompted these authors to say that more accurate computational methods are needed to accurately model the energies and lifetimes of dicationic electronic states. Moreover, these authors state that clearly further studies of the spectroscopy of dications are necessary[32].

1.4.2 Coincidence Methodologies

Perhaps the most powerful techniques developed for studying dicationic states, and their properties, combine photoionisation with coincidence detection. Photoionisation allows the ionisation process to be state selective and offers much "finer tuning" than EI since the full-width-half-maximum of the ionising electron energy distribution is generally wider than the energy spread of the ionising photon energy. Coincidence detection simply means that two or more species from a single ionisation event are detected in a correlated manner. These species can be photoion fragments, photoelectrons, dications or fluorescence photons. Since the pioneering work of

McCulloh *et al*[112], who developed the idea of coincidence detection for the study of multiply charged ions in 1965, several research groups have implemented such techniques. However, none have adopted the coincidence methodology to the extent of the Eland group. With their 1985 publication[113], Curtis and Eland renewed interest in the use of coincidence methodologies, in particular for the study of multiply charged species. Curtis and Eland used TOF spectrometry to detect, in coincidence, the two photoion fragments that were produced by dissociative photo–ionisation of neutral molecules. Detection of these two fragment ions in coincidence is termed the photoion–photoion–coincidence (PIPICO) technique. At this time, five diatomic molecules were studied (O_2, NO, I_2, ICl and HCl), six triatomics (N_2O, CO_2, COS, CS_2, SO_2 and H_2S) and three penta–atomics (CF_4, CCl_4 and CH_3I). Using the PIPICO technique, Curtis and Eland were able to distinguish the identity of the different dissociation channels of the above molecules. Moreover, these authors could even use the measured kinetic energy release to reveal the energies of the precursor dication states[113].

In the following decades, the Eland group, and others, developed a large number of related techniques based on the combination of TOF spectrometry, fluorescence spectroscopy and coincidence detection. Specifically: the photoelectron–photoelectron–coincidence (PEPECO), photoelectron–photoion coincidence (PEPICO), threshold photoelectrons coincidence (TPEsCO), photoelectron–photoion–photoion coincidence (PEPIPICO), photoelectron–photoelectron–photoion coincidence (PEPEPICO), photoelectron–photoelectron–photoion–photoion coincidence (PEPEPIPICO), photoion–fluorescence coincidence (PIFCO), photoelectron–photoion–fluorescence coincidence (PEPIFCO) and the photoelectron–photoelectron–fluorescence coincidence (PEPEFCO) techniques. The Eland group alone has used this plethora of methodologies to investigate the double ionisation and dissociation dynamics of over 200 atoms or molecules, resulting in over 100 publications on this subject. These target species encompass a wide selection of atoms and molecules, for example, atoms such as He[114], Ar[115,116], Xe[117-120], Hg[121,122] and Cd[123] for which extremely high resolution double ionisation spectra were obtained. Exotic molecules such as P_4^{2+}[124] and substituted metal dications such as $Fe(CO)_5^{2+}$[125] were also studied by the Eland group *via* their coincidence techniques. Doubly ionised large organic molecules including benzene[126,127], hexafluorobenzene[128], s–tetrazine[129], toluene[130], naphthalene[60,127] and related heterocyclic compounds[59], PAHs such as those thought to exist in the interstellar medium[61], and n–alkanes up to triacontane[131] have also been investigated. For smaller neutral molecules such as O_2, NO, CO, H_2O or N_2O, numerous studies have been carried out and the Eland group alone has at least eight publications pertaining to the study of CO^{2+} and six involving the study of O_2^{2+} *via* various TOF and fluorescence coincidence methods. Consequently, for small dications such as CO^{2+} and O_2^{2+}, the DIE and low lying electronic states are well characterised.

The properties of dications have clearly received widespread attention and, employing the methodologies described above, accurate double IEs have been determined for many atoms and molecules. The dissociation dynamics of nascent dications, formed by EI, photoionisation or CS, have also been extensively investigated. In contrast, the reactions of dications are far less well studied. Several methodologies have been employed to investigate dication–neutral reactivity and these are described in the next sections (1.4.3 – 1.4.5). These experimental methodologies were often developed to study monocation–neutral reactivity, however, the next sections only deal with their application to studies of dication–neutral reactivity.

1.4.3 Selected–Ion–Flow–Tube Experiments

The selected–ion–flow–tube technique was first introduced by Adams and Smith in 1976[132]. Briefly, a mass–selected low energy ion beam is injected into a flowing gas and at some point "downstream" the reactant neutral is also injected. Whilst the ion and neutral concomitantly flow down the drift–tube, reactions occur and the products are identified by quadrupole mass–spectrometry. The inclusion of multiple injection ports for the neutral allows the study of consecutive reactions with different gases. Using SIFT experiments, the rate constants for several dication–neutral reactions were determined, principally between rare gas dications with rare gases and molecules such as H_2, N_2, O_2, CO, CO_2 and CH_4. In addition, the branching ratios into separate ion–neutral reaction channels can be determined[133-136].

1.4.4 Crossed–Beam Experiments

Some of the earliest studies of dication–neutral reactivity involved collisional experiments using modified mass–spectrometers, these interactions tended to be at keV collision energies[137–139]. Later, crossed beam mass–spectrometers allowed for the study of dication–neutral interactions at low collision energies of a few eV. In general, crossed–beam experiments involve the production of dications *via* EI, followed by extraction and mass–selection of the beam. The beam of ions then passed into a reaction region where the neutral beam is introduced perpendicularly, generally *via* a pulsed valve. The potential of the collision cell is set to define the collision energy of the system. Products are extracted into a mass–spectrometer and analysed. The crossed–beam experiment used by Price *et al* in the 1990s employed time–of–flight (TOF) mass–spectrometry to analyse the products[70]. Using this crossed–beam apparatus, Price and others studied the interactions of many dications with neutrals including those of CO^{2+}[70], OCS^{2+}, CO_2^{2+}[71], CF_2^{2+}[140], CF_3^{2+}, SF_3^{2+} and SF_4^{2+}[141] with the rare gases. In addition, an extensive study was carried out looking at the reactivity of CF^{2+}, CF_2^{2+}, CF_3^{2+}, SF_4^{2+}, SF_3^{2+}, SF_2^{2+}, CO_2^{2+} and OCS with the neutrals Xe, D_2, O_2, N_2, NO and CO[73].

The EVA II crossed–beam apparatus built by the Herman group uses magnetic sector mass–spectrometry to analyse the product ions, a schematic of this experiment is shown in Figure 1.6[81].

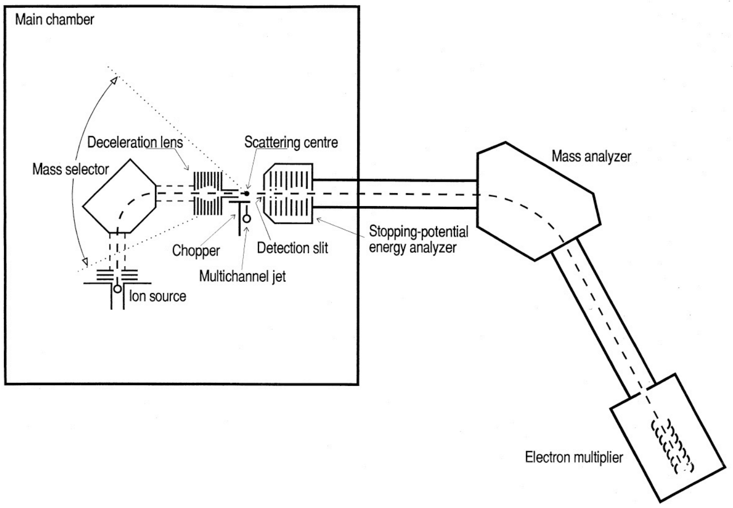

Figure 1.6 The EVA II crossed–beam mass–spectrometer built by the Herman group. The spectrometer is used to determine the relative differential cross–sections of products formed following dication–neutral interactions. From ref. [81].

Ions are formed by EI and mass–selected, decelerated to the desired collision energy and they then interact with the neutral that is injected perpendicularly to the ion beam. Products travel through a detection slit and energy and mass analysed. This spectrometer is an updated version of an earlier design[142], but both have the intriguing capability to obtain angularly resolved scattering of the product ions from dication–neutral reactions. Angular distributions are obtained by rotating the beams about the scattering centre. Such angular distributions have allowed the reaction dynamics of a wide range of systems to be determined.

In the 1980s, the crossed beam design described above was employed to determine the relative differential cross–sections of products following collisions of atomic dications with atomic neutrals[142–144]. More recently, crossed–beam experiments have been used to elucidate the electronic states involved in the SET reaction between CO_2^{2+} and CO_2[145]. Other recent applications of angularly–resolved crossed–beam spectrometry include the study of the dynamics of reactions between CF_3^{2+} and D_2[146], $C_4H_3^{2+}$ and Kr, Xe, H_2, N_2, NO, NH_3, C_2H_2 and CH_4[83].

1.4.5 Guided Ion–Beam Experiments

Guided ion–beam experiments are generally very similar to crossed–beam experiments in that ions are generated and mass–selected before entering a collision region. The principle experimental difference between the former from the latter is that the collision region in guided ion–beam experiments is commonly electrostatically constrained by an octopole ion guide in order to prevent the losses of any product ions formed with transverse velocities. Products are then identified by use of a quadrupole mass spectrometer. Guided ion–beam experiments are generally in a linear configuration. The principle difference between crossed–beam and guided ion–beam experiments is that the former are very useful for determining reaction dynamics, whereas the latter can be used to determine very accurate reaction channel cross–sections. Conversely, accurate cross–sections are difficult to obtain using crossed–beam experiments and dynamics are difficult to obtain using guided ion–beam experiments. Therefore, these two techniques can be employed in a complimentary manner for increasing our overall understanding of dication–neutral reactivity.

In Prague, Schröder *et al* employ a guided ion–beam technique in a QOQ configuration (where Q stands for quadrupole and O stands for octopole). In this experiment, ions are generated by EI, mass selected by the first quadrupole and interact with the neutral in the octopole collision cell. The second quadrupole analyses the product masses[85]. Guided ion–beam experiments do not allow for angularly resolved data to be collected, however, often the mass–resolution is very good. Recent studies undertaken in Prague include investigations of the reactivity of dications, generated by dissociative double ionisation of PAH precursors, towards rare gases[147]. As discussed earlier, dissociative double ionisation of PAHs is thought to occur in the ISM and so such studies begin to give insights into how the chemistry of the PAHs might unfold.

The CERISES (Collision et Reaction d'Ions Selectionnares par Electrons de Seuil) guided ion–beam experiment in Paris has been extensively used to study ion–neutral reactions of relevance to planetary ionospheres. In contrast to the majority of techniques described here, the ions at CERISES are generated by photoionisation with Synchrotron radiation. The CERISES experiment has a QOQ arrangement where the components are operated in the same manner to the Prague experiment. Dication–neutral reactions of ionospheric importance that have been studied employing CERISES include that of $CHCl^{2+}$ with Ar and D_2[148] and CO_2^{2+} with CO_2 and CO[149].

Another guided ion–beam experiment in Trento, Italy has been employed to investigate dication–neutral reactions. Here, EI is used to generate ions, they are mass–selected using a magnetic sector mass–spectrometer and interact with the neutral in an octopole ion guide. Products are collected and analysed using a quadrupole. This apparatus has been used to study the bond–forming reactions following collisions of Ar^{2+} with O_2[89] and CO^{2+} with Ar[86].

A similar feature of most these guided ion–beam experiments is that the collision energies of effectively zero eV, with some spread, can be achieved by varying the potential of the octopole relative to the rest potential of the ion beam. Varying the collision energy in such experiments is also comparatively simple, so collision energy dependences of reaction channels can be extracted. In part due to the use of guided ion–beam experiments, we now know that the cross–sections for chemical reaction channels between dications and neutrals generally decrease rapidly with increasing collision energy and peak near zero collision energy. For example, the $ArCF_2^{2+}$ bond–forming product, observed following collisions of CF_3^{2+} with Ar in a guided ion–beam experiment, shows a strong collision energy dependence peaking at zero eV, as shown in Figure 1.7.

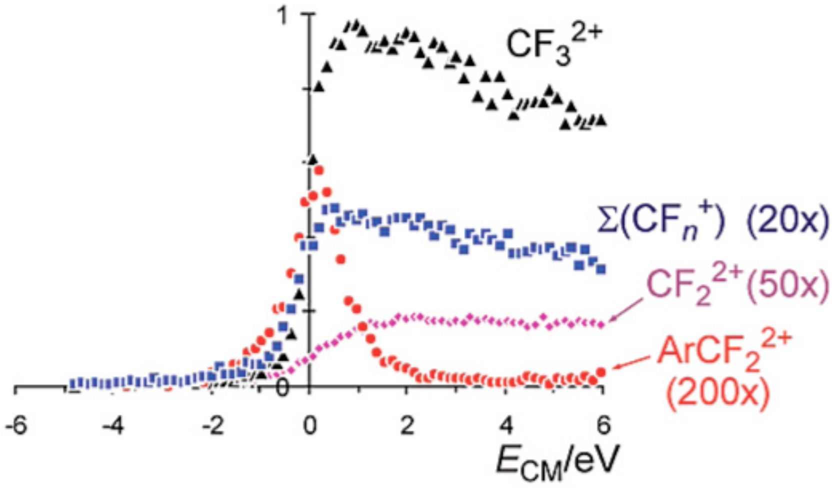

Figure 1.7 Centre-of-mass frame energy dependence of the major reaction channels between CF_3^{2+} and Ar. The red circles show the energy dependence of the bond-forming channel yielding $ArCF_2^{2+}$, which shows a distinct peak at "zero" collision energy. From ref. [150].

All of these methodologies that have been used to study dication-neutral reactivity suffer a similar drawback, specifically, the results take the form of a one-dimensional mass spectrum from which products have to be identified. However, it is often difficult or impossible to determine which monocations are formed together in the same dicationic reaction channel. For example, NO^+ has been detected, following interactions of N_2^{2+} with O_2, employing guided ion-beam mass spectrometry. In this reaction channel, the partner ion could be NO^+, N^+ or O^+. Coincidence detection of the product ions removes this ambiguity since product ions formed in the same reactive event are detected in a correlated manner. The results presented in this thesis were obtained employing a crossed-beam apparatus that incorporates coincidence detection of both monocationic products, allowing for more information on dication-neutral reactions to be elucidated than ever before. A description of the experimental method is given in Chapter 2.

1.5 Collision Theory

The theoretical approaches used to model and explain dication-neutral reactivity is extensive. Perhaps one of the most prolific and only widely applied theory is the Landau-Zener Reaction Window (LZRW) theory of electron-transfer reactions. The LZRW theory will be outlined in section 1.5.1. In addition, a theoretical approach to chemical reaction channels between dications and neutrals is also described in section 1.5.2.

1.5.1 Landau–Zener Reaction Window Theory

The LZRW theory is an extension of Landau–Zener theory, which describes the potential energy curve crossings in atom–atom collisions[151]. LZRW theory, which is a semi–classical depiction of atomic collisions, allows the probability of SET between a dication and neutral to be calculated[70]. Specifically, an ET reaction between a dication and neutral occurs at the crossing between the potential energy curve (PEC) for the reactants and that of the products as seen schematically in **Figure 1.8**. The reactant potential is dominated by polarisation attraction between the dication and neutral, and the product potential is dominated by the Coulomb repulsion between the two monocations. The interspecies separation at which these two PECs cross is termed the "crossing radius" R_c, as seen in Figure 1.8. The probability of SET is determined, among other things, by the extent of coupling between the reactant and product PECs at R_c.

Qualitatively, the extent of the coupling between the PECs is generally optimal, maximising the probability of SET, when R_c lies between 3 and 6 Å. This range of interspecies separations is termed the "reaction window". If R_c lies outside the reaction window then the probability of SET is greatly reduced. At separations larger than 6 Å, this is due to the low level of coupling between the product and reactant PECs. Conversely, at separations smaller than 3 Å, the coupling between the PECs is too strong. This strong coupling allows the curve crossing to happen too readily; SET will occur as the reactant species approach one another, and again as the monocations fly apart. Hence, the electron is transferred twice, once to the reactant dication and then back again to the reactant neutral; consequently, no net ET occurs. A compromise is reached in the reaction window, where the intermediate coupling between the PECs favours net SET.

In order for net SET to take place, the electron must be transferred from the neutral to the dication only once, whereas the system passes through R_c twice. Thus, SET must occur on either the first (Figure 1.8 (a)) or second (Figure 1.8 (b)) instance of curve crossing. Consequently, the optimum probability of SET occurring at a single curve crossing is 0.5, to allow net SET to take place. The probability of the system remaining on the same PEC after a PEC crossing δ is given by Equation (1.20). Thus, the overall probability of SET is given by 2δ(1-δ) and reaches a maximum at 0.5.

$$\delta = \exp\left(\frac{-\pi \left| H_{12} \right|^2}{2\hbar \left| V_1^{'} - V_2^{'} \right| \ v_r} \right) \tag{1.20}$$

The LZRW theory can be used to calculate accurate cross–sections for SET reactions between dications and neutrals. Quantitative details of this calculation and the mathematical derivation of the LZRW theory are given in Chapter 3.

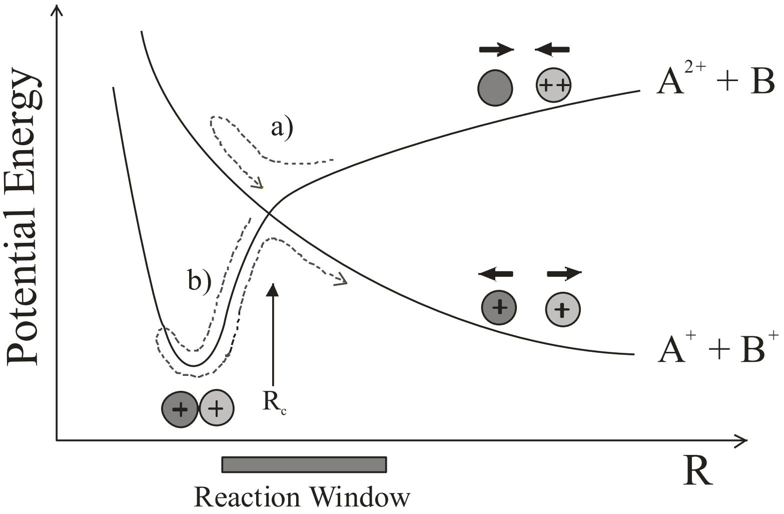

Figure 1.8 Schematic of the potential energy curves involved in a simple single electron–transfer between and dication and neutral. At significant interspecies separation, the potential between A^{2+} and B is dominated by polarisation attraction and at small interspecies separation is dominated by the repulsive wall. Over all separations, the potential between A^{+} and B^{+} has the form of Coulomb repulsion. The crossing between these potentials is labelled R_c. Two possible pathways are shown that involve (a) crossing between the PECs at reaching R_c for the first time and (b) crossing between the PECs at reaching R_c for the second time.

Molecular dications may be non–spherically symmetric and hence have an anisotropic potential energy surface (PES). The anisotropy of the PES introduces an angular dependence of the curve crossing probability in ET reactions[70]. Moreover, in some cases, large molecular dications can be approximated by two isolated positive charges residing on separate parts of the molecule. These factors may alter the representation of PEC/PES coupling in the reaction window theory[70]. Hence, for very large and/or less symmetric molecular dications, the LZRW theory may have limited application.

1.5.2 Bond–Forming Reactions

A model of the potential energy surfaces (PESs) involved in dication–neutral bond–forming reactions has been developed by Herman *et al*[81,152]. The model successfully explains both SET and bond–forming reactivity and their competition. A general form of this model is shown in Figure 1.9.

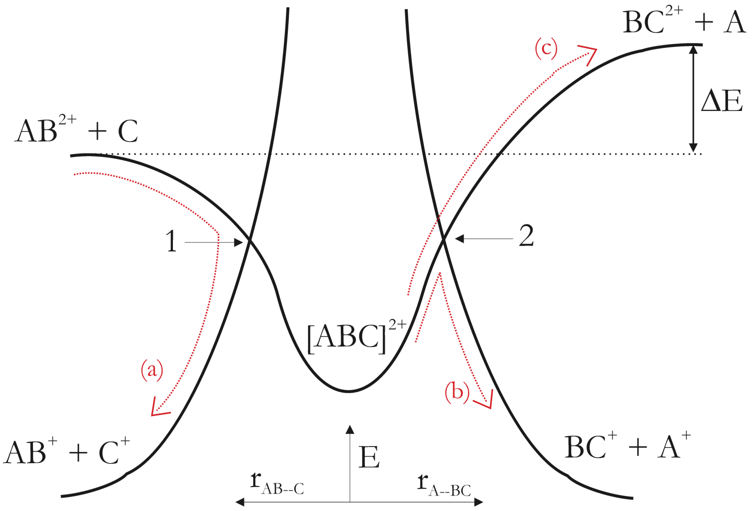

Figure 1.9 Schematic of the potential energy curves involved in complex formation and subsequent bond–forming reaction between a dication AB^{2+} and neutral C. If the system crosses at crossing 1, then the effect is simple SET. A complex $[ABC]^{2+}$ is formed at the distance of closest approach. Such a complex may dissociate to give products with new connectivity of the atoms BC^{2+} and A. As these products separate, the system passes through another curve crossing with the PES for two monocations BC^{+} and A^{+}.

The schematic PESs shown in Figure 1.9 can be divided into two regions. Firstly, that of the reactant approach, on the left hand side of the figure, and that of the product "departure", on the right hand side of the figure. In the centre of the figure is the pseudo–complex between the reactants $[ABC]^{2+}$. On the left hand side, as the reactants approach they pass through the curve crossing with the PES for two monocationic products directly derived from the reactants, crossing 1. If the system crosses at this point, then the result is a SET reaction, shown by pathway (a). On the right hand side of the figure, the connectivity of the reactant atoms has changed. As these products separate, they may undergo another curve crossing (2) that results in two monocationic products with different connectivity, pathway (b). Alternatively, the new products may continue to separate without crossing at crossing 2, resulting in a product dication and a neutral, again with different connectivity to the reactants, pathway (c). Of course, another alternative is that the complex simply fragments *via* the same potential as the approach, in which case there has been no reaction and the reactants are regenerated. This model of dicationic reactivity emphasises the direct competition between SET and the two types of bond–forming reactivity.

1.6 Summary

In this Chapter dications have been introduced, firstly with a discussion of their properties and potential energy surfaces on which they exist. Secondly, an explanation of the environments where dications may be significant has been given. These environments principally comprise planetary ionospheres and the interstellar medium. An overview of possible dication–neutral reactivity has also been given. Experimental methods employed to probe the properties and reactions of dications have also been explained. Lastly, a qualitative account of the Landau–Zener Reaction Window theory that has been used extensively to rationalize dication–neutral SET reactivity was given. In the next Chapter, a detailed explanation of the experimental methodology used to further our knowledge of dication–neutral reactivity is given.

1.7 References

[1] Conrad, R, *Phys. Z.* **1930**, *31*, 888.

[2] Vaughan, A, *Phys. Rev.* **1931**, *38*, 1687.

[3] Hagstrum, H D and Tate, J T, *Phys. Rev.* **1941**, *59*, 354.

[4] Tate, J T, Smith, P T and Vaughan, A, *Phys. Rev.* **1935**, *48*, 525.

[5] Pauling, L, *J. Chem. Phys.* **1933**, *1*, 56–59.

[6] Schroder, D and Schwarz, H, *J. Phys. Chem. A* **1999**, *103*, 7385–7394.

[7] Newson, K A and Price, S D, **1997**, *269*, 93–98.

[8] Mathur, D, Andersen, L H, Hvelplund, P, Kella, D and Safvan, C P, *J. Phys. B* **1995**, *28*, 3415–3426.

[9] Andersen, L H, Posthumus, J H, Vahtras, O, Agren, H, Elander, N, Nunez, A, Scrinzi, A, Natiello, M and Larsson, M, *Phys. Rev. Lett.* **1993**, *71*, 1812–1815.

[10] Hvelplund, P, Andersen, L H, Haugen, H K, Lindhard, J, Lorents, D C, Malhotra, R and Ruoff, R, *Phys. Rev. Lett.* **1992**, *69*, 1915–1918.

[11] Steger, H, Devries, J, Kamke, B, Kamke, W and Drewello, T, *Chem. Phys. Lett.* **1992**, *194*, 452–456.

[12] Field, T A and Eland, J H D, *J. Elec. Spec. Rel. Phenom.* **1995**, *73*, 209–216.

[13] Lammertsma, K, Schleyer, P V and Schwarz, H, *Angew. Chem.–Int. Edit. Engl.* **1989**, *28*, 1321–1341.

[14] Jayaweera, P, Blades, A T, Ikonomou, M G and Kebarle, P, *J. Am. Chem. Soc.* **1990**, *112*, 2452–2454.

[15] Katta, V, Chowdhury, S K and Chait, B T, *J. Am. Chem. Soc.* **1990**, *112*, 5348–5349.

[16] Ast, T and Beynon, J H, *Int. J. Mass Spectrom. Ion Process.* **1980**, *32*, 385–390.

[17] Harris, F M, *Int. J. Mass Spectrom. Ion Process.* **1992**, *120*, 1–43.

[18] Petrie, S and Bohme, D K, *Mon. Not. Roy. Astron. Soc.* **1994**, *268*, 103–108.

[19] Smith, D and Spanel, P, *Mass Spec. Rev.* **1995**, *14*, 255–278.

[20] Mathur, D, *Phys. Rep.–Rev. Sect. Phys. Lett.* **1993**, *225*, 193–272.

[21] Yau, A W, Whalen, B A and Sagawa, E, *Geophys. Res. Lett.* **1991**, *18*, 345–348.

[22] Yau, A W, Whalen, B A, Goodenough, C, Sagawa, E and Mukai, T, *J. Geophys. Res–Space Phys.* **1993**, *98*, 11205–11224.

[23] Craven, P D, Olsen, R C, Chappell, C R and Kakani, L, *J. Geophys. Res–Space Phys.* **1985**, *90*, 7599–7605.

[24] Vuitton, V, Yelle, R V and Lavvas, P, *Philos. Trans. R. Soc. A–Math. Phys. Eng. Sci.* **2009**, *367*, 729–741.

[25] Cravens, T E, Robertson, I P, Clark, J, Wahlund, J E, Waite, J H, Ledvina, S A, Niemann, H B, Yelle, R V, Kasprzak, W T, Luhmann, J G, McNutt, R L, Ip, W H, De La Haye, V, Muller–Wodarg, I, Young, D T and Coates, A J, *Geophys. Res. Lett.* **2005**, *32*,

[26] Robertson, I P, Cravens, T E, Waite, J H, Yelle, R V, Vuitton, V, Coates, A J, Wahlund, J E, Agren, K, Mandt, K, Magee, B, Richard, M S and Fattig, E, *Planet Space Sci.* **2009**, *57*, 1834–1846.

[27] Cravens, T E, Robertson, I P, Waite, J H, Yelle, R V, Vuitton, V, Coates, A J, Wahlund, J E, Agren, K, Richard, M S, La Haye, V, Wellbrock, A and Neubauer, F M, *Icarus* **2009**, *199*, 174–188.

[28] Vuitton, V, Yelle, R V and McEwan, M J, *Icarus* **2007**, *191*, 722–742.

[29] Thissen, R, Vuitton, V, Lavvas, P, Lemaire, J, Dehon, C, Dutuit, O, Smith, M A, Turchini, S, Catone, D, Yelle, R V, Pernot, P, Somogyi, A and Coreno, M, *J. Phys. Chem. A* **2009**, *113*, 11211–11220.

[30] McEwan, M J, Scott, G B I and Anicich, V G, *Int. J. Mass Spec.* **1998**, *172*, 209–219.

[31] McEwan, M J and Anicich, V G, *Mass Spectrom. Rev.* **2007**, *26*, 281–319.

[32] Pettersson, L G M, Siegbahn, P E M, Brostrom, L, Mannervik, S and Larsson, M, *Chem. Phys. Lett.* **1992**, *191*, 279–286.

[33] Petrie, S, *Icarus* **2001**, *151*, 196–203.

[34] Dimitrov, V and BarNun, A, *Prog. React. Kinet.* **1997**, *22*, 67–81.

[35] Ricketts, C L, Schroder, D, Alcaraz, C and Roithova, J, *Chem.–Eur. J.* **2008**, *14*, 4779–4783.

[36] Roithova, J and Schroeder, D, *J. Am. Chem. Soc.* **2006**, *128*, 4208–4209.

[37] Witasse, O, Dutuit, O, Lilensten, J, Thissen, R, Zabka, J, Alcaraz, C, Blelly, P L, Bougher, S W, Engel, S, Andersen, L H and Seiersen, K, *Geophys. Res. Lett.* **2002**, *29*, 1263.

[38] Gronoff, G, Lilensten, J, Simon, C, Witasse, O, Thissen, R, Dutuit, O and Alcaraz, C, *Astron. Astrophys.* **2007**, *465*, 641–645.

[39] Taylor, H A, Brinton, H C, Wagner, T C G, Blackwell, B H and Cordier, G R, *IEEE Trans. Geosci. Remote Sensing* **1980**, *18*, 44–49.

[40] Dibeler, V H, *Anal. Chem.* **1954**, *26*, 58–65.

[41] Meinel, A B, *Rep. Prog. Phys.* **1951**, *14*, 121–&.

[42] Hoffman, J H, *Science* **1967**, *155*, 322–&.

[43] Breig, E L, Torr, M R, Torr, D G, Hanson, W B, Hoffman, J H, Walker, J C G and Nier, A O, *J. Geophys. Res–Space Phys.* **1977**, *82*, 1008–1012.

[44] Hoffman, J H, *J. Geophys. Res.* **1967**, *72*, 1883–&.

[45] Hoffman, J H, *Proc. IEEE* **1969**, *57*, 1063–&.

[46] Simon, C, Lilensten, J, Dutuit, O, Thissen, R, Witasse, O, Alcaraz, C and Soldi–Lose, H, *Ann. Geophys.* **2005**, *23*, 781–797.

[47] Breig, E L, Torr, M R and Kayser, D C, *J. Geophys. Res–Space Phys.* **1982**, *87*, 7653–7665.

[48] Chandler, M O, Ponthieu, J J, Cravens, T E, Nagy, A F and Richards, P G, *J. Geophys. Res–Space Phys.* **1987**, *92*, 5885–5895.

[49] Chappell, C R, Olsen, R C, Green, J L, Johnson, J F E and Waite, J H, *Geophys. Res. Lett.* **1982**, *9*, 937–940.

[50] Prasad, S S and Furman, D R, *J. Geophys. Res.* **1975**, *80*, 1360–1362.

[51] Donahue, T M, Zipf, E C and Parkinso.Td, *Planet Space Sci.* **1970**, *18*, 171–&.

[52] Carroll, P K, *Can. J. Phys.* **1958**, *36*, 1585–&.

[53] Ehresmann, A, Liebel, H, Schmoranzer, H, Zimmermann, B, Kammer, S, Schartner, K H, Demekhin, P V and Sukhorukov, V L, *J. Phys. B–At. Mol. Opt. Phys.* **2003**, *36*, 3669–3681.

[54] Avakyan, S V, *J. Opt. Technol.* **1998**, *65*, 870–875.

[55] Avakyan, S V, *Phys. Chem. Earth Pt. C–Solar–Terr. Planet. Sci.* **2001**, *26*, 259–263.

[56] Snow, T P and Bierbaum, V M, *Annu. Rev. Anal. Chem.* **2008**, *1*, 229–259.

[57] Leach, S, *Planet Space Sci.* **1995**, *43*, 1153–1164.

[58] Leach, S, *J. Elect. Spec. Rel. Phenom.* **1986**, *41*, 427–438.

[59] Leach, S, Eland, J H D and Price, S D, *J. Phys. Chem.* **1989**, *93*, 7575–7583.

[60] Leach, S, Eland, J H D and Price, S D, *J. Phys. Chem.* **1989**, *93*, 7583–7593.

[61] Hagan, D A and Eland, J H D, *Rapid Commun. Mass Spectrom.* **1991**, *5*, 512–517.

[62] Price, S D, *Phys. Chem. Chem. Phys.* **2003**, *5*, 1717–1729.

[63] Harper, S M, Hu, W P and Price, S D, *J. Phys. B* **2002**, *35*, 4409–4423.

[64] Ricketts, C L, Harper, S M, Hu, S W P and Price, S D, *J. Chem. Phys.* **2005**, *123*,

[65] Mathur, D, Kingston, R G, Harris, F M, Brenton, A G and Beynon, J H, *J. Phys. B–At. Mol. Opt. Phys.* **1987**, *20*, 1811–1822.

[66] Mathur, D, Reid, C J and Harris, F M, *J. Phys. B–At. Mol. Opt. Phys.* **1987**, *20*, L577–L581.

[67] Hasted, J B and Smith, R A, *Proc. Royal Soc. Lond. Series A: Math. Phys. Sci.* **1956**, *235*, 354–358.

[68] Dolejsek, Z, Farnik, M and Herman, Z, *Chem. Phys. Lett.* **1995**, *235*, 99–104.

[69] Mrazek, L, Zabka, J, Dolejsek, Z and Herman, Z, *Collect. Czech. Chem. Commun.* **2003**, *68*, 178–188.

[70] Rogers, S A, Price, S D and Leone, S R, *J. Chem. Phys.* **1993**, *98*, 280–289.

[71] Price, S D, Rogers, S A and Leone, S R, *J. Chem. Phys.* **1993**, *98*, 9455–9465.

[72] Price, S D, *J. Chem. Soc.–Faraday Trans.* **1997**, *93*, 2451–2460.

[73] Price, S D, Manning, M and Leone, S R, *J. Am. Chem. Soc.* **1994**, *116*, 8673–8680.

[74] Roithova, J and Schroder, D, *Phys. Chem. Chem. Phys.* **2007**, *9*, 2341–2349.

[75] Chatterjee, B K and Johnsen, R, *J. Chem. Phys.* **1989**, *91*, 1378–1379.

[76] Tonkyn, R and Weisshaar, J C, *J. Am. Chem. Soc.* **1986**, *108*, 7128–7130.

[77] Weisshaar, J C, *Accounts Chem. Res.* **1993**, *26*, 213–219.

[78] Roth, L M and Freiser, B S, *Mass Spectrom. Rev.* **1991**, *10*, 303–328.

[79] Roithova, J, Zabka, J, Herman, Z, Thissen, R, Schroder, D and Schwarz, H, *J. Phys. Chem. A* **2006**, *110*, 6447–6453.

[80] Herman, Z, *Int. Rev. Phys. Chem.* **1996**, *15*, 299–324.

[81] Herman, Z, Zabka, J, Dolejsek, Z and Farnik, M, *Int. J. Mass Spectrom.* **1999**, *192*, 191–203.

[82] Mrazek, L, Zabka, J, Dolejsek, Z, Hrusak, J and Herman, Z, *J. Phys. Chem. A* **2000**, *104*, 7294–7303.

[83] Jasik, J, Roithova, J, Zabka, J, Thissen, R, Ipolyi, I and Herman, Z, *Int. J. Mass Spectrom.* **2006**, *255*, 150–163.

[84] Hu, W P, Harper, S M and Price, S D, *Meas. Sci. Techn.* **2002**, *13*, 1512–1522.

[85] Ascenzi, D, Tosi, P, Roithova, J, Ricketts, C L, Schroeder, D, Lockyear, J F, Parkes, M A and Price, S D, *Phys. Chem. Chem. Phys.* **2008**, *10*, 7121–7128.

[86] Lu, W Y, Tosi, P and Bassi, D, *J. Chem. Phys.* **2000**, *112*, 4648–4651.

[87] Tosi, P, Correale, R, Lu, W, Falcinelli, S and Bassi, D, *Phys. Rev. Lett.* **1999**, *82*, 450–452.

[88] Tosi, P, Lu, W Y, Correale, R and Bassi, D, *Chem. Phys. Lett.* **1999**, *310*, 180–182.

[89] Ascenzi, D, Franceschi, P, Tosi, P, Bassi, D, Kaczorowska, M and Harvey, J N, *J. Chem. Phys.* **2003**, *118*, 2159–2163.

[90] Dorman, F H and Morrison, J D, *J. Chem. Phys.* **1961**, *35*, 575–&.

[91] Harper, S, Calandra, P and Price, S D, *Phys. Chem. Chem. Phys.* **2001**, *3*, 741–749.

[92] King, S J and Price, S D, *J. Chem. Phys.* **2011**, *134*,

[93] King, S J and Price, S D, *Int. J. Mass Spectrom.* **2008**, *277*, 84–90.

[94] Dorman, F H and Morrison, J D, *J. Chem. Phys.* **1963**, *39*, 1906–&.

[95] Fainelli, E, Maracci, F, Platania, R and Avaldi, L, *J. Electron Spectrosc. Relat. Phenom.* **1998**, *87*, 169–176.

[96] Alberti, G, Fainelli, E, Maracci, F, Mastropietro, M, Platania, R and Avaldi, L, *Rev. Sci. Instrum.* **2005**, *76*,

[97] Fainelli, E, Maracci, F, Platania, R and Avaldi, L, *J. Electron Spectrosc. Relat. Phenom.* **2001**, *119*, 81–93.

[98] Fainelli, E, Alberti, G, Flammini, R, Maracci, F, Bolognesi, P, Mastropietro, M and Avaldi, L, *J. Electron Spectrosc. Relat. Phenom.* **2007**, *161*, 51–57.
[99] Moddeman, W E, Carlson, T A, Krause, M O, Pullen, B P, Bull, W E and Schweitz.Gk, *J. Chem. Phys.* **1971**, *55*, 2317–&.
[100] Lablanquie, P, Penent, F, Hall, R I, Kjeldsen, H, Eland, J H D, Muehleisen, A, Pelicon, P, Smit, Z, Zitnik, M and Koike, F, *Phys. Rev. Lett.* **2000**, *84*, 47–50.
[101] Penent, F, Lablanquie, P, Hall, R I, Palaudoux, J, Ito, K, Hikosaka, Y, Aoto, T and Eland, J H D, *J. Electron Spectrosc. Relat. Phenom.* **2005**, *144*, 7–11.
[102] Brenton, A G and Lock, C M, *Rapid Commun. Mass Spectrom.* **1997**, *11*, 1155–1170.
[103] Brenton, A G, *J. Mass Spectrom.* **1995**, *30*, 657–665.
[104] Krishnamurthy, M and Mathur, D, *Chem. Phys. Lett.* **1993**, *216*, 203–208.
[105] Safvan, C P and Mathur, D, *J. Phys. B–At. Mol. Opt. Phys.* **1993**, *26*, L793–L798.
[106] Appell, J, Durup, J, Fehsenfe.Fc and Fournier, P, *J. Phys. B–At. Mol. Opt. Phys.* **1973**, *6*, 197–205.
[107] Furuhashi, O, Kinugawa, T, Nakamura, N, Masuda, S, Yamada, C and Ohtani, S, *J. Chin. Chem. Soc.* **2001**, *48*, 531–534.
[108] Andrews, S R and Harris, F M, *Rapid Commun. Mass Spectrom.* **1993**, *7*, 548–551.
[109] Fournier, P G, Fournier, J, Salama, F, Richardson, P J and Eland, J H D, *J. Chem. Phys.* **1985**, *83*, 241–246.
[110] Fournier, P G, Fournier, J, Salama, F, Stark, D, Peyerimhoff, S D and Eland, J H D, *Phys. Rev. A* **1986**, *34*, 1657–1666.
[111] Cossart, D, Launay, F, Robbe, J M and Gandara, G, *J. Mol. Spectrosc.* **1985**, *113*, 142–158.
[112] McCulloh, K E, Sharp, T E and Rosensto.Hm, *J. Chem. Phys.* **1965**, *42*, 3501–&.
[113] Curtis, D M and Eland, J H D, *Int. J. Mass Spectrom. Ion Process.* **1985**, *63*, 241–264.
[114] Lablanquie, P, Ito, K, Morin, P, Nenner, I and Eland, J H D, *Z. Phys. D–Atoms Mol. Clusters* **1990**, *16*, 77–79.
[115] Lablanquie, P, Eland, J H D, Nenner, I, Morin, P, Delwiche, J and Hubinfranskin, M J, *Phys. Rev. Lett.* **1987**, *58*, 992–995.
[116] Lablanquie, P, Andric, L, Palaudoux, J, Becker, U, Braune, M, Viefhaus, J, Eland, J H D and Penent, F, *J. Electron Spectrosc. Relat. Phenom.* **2007**, *156*, 51–57.
[117] Price, S D and Eland, J H D, *J. Phys. B* **1989**, *22*, L153–L158.
[118] Okuyama, K, Eland, J H D and Kimura, K, *Phys. Rev. A* **1990**, *41*, 4930–4935.
[119] Sheinerman, S, Lablanquie, P, Penent, F, Palaudoux, J, Eland, J H D, Aoto, T, Hikosaka, Y and Ito, K, *J. Phys. B–At. Mol. Opt. Phys.* **2006**, *39*, 1017–1033.
[120] Hikosaka, Y, Lablanquie, P, Penent, F, Kaneyasu, T, Shigemasa, E, Eland, J H D, Aoto, T and Ito, K, *Phys. Rev. Lett.* **2007**, *98*,
[121] Price, S D and Eland, J H D, *J. Phys. B* **1990**, *23*, 2269–2276.
[122] Eland, J H D, Feifel, R and Edvardsson, D, *J. Phys. Chem. A* **2004**, *108*, 9721–9725.
[123] Linusson, P, Fritzsche, S, Eland, J H D, Hedin, L, Karlsson, L and Feifel, R, *Phys. Rev. A* **2011**, *83*,
[124] Hsieh, S and Eland, J H D, *Chem. Phys.* **1994**, *188*, 381–386.
[125] Hsieh, S and Eland, J H D, *Int. J. Mass Spectrom.* **1997**, *167*, 415–424.
[126] Richardson, P J, Eland, J H D and Lablanquie, P, *Org. Mass Spectrom.* **1986**, *21*, 289–294.
[127] Eland, J H D, *Chem. Phys.* **2008**, *345*, 82–86.

[128] Ibrahim, K, Lablanquie, P, Hubinfranskin, M J, Delwiche, J, Furlan, M, Nenner, I, Hagan, D and Eland, J H D, *J. Chem. Phys.* **1992**, *96*, 1931–1941.

[129] Nenner, I and Eland, J H D, *Z. Phys. D–Atoms Mol. Clusters* **1992**, *25*, 47–56.

[130] Molloy, R D and Eland, J H D, *Chem. Phys. Lett.* **2006**, *421*, 31–35.

[131] Hagan, D A and Eland, J H D, *Org. Mass Spectrom.* **1992**, *27*, 855–863.

[132] Adams, N G and Smith, D, *Int. J. Mass Spectrom. Ion Process.* **1976**, *21*, 349–359.

[133] Smith, D, Adams, N G, Alge, E, Villinger, H and Lindinger, W, *J. Phys. B* **1980**, *13*, 2787–2799.

[134] Adams, N G and Smith, D, *Int. J. Mass Spectrom. Ion Process.* **1980**, *35*, 335–342.

[135] Smith, D, Grief, D and Adams, N G, *Int. J. Mass Spec. Ion Phys.* **1979**, *30*, 271–283.

[136] Adams, N G, Smith, D and Grief, D, *J. Phys. B–At. Mol. Opt. Phys.* **1979**, *12*, 791–800.

[137] Agee, J H, Wilcox, J B, Abbey, L E and Moran, T F, *Chem. Phys.* **1981**, *61*, 171–179.

[138] Bearman, G H, Ranjbar, F, Harris, H H and Leventhal, J J, *Chem. Phys. Lett.* **1976**, *42*, 335–338.

[139] Maier, W B and Stewart, B, *J. Chem. Phys.* **1978**, *68*, 4228–4232.

[140] Manning, M, Price, S D and Leone, S R, *J. Chem. Phys.* **1993**, *99*, 8695–8704.

[141] Price, S D, Manning, M and Leone, S R, *Chem. Phys. Lett.* **1993**, *214*, 553–558.

[142] Friedrich, B and Herman, Z, *Chem. Phys. Lett.* **1984**, *107*, 375–380.

[143] Friedrich, B, Vancura, J, Sadilek, M and Herman, Z, *Chem. Phys. Lett.* **1985**, *120*, 243–246.

[144] Friedrich, B, Vancura, J and Herman, Z, *Int. J. Mass Spectrom. Ion Process.* **1987**, *80*, 177–185.

[145] Zabka, J, Ricketts, C L, Schroder, D, Roithova, J, Schwarz, H, Thissen, R, Dutuit, O, Price, S D and Herman, Z, *J. Phys. Chem. A* **2010**, *114*, 6463–6471.

[146] Lambert, N, Kaltsoyannis, N, Price, S D, Zabka, J and Herman, Z, *J. Phys. Chem. A* **2006**, *110*, 2898–2905.

[147] Zins, E L and Schroder, D, *Int. J. Mass Spectrom.* **2011**, *299*, 53–58.

[148] Roithova, J, Thissen, R, Zabka, J, Franceschi, P, Dutuit, O and Herman, Z, *Int. J. Mass Spectrom.* **2003**, *228*, 487–495.

[149] Franceschi, P, Thissen, R, Zabka, J, Roithova, J, Herman, Z and Dutuit, O, *Int. J. Mass Spectrom.* **2003**, *228*, 507–516.

[150] Lockyear, J F, Douglas, K, Price, S D, Karwowska, M, Fijalkowski, K J, Grochala, W, Remes, M, Roithova, J and Schroder, D, *J. Phys. Chem. Lett.* **2010**, *1*, 358–362.

[151] Zener, C, *Proc. Roy. Soc. Lond. Ser. A* **1932**, *137*, 696.

[152] Price, S D, *Int. J. Mass Spec.* **2007**, *260*, 1–19.

Chapter 2: Experimental Methodology, Data Processing and Interpretation

2.1 Overview

This Chapter provides a detailed description and discussion of the position–sensitive coincidence (PSCO) time–of–flight (TOF) mass spectrometer (MS) that was employed to carry out the experimental work reported in this thesis. Additionally, in this chapter a detailed account of the data processing, which converts raw results to scattering diagrams, will be given. Since its initial conception and construction there have been several modifications to the PSCO experimental arrangement, these will also be described in this chapter.

The PSCO spectrometer is a "home–built" apparatus designed to study the bimolecular reactions between dications and neutrals, particularly those that form a pair of monocations[1]. However, as discussed in Chapter 1, the majority of dication–neutral reactions do indeed form pairs of ions. A TOF MS coupled with a position–sensitive detector (PSD) is used to collect these pairs of product ions in coincidence. Thus, these dication–neutral reactions are probed on an event–by–event basis. The position–sensitive detection technique allows us to determine both the identity of the reaction products and their initial velocity vectors. A schematic of the experimental set up is shown in Figure 2.1. A brief overview of the technique is initially presented, followed by a more detailed description of each section of the apparatus and its operation.

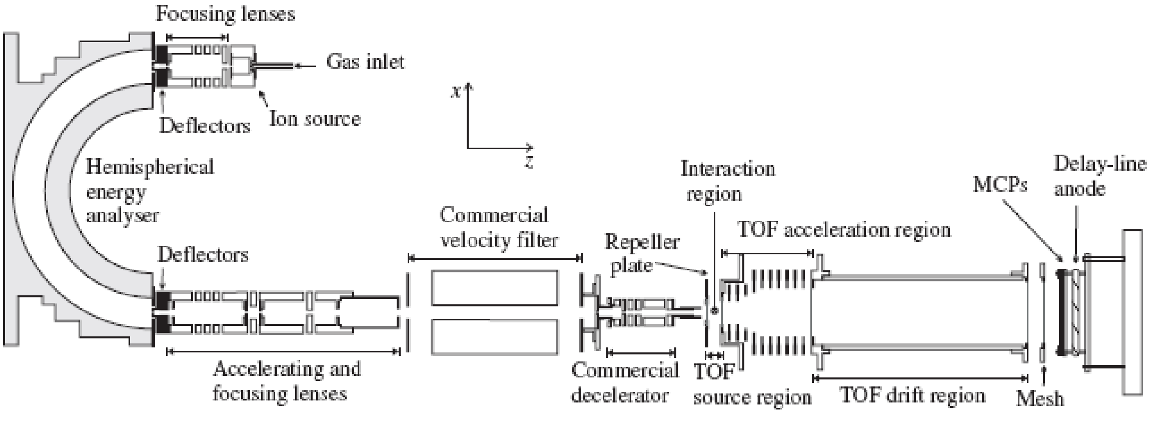

Figure 2.1 Schematic of the PSCO experimental apparatus. From ref. [1].

In the PSCO experiment, reactant ions are generated in an ion source *via* electron ionisation of the appropriate precursor gas. Any ions formed in the source are then extracted and passed round a hemispherical energy analyser, which selects only ions with a narrow range of kinetic energies. At the exit of this hemisphere, the ion beam is pulsed to form "packets" of ions. These ion pulses are then focused by a series of lenses and then pass through a velocity filter. The function of the velocity filter is to select the dications of interest, which have a certain *m/z*. Before entering the interaction region, the ion pulses are decelerated to the desired collision energy. The interaction region is where the neutral gas is introduced and reactant collisions occur. The interaction region also doubles as the source region of a TOF MS. After the dication–neutral interactions, the repeller plate of the spectrometer is pulsed to a positive voltage in order to drive any product or un-reacted ions out of the source region and into the acceleration and field–free drift regions of the MS. At the end of the drift region the ions impact upon the PSD, which consists of a pair of micro–channel plates (MCPs) and a delay–line anode. The PSD allows the position of the ion impact on the face of the detector to be measured. Consequently, the initial velocity vectors of the products can be derived.

The experimental set up described above is housed in a series of stainless steel chambers and experiments are conducted under high vacuum conditions to minimise collisions of the dications with background gasses. Moreover, coincidence experiments must be carried out under single–collision–conditions to minimise false coincidences. Therefore the base pressure is kept around 10^{-7} Torr and the pressure in the interaction region is around 3×10^{-6} Torr during data collection. These low pressures are obtained, and maintained, by three diffusion pumps and a turbo–molecular pump that are all backed by rotary pumps. The following sections provide an in–depth description of each stage of the PSCO experiment.

2.2 Ion Formation

In the PSCO apparatus ions are formed by EI. A high current (4 A) through a filament causes electrons to be ejected by thermionic emission. Appropriate voltages then accelerate these electrons into a chamber that contains a suitable precursor gas. The precursor gas is introduced *via* a needle valve. The pressure in the chamber that houses the dication source is kept around 3×10^{-6} Torr during dication formation, however, the actual pressure inside the source block is likely to be at least a factor of ten higher than this. The choice of filament material depends on the precursor gas being used. For example, the standard filament material is tungsten, which is suitable for gasses such as N_2 or CO, but O_2 reacts efficiently with the tungsten filament at the operating temperatures used, rapidly degrading the filament. Thus, when O_2 is the precursor gas, an yttrium–coated tungsten filament is used. Conversely, when SF_6 is used as the precursor gas, the yttrium–coated filaments very rapidly degrade and so only uncoated tungsten filaments can be used with this particular precursor gas. The EI energy is typically between 100 and 200 eV, but is varied to optimise production of the desired dication from the particular precursor species. Depending on the identity of the precursor, parent monocations and dications will be formed at these electron energies, in addition to a variety of fragment monocations and dications.

The source block itself has a small positive voltage applied that defines the "rest potential" of the ions as they are formed. This voltage is normally between 2 and 10 V. Varying this rest potential allows us to vary the speed at which the ions are travelling when they enter the reaction region and thus vary the collision energy between the dication and neutral. Consequently, collision energy effects can also be investigated employing the PSCO apparatus.

2.2.1 Advantages and Disadvantages of Electron Ionisation

The principle advantage of EI is that it is a simple and robust manner in which to form dications. However, it is a "hard" ionisation technique that results in a large degree of ion fragmentation when molecular precursor gasses are used. If one wished to study the reactions of a large molecular dication using the PSCO apparatus, better ion counts might be achieved using a "soft" ionisation technique such as electro–spray ionisation.

The main disadvantage of EI is that it is not a state–selective method of ionisation. In principle, EI means that any electronic or rovibrational state of the dication could be formed, provided it has energy lower than the energy of the ionising electrons. For some species, this could result in several states being formed, all of which will be transmitted to the reaction region provided they have a long enough lifetime. However, on average, the time taken for the ions to reach the reaction region from the source block is around 100 to 200 μs, thus there is a kind of "auto–selectivity" inherent in the experimental set–up. Specifically, ions formed in a state with a lifetime of less than 100 μs will dissociate before undergoing collisions with the neutral. Population of a range of vibronic states of the reactant dications in the source is disadvantageous as this initial energy spread broadens the translational energy release (ΔE_T) spectra that we determine from our data (section 2.17). If state–selective dication formation were possible in the PSCO experiments then our ΔE_T distributions should clearly reveal the product vibrational state distributions. In addition, as will be seen for the reactions of SF_4^{2+}, on occasion the different electronic states that may be present in the beam have different molecular structures resulting in differing reactivity. In such cases it would be valuable to selectively form only a single state in order to deconvolute the effect of the different dicationic structures on the reactivity. Threshold photo–electron photo–ion VUV ionisation techniques have been successfully employed to study the reactivity of a selected, single, state of an ion with a neutral[2]. Clearly, such techniques are a desirable, yet impractical extension to the current PSCO apparatus.

2.3 Ion extraction and Hemispherical Analyser

A lens with an applied voltage of –250 V extracts the monocations and dications from the source. A series of three lenses (L1, L2 and L3) then guide the beam of ions into an accelerating lens. The voltages applied to L1, L2, L3 are between 0 and –10 V and the accelerating lens is typically held around 0 V. The ion beam then passes a pair of vertical deflectors and a pair of horizontal deflectors that can be used to align the trajectory of the ions with the entrance to the hemispherical analyser. A schematic of the lenses and deflectors can be seen in Figure 2.2.

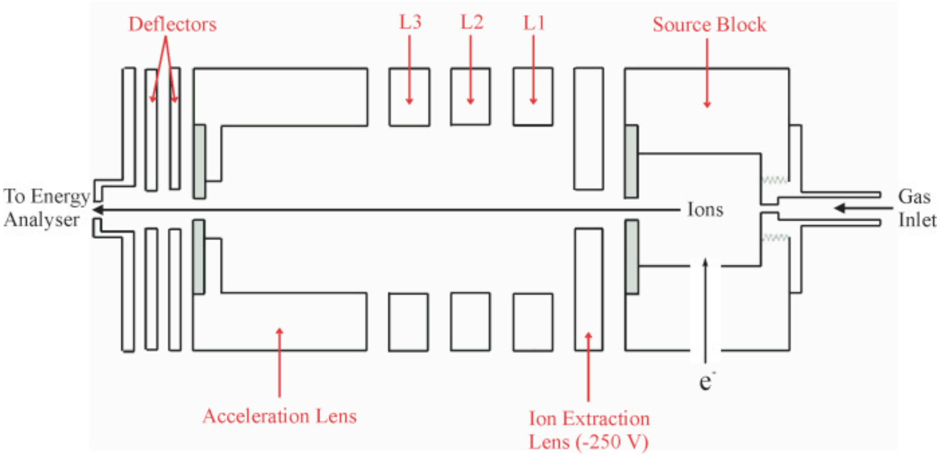

Figure 2.2 Schematic of the ion source, the extraction lenses and deflectors at the entrance to the hemispherical energy analyser.

The ions formed in the source have a range of translational energies that are centred about the "rest potential" that is set by the voltage applied to the source block. In order to maximise the energy resolution of our data, and facilitate pulsing, it is desirable to select ions with a narrow range of translation energies. We want to minimise the ratio of the translational energy spread to the modal translational energy ($\Delta E/E_0$) for the ion beam. In order to select this narrow range of energies, the ion beam is passed around a hemispherical energy analyser. The analyser has an inner radius of 130 mm and an outer radius of 170 mm, as shown in Figure 2.3. The mean radius of the analyser is 150 mm, which gives an average ion path length around the hemisphere of 942 mm. There are several methods that can be used for energy monochromatisation of an ion beam such as a cylindrical energy analyser[3] or a magnetic bottle[4]. However, the hemispherical analyser used is effective over a wide range of ion energies and the large scale of the one used in the PSCO apparatus gives good ion transmission[5-7].

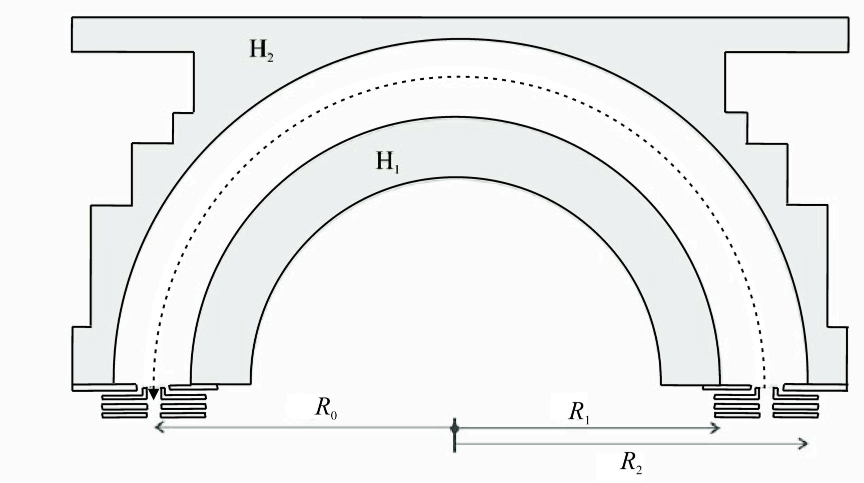

Figure 2.3 Schematic of the hemispheric energy analyser that consists of two hemispheres H_1 and H_2 with radii R_1 and R_2 of 130 mm and 170 mm, respectively. The mean radius R_0 is 150 mm.

The pass translational energy E_0 is defined by the voltages applied to the smaller (V_{inner}) and larger (V_{outer}) hemispheres. Only ions with a particular translational energy will pass through the analyser and others will be deflected. Of course, there will be a spread in the "pass energy" E_0 of the ions and, as ever, a compromise must be reached between ΔE and ion transmission in order to achieve practical dication beam fluxes. We define the energy resolution of the beam as the ratio between the full-width-at-half-maximum (FWHM) of the energy distribution $\Delta E_{1/2}$ and E_0, Equation (2.1).

$$\Delta E_{1/2} / E_0 \tag{2.1}$$

The best energy resolution, whilst maintaining good ion transmission, is generally achieved with an E_0 of 4 V. The theoretical energy resolution of the analyser is around 1.1 %. However, due to the angular spread of the experimental beam, the actual resolution is slightly degraded to around 4.0 %, which has been measured by retarding field analysis.

2.4 Pulsing the Beam

At the exit slit of the hemispherical energy analyser are another set of vertical and horizontal deflectors. The vertical deflectors can be used to adjust the trajectory of the beam if it is necessary and the main function of the horizontal deflectors is to pulse the ion beam to create small "packets" of ions. Pulsing the ion beam is achieved by application of a triangular oscillating waveform to each deflector and setting these waveforms to be out of phase with each other. The effect of this oscillating pair of voltages on the ion beam is that the beam trajectory oscillates across a central aperture, thereby creating spatially and temporally separated ion pulses. The duration of the ion pulse depends on the amplitude of the waveforms and the separation of the pulses depends on the frequency of the waveforms. Typical waveform, and consequently pulse, frequencies are around 10 – 30 kHz. If the oscillating waveforms are not 180° out of phase with each other, then asymmetrical pulse shapes can be formed.

2.4.1 Advantages and Monitoring

The motives for pulsing the ion beam are manifold. The primary reason is to reduce "noise" in the data we collect. This noise appears as false coincidences in the spectra collected. When a continuous ion beam is used, then, prior to the repeller plate pulse, the ion beam is present in the acceleration and drift regions of the TOF MS as well as the source region. When the repeller plate is pulsed, all of the reactant ions that are in the source region of the spectrometer will be appropriately focussed and accelerated to the same potential and therefore have a single TOF. However, whilst the repeller plate is not energised, the appropriate voltages are still applied in the acceleration and drift regions of the spectrometer. Thus, ions that have entered the acceleration region before the repeller plate is pulsed, will also be accelerated by the fields and be detected. However, due to the magnitude of the voltages, these ions will arrive at the detector with a shorter TOF than those ions that were in the source region. The TOF focussing conditions do not, of course, apply to ions in the acceleration region, resulting in a high level of unstructured ion arrivals in the mass spectrum. This "noise" appears at TOFs shorter than that of the ion "peak", Figure 2.4 (a). This high level noise will overwhelm any product signals that arise from products with m/z lower than that of the reactant ion beam.

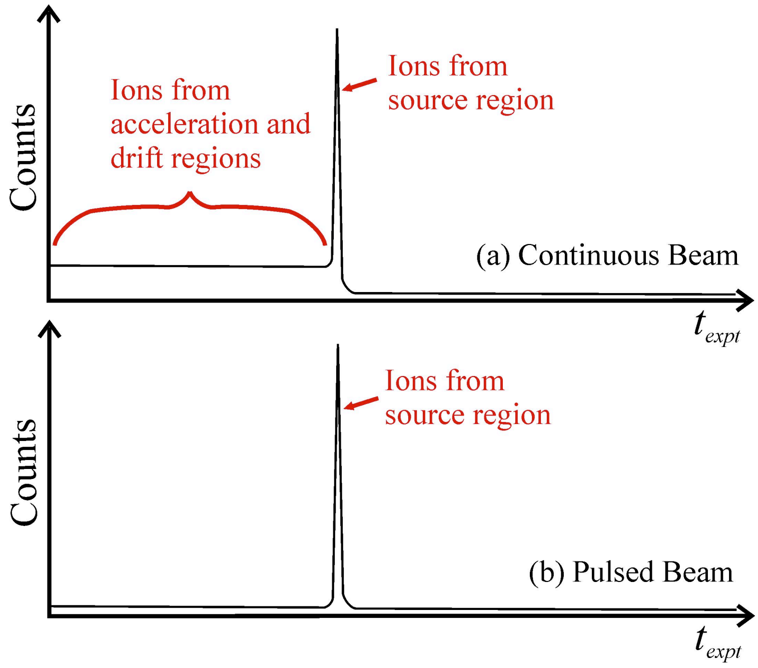

Figure 2.4 Schematics of the one-dimensional mass-spectra recorded when the ion beam is (a) continuous or (b) pulsed. When the beam is continuous, a high level of background noise is recorded at TOFs shorter than that of the reactant ions.

In contrast, with a pulsed ion beam that is only of finite length, the repeller plate is only pulsed when the ion pulse is within the source region of the spectrometer. Therefore, all reactant ions will be appropriately focussed to form a sharp peak in the mass spectrum and there will only be a low level of background noise due to "dark counts" or electrical noise that is evenly distributed over all TOFs, Figure 2.4 (b). The frequency of the oscillating waveforms that create the ion pulses is chosen such that there will only be a single pulse in the MS region of the apparatus at a given time. Typical pulse separations are around 30 – 80 μs and the ion pulse length is around 1 cm.

The last point above brings us onto the second and third advantages of using a pulsed, rather than continuous, ion beam. The source region of the spectrometer is 1.63 cm long and with a continuous beam would be completely filled with reactant ions. Whereas, the ion pulses are only around 1 cm in length, reducing by around a third the span in the z direction (where z is defined as the principle axis of the MS) over which the reactants may interact. If the interaction region between the reactant dication and neutral is smaller, then the mass resolution of the resultant data will be enhanced for the product ions. In turn, this increases the energy resolution of the data collected. A smaller interaction region also means that the position of the reactant interaction in the (x, y) plane in the source may be slightly better defined. Knowing the (x, y) position of the reaction centre more precisely reduces some of the broadening introduced by the data analysis due to assuming a single point source of all product ions.

The FWHM of the temporal distribution of the ion pulses is set, for each particular reactant beam, so that the spatial width is around 1 cm. The standard relation between kinetic energy (KE) and velocity v, Equation (2.2), means that reactant ions of differing mass m and the same KE (as defined by the pass energy of the hemispherical analyser) will have differing velocity.

$$KE = \frac{1}{2}mv^2 \tag{2.2}$$

Consequently, the relation between velocity, distance and time means that to create pulses of around 1 cm in length, pulses of different dications will have different temporal widths. For example, for beam energy of 4 V, pulses of Ar^{2+} and N_2^{2+} dications that are 1 cm in length will have temporal FWHMs of 2.28 μs and 1.90 μs respectively. Altering the frequency and magnitude of the oscillating waveforms varies the basic pulse shapes and widths. Once these parameters are correctly set, another monitoring procedure must be carried out, as described in the next paragraph.

It is essential to ensure that the pulsing of the reactant beam does not alter or broaden the rest potential of the ions from that of the continuous beam. If the deflectors are pulsed too fast or the magnitude of the deflector voltage is too high, then the ions do not have enough time to adjust to the changing voltages and their energy can be perturbed. Energy perturbation occurs when the rate of change of the deflector voltages is of the order of the ion transit time across the aperture. In order to monitor the effect of the pulsing on the beam energy we measure the modal TOF of the pulsed beam and compare this to the modal TOF of the continuous beam. Since the TOF is a sensitive probe of the ion energy, these pulsed and un–pulsed modal TOFs should be the same if the beam energy is unperturbed. Therefore, for experimental operation the pulse duration is set as short as possible, whilst ensuring that the beam energy is not perturbed.

2.5 Acceleration and Focusing with Ion Lenses

After the ion beam has been pulsed by the deflectors at the exit of the hemispherical analyser, the ion pulses are accelerated and focussed by a series of electrostatic lenses, Figure 2.5. The voltages on these lenses can be varied independently to optimise the angular spread, or “shape”, and transmission of the beam. After the ion beam has passed through these lenses, the ions enter the velocity filter, which will be described in the next section.

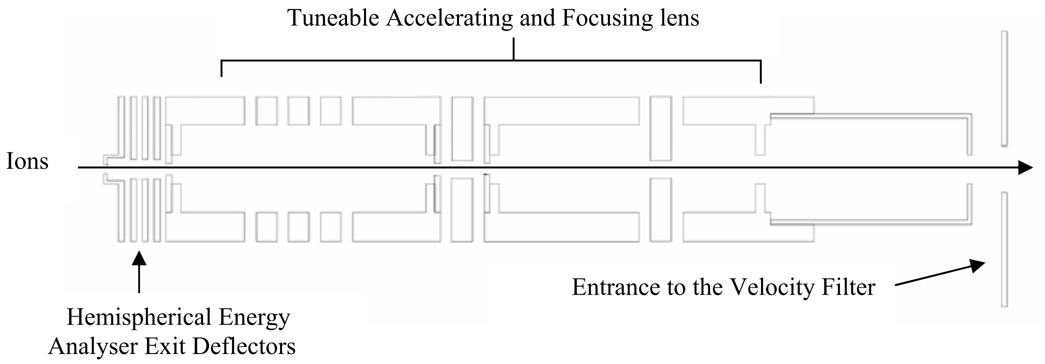

Figure 2.5 Schematic of the region of the apparatus between the exit of the energy analyser and the entrance to the velocity filter than contains the accelerating and focussing lenses.

2.6 Velocity Filter

The beam of ions that has been energy selected, focussed and accelerated then enters the velocity filter. The velocity filter is used to select the desired reactant dications, which have a specific m/z, from the ion pulses and discard any other ions. The relation between KE and velocity (Equation (2.2)), along with the fact that the beam is already energy selected, means that selecting only a single ion velocity is equivalent to selection of ions of a single m/z.

Velocity selection is achieved by employing a commercial velocity filter. The filter consists of an electro–magnet and a pair of electrostatic deflection plates; these generate perpendicular magnetic and electric fields. The magnetic force exerted on the ion F_B is given by Equation (2.3), where B is the magnetic field strength, q is the charge on the ion and v is it's velocity. The accompanying electrostatic force exerted on the ion F_E is given by Equation (2.4), where E is the electric field strength.

$$F_B = Bqv \tag{2.3}$$

$$F_E = Eq \tag{2.4}$$

When F_B is equal to F_E, then only ions of a particular velocity v_1 can pass through the filter and ions with $v < v_1$ or $v > v_1$ are deflected. In practice, the magnetic field is kept constant and the electric field is tuned to transmit only ions of the desired v_1 and consequently the desired m/z.

The velocity filter can only select ions of a certain m/z and not simply m. As a result, monocations with the same m/z but half the dicationic mass will also be transmitted through the filter. For example, selection of O_2^{2+} at m/z = 16 will also allow O^+ to be transmitted to the reaction region; a beam of N_2^{2+} will also include some N^+ (m/z = 14) and a beam of $C_2H_2^{2+}$ will include some CH^+ (m/z = 13). However, reactions of these monocations will not negatively affect the data collected. More specifically, the coincidence technique employed only counts events where two ions arrive in coincidence, after a single repeller pulse, as arising from a dication–neutral reaction. Monocation neutral reactions will only ever form a single monocation and so do not produce signals in the coincidence spectra. However, as detailed later in section 2.13.2, when a high repeller plate voltage is employed, monocation–neutral reactions occurring in the acceleration region can sometimes result in "tails" in the coincidence spectra, although these can be easily identified and disregarded. Monocation–neutral reactions can also contribute to false coincidences in the PSCO spectra.

2.7 Decelerator – Achieving the Desired Collision Energy

After the velocity filter, the pulses of ions are decelerated to the desired collision energy employing a commercial decelerator. The collision energies that are employed are typically a few eV in the laboratory frame. These low collision energies are employed as dication–neutral bond–forming reactions have been shown to have cross–sections that increase at low collision energy[8]. The commercial set up of the decelerating lenses is shown in Figure 2.6, where the lenses are labelled 1 to 8.

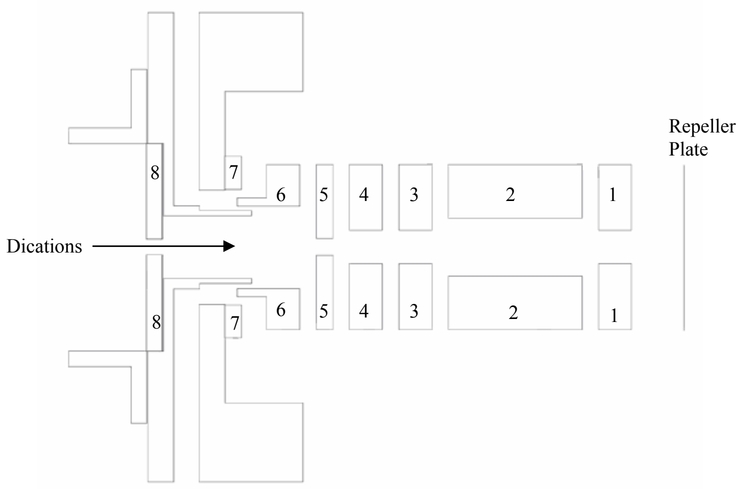

Figure 2.6 Schematic of the decelerating lenses that are situated after the velocity filter and prior to the repeller plate.

The first two ion optics, 8 and 7, are typically held at the beam potential as it exits the velocity filter, a potential of −250 V. Optics 6, 5 and 4 are used to decelerate the beam, 6 and 5 are typically held close to −250 V and 4 is set to an intermediate potential of −150 V. The final electrostatic lenses in the deceleration region, 1, 2 and 3, are operated as an Einzel lens[2]. Specifically, 1 and 3 are held close to 0 V, while 2 is varied for the best focusing. Lens 2 is typically between −5 and −15 V and, of all the ion optics, has the largest effect on the beam shape.

2.8 Reaction Region

Following deceleration, the reactant ion pulse passes through a small, grid covered, aperture in the repeller plate into the reaction region that doubles as the source region of the TOF MS. In the reaction region the dications encounter the neutral reactant. Initially, the reaction region is kept in a field–free state to ensure the dication–neutral interactions all occur at the same low collision energy. Once the dication pulse reaches the centre of the source region, the repeller plate is pulsed to a positive voltage in order to drive any product ions or unreacted dications into the acceleration and drift regions of the MS. After a delay that is long enough for even the heaviest possible product ion to reach the detector, the repeller plate is returned to zero V, ready for the next pulse of dications to enter the field–free reaction region.

In the reaction region, single collision conditions must be maintained in order that only a single reactive event occurs per repeller plate pulse. In fact, for coincidence experiments, signal–to–noise ratio is optimal for zero reactant count rates! The typical count rate of the ion beam is such that there is on average less than one dication per ion pulse. The pressure of the reactant neutral must also be kept low, around 3×10^{-6} Torr, so that the reaction products do not undergo secondary collisions and react further.

2.9 Time–of–Flight Mass Spectrometer

The reaction region, where the dication and neutral collide, doubles as the source region of a TOF MS. The TOF MS consists of three regions, the source, acceleration and drift. As the dication pulse enters the centre of the source region, the repeller plate is brought up to a positive voltage, which creates a potential gradient meaning the ions are driven towards the acceleration region. The electrostatic optics in the acceleration region produce another linear potential gradient that further accelerates the ions, after which they pass into the field–free drift region. At the end of the drift tube the ions are rapidly accelerated before impinging on the PSD, resulting in their detection. A schematic of this "two–field" TOF MS is shown in Figure 2.7.

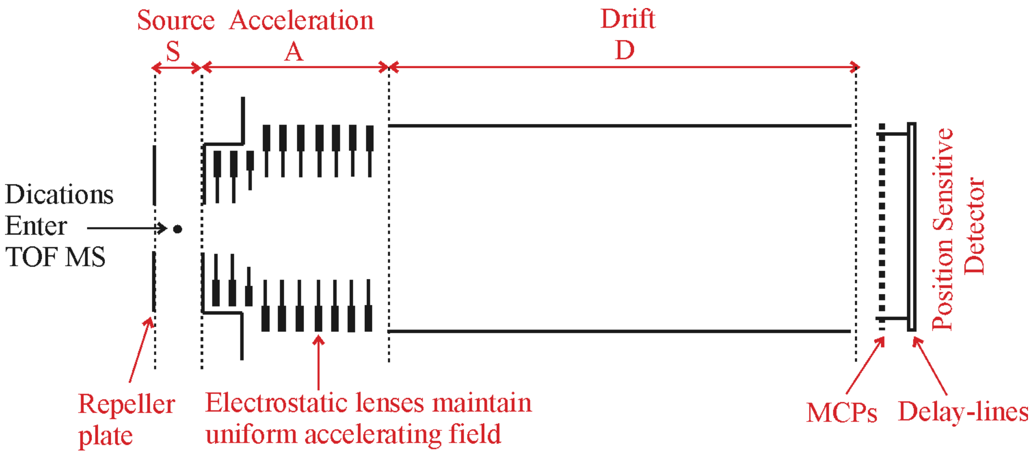

Figure 2.7 Schematic (not to scale) of the PSCO two–field time–of–flight mass spectrometer.

The basis of TOF mass–spectrometry is the fact that ions of a different m/z will take different times to traverse a constant distance when they are all accelerated to the same KE[9]. Therefore, recording the TOF of an ion across a known distance allows its *m/z* to be determined. The first TOF mass spectrometers only used a single accelerating field (the source region) and a drift region; this is termed "single–field" TOF mass spectrometry[9]. In such experiments, the ions at different points in the source region experience different accelerating potentials and as such are accelerated to different maximum velocities as they reach the start of the drift region. However, the spread in initial ion positions is negated by the fact that ions formed near the start of the source will "catch–up" with those formed near the end of the source, resulting, in principle, in a single TOF for ions of the same *m/z*. For example, ions X and Y have the same *m/z* but X is close to the repeller plate when it is pulsed and Y is near the end of the source region. Ion X will have further to travel across the region and so will be accelerated to a greater potential than ion Y and will eventually catch up with ion Y and arrive at the detector at the same time. When ions formed in different positions in the source arrive at the detector at the same time, this is termed "space–focussing". However, if the lengths of the source and acceleration regions are not exactly engineered to achieve these focussing conditions, the result is that ions of the same *m/z* will arrive with a range of TOFs. Thus, the focussing of a single–field TOF MS is critically dependent on its construction, a major disadvantage. However, in 1955 Wiley and McLaren discovered that space focussing could be achieved using two separate accelerating fields with magnitudes in a specific ratio, termed "two–field" TOF mass spectrometry[10]. Moreover, the applied fields can readily be varied to achieve good focussing conditions, meaning that fabricating the MS to exact dimensions is not as important as in a single–field TOF MS. So, from a construction standpoint, two–field TOF mass–spectrometry is far more practical.

Newtonian mechanics can be used to determine the flight time *t* for each region (see Appendix for details), can be used to show that the TOF of an ion is proportional to the square root of its *m/z*, Equation (2.5)[10] and determine the space–focussing conditions. Where *c* is a constant encompassing the magnitudes of the source and acceleration fields and the dimensions of the spectrometer.

$$TOF = c\sqrt{\frac{m}{z}} \tag{2.5}$$

Two–field TOF mass spectrometry, derived by Wiley and McLaren, and the single–field arrangement both achieve “first–order” space focussing conditions. First–order space focussing ensures that, to first order, the spread in TOF of ions of the same *m/z* is independent of source position S about the centre of the source (S = 0), Equation (2.6).

$$\left(\frac{d(TOF)}{dS}\right)_{S=0} = 0 \qquad (2.6)$$

First–order space focusing is very effective, however, in 1993 Eland discovered that further improvements could be made to the space focussing conditions[11]. By constraining the geometry and the magnitudes of the fields in a two–field apparatus, it is possible that both the first and second derivatives of TOF with source position become equal to zero. Second–order space focussing means that the spread of TOFs for ions of the same *m/z* with different initial source position is even smaller than for first–order space focussing. What is more, the space–focussing conditions apply over a wider range of initial S. The magnitudes of the fields required for this new second–order focussing meant that many traditional first–order TOF MS designs were impractical and the experimental geometries had to be changed. The main difference between first and second–order experimental designs is that a longer acceleration region is required to achieve second–order focussing conditions with practical voltages. The PSCO MS was designed as a two–field, second–order space focussing MS with source, acceleration and drift lengths of 1.63 cm, 11 cm and 27.5 cm respectively[1]. Typically, when 300 V is applied to the repeller plate, an accelerating voltage of –1990 V is employed. These voltages give parent ion peaks in the mass spectrum with FWHM of approximately 3 ns.

2.10 Position Sensitive Detector

The PSD, which is used to detect product and unreacted ions, is mounted at the end of the drift region of the TOF MS. The PSD is a commercial device consisting of a pair of MCPs and a pair of wire–wound delay line anodes[12,13]. A schematic of the PSD is shown in Figure 2.8.

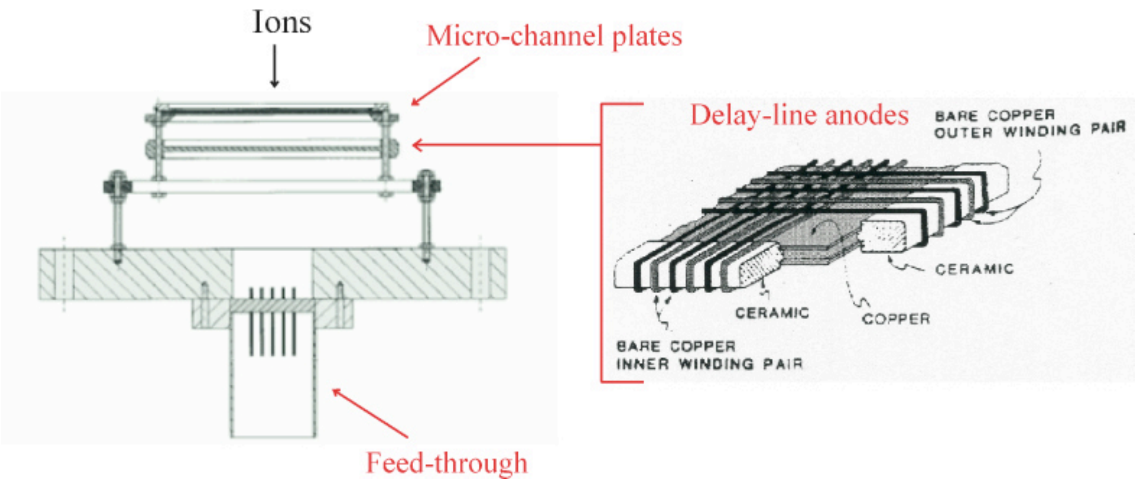

Figure 2.8 Schematic of the position-sensitive detector that consists of a pair of MCPs in front of a wire-wound delay line anode.

The MCPs contain channels that are around 10 microns wide that produce a cascade of electrons that is emitted from the end of the channel after an ion has impinged upon the front. In order that the ion impact is energetic enough to cause an electron cascade in the MCP, the ions are accelerated to around 2 kV just before reaching the detector. The cascade of electrons from the MCPs then impinges on the delay-lines, of which there are two, that are wound around a former in both the x and y directions, perpendicular to the axis of the spectrometer. The charge pulse propagates in both directions along both the x and y oriented delay-lines. Once the charge pulse reaches an end of a particular wire, this is passes as a "stop" signal to the timing circuitry. Therefore, for each wire two stop signals are generated, meaning there are four stops in total for each ion that hits the detector. These times [$t_{xa}(i)$, $t_{xb}(i)$, $t_{ya}(i)$, $t_{yb}(i)$], where $i = 1$ or 2 for events a pair of ions are detected in coincidence, are measured relative to the start of the repeller plate pulse. The time between the start of the repeller plate pulse and the measured voltage "spike" on the MCPs upon ion impact gives the experimental TOF $t_{expt}(i)$ of the ion. Thus, for each ion detected, the data set consists of five separate times. It follows that for each pair of ions detected arising from a dication-neutral reaction there are ten times recorded, eight from the delay line anodes and two from the MCPs.

2.11 Time-to-Digital Converter and Signal Processing

The ten signals from the MCPs and delay-lines are fed into a commercial RoentDek ATR-19 time-to-digital converter (TDC) that also amplifies the signal. Each of the five inputs has a threshold that must be set appropriately to ensure complete collection of each “real” ion arrival but minimise electronic noise. For each ion, all five times, from the MCPs and delay–lines, must be recognised by the TDC for the event to be considered as a real ion impact on the detector. The digitised data is then transferred to data collection programme on a PC. Events that involve detection of a single ion after a pulse of the repeller plate are termed “singles” and the TOFs of such events are simply added to a one–dimensional mass–spectrum. Events where a pair of ions is detected in coincidence after a single pulse of the repeller are termed “pairs” and all ten times are stored in a list of pairs data and are analysed as described below.

2.12 Data Processing

Once the raw data, which consists of lists of ten times, is stored on the PC, it can be transformed into a “coincidence spectrum” and then further processed off–line to reveal reaction dynamics and energetics. These processes will be described in the next few sections.

2.13 Coincidence Spectra

The first step in analysis of the raw data is transformation of the pairs of $t_{expt}(i = 1$ and 2) into a coincidence spectrum. A coincidence spectrum is a two–dimensional histogram which plots the $t_{exp}(1)$ against $t_{expt}(2)$ for every single ion–pair detected. In this two–dimensional plot, individual reaction channels between the dication and neutral appear as lozenge shaped peaks. The sets of pairs that correspond to the reaction channel can readily be selected from the data set for further analysis, as described in sections 2.14 to 2.17. A representative “whole” coincidence spectrum and two representative sections of coincidence spectra are shown in Figure 2.9.

Figure 2.9 (a) shows the complete spectrum collected following interaction of Ar^{2+} with C_2H_2. Figure 2.9 (b) shows a section of this spectrum taken from near the centre of the diagram that exhibits a peak that has a tail and (c) shows a section exhibiting a peak that does not have a tail, taken from a region slightly to the right of (b). Often, coincidence spectra are displayed as an intensity plot rather than a “spot” plot as shown in **Figure 2.9**, since these spot plots over–emphasise single counts. The origin of the principal features of the coincidence spectra such as peaks, tails and the vertical and horizontal strips will now be described.

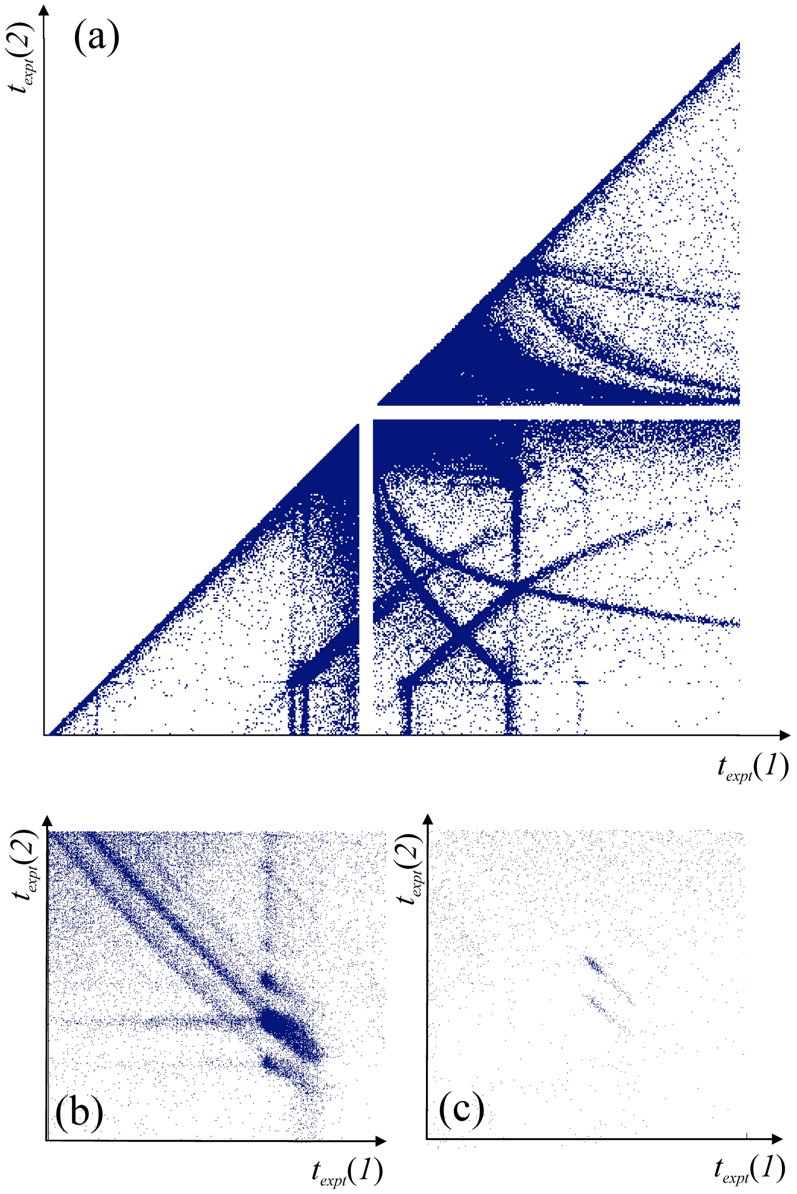

Figure 2.9 (a) The coincidence spectrum recorded following interactions of Ar^{2+} with C_2H_2. The data only fills half of the entire two-dimensional histogram since it is symmetrical about the diagonal. (b) A section of the spectrum that shows three peaks due to SET which exhibit fairly strong tails to the "top left" of the peak. (c) A section of the spectrum above that shows the peaks due to chemical channels, which do not exhibit any tails. Often, such "spot" plots are converted to intensity plots as the spot plots such as the one shown in this figure over-emphasise single counts.

2.13.1 Origin of Peaks and "Tails" in the Spectra

The actual peaks in the coincidence spectra arise from dication-neutral reactions that occur in the source region of the MS. As such, the products are appropriately second-order space-focussed by the two electric fields, as described in section 2.9.

However, as is clear from Figure 2.9 (a) and (b), some reaction channels exhibit long curved tails. These tails arise from a reaction between the dication and neutral that forms the same pairs as the peak from which they originate, but the reaction occurs in the acceleration region of the MS. Due to diffusion, there is a non–negligible density of the reactant neutral in the acceleration region, although this concentration is much lower than in the source. As un–reacted dications are accelerated out of the source region by the repeller plate, some will react with the neutrals that have drifted down into the acceleration region. The field gradient in the acceleration region does not appropriately focus product ions of the same mass to the correct TOF. Moreover, due to the fact that the coincidence spectra are always plotted with the TOF of the heaviest ion on the *x* axis, the relative mass of the reactants and subsequent products defines the "direction" of the tail. For a schematic explanation of the source of tails and their directions see Figure 2.10, with a more detailed discussion of the figure in the paragraph below.

Imagine a hypothetical SET between A^{2+} and B forming A^+ and B^+. In this case, the mass of A is greater than that of B. If the reaction occurs in the acceleration region, then the A^+ product that eventually arrives at the detector will do so with a shorter flight time than expected since some of its flight time was spent as A^{2+}, which has half the m/z of A^+. Thus, A^{2+} undergoes greater acceleration in the acceleration field than A^+. Conversely, the nascent B^+ formed by a reactive event in the acceleration region will be accelerated over a shorter distance and thus to a lower maximum potential than a B^+ product formed in the source region. The resulting flight time of the B^+ formed in the acceleration region is longer than expected. Since the t_{expt} of heavier product (A^+) is always plotted on the *x* axis, the scenario described above results in a tail in the coincidence spectrum that curves off to the "top left" of the peak. In contrast, if the reaction is reversed so that the dication is lighter than the neutral reactant i.e. $B^{2+} + A \rightarrow B^+ + A^+$, where A^+ is still the heavier product, then the resulting tail will curve off to the "bottom right" of the peak. In fact, the intensities of the tails themselves are convolved with the collision energy dependence of the reaction cross–section.

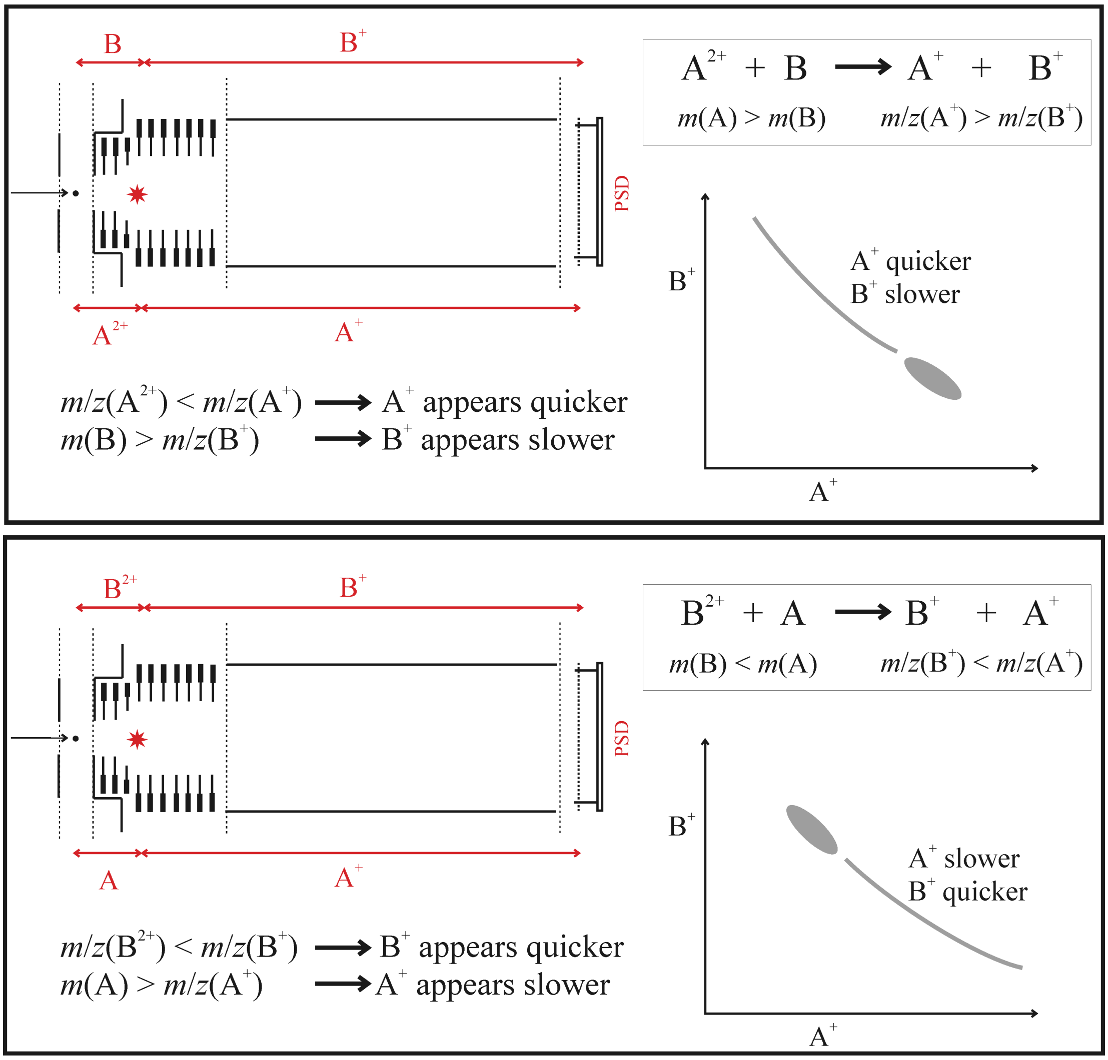

Figure 2.10 A pair of schematic diagrams illustrating the origin of tails in the coincidence spectra. If a dication reacts with a neutral in the acceleration region of the spectrometer, as indicated by the red star, then a tail is observed in the coincidence spectrum; the "direction" of this tail depends on the relative m/z of the products. If the dication A^{2+} is heavier than the neutral B, resulting in a pair of products $A^+ + B^+$ where the m/z of A^+ is greater than that of B^+, then the tail will go to the "top left" of the peak. Conversely, if the dication B^{2+} is lighter than the neutral A, then the tail will go off to the "bottom right" of the peak.

Occasionally, peaks are observed that do not exhibit any tail at all (Figure 2.9 (c)) indicating that the cross-section for the reaction in question drops off rapidly with increasing collision energy. The reaction does not occur in the acceleration region. Generally, the reaction cross-sections for bond-forming processes decrease at collisions energies higher than a few eV. Consequently, peaks in the coincidence spectrum that do not have tails are generally due to chemical channels.

2.13.2 Reactions of Monocations

As detailed in section 2.6, the energy and velocity selection methods that are employed in these experiments only allow the *m/z* of the ion pulse to be selected. As a consequence, monocations that are isobaric with the dication are also transmitted to the reaction region. In principle these ions do not affect the coincidence spectrum as monocation–neutral reactions only result in a single charged product. This statement holds true for the monocation–neutral reactions that occur in the source region of the spectrometer. However, as stated above, some of the neutral reactant diffuses into the acceleration region and the monocations that are accelerated down this region during the repeller pulse may react with these neutrals, predominantly by ET. When high repeller plate and acceleration voltages are employed, the monocation can be sufficiently accelerated prior to the interaction, that the nascent neutral product that is formed in the reaction continues travelling towards the detector with sufficient energy to cause an electron cascade on the MCP. That is, neutrals with a high velocity can be detected. When low repeller and acceleration voltages are employed, the neutrals do not have sufficient velocity to trigger an electron cascade upon impact with the MCPs. To illustrate this phenomenon more clearly, the example of the $C_2H_2^{2+}$ – Ar collision system will be discussed. The coincidence spectra collected following collisions of $C_2H_2^{2+}$ (and the isobaric CH^+) with Ar at E_{CM} of 6 eV, employing 50 V and 300 V on the repeller plate are shown in Figure 2.11 (a) and (b) respectively. In both Figure 2.11 (a) and (b) a cluster of tails are obvious that have been labelled **1**, these signals are due to the three "real" reaction channels that we detect following interaction of $C_2H_2^{2+}$ and Ar. More detail regarding these three reactions is given in Chapter 6. In addition to the spectra in Figure 2.11, a spectrum was collected employing 300 V on the repeller plate but no neutral Ar collision gas was introduced. From this spectrum it is obvious that tail **2**, and the corresponding peak due to detection of C_2H^+ + H^+ in coincidence, is due to a uni-molecular decay of the dication, yielding C + H^+, rather than a collision induced dissociation.

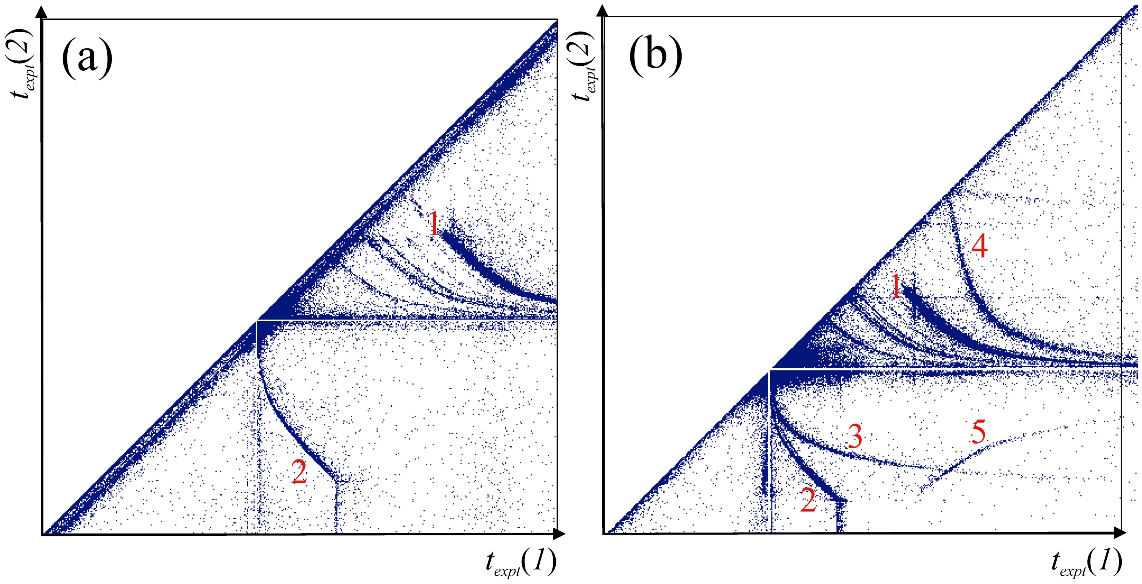

Figure 2.11 Coincidence spectra recorded following collisions of $C_2H_2^{2+}$ with Ar at E_{CM} of 6 eV employing (a) 50 V on the repeller plate and (b) 300 V on the repeller plate. Any tails that are not labelled **1–5** are due to reactions of the dication with trace background gases such as N_2 and O_2.

However, what is most striking about the spectra shown in Figure 2.11 (a) and (b) is that there are three tails, **3**, **4** and **5**, that only appear when 300 V is applied to the repeller. In the aforementioned spectrum, where no Ar was introduced, **3**, **4** and **5** were notably absent, indicating that they arise due to an interaction between the ion pulse and the neutral reactant. A series of simulations, which used Newtonian principles to calculate the TOFs of products from CH^+ – Ar interactions at various points along the acceleration region, were carried out. By varying the reaction products, the monocation–neutral reactions responsible for tails **3** and **4** were identified empirically by fitting to the experimental data. It was found that tail **3** is due to collision induced dissociation of the dication, resulting in C + H^+ + Ar products, reaction (2.7). The tail is made up of events where C and H^+ are detected in coincidence.

$$CH^+ + Ar \rightarrow C + H^+ + Ar \qquad (2.7)$$

Tail **4** is due to electron transfer between CH^+ and Ar yielding CH and Ar^+, reaction (2.8).

$$CH^+ + Ar \rightarrow CH + Ar^+ \qquad (2.8)$$

The experimental pairs of TOFs that make up tails **3** and **4** are shown in Figure 2.12, along with the TOFs generated by the simulation. Clearly, the simulation almost exactly replicates the experimentally measured TOFs, confirming their identity.

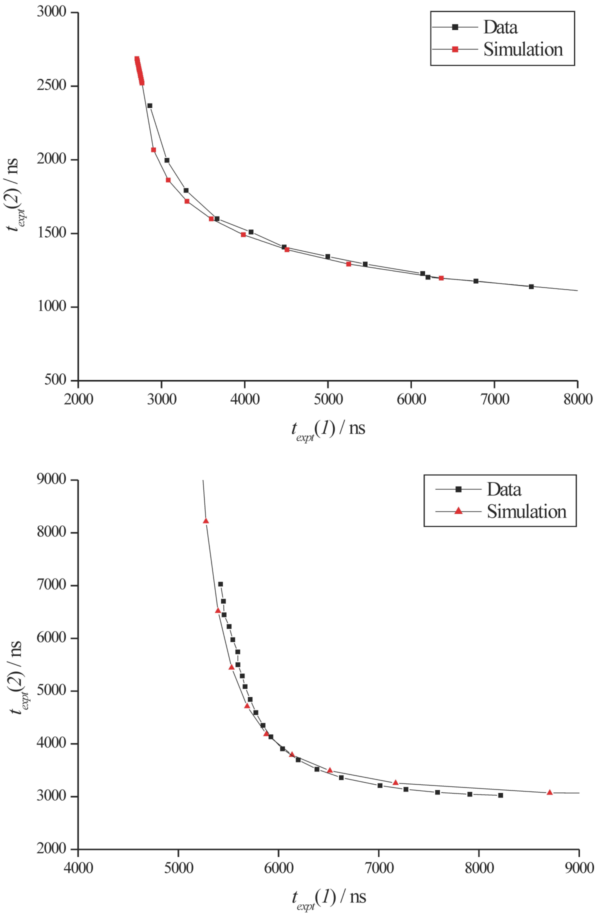

Figure 2.12 A comparison of experimental (black) and simulated (red) TOFs for (top) the collisional dissociation of CH^+ into C + H^+, and (bottom) the electron transfer reaction between CH^+ and Ar yielding Ar^+ and CH. These monocation–neutral reactions occur in the acceleration region of the TOF MS.

The tail that has been labelled **5** cannot be modelled using the simple Newtonian simulation that has been used to clearly identify the origins of **3** and **4**. The probable reason for this failure in the simulation is that we believe **5** to be due to a two–step reaction, specifically, that there is some kind of secondary dissociation. One possible explanation could be reaction, yielding C^+ + Ar products. The current simulation does not have the capability to model the outcome of a two–step mechanism.

$$CH^+ + Ar \rightarrow ArC^+ + H \text{ then } ArC^+ \rightarrow C^+ + Ar \qquad (2.9)$$

In conclusion, the isobaric monocations that are transmitted to the reaction region along with the dications can occasionally produce signals in the coincidence spectrum. These instances occur when the monocation reacts efficiently with the neutral collision partner at elevated collision energy. When a high repeller and accelerating voltage are employed, the resulting product neutral and monocation both have sufficient velocity upon hitting the MCP to produce a signal, giving a data point in the coincidence spectrum. These monocation neutral reactions can almost all be elucidated by means of a Newtonian simulation that replicates extremely well the characteristic tails in the coincidence spectra, provided that the reaction does not involve a two–step mechanism.

2.13.3 The "Exclusion Zone"

In every coincidence spectrum there is an intense strip of false coincidences in the vicinity of the TOF of the dication. This intense strip is due to false coincidences with unreacted dications. Despite the fact that there is on average less than one dication per pulse, there are still many more dications detected than any other ion; the unreacted dication signal far outweighs the product signal. As such, unreacted dications are comparatively likely to be detected in coincidence with an erroneous or "dark" count that can be due to electronic noise or cosmic rays. These false coincidences have such a great intensity that they would swamp the spectrum and so we set an exclusion zone in the vicinity of the reactant TOF, within which any signals are not added to the data set.

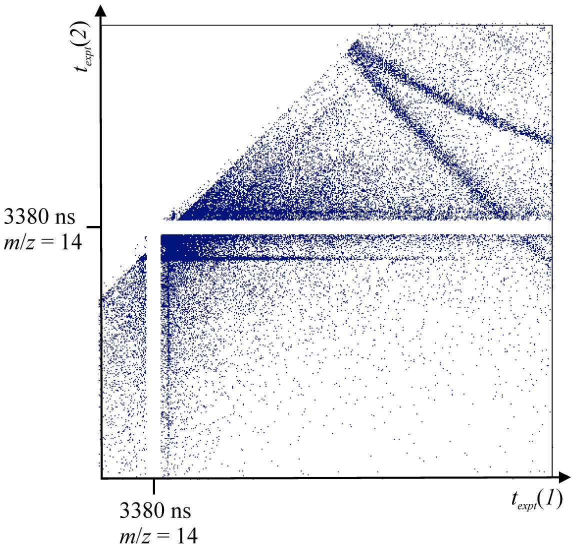

Figure 2.13 Section of a coincidence spectrum recorded following interactions of N_2^{2+} with CO. As is clear, we set an exclusion zone around the TOF of the reactant dication so that this region is not overwhelmed by false coincidences.

Figure 2.13 shows a representative section of a coincidence spectrum in the vicinity of the TOF of the reactant dication. Specifically, the spectrum shown in Figure 2.13 was recorded following interaction of N_2^{2+} with CO. The N_2^{2+} dication has a TOF of 3380 ns and the exclusion zone is clearly visible. For some collision systems this exclusion zone causes a slight inconvenience as a product monocation may have the same m/z as the reactant and so the peak occurs in the vicinity of the exclusion zone. However, due to the considerable translational energy release in dication–neutral reactions, product flight times are often altered from that of an ion of the same mass and zero initial kinetic energy, meaning the peak lies "across" the exclusion zone. In such cases, there are simple corrections that can be made to estimate the correct number of counts in the peak and therefore calculate accurate branching ratios. More details on these corrections are given in Chapter 4.

2.14 Product Velocities in the Laboratory Frame

The sets of ten times that are collected for a pair of product ions detected in coincidence, for each pair that make up a particular reaction channel (peak), can be selected for further analysis. In order to derive the reaction dynamics and energetics of the dication–neutral reactions under investigation, firstly, the x, y and z components of the product velocity vectors need to be determined in the laboratory (LAB) frame. In the laboratory frame, the movement of the ions is defined relative to the axes of the PSCO apparatus, where the z direction is along the MS in the same direction as the reactant travel. To derive the x and y components of an ion product's velocity, $v_x(i)$ and $v_y(i)$, the position of the ion arrival on the PSD must be calculated. From the PSD we have a set of four times corresponding to the time taken for the charge pulse to reach each end of each delay line. The position of the ion impacts $x(i)$ and $y(i)$ are measured relative to the centre of the detector and are given by Equations (2.10) and (2.11) where s_x and s_y are the propagation speeds of the charge pulse along the x and y oriented delay-lines respectively. These propagation speeds are determined by calibration and depend on the specific delay-line anodes.

$$x(i) = [t_{xa}(i) - t_{xb}(i)] / s_x \qquad (2.10)$$

$$y(i) = [t_{ya}(i) - t_{yb}(i)] / s_y \qquad (2.11)$$

Additionally, the x and y coordinates of the reactant ion in the reaction region (x_0, y_0) must be known. (x_0, y_0) can readily be calculated using (2.10) and (2.11) from the position of the unreacted beam on the detector. The final piece of information required to calculate $v_x(i)$ and $v_y(i)$ is the total TOF of the ion, which is given by $t_{\text{expt}}(i)$ plus a correction allowing for the electronic delay between pulsing the repeller plate and the start of data collection. Thus, $v_x(i)$ and $v_y(i)$ can be calculated using (2.12) and (2.13).

$$v_x(i) = \frac{x(i) - x_0}{t_{\text{expt}}(i) + c} \tag{2.12}$$

$$v_y(i) = \frac{y(i) - y_0}{t_{\text{expt}}(i) + c} \tag{2.13}$$

The z component of the ion velocity $v_z(i)$ is calculated from the deviation of $t_{expt}(i)$ from the flight time of an ion of the same mass but zero initial KE, $t_0(i)$. For this calculation of $v_z(i)$, the Wiley–McLaren "braking time" relationship is used, Equation (2.14). In this equation e is the charge on an electron, Z is the charge number of the ion, F is the electric field strength in the source region that is determined by a calibration experiment and $m(i)$ is the mass of the ion. Calibration of the electric field strength is carried out by measuring the TOF of an ion of known m/z, for example Ar^{2+}, whilst varying the rest potential of the ions.

$$v_z(i) = -(t_{\text{expt}}(i) - t_0(i))eZF/m(i) \tag{2.14}$$

Using the procedure outlined above, the LAB frame ion velocity $v(i) = (v_x, v_y, v_z)$ for $i = 1$ and 2 can be derived for every pair of ions detected.

2.15 The Centre–of–Mass Frame

The dynamics of a particular dication–neutral reaction channel are most clearly revealed when the product velocities are expressed in the centre–of–mass (CM) frame. In the CM frame the sum of the momenta of the reactants equals zero. The motion of the reactants and products can be expressed relative to the direction of the CM in the LAB frame, which makes interpretation of the dynamics more facile than expressing them in the LAB frame. In the CM frame the reactants appear to be travelling "toward" one another, whereas in the LAB frame the dication is travelling with a very large velocity in the z direction and the neutral is almost stationary. The overwhelmingly large velocity of the dication compared to the neutral, means that in the LAB frame, any products will continue travelling in effectively the same direction as the reactant dication prior to the collision. Working in the CM frame effectively means the large velocity of the dication is subtracted.

2.15.1 Deriving the Velocity of the Centre–of–Mass

In order to convert the product velocities to the CM frame, the velocity of the CM of the collision system in the LAB frame must first be derived. Conversion from the LAB to the CM frame can be done in two ways. The first method depends on knowledge of the mass and velocity of the neutral, m_{nu} and v_{nu}, and the dication, m_{di} and v_{di}. Given that the angular spread of the dication beam in the x and y directions is negligible, it follows that the x and y components of the CM velocity are insignificant. Thus, the z component of the CM velocity v_z^c can be calculated using Equation (2.15).

$$v_z^c = \frac{m_{di}v_{di} + m_{nu}v_{nu}}{m_{di} + m_{nu}} \qquad (2.15)$$

However, note that the momentum of the neutral, at the collision energies we achieve, is negligible compared to that of the dication. Thus, Equation (2.15) reduces to Equation (2.16). This first method calculates a single value for v_z^c that is used in subsequent calculations for every reactive event.

$$v_z^c = \frac{m_{di}v_{di}}{m_{di} + m_{nu}} \qquad (2.16)$$

The second method for calculation of the CM velocity of the collision system, calculates v^c on an event–by–event basis for each product ion pair. Calculation of the CM velocity on an event–by–event basis can only be carried out for two–body reactions, where only two ionic products are formed. This second method requires that both of the ionic product velocity vectors, $v(i)$ i = 1 or 2, for a two–body reaction are known in the LAB frame. The CM velocity, v^c, can then be calculated using Equation (2.16). Both of these methods yield values for the CM velocity that are in good agreement with each other.

$$v^c = \frac{m(1)v(1) + m(2)v(2)}{m(1) + m(2)} \tag{2.16}$$

2.15.2 Converting the LAB Frame Product Velocities to the Centre–of–Mass Frame

Now that the CM velocity has been calculated, the velocities of the product ions in the CM frame, $w(i)$, can be calculated using Equation (2.17). Kinetic energy release (KER) distributions and detailed angular scattering information can then be extracted by manipulation of the ionic product velocity vectors in the CM frame.

$$w(i) = v(i) - v^c \tag{2.17}$$

Hence, after the procedures described above are carried out, the data set consists of pairs of velocity vectors for the product monocations in the CM frame.

2.15.3 Velocity of a Third Body

The PSCO technique detects both ions formed in the dication–neutral reaction, allowing the determination of their CM frame velocities, as described above. Clearly, when two ionic products are formed then they will have nascent velocities oriented at 180° to each other. However, in some reactions a neutral species is also formed, making the dynamics of the reaction more complex. The velocity of the neutral cannot be directly determined as these products are not detected by the PSD. Nevertheless, with knowledge of the exact momenta of the two ionic products, the velocity of the neutral product can be determined *via* conservation of momentum in the CM frame using Equation (2.18).

$$w(3) = -[m(1)w(1) + m(2)w(2)]/m(3) \tag{2.18}$$

Hence the CM frame velocity vectors for all reaction products for each reactive event detected are obtained for two and three–body reactions. Full dynamics and energetics can then be determined for any two or three–body reactions.

2.16 Scattering Diagrams

For ease of interpretation of the product velocities in the CM frame we display them pictographically in the form of scattering diagrams. The angle between the ionic product velocity vectors Θ can be determined using Equation (2.19). For a two-body event, conservation of momentum dictates that $\Theta = 180^{\circ}$.

$$\cos(\Theta) = \frac{w(1) \cdot w(2)}{|w(1)||w(2)|} \tag{2.19}$$

In addition, for the construction of the scattering diagram, the angle θ between the ionic product velocity vector $w(i)$ and the CM velocity v^c must also be determined. Determination of θ is carried out by simply taking the dot product of $w(i)$ with v^c.

2.16.1 Centre-of-Mass Frame

The scattering diagram for the reaction in the CM frame, which is a polar (r, θ) histogram, can now be constructed. Scattering diagrams plot, on an event by event basis, the velocity and scattering angle $\theta(i)$ (i = 1, 2) of each ionic fragment with respect to v^c. In practice, v^c is almost the same as the direction of the reactant dication prior to the collision in the CM frame, so often the product velocities are expressed relative to the directions of the reactants prior to the collision. The scattering of each ion is cylindrically symmetric about v^c and so we plot the scattering data for one ion in the upper half of the figure and the scattering data for the other ion in the lower half. In this way, the scattering directions of both product ions can be displayed simultaneously. The form of the scattering diagrams can give great insights into reaction dynamics.

There are two scattering diagram motifs that are regularly observed; specifically these are due to mechanisms involving “forward scattering” and “isotropic scattering”. A representative scattering diagram that exhibits strong forward scattering is shown in Figure 2.14. Figure 2.14 shows the scattering of the $C_2H_2^+$ and Ar^+ products of SET between $C_2H_2^{2+}$ and Ar. The full-headed arrows that point to the right and left of the figure, respectively, indicate the directions of the dication and neutral, prior to the collision, in the CM frame. As mentioned before, the direction of the dication prior to the collision is almost the same as the direction of v^c. For each pair of ions that is detected, we calculate their associated CM frame velocity vectors and these will be plotted as a pair of points on the scattering diagram. Thus, the scattering diagram is, in reality, a two-dimensional histogram of all the pairs of points that make up the particular reaction channel as seen in Figure 2.14 (a). These "spot" plots emphasise single counts, so it is often more useful to convert these data point-based diagrams to an intensity plot, as seen in Figure 2.14 (b).

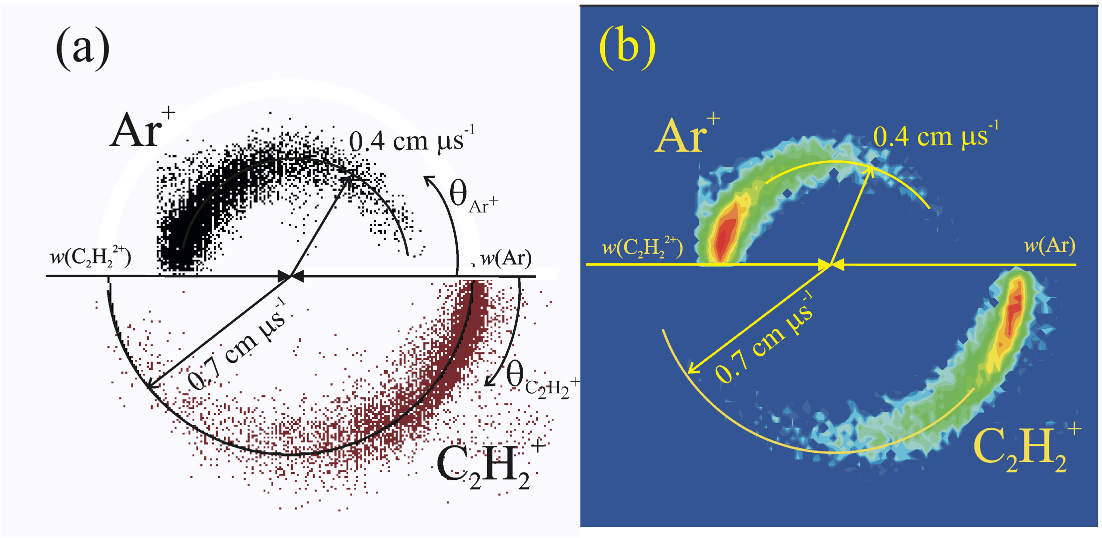

Figure 2.14 CM frame scattering of the $C_2H_2^+$ and Ar^+ products of the non-dissociative SET between $C_2H_2^{2+}$ and Ar. (a) shows the raw data scattering diagram and (b) shows the same data but converted to an intensity plot. The directions of the reactants are shown by the full-headed arrows; the dication was travelling to the "right" prior to the collision and the neutral was travelling to the "left" prior to the collision. Clearly, the directions of the products are anisotropic and largely still in the directions of the associated reactants prior to the collision.

As is clear from Figure 2.14, the average scattering direction of the $C_2H_2^+$ product is predominantly in the same direction as the $C_2H_2^{2+}$ reactant prior to the collision. Conversely, the Ar^+ product is predominantly scattered in the same direction as the reactant Ar in the CM frame. This distinctive forward scattering arises because the electron was transferred from the Ar to the $C_2H_2^{2+}$ at a relatively large interspecies separation. As described in Chapter 1, the Landau-Zener reaction window theory says that ET is likely to occur when the reactant and product PEC crossing lies between 3 and 6 Å. Therefore, this relatively large separation between the reactants at the instant of electron-transfer means that there is no long term association of the reactants, they simply fly past one another and the electron rapidly "hops" from the neutral to the dication. The product monocations then broadly retain the directions of their associated reactant precursors.

Note that despite the predominant forward scattering apparent in Figure 2.14, there are a small number of events where the $C_2H_2^+$ product is scattered to near 180° (the direction of the neutral reactant prior to the collision). Such events arise from a head–on collision of the reactants and the $C_2H_2^+$ is returned along the path of the $C_2H_2^{2+}$. Note also that there is a very low probability of the product $C_2H_2^+$ monocation being scattered towards exactly 0° (the direction of the dication prior to the collision). The diminishing probability of reactive events that result in scattering towards 0° and 180° is due to the fact that, geometrically, the number of dication trajectories resulting in scattering towards exactly 0° and 180° is very small. Conversely, the number of trajectories resulting in scattering towards 90° is much larger because this distribution of trajectories is sinusoidal in shape. Another way to explain this scattering angle effect is that the volume of the integration over the azimuthal angle increases with increasing angle and is zero at 0° and 180°, shown schematically in Figure 2.15.

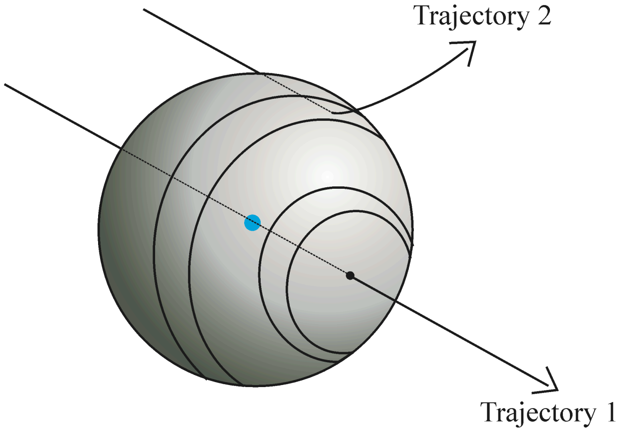

Figure 2.15 Schematic showing that the volume of the integration over the azimuthal angle increases with increasing angle. The perimeter of the sphere represents the radius at which the reactant and product PECs cross.

Thus, even for reactions that exhibit very strong forward scattering in the scattering diagram, the peak in scattering directions is displaced away from 0° and generally a tail is observed that extends to higher angles. Forward scattering is commonly observed for SET reactions, but also occasionally for bond–forming channels.

The second common type of scattering motif is isotropic scattering. Such scattering arises when the reactants have stuck together to form a complex. The complex then survives for several of its rotational periods and then fragments into the observed products. The rotation of the complex scrambles any "memory" the system has of the reactant directions prior to the collision and so upon fragmentation, the products are ejected towards all angles θ with equal probability. In terms of the schematic shown in Figure 2.15, the product ion trajectories fill the whole "reactive sphere" with equal intensity. A scattering diagram exhibiting isotropic scattering is shown in Figure 2.16. The distribution of scattering angles d(θ) for reactions exhibiting true isotropic scattering is sinusoidal in shape. Thus simply dividing the product angular distribution by sin(θ) easily identifies a true isotropic distribution.

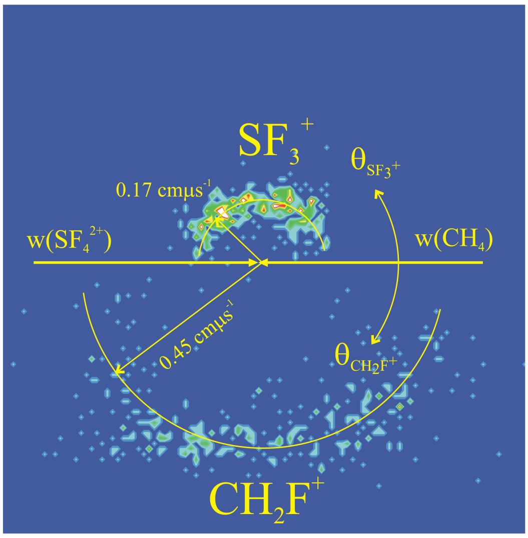

Figure 2.16 CM frame scattering diagram showing the isotropic scattering of the CH_2F^+ and SF_3^+ products of a chemical channel between SF_4^{2+} and CH_4. The product scattering directions are clearly not correlated in any way to the reactant directions prior to the collision, which are shown by the full-headed arrows.

2.16.2 Internal Frame Scattering Diagrams

In reactions where three products are formed, two monocations and a neutral, each of their velocity vectors can be determined. Therefore, in addition to CM frame scattering diagrams that plot the velocities of the ionic products with respect to v^c, the product scattering directions can be displayed with reference to each of the other products. These internal frame scattering diagrams plot the magnitude of $w(i)$ i = 1, 2, 3 as the radial coordinate and the angle θ between $w(i)$ and that of the reference product $w(i_{ref})$ i_{ref} = 1, 2, 3 as the angular coordinate. Similarly to the CM frame diagrams, the data for one product are plotted in the upper half of the figure and the data for the other product in the lower half. Examples of internal frame scattering diagrams for the dissociative SET reaction between O_2^{2+} and NO yielding O_2^+ + N^+ + O are shown in Figure 2.17. Figure 2.17 (a) shows the scattering of the N^+ and the O with respect to the O_2^+, (b) shows the scattering of O_2^+ and O with respect to the N^+ and (c) shows the scattering of O_2^+ and N^+ with respect to the neutral O.

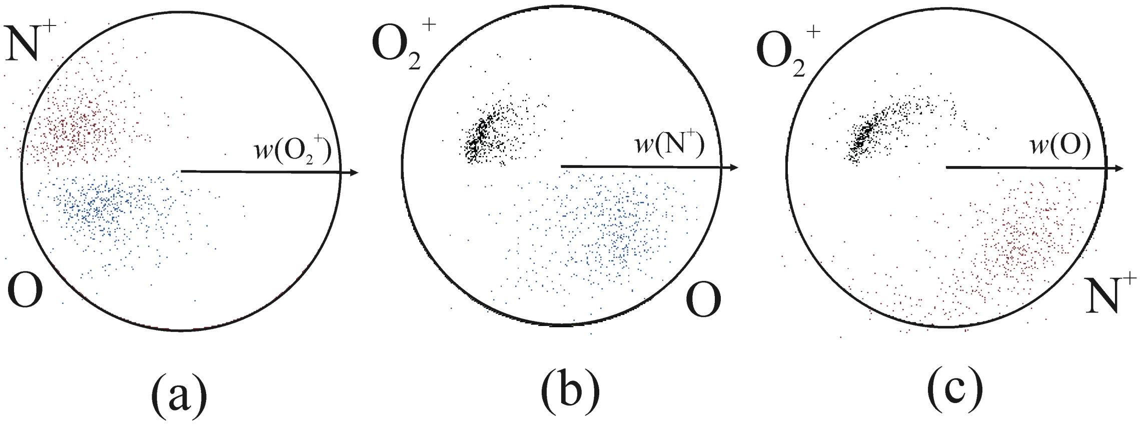

Figure 2.17 Internal frame scattering diagrams that show the relative directions of the O_2^+, N^+ and N products ions of dissociative SET between O_2^{2+} and NO. (a) Shows that the N^+ and O are scattered away from the O_2^+; (b) shows that the velocity of the O_2^+ is anti-correlated with that of the N^+ whereas the O velocity is correlated with that of the N^+ and (c) shows the analogous relations as the centre figure. The obvious conclusion from this characteristic set of relationships between the product velocities is that the SET occurred at significant interspecies separation and the nascent NO^+ dissociated a period of time later.

The scattering of the products seen in Figure 2.17 is characteristic of dissociative SET where the ET occurs at significant interspecies separation to form O_2^+ + NO^+, then the NO^+ dissociates into N^+ and O some time later. This mechanism is clearly indicated by the fact that the N^+ and O have scattering that is anti-correlated with the motion of the O_2^+ (Figure 2.17 (a)), the O has a general motion that is correlated with that of the N^+ (Figure 2.17 (b)) and the motion of the O_2^+ is clearly anti-correlated with the motion of both the N^+ (Figure 2.17 (b)) and the O (Figure 2.17 (c)). Internal frame scattering diagrams will be discussed extensively in Chapter 4.

2.17 Translational Energy Release

Further analysis of the coincidence data for the individual ion pairs allows the determination of the translational energy release associated with a particular reaction channel. Determination of the translational energy release in the CM frame T, from the product ion velocities in the LAB frame for a two–body reaction is possible by using Equation (2.20), where μ_p is the reduced mass of the product ion pair and $v_{x,y,z}$ are the x, y and z components of the ionic velocity vectors.

$$T = \frac{1}{2}\mu_p[(v_{x1} - v_{x2})^2 + (v_{y1} - v_{y2})^2 + (v_{z1} - v_{z2})^2] \tag{2.20}$$

Subtraction of the E_{CM} from T for each reactive event yields an exothermicity distribution for the reaction channel, according to Equation (2.21). The E_{CM} can be calculated employing Equation (2.22) where μ_R is the reduced mass of the reactants and v_{di} is the velocity of the dication. In using Equation (2.22) it is assumed that the velocity of the neutral is negligible compared to that of the dication.

$$\Delta E = E_{\mathrm{Products}} - E_{\mathrm{Reactants}} = T - E_{CM} \tag{2.21}$$

$$E_{CM} = \frac{1}{2}\mu_R v_{di}^2 \tag{2.22}$$

The exothermicity of a reaction is the difference in energy between the reactant and product states. A schematic diagram showing the distinction between the exothermicity and kinetic energy release (KER) of a reaction is shown in Figure 2.18. As can be seen in Figure 2.18, the exothermicity of a reaction remains constant with varying E_{CM}. The exothermicity distribution for a reaction channel can be compared to literature exothermicities. Thus, sometimes the electronic states, and even range of vibrational states, participating in the reaction can be identified. The ability to extract KER distributions is a very powerful feature of the PSCO methodology.

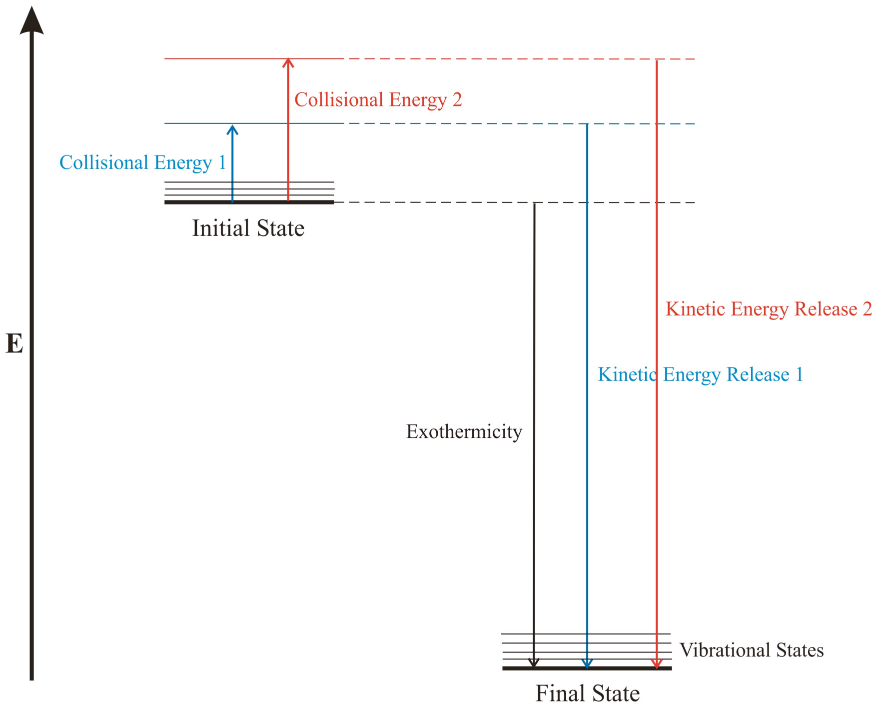

Figure 2.18 A schematic showing the KER and exothermicity of a reaction. The blue and red arrows indicate how the measured KER of a reaction depends on the collision energy of the system whereas the exothermicity of the reaction remains constant.

2.18 High vs. Low Repeller Plate Voltages

There are several advantages and disadvantages of employing a high or low repeller plate voltage when operating the PSCO MS. Firstly, with a high repeller voltage, typically 250–300 V, the TOF of the product ions is comparatively short. With this short TOF, small variations in product velocities cannot be distinguished very precisely; the energy resolution is low. Conversely, if a low repeller plate voltage, typically 50 V, is applied, the ion TOFs are much longer and product ions will have time to "spread out" in the drift tube. Thus, small differences in product initial velocities are more discernible when using a low repeller plate voltage; the energy resolution is high. In conclusion, the energy resolution of the PSCO dataset is markedly lower at high repeller plate voltages than at lower repeller plate voltages.

Despite, the obvious advantage of improved energy resolution at low repeller plate voltage, there are also several disadvantages. The principle problem is that when employing low repeller and accelerating voltages, ions that are formed with large x or y velocity components will not reach the detector. As a result, ions scattered to a range of angles centred around 90° will not be detected. Clearly, failing to detect a proportion of the events that make up a reaction channel has an affect on the peak we observe in the coincidence spectrum. Specifically, the peaks are split into two sections, consisting of products that are scattered to low angles and those to high angles. Representative sections of coincidence spectra, recorded employing a high or low repeller plate voltage are shown in Figure 2.19. Also shown in Figure 2.19 are the CM frame scattering diagrams constructed by selecting the events that make up the peaks in the coincidence spectra.

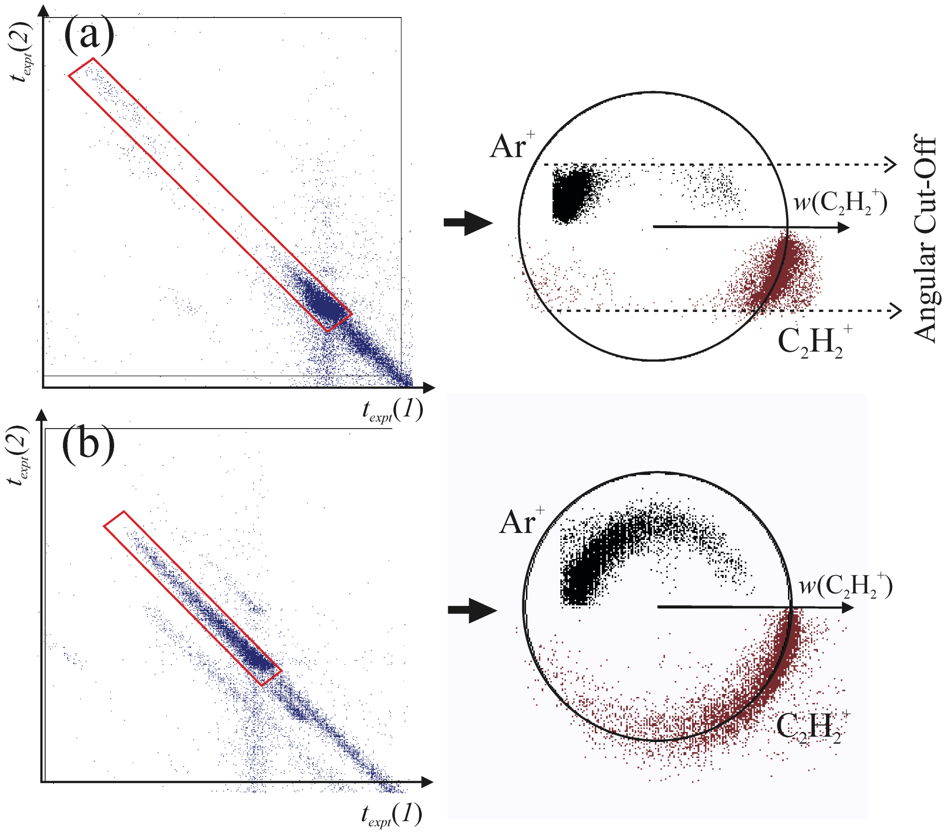

Figure 2.19 Sections of the coincidence spectra recorded following collisions of $C_2H_2^{2+}$ with Ar employing 50 V (top) and 300 V (bottom) to the repeller plate. The peak outlined in red corresponds to the non-dissociative SET channel, for which the CM frame scattering diagram has been constructed and is shown to the right of the spectrum. The peak recorded when 50 V was applied to the repeller has a split shape due to the loss of ions that are scattered towards intermediate angles, as is clear in the CM frame scattering diagram.

Figure 2.19 (a) shows the coincidence spectrum recorded following collisions of $C_2H_2^{2+}$ with Ar employing 50 V on the repeller plate. From this coincidence spectrum the events corresponding to the non-dissociative SET has been selected and the CM frame scattering diagram constructed. In contrast, Figure 2.19 (b) shows the analogous coincidence spectrum and CM frame scattering diagram for the same non-dissociative

SET channel but recorded employing 300 V on the repeller plate. The split peak shape and angular "cut–off" in the scattering diagram are clear in Figure 2.19 (a). Failing to detect a significant proportion of reactive events in a channel has several consequences. Firstly, accurate relative branching ratios cannot be determined and secondly, it takes longer to accrue the same number of counts in a reaction channel than when employing a higher repeller voltage.

2.19 Modifications

Over the course of this PhD, several modifications to the PSCO experimental design were implemented. These include the installation of a new TOF MS and detector, incorporation of a molecular beam to introduce the neutral reactant and a procedure that allows the first few electrostatic lenses of the acceleration region to be pulsed. In the next section, the motivation for carrying out these modifications and the advantages they provide to the PSCO methodology will be described.

2.19.1 Increasing the Angular Acceptance of the PSCO Apparatus

In order to try to increase the angular acceptance of the PSCO MS, which is particularly important when employing a low repeller plate voltage, the original TOF MS was replaced with a TOF MS with a larger diameter. The initial design of the PSCO apparatus included a TOF MS with a drift tube diameter of 8 cm. Clearly, using a TOF MS with a larger drift diameter means that when employing 50 V on the repeller plate, fewer ions will hit the walls and be lost. The dimensions of the new TOF MS in the z direction are almost exactly the same as the initial design, specifically the source region is 1.7 cm long, the acceleration region is 11 cm long and the drift region is 27.7 cm long. However, the new TOF has a drift diameter of 12 cm.

Of course, a wider TOF MS affords no benefit unless a detector of the same diameter is also employed. Consequently, in addition to the TOF MS with a larger diameter, a new RoentDek PSD with a diameter of 120 mm was also installed enabling detection of ions that are scattered to the (x, y) limits of the drift region. This new PSD is of the same design as that described in section 2.10. Specifically, it consists of a pair of micro–channel plates in conjunction with a pair of perpendicular delay–line anodes.

Indeed, it has been shown by calibration experiments that the angular acceptance of the PSCO apparatus is increased with the new TOF MS compared with the old TOF MS.

2.19.2 Molecular Beam for Introduction of the Neutral

2.19.2.1 Advantages and Disadvantages of the Effusive Neutral Beam

The original design of the PSCO apparatus introduced the neutral to the reaction region *via* an effusive jet through a needle valve. There are several advantages to this method of introducing the neutral. Principally, it is a simple method and uses a comparatively small volume of reactant gas per unit time. However, there are two disadvantages to this method of introducing the neutral.

The dominant degree of broadening in the energy resolution caused by using an effusive neutral beam is introduced by the fact that the neutral beam is not well collimated. In principle, the effusive neutral reactant could be travelling in every direction in the interaction region resulting in a kind of collision energy Doppler shift. However, in reality, the effusive jet will retain a degree of collimation even in the centre of the interaction region. Clearly, if the neutral interacts with the dication in a "head on" collision where the neutral is travelling in the opposite direction to the dication beam, then the effective collision energy is increased from that with a stationary neutral. Conversely, if the neutral is travelling in the same direction as the dication when they collide then the effective collision energy is reduced. For example, collisions of Ar^{2+} with He at a centre–of–mass collision energy E_{CM} of 0.4 eV and 1.2 eV will have a maximum theoretical E_{CM} spread due to the motion of the He of 0.4 eV and 0.6 eV, respectively. Clearly, at low E_{CM} the maximum spread in collision energies due to the motion of the neutral can theoretically be quite large. The effusive beam does retain a degree of collimation and so these quoted E_{CM} spreads are theoretical maxima and in reality the E_{CM} spread will be much less.

A minor disadvantage of introducing the neutral effusively is that the neutral will have a thermal rovibrational distribution, which, although predominantly consisting of ground state species does introduce a small degree of broadening to the translational exothermicity distributions that we measure for each reaction channel. Nevertheless, there are modifications that can be made to the experimental design that dramatically reduce the drawbacks of an effusive jet, as described in the next section.

2.19.2.2 Advantages of a Molecular Beam

In order to reduce the negative aspects of introducing the neutral reactant effusively, a modification has been made to the original PSCO design that allows the neutral to be introduced as a "molecular beam". A molecular beam is a supersonic expansion of gas, in which the translation, vibrational and rotational temperatures of the constituent species is very low. The molecular beam is then passed through a skimmer than collimates the gas into a very narrow jet. In order to form a molecular beam, a gas at high pressure is allowed to expand through a very small aperture into a region of lower pressure. The resulting flow of gas must be non–turbulent to prevent collisions between the species that would increase the temperature of the gas. Gas species with the appropriate trajectories pass through the skimmer, resulting in a beam with a very small diameter. The molecular beam on the low–pressure side of the skimmer (the reaction region) consists of atoms or molecules that are all moving in the same direction with almost equal velocities. The expansion of the gas causes a rapid cooling resulting in a beam comprising almost exclusively ground state species. Thus, one of the disadvantages of using an effusive jet, the thermal distribution of rovibrational states, is removed by use of the molecular beam.

The major advantage of using the molecular beam to introduce the neutral is that in the finely collimated jet, the reactants are all travelling in the same direction. Therefore, the spread in collision energies due to the motion of the neutral towards or away from the oncoming beam of dications is all but removed. Clearly, the neutrals in the molecular beam are travelling very rapidly, which will increase the collision energy of a dication–neutral collision compared to a dication–neutral collision with a stationary neutral. However, this E_{CM} offset is the same for every interaction. Figure 2.20 shows a representation of the difference between the effusive and molecular beam methods for introduction of the neutral.

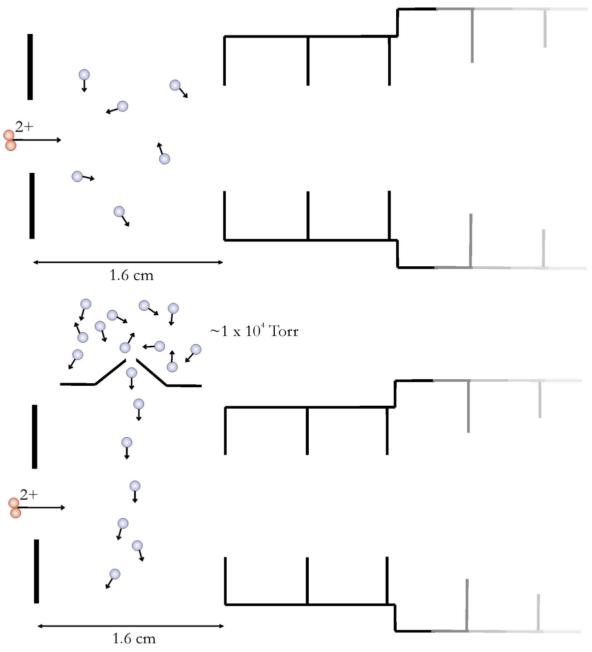

Figure 2.20 Schematic of the source and first few electrostatic lenses of the acceleration region where the dication enters from the left. The figure shows a representation of the difference between an effusive beam of neutrals (top figure) and a molecular beam (bottom figure). Clearly, use of a molecular beam reduces the spread in directions of the neutral and therefore the spread in E_{CM}.

In conclusion, introducing the neutral in the form of a molecular beam dramatically reduces the uncertainty in collision energies over a particular data set. An account of the commissioning of the molecular beam source is given in the next section.

2.19.2.3 Building and Commissioning a Supersonic Neutral Molecular Beam Source

A schematic of the molecular beam set up in shown in Figure 2.21. An additional stainless steel vacuum chamber was attached to the chamber that houses the reaction region. These two chambers are effectively isolated from each other as the 580 μm aperture in the skimmer gives the only connectivity. A General pulsed valve, positioned around 2 cm above the skimmer aperture is used to introduce the neutral gas with a backing pressure of around 1 Torr. However, due to difficulties in getting the dication pulse and neutral pulse to interact, a continuous flow of gas is currently used. This highlights the major disadvantage of employing a molecular beam, this method consumes far more of the neutral gas per unit time than an effusive jet. The majority of this gas is pumped away by a 1000 ls^{-1} turbo–molecular pump into a backing line. A small amount of the gas that exits the pulsed valve gas has exactly the right trajectory to pass through the skimmer aperture and into the reaction region in a comparatively dense jet. Clearly, despite the fact that the gas species in the molecular beam have almost exactly the same velocity, there will be some slight variations in neutral trajectories as the species pass through the skimmer, which results in a gradual broadening of the size of the molecular beam. The size of the skimmer aperture means that the diameter of the molecular beam is expected to be around 2 mm once it reaches the centre of the reaction region.

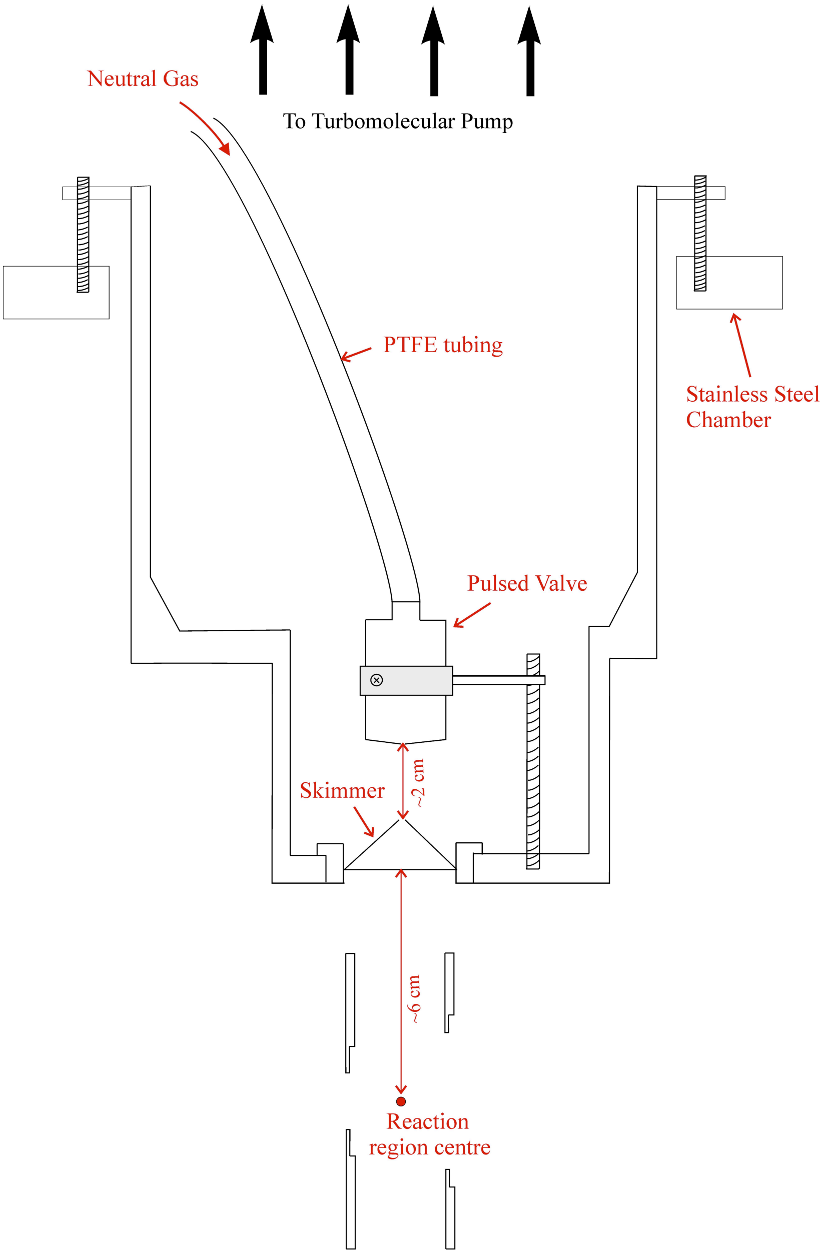

Figure 2.21 Schematic of the apparatus used to form the supersonic molecular beam of neutral species. At the bottom of the figure is seen the reaction region of the TOF MS and the bottom of the skimmer is positioned approximately 6 cm above the centre of this region. The general pulsed valve is positioned approximately 2 cm above the top of the skimmer.

In order to characterise the molecular beam of neutrals, a series of investigations was carried out. These investigations also established that the dication and neutral beam trajectories were intersecting. The non–dissociative SET reaction between N_2^{2+} and Ar, yielding N_2^+ and Ar^+, was studied using a low repeller plate voltage of 50 V. Two experimental runs were carried out, in the first the neutral was introduced effusively (Figure 2.22 (a)) and in the second the neutral was introduced as a molecular beam (Figure 2.22 (b)). The peak in the coincidence spectrum due to detection of N_2^+ and Ar^+ in coincidence is much narrower when the neutral is introduced in the form of a molecular beam, seen in Figure 2.22 (b), than when the neutral is introduced effusively, seen in Figure 2.22 (a).

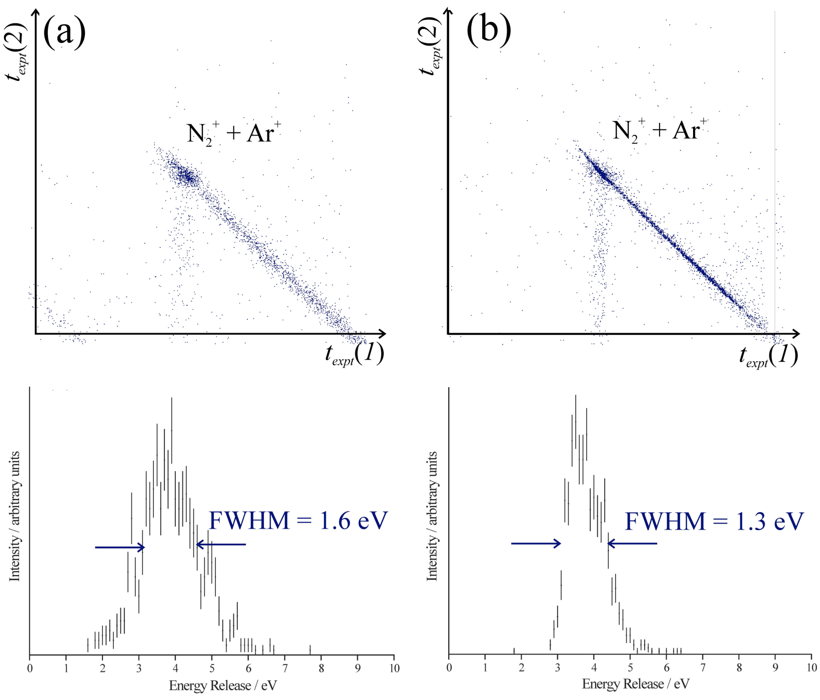

Figure 2.22 Sections of the coincidence spectra collected following interaction of N_2^{2+} with Ar where the neutral was introduced (a) effusively and (b) via the molecular beam. Clearly, the peak in the coincidence spectrum is narrower when the neutral is introduced in a molecular beam. Below the coincidence spectra are shown the corresponding KER distributions derived from the data in the non–dissociative SET peak shown. These KER distributions have comparable FWHMs.

Such narrowing is a good indication that the neutral molecular beam is spatially narrow and that the translational temperature of the beam is low. Moreover, the data collection rates that are observed when employing the molecular beam are greatly increased. These increased rates indicate that the collision probability between a dication and neutral is increased when the neutral is introduced as a molecular beam compared to when it is introduced effusively. This increased collision probability is a good indication that the dication and neutral beam trajectories have a good level of overlap. Consequently, it seems clear that we now have the capability to introduce the neutral to the PSCO apparatus as a supersonic molecular beam.

Also shown in Figure 2.22 (c) and (d) are the KER distributions derived from the data in the non–dissociative SET peak in the coincidence spectra above in (a) and (b). Despite the narrowing of the coincidence spectrum peak, the FWHM of the KER distribution derived from the "effusive run" data is only around 0.3 eV narrower than of the KER distribution derived from the "molecular beam run" data. There is obviously another source of broadening that outweighs the reduction in broadening introduced by using the neutral molecular beam. One potential source of this broadening is proposed to be due to penetration of the accelerating field from the acceleration region into the "field–free" source region of the TOF MS, resulting in a spread in E_{CM}. More details about this penetrating field, its negative effects and the measures taken to counteract it are given in the next section.

2.19.3 Pulsing the First Lens of the Acceleration Region

As the dication pulse enters the source region, the repeller plate is at ground in order that the source region is kept field free. However, the accelerating voltages are not pulsed in the same way as the repeller plate and so are constantly set. Ten electrostatic lenses that are evenly spaced along the acceleration region maintain the field uniformity in the region. When a repeller plate voltage of 300 V is employed, the maximum accelerating voltage is set to –1990 V, meaning the first and second lenses are set to –199 V and –398 V, respectively. A fine metal mesh is positioned between the source and acceleration regions to minimise penetration of the field from the latter region to the former. However, this mesh does not impede 100 % of the electric field and as such there is some field penetration into the source. Therefore, as the dications traverse the source region they are accelerated slightly by this potential gradient resulting in a spread in dication–neutral collision energies. This spread in E_{CM} broadens the exothermicity distributions that are determined from the data. The penetrating field effect also occurs with a low accelerating voltage, but the resulting magnitude of the gradient across the source region is less and so the E_{CM} spread is less pronounced.

Figure 2.23 shows a cross-section of the source region and the first three accelerating lenses. Field gradient simulations were carried out employing SIMION, which has been used to plot contour lines of constant field strength. The first three lenses in Figure 2.23 are set to −111 V, −222 V and −333 V. In the SIMION simulations, shown in Figure 2.23, the repeller plate is set to 0 V, as it would be when the dication enters the source region. The standard method of modelling grids in SIMION is used to model the grid between the source and acceleration regions. This model allows some penetration of the electric field from the acceleration into the source region. As is clear from Figure 2.23, the SIMION model undoubtedly predicts a degree of electric field penetration from the acceleration to the source region.

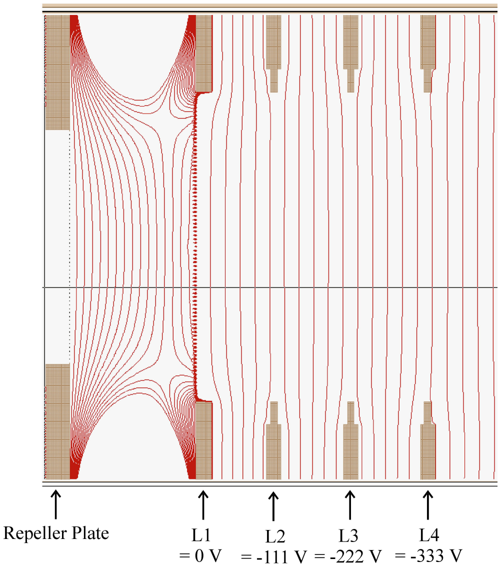

Figure 2.23 SIMION simulation of the contours of constant electric field strength in the source and start of the acceleration region of the PSCO TOF MS. The repeller plate and L1 have 0 V applied and L2, L3 and L4 have voltages of −111 V, −222 V and −333 V, respectively.

It was proposed that pulsing the first accelerating lens voltage at the same time as the repeller plate might reduce the magnitude of the penetrating field and consequently the broadening due to a spread in E_{CM}. More specifically, as the dication enters the source region, the repeller and first accelerating lens are both set at a ground potential and then both of these voltages are pulsed simultaneously to their correct voltages. Initially, SIMION was employed to model the effect of setting the first few lenses to 0 V or to a positive bias voltage. Several combinations of voltages were applied to the first three accelerating lenses (L2, L3 and L4) in the SIMION model, for example, setting L2 and L3 to 0 V (Figure 2.24 (a)), setting L2, L3 and L4 to 0 V (Figure 2.24 (b)) or setting L2 and

L3 to a positive bias voltage of +50 V (Figure 2.24 (c)). From Figure 2.24 it is clear that these combinations of lens voltages all reduce the magnitude of the penetrating field, yet none remove it completely.

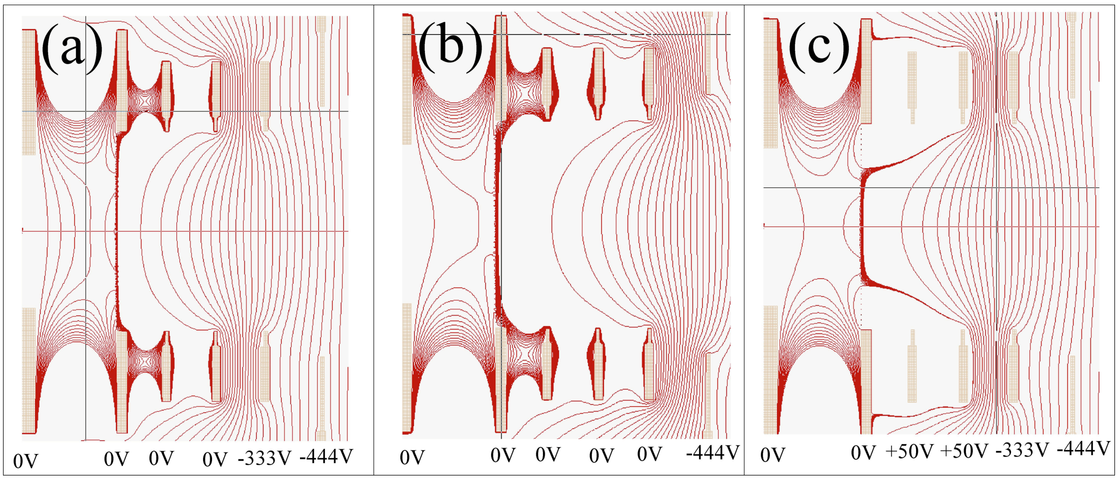

Figure 2.24 Schematic diagrams of the source and start of the acceleration regions of the TOF MS. Contours of constant field strength were calculated employing SIMION. (a) shows the extend of the penetrating field when L2 and L3 are set to 0 V. (b) shows the extent of the penetrating field when L2, L3 and L4 are set to 0 V. (c) shows the extent of the penetrating field when L2 and L3 are set to a positive bias voltage of +50 V.

Given that the SIMION simulations imply that pulsing the first accelerating lenses at the same time as the repeller plate may greatly reduce the effect of the penetrating field, this was investigated experimentally. The ET reaction between Ar^{2+} and He was studied, the He was introduced in a molecular beam and 100 V was employed on the repeller plate. When 100 V is applied to the repeller plate, the maximum accelerating voltage is –600 V, meaning the first and second lenses are set to –60 V and –120 V. Figure 2.25 shows the CM frame scattering diagrams and exothermicity distributions for the SET reaction between Ar^{2+} and He that were derived from four different data sets. The first of these data sets was collected under normal experimental conditions. The second data set was collected whilst pulsing the first accelerating lens to –60 V at the same time as the repeller plate and this lens was set to 0 V otherwise. The third data set was collected whilst pulsing the first accelerating lens but setting it to a positive bias voltage of +36 V otherwise. The final data set was collected whilst pulsing the first and second accelerating lenses and setting these to 0 V otherwise.

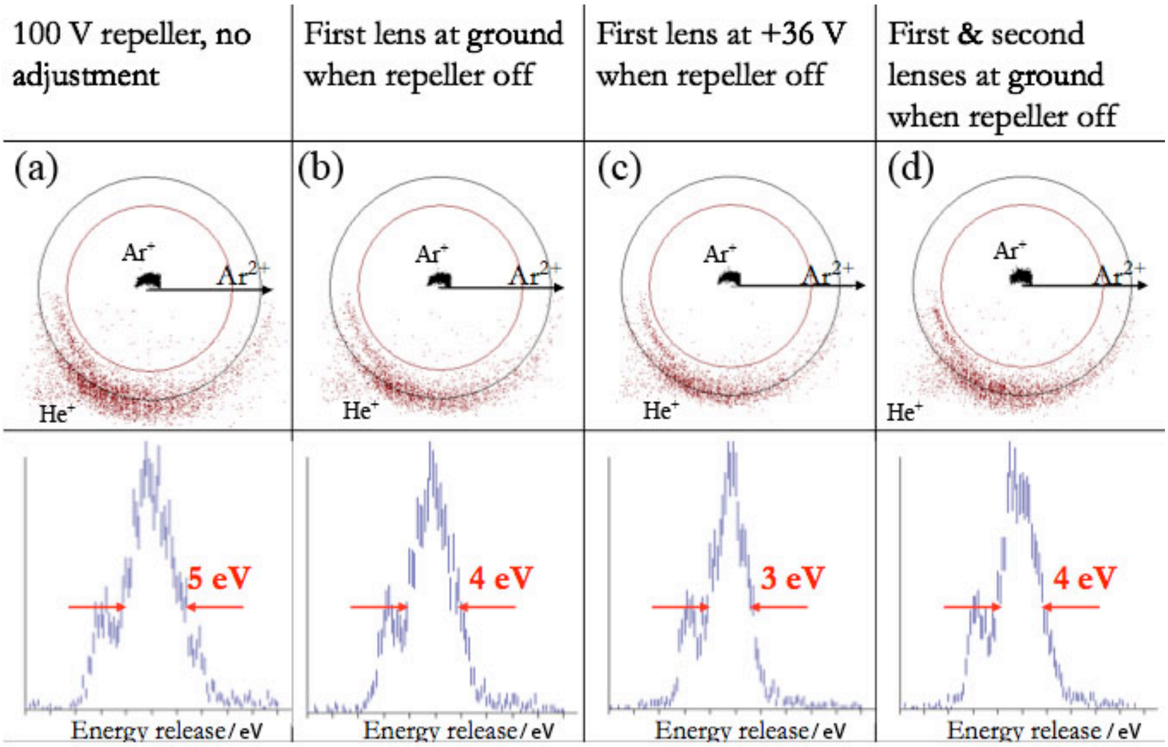

Figure 2.25 CM frame scattering diagrams and KER distributions for the SET reaction between Ar^{2+} and He. The data in (a) were collected under normal experimental conditions with 100 V applied to the repeller plate and the He was introduced to the reaction region in a molecular beam. The data in (b), (c) and (d) were collected under the same experimental conditions as (a) but pulsing on the first, or first and second, accelerating lenses at the same time as the repeller plate. Whilst the repeller was "off", the accelerating rings were set to the voltages specified above the diagrams.

The FWHM of the KER peak centred at 4.9 eV, derived from the data set collected under normal experimental conditions is around 5 eV. As is clear from Figure 2.25 (c), the optimum reduction in broadening due to the penetrating field is achieved when the first accelerating lens is set to a positive bias voltage of +36 V when the repeller is off, in which case the FWHM of the equivalent KER peak is reduced to 3 eV. In conclusion, by pulsing the first accelerating lens as well as the repeller plate we can affect a fairly significant reduction in the FWHM of the peaks in the KER distributions. Further investigations need to be carried out at higher and lower repeller plate voltages in order to ascertain the extent of this possible improvement to the PSCO technique.

2.20 Summary

This chapter has explained the PSCO experiment that was employed to undertake the investigations of dication–neutral reactivity reported in this thesis. In addition, a detailed description of the data analysis was given and several modifications to the original PSCO design were described. Additional modifications such as the implementation of velocity map imagine have undergone preliminary investigation but require further work and so will be outlined in the final chapter.

2.21 References

[1] Hu, W P, Harper, S M and Price, S D, *Meas. Sci. Techn.* **2002**, *13*, 1512–1522.

[2] Dutuit, O, Alcaraz, C, Gerlich, D, Guyon, P, Hepburn, J, Metayer–Zietoun, C, Ozenne, J, Schweizer, M and Weng, T, *Chem. Phys.* **1996**, *209*, 177.

[3] Vaughan, A, *Phys. Rev.* **1931**, *38*, 1687.

[4] Hagstrum, H D and Tate, J T, *Phys. Rev.* **1941**, *59*, 354.

[5] Price, S D and Eland, J H D, *Meas. Sci. Techn.* **1992**, *3*, 306–315.

[6] Tate, J T, Smith, P T and Vaughan, A, *Phys. Rev.* **1935**, *48*, 525.

[7] Curtis, D M and Eland, J H D, *Int. J. Mass Spectrom. Ion Process.* **1985**, *63*, 241–264.

[8] Price, S D, *Phys. Chem. Chem. Phys.* **2003**, *5*, 1717–1729.

[9] Dibeler, V H, *Anal. Chem.* **1954**, *26*, 58–65.

[10] Wiley, W C and McLaren, I H, *Rev. Sci. Instr.* **1955**, *26*, 1150–1157.

[11] Eland, J H D, *Meas. Sci. Technol.* **1993**, *4*, 1522–1524.

[12] Ali, I, Dorner, R, Jagutzki, O, Nuttgens, S, Mergel, V, Spielberger, L, Khayyat, K, Vogt, T, Brauning, H, Ullmann, K, Moshammer, R, Ullrich, J, Hagmann, S, Groeneveld, K O, Cocke, C L and Schmidt–Bocking, H, *Nucl. Instrum. Methods Phys. Res. Sect. B–Beam Interact. Mater. Atoms* **1999**, *149*, 490–500.

[13] Oelsner, A, Schmidt, O, Schicketanz, M, Klais, M, Schonhense, G, Mergel, V, Jagutzki, O and Schmidt–Bocking, H, *Rev. Sci. Instrum.* **2001**, *72*, 3968–3974.

Chapter 3: Ar^{2+} + He

3.1 Introduction

There is currently considerable interest in the collisional reactivity of atomic and molecular dications, in part stimulated by the observation of bond–forming chemistry in many of these collision systems[1-13]. Despite this focus on bond–forming reactivity, single electron–transfer reactions (SET, Equation 3.1) usually dominate the product ion yield following dication–neutral collisions. In this context, studies of the collisions between argon dications and neutral helium are of fundamental importance, as the reactivity in this simple collision system allows the detailed study of the SET process.

$$Ar^{2+}\,(^3P,\,^1D,\,^1S) + He\,(^1S) \rightarrow Ar^{+}\,(^2P) + He^{+}\,(^2S) \qquad (3.1)$$

The Ar^{2+} dication has a [Mg]$3p^4$ ground electronic configuration giving a ^3P ground electronic state and ^1D and ^1S metastable excited states. These excited states lie 1.74 eV and 4.12 eV, respectively, above the ground ^3P state[14]. At low collision energies only the ground electronic states of the Ar^+ and He^+ products of SET between Ar^{2+} and He are energetically accessible, neglecting the spin–orbit splitting of $Ar^+(^2P)$. As such, the different reactivity of these three reactant electronic states, which are usually all present in beams of Ar^{2+} ions formed *via* electron ionisation[15], can often be distinguished[16-19]. The ground state exothermicity of this SET reaction is 3.04 eV[14].

3.1.1 Previous Study of Ar^{2+} + He Single Electron Transfer

Single electron transfer between Ar^{2+} and He has been studied using a variety of experimental techniques (selected ion–flow tube experiments[14,17,20], drift–tube experiments[16], guided–ion beam experiments[21-23], translational energy spectroscopy[18,24-28] and crossed–beam techniques[29]), yielding rate coefficients and reaction cross–sections. Regarding the dynamics of this reaction, in 1984 crossed–beam studies by Friedrich and Herman[29] revealed marked variations in the angular distributions of the Ar^+ ions arising from Reaction (3.1), for the reaction of the ^3P and ^1D states of Ar^{2+}, at centre–of–mass (CM) collision energies (E_{CM}) between 0.5 eV and 1.6 eV. These experiments showed that product Ar^+ ions, formed from the ^3P state of Ar^{2+}, are scattered predominantly forward in the CM frame; this angular distribution remaining broadly constant over the range of collision energies investigated. In contrast, the angular distribution of Ar^+ ions formed from the reaction of the ^1D state of Ar^{2+} was observed to be peaked "sideways", relative to the direction of the reactant velocities, at the lowest collision energies[29]. At higher collision energies, Friedrich and Herman observed that the angular distribution of Ar^+ ions formed from the ^1D state of Ar^{2+} has two significant peaks, arising from a "forward" scattered component in addition to a "sideways" scattered component[29]. Although experiments indicate their Ar^{2+} beam should contain the ^3P, ^1D and ^1S electronic states of Ar^{2+} in their statistical ratio[15], Friedrich and Herman observed no significant contribution to the SET reactivity from the $Ar^{2+}(^1S)$ state.

Broad agreement with the reactivity trends observed by Friedrich and Herman emerged from angularly–resolved translational energy spectroscopy experiments by Koslowski *et al.*[27] and Itoh[25]. In these investigations, at CM collision energies of 36 eV and 0.91 eV respectively, the SET reactions of the ^3P and ^1D states of Ar^{2+} are observed, whilst the contribution to the overall reactivity from the $Ar^{2+}(^1S)$ state appeared much weaker.

Guided ion–beam studies of the integral and differential cross–sections for the SET reaction of Ar^{2+} (^3P) with He were carried out by Gerlich[22,23]. The reactivity of the ^3P state of Ar^{2+} was isolated from that of the ^1D state by quenching the metastable excited states of Ar^{2+} before the interaction with He. These experiments measured the total reaction cross section, at excellent energy resolution down to 300 K; a cross section that agreed well with a simple electrostatic model of the Ar^{2+} – He interaction. The angular data obtained from these guided ion beam experiments again reveals significant variation in the differential cross–section for the reaction of $Ar^{2+}(^3P)$ with He between collision energies of 0.1 eV and 1.6 eV. Specifically, broadly isotropic scattering prevails at E_{CM} = 0.1 eV with increasing sideways scattering observed as E_{CM} varies from 0.2 to 0.5 eV. At E_{CM} of 1.6 eV, the guided ion beam experiments reveal distinct forward scattering. The angular data from these guided ion beam experiments at E_{CM} = 0.5 eV and 1.6 eV are in good accord with the observations of Friedrich and Herman, discussed above[29].

This chapter presents an investigation of the reactivity of Ar^{2+} with He at values of E_{CM} between 0.4 and 1.2 eV, extending the available data on the angular scattering resulting from the reactivity of the ^{1}D electronic state of Ar^{2+} to lower collision energies than have previously been investigated. In these studies we record the complete angular scattering for both the He^+ and Ar^+ products, at an improved angular resolution than the pioneering studies of Friedrich and Herman[29] and Gerlich[22,23]. The data allows us to easily distinguish the reactivity of the ^{3}P and ^{1}D electronic states of Ar^{2+} and marked differences in the angular scattering for these channels are apparent, which vary dramatically as a function of collision energy.

3.2 Landau–Zener Calculation Methodology

In addition to recording the spectra employing the PSCO methodology, as described in Chapter 2, a series of calculations have been performed to help rationalise our experimental data, in particular the relative intensity of the different reaction channels. In general, the theoretical approach for modelling electron transfer considers the SET reaction to occur *via* non–adiabatic interactions between relevant potentials of the of the quasi–molecule formed by the association of the reactants[30]. The relevant potentials must correlate with the reactant and product asymptotes and must be of the same symmetry. The reactant and product potentials are coupled by a radial interaction potential[30,31]. Specifically for Reaction (3.1), which involves the quasi–molecule $[ArHe]^{2+}$, and neglecting the spin–orbit interaction which cannot be resolved experimentally, states of $^3\Pi$ symmetry can couple $Ar^{2+}(^3P)$ to the product asymptote. For the ^{1}D and ^{1}S states of the reactant, potentials of ($^1\Sigma^+$, $^1\Pi$) and $^1\Sigma^+$ symmetry can couple the reactants to the products. Thus, there should be no formal symmetry restrictions on the SET reactivity of the Ar^{2+} states present in our dication beam. Our calculations are based on the Landau–Zener theory of avoided–crossings, commonly used to model SET reactions[32,33]. The methodology for these calculations has been described in detail previously[1,34,35]. The Landau–Zener model pictures the SET occurring at the intersection of a reactant and a product potential; this intersection occurs at an interspecies separation labelled the crossing radius R_c (Figure 3.1). In the Ar^{2+}–He collision system, the reactant potential is due to the interaction of a dication and neutral, whilst the product potential results from a pair of monocations.

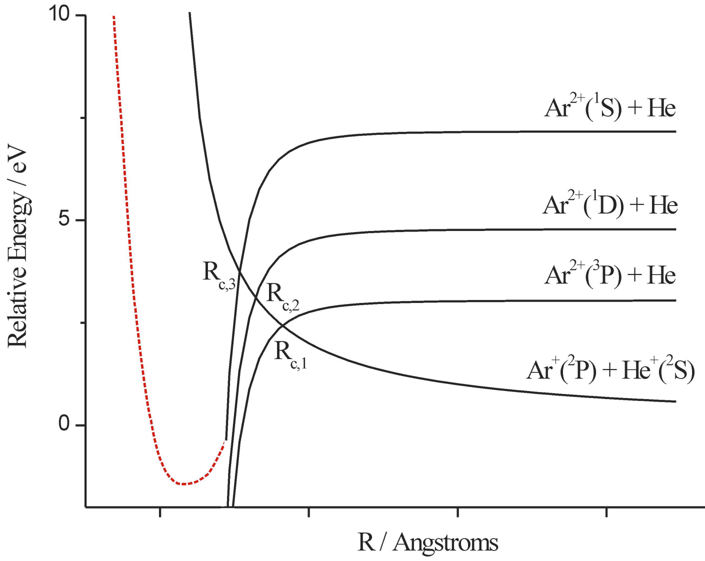

Figure 3.1 Model potential energy curves used to calculate the curve-crossing radii and relative cross-sections for the ET reaction of He with Ar^{2+} (^3P), Ar^{2+} (^1D) and Ar^{2+} (^1S). The energy zero is the Ar^+ (^2P) + He^+ (^2S) product asymptote and the associated product potential involves simply Coulomb repulsion. The reactant potentials are described by a polarisation attraction interaction with an appropriate energetic offset. The dashed red curve represents an additional Lennard-Jones repulsive term which becomes significant at small inter-nuclear separation, effectively adding a repulsive wall at 1.15 Å, which is incorporated in the reactant potential used for the classical trajectory calculations described in the text. This repulsive potential is not shown to scale. The curve-crossing radii $R_{c,1}$, $R_{c,2}$ and $R_{c,3}$ of the product potential with the ^3P, ^1D and ^1S reactant states of Ar^{2+} are at 4.8 Å, 3.1 Å and 2.1 Å respectively.

In our implementation of the Landau-Zener approach, the reactant potential energy curve (PEC) is modelled by polarisation attraction between the dication and neutral, and the product PEC is modelled simply *via* the Coulomb repulsion between the pair of product monocations, as shown in Figure 3.1. Such simple potential models have been widely used to model dication-neutral interactions. The simple form of these PECs, when constructed on reactant and product asymptotes separated by the established reaction exothermicity (3.04 eV), readily allows R_c to be calculated. The probability δ of the system remaining on one of these PECs after passing through the curve crossing, is given by Equation (3.2) (over page), and is a function of the relative radial velocity v_r, the gradients of the two PECs at the crossing point V_1' and V_2' and the electronic coupling matrix element H_{12}[34]. For a given collision energy and impact parameter, the value of v_r can be calculated by simple kinematics and V_1' and V_2' can be determined from the form of the potentials at the crossing radius. In our calculations H_{12} is estimated, using the semi–empirical equations of Olson *et al*[36], to be 0.00644 eV for $Ar^{2+}(^3P)$ + $He(^1S)$, 0.192 eV for $Ar^{2+}(^1D)$ + $He(^1S)$ and 1.16 eV for $Ar^{2+}(^1S)$ + $He(^1S)$. The value of H_{12} for the ^3P state is in good agreement with the values derived in previous theoretical investigations[30,37].

$$\delta = \exp\left(\frac{-\pi |H_{12}|^2}{2\hbar \left| V_1' - V_2' \right| v_r} \right) \tag{3.2}$$

For net electron transfer, the reaction probability $P(b)$ for a single encounter is given by $2\delta(1-\delta)$, as a successful SET reaction involves passing through the crossing twice (on approach and separation) but only crossing between the reactant and product PECs once. Note that, even for trajectories at a given CM collision energy, P is a function of the impact parameter b as the radial velocity through the crossing v_r depends on b. Our Landau–Zener algorithm integrates P over appropriately weighted values of b, out to the maximum impact parameter for which the collision system can reach the crossing radius, to give the SET reaction cross section at a given collision energy. According to the Landau–Zener model, a SET reaction is likely to occur if the reactant and product PECs cross at an inter–species separation between 3 and 6 Å. Over this range of inter–species separations, the reaction window, the intermediate coupling between the PECs allows P to approach its maximum possible value of 0.5.

3.3 Results

3.3.1 Experiments Employing a Repeller Plate Voltage of 50 V

Initial experiments were carried out with 50 V applied to the repeller plate; at this low repeller voltage the TOF of the ions is comparatively long and thus the energy resolution is high. The CM frame scattering diagram and translational energy release spectrum recorded following collisions of Ar^{2+} with He at E_{CM} of 0.76 eV are shown in Figure 3.2. As is clear from Figure 3.2, in both the energy release spectrum and the scattering diagram, we can easily distinguish the reactivity of $Ar^{2+}(^3P)$ and $Ar^{2+}(^1D)$ with He. Four different CM collision energies (0.33, 0.42, 0.76 and 1.29 eV) were studied utilizing this low repeller plate voltage and none of the data sets showed any signal due to the reaction of $Ar^{2+}(^1S)$. Hence we can say that, within our collision energy range, the $Ar^{2+}(^1S)$ state does not undergo SET with He on any statistically significant level.

Unfortunately, at this low repeller plate voltage, some ions that are scattered sideways with a large amount of kinetic energy do not reach the detector, as is apparent in Figure 3.2. Thus, we cannot extract accurate relative cross–sections or 180° of scattering products from the 50 V repeller plate data.

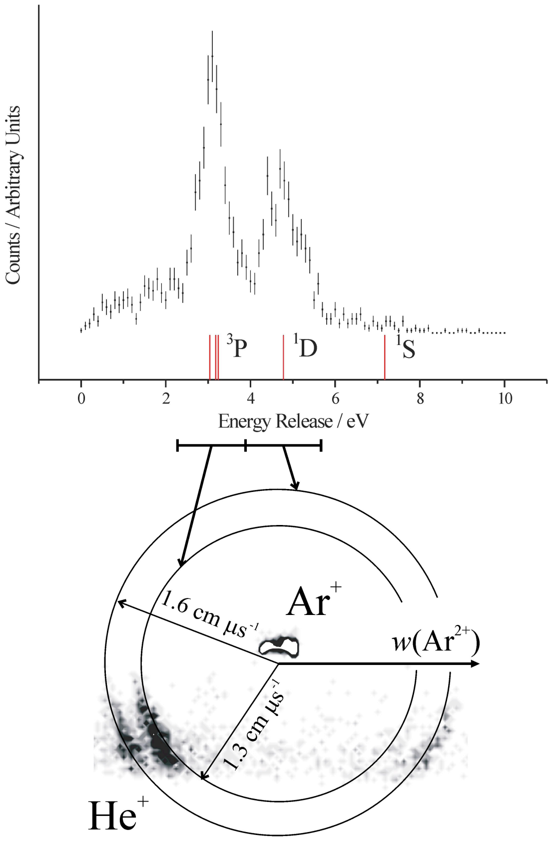

Figure 3.2 (top) The translational exothermicity spectrum for the SET reaction between Ar^{2+} and He at E_{CM} = 0.6 eV. The literature exothermicities corresponding to the SET reaction with the ^{3}P, ^{1}D and ^{1}S states of Ar^{2+}, to give Ar$^+$($^2P_{3/2}$) and He$^+$(^{2}S) products, are shown by the vertical lines. No statistically significant signal is detected for the reaction with Ar^{2+}(^{1}S). Also shown (bottom) is the CM scattering diagram revealing two rings of scattered products from the reaction of the ^{3}P and ^{1}D states of Ar^{2+}. The direction of the reactant Ar^{2+} velocity is labelled w(Ar^{2+}).

3.3.2 Experiments Employing a Repeller Plate Voltage of 150 V

In order to calculate accurate relative cross–sections for the reactivity of the ^{3}P, ^{1}D and ^{1}S states of Ar^{2+}, all product ions scattered between 0° and 180° must be collected. It was found that at a repeller plate voltage of 150 V we ensure complete product ions detection, whilst maintaining the ability to differentiate the reaction of Ar^{2+}(^{3}P) and Ar^{2+}(^{1}D). Thus, the SET between He and Ar^{2+} has been studied with 150 V applied to the repeller plate at five CM collision energies ranging from 0.4 – 1.2 eV. A spectrum recorded at E_{CM} = 0.6 eV gives the translational exothermicity spectrum shown in Figure 3.3 (a). Figure 3.3 clearly shows that the ground ^3P state and the metastable ^1D excited state of $Ar^{2+}(3p^{-2})$ participate in the SET reaction with He to form ground state products, $He^+(^2S)$ and $Ar^+(^2P)$.

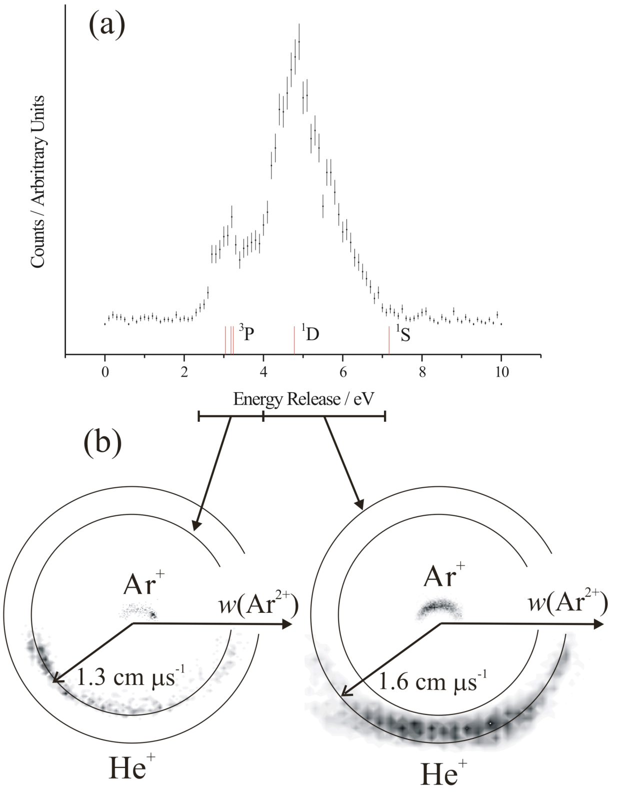

Figure 3.3 (a) The translational exothermicity spectrum for the SET reaction between Ar^{2+} and He at E_{CM} = 0.6 eV. The literature exothermicities corresponding to the SET reaction with the ^3P, ^1D and ^1S states of Ar^{2+}, to give $Ar^+(^2P_{3/2})$ and $He^+(^2S)$ products, are shown by the vertical lines. No statistically significant signal is detected for the reaction with $Ar^{2+}(^1S)$. Also shown (b) are the CM scattering diagrams revealing the different angular scattering for the products from the reaction of the ^3P and ^1D states of Ar^{2+}. The direction of the reactant Ar^{2+} velocity is labelled $w(Ar^{2+})$.

3.3.2.1 Cross–Sections for $Ar^{2+}(^3P)$, $Ar^{2+}(^1D)$ and $Ar^{2+}(^1S)$

In all of the translational exothermicity spectra recorded as part of this study, no signal due to the SET reaction of the metastable ^1S excited state of $Ar^{2+}(3p^{-2})$ was observed. As discussed above, experiments indicate that ^3P, ^1D and ^1S electronic states of Ar^{2+} should be present in our dication beam in their statistical ratio[15]. Thus, our experimental spectra allow us to place an upper limit of 0.02 on the relative cross–section for the $Ar^{2+}(^1S)$ reactivity with respect to the $Ar^{2+}(^1D)$ reactivity. In agreement with the above observation, the crossed–beam studies of Friedrich and Herman[29] also showed that the ^1S state of Ar^{2+} does not undergo effective SET with He at a similar range of collision energies to those employed in our experiments.

Using the simple electrostatic approach described above, we determine the crossing radii for the SET reaction of the ^3P, ^1D and ^1S states of Ar^{2+} with He as 4.8, 3.1 and 2.1 Å respectively; the value for the ^3P state is in agreement with previous determinations[23,29,30,37]. The crossing radius for the reaction of $Ar^{2+}(^1S)$ lies at a small interspecies separation. At such small interspecies separations the Hamiltonian matrix element that gives the coupling between the reactant and product potentials is significant (1.16117 eV for $Ar^{2+}(^1S) + He(^1S)$), and thus δ is small. Hence, although the probability of a curve crossing is large as the reactants approach each other, the system will efficiently cross back from the product potential to the reactant potential as the collision system separates, and no net ET results; $2\delta(1-\delta)$ is small. Conversely for the ^3P and ^1D states of Ar^{2+} the coupling between the reactant and product potentials is such that $2\delta(1-\delta)$ is significant and ET is efficient. Thus, a simple consideration of the coupling between the product and reactant PECs readily explains why the reactions of the ^3P and ^1D states of Ar^{2+} dominate the product ion yield following SET reactions with He.

From the PSCO datasets recorded at 150 V repeller plate potential, the signal strengths in the exothermicity spectra, which were extracted by fitting Gaussian functions to the peaks, show that the relative cross–section for the reaction of the ^1D and ^3P states of Ar^{2+} (Table 3.1) is approximately 5 : 1 (^1D : ^3P). Within their mutual error limits, this ratio is constant over the range of collision energies we investigated. In our experiments the principal uncertainty in E_{CM} arises from the motion of the effusively introduced reactant He. We can calculate limiting spreads in the collision energy, at each nominal experimental value of E_{CM}, by considering the He atoms (300 K) travelling with their modal velocity oriented directly towards, or away from, the propagation direction of the dication beam. This maximal estimated energy uncertainty is shown in Table 3.1. In reality, the effusive jet introduces the neutral reactant broadly perpendicular to the direction of travel of the dication beam, and the neutral reactant is unconfined by any sort of collision cell. Thus we would expect the actual spread in E_{CM} to be less than the conservative estimates shown in Table 3.1.

Table 3.1 Relative cross-sections for the SET reactivity with He of the ^{1}D state and the ^{3}P state, of Ar^{2+} as a function of E_{CM}. The table also includes an estimate of the expected spread in E_{CM} for each experiment. See text for details.

E_{CM} / eV	Max E_{CM} / eV	Min E_{CM} / eV	Relative Cross-Section (^{1}D : ^{3}P)
0.4	0.6	0.2	5.7 ± 1.8
0.53	–	–	3.1[a]
0.6	0.9	0.4	5.2 ± 1.5
0.8	1.1	0.6	5.1 ± 1.4
0.9	1.2	0.6	3.2 ± 1.5
1.2	1.5	0.9	4.4 ± 1.4
1.62	–	–	1.2[a]

[a] From crossed-beam experiments assuming a relative population of Ar^{2+}(^{3}P:^{1}D) of 2:1[29].

As shown in Table 3.1, our relative cross sections for the reactivity of Ar^{2+}(^{3}P) and Ar^{2+}(^{1}D) are in good general agreement with the results of Friedrich and Herman[29]. As clearly shown by Gerlich[22,23], the total reaction cross-section for Ar^{2+}(^{3}P) falls steadily with increasing E_{CM}, up to E_{CM} = 1 eV. Above E_{CM} = 1 eV the reaction cross-section for Ar^{2+}(^{3}P) is approximately constant up to E_{CM}= 3 eV. Hence, the data in Table 3.1 perhaps hints that the reaction cross section for the ^{1}D state falls more rapidly than that for the ^{3}P state, since the relative cross section (^{1}D:^{3}P) seems to be falling at higher E_{CM}. Such behaviour is hard to explain, as the inelastic scattering channels, where Ar^{2+}(^{1}D) is promoted to Ar^{2+}(^{1}S) or Ar^{2+}(^{3}P) is promoted to Ar^{2+}(^{1}D), which potentially compete with SET have thresholds of 1.74 and 3.38 eV respectively. Clearly accurate measurements of the total reaction cross-section for Ar^{2+}(^{1}D) are required.

Using the crossing radii calculated using the electrostatic approach, and appropriately weighting for the state degeneracy, our Landau-Zener calculations predict that the relative cross-section of the ^{1}D to ^{3}P reactivity varies between 3 and 7 at E_{CM} = 0.2 – 1.1 eV, in general agreement with our experimental results, particularly given the simplifications inherent in the theoretical approach. In addition, the calculated relative cross-section for the ^{1}S reactivity, with respect to the ^{1}D reactivity, is less than 10^{-4}, in agreement with our experimentally derived upper limit.

3.3.3 Scattering Angle Changes with Collision Energy and State

A powerful feature of the PSCO methodology is that we can distinguish in the experimental dataset the reactive events corresponding to the reactions of either the ^{3}P or ^{1}D states of Ar^{2+}. Thus, for each of the five collision energies at which the Ar^{2+}–He collision system was studied employing 150 V on the repeller plate, the angular distributions of the product ions arising from the reaction of both the ^{3}P and ^{1}D states of Ar^{2+} can be extracted. Figure 3.3 (b) illustrates how we can examine the scattering angles of products from $Ar^{2+}(^3P)$ and $Ar^{2+}(^1D)$ reactions independently. The Ar^+ angular distributions shown in Figure 3.4 (a) and Figure 3.4 (b) arise from $Ar^{2+}(^3P)$ and $Ar^{2+}(^1D)$ reactants, respectively. Also shown in Figure 3.4 (a) and (b) are the data of Friedrich and Herman[29] (red circles) and of Gerlich[22,23] (black squares).

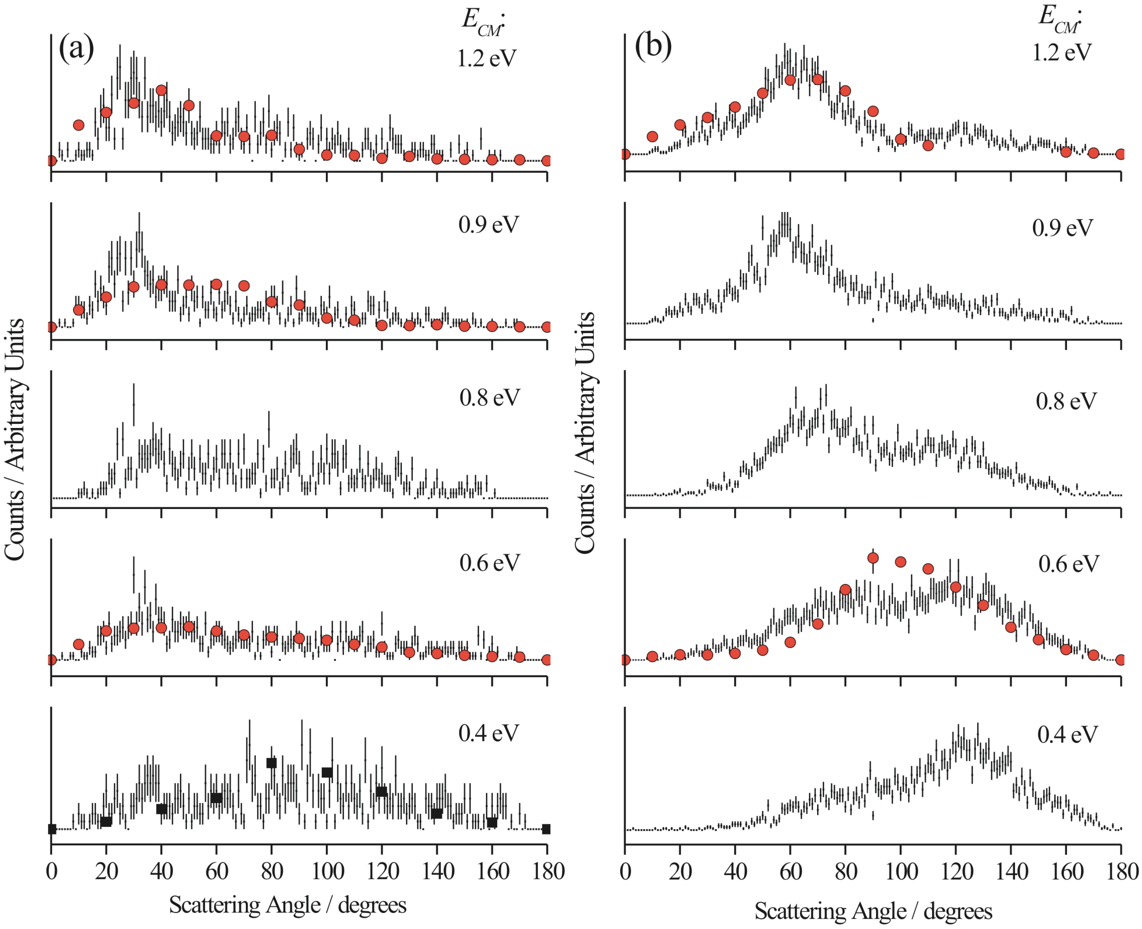

Figure 3.4 Scattering angle distributions of product Ar^+ ions arising from the ET reaction of He with (a) the ^{3}P ground state of Ar^{2+}, and (b) the ^{1}D state of Ar^{2+} at E_{CM} = 0.4 – 1.2 eV. The distributions are normalised to give an equal area under each curve. The data represented by solid shapes are values derived from the differential cross-sections (0.53 eV, 0.93 eV and 1.62 eV, circles) of Friedrich and Herman[29] and (0.5 eV, squares) Gerlich[22,23]. See text for details.

As explained fully in Chapter 2, our angular data involves a summation of the intensity over the azimuthal angle as we detect all reactive events. To directly and robustly compare our angular data with the differential cross sections of Friedrich and Herman[29] and Gerlich[22,23] we must transform their cross–sections by multiplying by sin(θ). The alternative approach of dividing our data by sin(θ) generates severe inaccuracies where sin(θ) approaches zero. At comparable collision energies the transformed differential cross–sections of Friedrich and Herman and Gerlich show excellent agreement with our experimental angular distributions (Figure 3.4) for both the $Ar^{2+}(^3P)$ and $Ar^{2+}(^1D)$ states. Calculations of the differential cross sections of the $Ar^{2+}(^3P)$ reaction that were carried out by Braga *et al*[37] and Friedrich *et al*[30] generated cross sections in good agreement with those determined experimentally by Friedrich and Herman[29] and Gerlich[22,23] and thus, although not shown in Figure 3.4 these calculations are in excellent accord with our experimental results for the ^3P state.

Of course, we also obtain from our experimental data the scattering angle for the formation of He^+, but this angular distribution contains no additional information as the angle between the velocities of the Ar^+ and He^+ products is constrained to 180° by conservation of momentum. Thus, as expected, the He^+ angular distribution is simply a "mirror image" of the Ar^+ angular distribution.

It is clear from Figure 3.4 (a) and Figure 3.4 (b) that there is a pronounced difference in the angular distributions of the product Ar^+ ions from the reaction of He with $Ar^{2+}(^3P)$ and with $Ar^{2+}(^1D)$. At the largest E_{CM} investigated, 1.2 eV, (Figure 3.4 (a)) the product angular distribution arising from $Ar^{2+}(^3P)$ is peaked at an angle of approximately 30°. With decreasing E_{CM}, the fraction of product ions that are scattered to higher angles increases. At the lowest E_{CM} (0.4 eV) the angular distribution of Ar^+ ions from the SET reaction of $Ar^{2+}(^3P)$ with He is centred about 90° and is broadly isotropic. The angular distribution of Ar^+ product ions formed in the SET reaction of He with $Ar^{2+}(^1D)$ changes even more dramatically with the collision energy than that of the Ar^+ ions arising from the reaction of the $Ar^{2+}(^3P)$ state. At E_{CM} of 1.2 eV (Figure 3.4 (b)), the product Ar^+ ions formed upon the reaction of He with $Ar^{2+}(^1D)$ have an angular distribution peaked at approximately 60°. With decreasing E_{CM} this distribution shifts markedly towards a higher scattering angle of approximately 120°. The angular resolution of our data (Figure 3.4) reveals features in the angular distributions that have not been apparent before. For example, the marked "double–peaked" form of the $Ar^{2+}(^1D)$ angular distributions, which could be viewed as comprising two distributions centred at 60^0 and 130^0, with the former signals dominant at higher collision energies and the relative importance of the latter distribution increasing with decreasing collision energy. However, to attempt to account for the differences in the angular scattering from these two reactant states, a more detailed consideration of the interaction between the reactants is required.

3.4 Scattering Model

Friedrich and Herman[29] put forward a qualitative interpretation of the different angular scattering they observed experimentally for the reaction of $Ar^{2+}(^3P, ^1D)$. If the SET reaction is dominated by a curve crossing as the reactants approach each other, the distribution of the product scattering angles should be biased toward large scattering angles. Conversely if the curve crossing occurs predominantly as the reactants separate, on the second pass though the crossing radius, a more forward scattered distribution of products is expected. Our scattering data (Figure 3.4 (a) and Figure 3.4 (b)) conforms to this interpretation proposed by Friedrich and Herman, where the significant sideways scattering of the reaction products from the ^1D state can be viewed as resulting from an "early" crossing, whilst the more forward scattered products from the reaction of the $Ar^{2+}(^3P)$ appear characteristic of a "late" crossing.

Although providing a satisfactory rationalization of the scattering data it is clear that a realisation of predominantly "early" or "late" ET cannot occur under the simple two–state Landau–Zener model. Specifically, for a given reactant state the probabilities of reactive events involving transfer of the electron on the first or second pass through the curve crossing are equal at $\delta(1-\delta)$, although δ differs for the reactions of the $Ar^{2+}(^3P)$ and $Ar^{2+}(^1D)$ states. Thus, under the simple two–state Landau–Zener model the changes in the angular distributions in Figure 3.4 (a) and (b) with collision energy, and, more specifically, the differences between the angular distributions which result from the reaction of the $Ar^{2+}(^3P)$ and $Ar^{2+}(^1D)$ states, cannot be ascribed to preferential ET at a given pass through the crossing. However, certainly the SET reaction of the $Ar^{2+}(^1D)$ ion with He is not a simple two–state system. As the monocationic products of this interaction separate they will cross the lower lying triplet potential arising from the interaction of $Ar^{2+}(^3P)$ with He and further curve crossings are then possible. One might therefore expect the simple two–state Landau–Zener model to approximate the scattering dynamics of the $Ar^{2+}(^3P)$ reactant but fail for $Ar^{2+}(^1D)$.

To address this question we have performed simple classical trajectory simulations for collisions of Ar^{2+} with He at collision energies corresponding to the experimental data displayed in Figure 3.4. In these simulations, which aim only to achieve qualitative accuracy for the angular distributions, the potential for the interaction between the dication and the neutral is approximated by a term representing the polarization attraction together with a repulsive term from an appropriate Lennard–Jones potential. The potential for the products is simply their mutual Coulomb repulsion. In the simulations, an electron is transferred between the reactants at the relevant crossing radius, with reactive events resulting in net ET occurring with equal probability on the first or second pass through the crossing radius, as the reactants approach or as they separate. A pictographic representation of the simulation is shown in Figure 3.5. A large number of trajectories are executed, chosen with an appropriately weighted distribution of the initial impact parameter and experimentally realistic distributions of the collision energy and initial velocities.

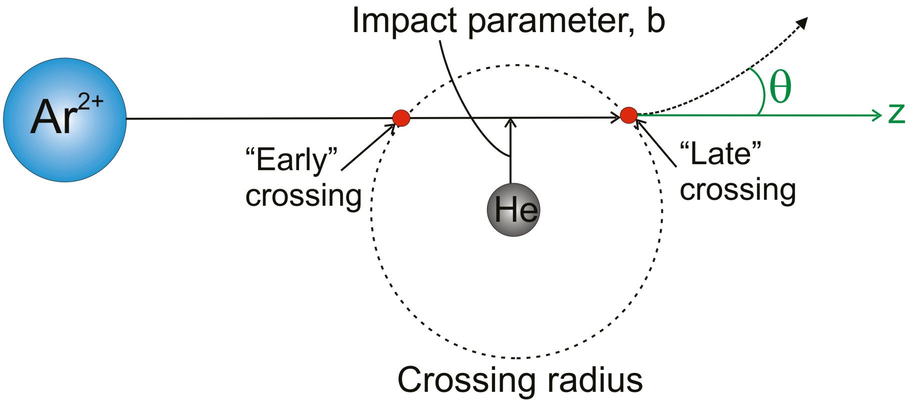

Figure 3.5 Illustrative representation of the classical trajectory simulation employed to model the angular distribution of products from the SET of $Ar^{2+}(^3P)$ and $Ar^{2+}(^1D)$ with He.

3.4.1 Successes and Failures of Model

Results of the simulation, for reactions of both the ^3P and ^1D states, can be seen in Figure 3.6. Such simulations, as has been discussed before, have been used to satisfactorily reproduce the angular distributions observed in atomic SET reactions[38,39]. Indeed, these classical trajectory simulations replicate qualitatively the key features of the experimental angular distributions seen in Figure 3.4 (a) for the reaction of $Ar^{2+}(^3P)$. Specifically, the simulated distributions are peaked at a low angle of approximately 20° at E_{CM} = 1.2 – 0.6 eV with a tail that extends towards higher angles. At the lowest E_{CM} of 0.4 eV, the simulations are dominated by two peaks of equal intensity at around 20° and 100°, implying sideways scattering is more dominant than at the higher collision energies as we see at E_{CM} = 0.4 eV. Similarly, in more sophisticated modelling, Friedrich and Herman's differential cross-sections for the reaction of $Ar^{2+}(^3P)$ are well reproduced by semi-classical and quantum simulations[30,37].

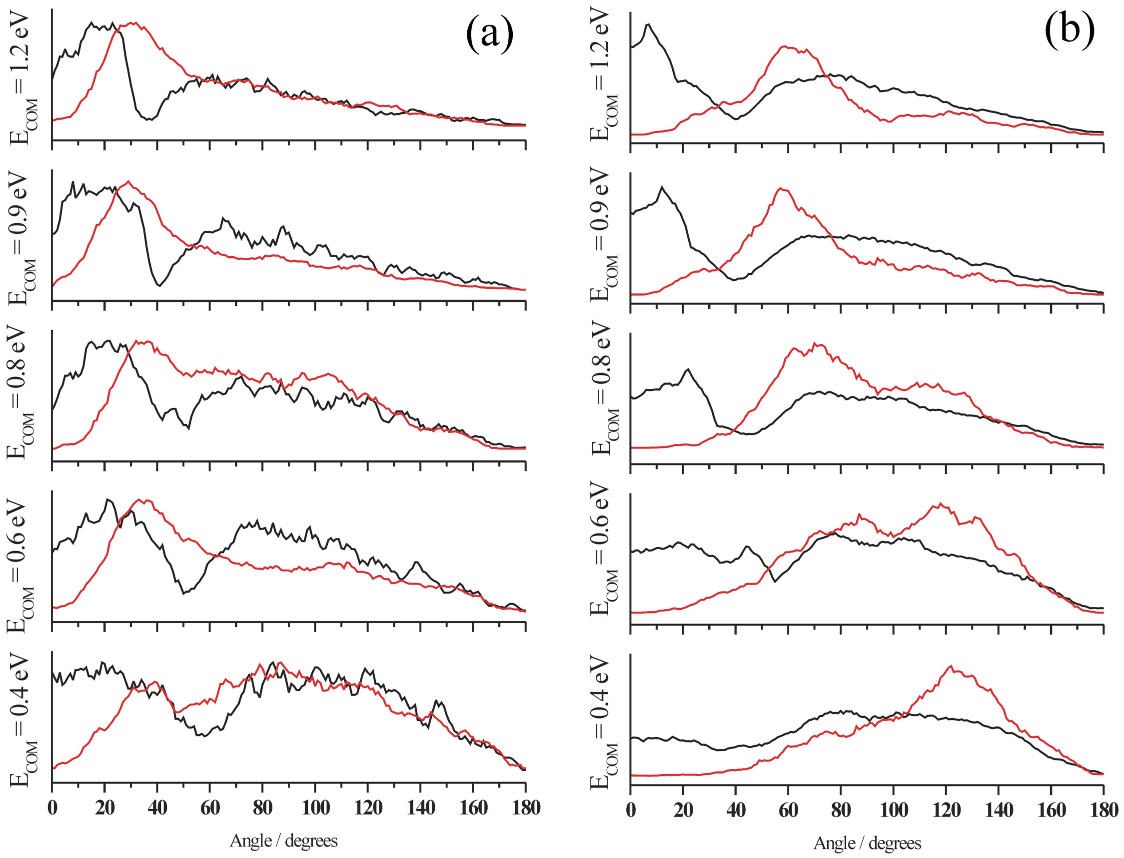

Figure 3.6 Red line – experimental data showing angular distributions of Ar^+ products from a reaction of (a) $Ar^{2+}(^3P)$ and (b) $Ar^{2+}(^1D)$ with He. Black line – simulation of the experimental scattering angle distributions employing a classical trajectory model, see text for details. The simulated lines have been normalised to the integrated area under the data curves.

It is clear from Figure 3.6 that all of the simulated distributions we generate consist of two peaks, these result from either "early" or "late" ET in the simulation. Unlike in our simulation, in reality, the crossing radius will have a finite width thus broadening the range of interspecies separations at which ET can occur. Such broadening of R_c could be due to the three distinct *J* states of the $Ar^{2+}(^3P)$ reactant or due to quantum tunnelling of the transferred electron. Of course, there will also be experimental broadening of the data and perhaps if a higher angular resolution was achieved, we would be able to distinguish these two humps in the experimental distribution. Thus, it is reasonable to state that, given the simplifications inherent in the model, the shapes and intensities of the data are indeed reasonably well reproduced by the simulation.

However, our simple classical trajectory model in no way reproduces the major features of the angular distributions we observe (Figure 3.4 (b)) for the reaction of $Ar^{2+}(^1D)$, Figure 3.6 (b). Specifically, the simulations are strongly dominated by forward scattering, with a peak at 10 – 20°, for the three highest collision energies, with a second, smaller, broad feature at around 80°. At the lower collision energies, the simulated angular distributions appear nearly isotropic. However, Figure 3.4 (b) clearly shows that the scattering angle distributions of products arising from a reaction of $Ar^{2+}(^1D)$ have a single peak which occurs at around 60° at E_{CM} = 1.2 eV which shifts to around 130° at E_{CM} = 0.4 eV. However, if in our simulations the electron is allowed to cross between the PECs only at "early" crossings then the simulations reproduce fairly well (Figure 3.7) the observed angular distributions of Ar^+ produced from reactions of $Ar^{2+}(^1D)$, particularly at low E_{CM}. Although, within the remit of Landau–Zener theory, this is clearly not a realistic scenario as equal numbers of ET must occur at the "early" and "late" crossings.

In the light of the above, it seems clear that a more sophisticated model of the coupling between the reactant and product potentials is required to model the interactions present in these multiple–state dication–neutral collision systems at our low collision energies. Indeed, to the best of our knowledge, no previous classical or quantum simulations have been carried out to model the differential cross–sections for the reaction of $Ar^{2+}(^1D)$ with He. Detailed investigations of the relevant potentials, and their coupling, may reveal that the interaction of the triplet and singlet surfaces, or the involvement of different *J* states, means that the probabilities of "early" and "late" ET are not equal and can distinguish the reactivity of the ^1D and ^3P states of Ar^{2+}. Given the fundamental importance of dication SET reactions at low collision energies in planetary ionospheres and elsewhere, we can only advocate a comprehensive quantum mechanical investigation into this prototypical atomic collision system.

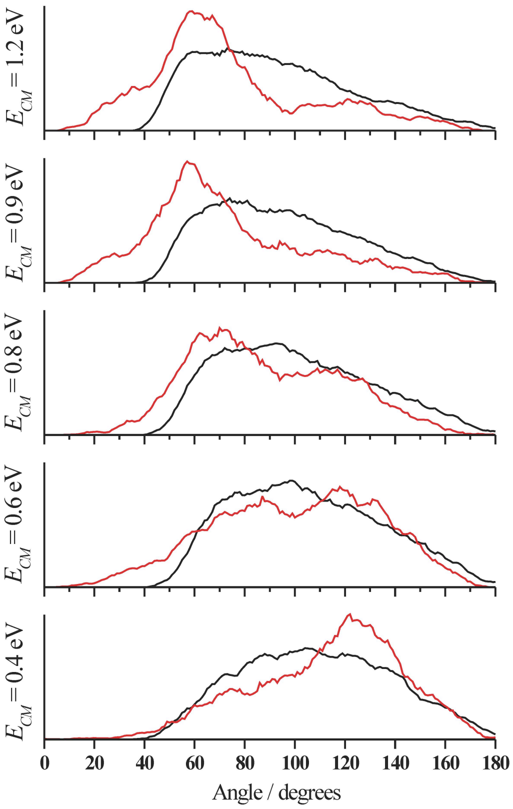

Figure 3.7 Red line – Data collected for the angular distribution of Ar^+ products from a reaction of $Ar^{2+}(^1D)$ with He at 5 different E_{CM}. Black line – simulation of the experimental scattering angle distributions employing a classical trajectory model where the electron is only allowed to transfer at the first pass through the crossing radius, see text for details. The simulated lines have been normalised to the integrated area under the data curves.

3.5 Conclusion

Complete angular distributions of the Ar^+ and He^+ product ions arising from the SET reaction between $Ar^{2+}(^3P,^1D)$ and He have been determined at centre-of mass collision energies ranging from 0.4 to 1.2 eV. The Ar^+ product ions formed by the reaction of the ^3P state of Ar^{2+} are predominantly forward scattered at collision energies between 1.2 and 0.6 eV but this scattering spreads over a wider angular range as the collision energy is reduced. The Ar^+ ions arising from the reaction of He with the ^1D state of Ar^{2+} have broad angular distributions that vary strongly with the collision energy. At these low collision energies it appears that a simple Landau-Zener model cannot reproduce the details of the angular scattering we observe and more sophisticated models of the interaction of the reactants and products are required to account for the experimental data.

3.6 References

[1] Herman, Z, *Int. Rev. Phys. Chem.* **1996**, *15*, 299–324.

[2] Schroeder, D and Schwarz, H, *Journal of Physical Chemistry* A **1999**, *103*, 7385-7394.

[3] Ascenzi, D, Franceschi, P, Tosi, P, Bassi, D, Kaczorowska, M and Harvey, J N, *J. Chem. Phys.* **2003**, *118*, 2159–2163.

[4] Dolejsek, Z, Farnik, M and Herman, Z, *Chem. Phys. Lett.* **1995**, *235*, 99–104.

[5] Price, S D, *Int. J. Mass Spec.* **2007**, *260*, 1–19.

[6] Roithova, J, Ricketts, C L, Schroeder, D and Price, S D, *Ange. Chem.–Int. Ed.* **2007**, *46*, 9316–9319.

[7] Ascenzi, D, Tosi, P, Roithova, J, Ricketts, C L, Schroeder, D, Lockyear, J F, Parkes, M A and Price, S D, *Phys. Chem. Chem. Phys.* **2008**, *10*, 7121–7128.

[8] Franceschi, P, Thissen, R, Zabka, J, Roithova, J, Herman, Z and Dutuit, O, *Int. J. Mass Spectrom.* **2003**, *228*, 507–516.

[9] Tafadar, N, Kearney, D and Price, S D, *J. Chem. Phys.* **2001**, *115*, 8819–8827.

[10] Javahery, G, Petrie, S, Wang, J R, Wincel, H and Bohme, D K, *J. Am. Chem. Soc.* **1993**, *115*, 9701–9707.

[11] Price, S D, Manning, M and Leone, S R, *Chem. Phys. Lett.* **1993**, *214*, 553–558.

[12] Mathur, D, *Phys. Rep. –Rev. Sec. Phys. Lett.* **2004**, *391*, 1–118.

[13] Milko, P, Roithova, J, Schroeder, D and Schwarz, H, *Int. J. Mass Spectrom.* **2007**, *267*, 139–147.

[14] Ralchenko, Y, Kramida, A E and Reader, J, **2010**, *NIST Atomic Spectra Database (ver. 4.0.1),* http://physics.nist.gov/asd, *2011 February 15*, National Institute of Standards and Technology Gaithersburg, MD

[15] Nakamura, T, Kobayashi, N and Kaneko, Y, *J. Phys. Soc. Jap.* **1985**, *54*, 2774-2775.

[16] Johnsen, R and Biondi, M A, *Phys. Rev. A* **1979**, *20*, 87–97.

[17] Smith, D, Adams, N G, Alge, E, Villinger, H and Lindinger, W, *J. Phys. B* **1980**, *13*, 2787–2799.

[18] Kamber, E Y, Jonathan, P, Brenton, A G and Beynon, J H, *J. Phys. B* **1987**, *20*, 4129–4142.

[19] Hu, W P, Harper, S M and Price, S D, *Meas. Sci. Techn.* **2002**, *13*, 1512–1522.

[20] Smith, D, Grief, D and Adams, N G, *Int. J. Mass Spec. Ion Phys.* **1979**, *30*, 271-283.

[21] Disch, R, Scherbarth, S and Gerlich, D In *Conference on the dynamics of molecular collisions held at Snowbird, Utah*; Truhlar, D., Ed.Eds.; Univ Minneapolis: 1985; Vol.

[22] Gerlich, D; Lorents, D., Meyerhof, W., Peterson, J., Ed.Eds.; Elsevier: 1986; Vol. 541.

[23] Gerlich, D, *Adv. Chem. Phys.* **1992**, *82*, 1–176.

[24] Huber, B A, *J. Phys. B* **1980**, *13*, 809–818.

[25] Itoh, Y, *J. Phys. Soc. Jap.* **1989**, *58*, 1871–1874.

[26] Jellenwutte, U, Schweinzer, J, Vanek, W and Winter, H, *J. Phys. B* **1985**, *18*, L779–L785.

[27] Koslowski, H R, Huber, B A and Staemmler, V, *J. Phys. B* **1988**, *21*, 2923–2937.

[28] Huber, B A and Kahlert, H J, *J. Phys. B* **1983**, *16*, 4655–4669.

[29] Friedrich, B and Herman, Z, *Chem. Phys. Lett.* **1984**, *107*, 375–380.

[30] Friedrich, B, Pick, S, Hladek, L, Herman, Z, Nikitin, E E, Reznikov, A I and Umanskii, S Y, *J. Chem. Phys.* **1986**, *84*, 807–812.

[31] Christensen, R B and Watson, W D, *Phys. Rev. A* **1981**, *24*, 1331–1341.
[32] Zener, C, *Proc. Roy. Soc. Lond. Ser. A* **1932**, *137*, 696.
[33] Stueckelburg, E C G, *Helv. Phys. Acta* **1932**, *5*, 369.
[34] Rogers, S A, Price, S D and Leone, S R, *J. Chem. Phys.* **1993**, *98*, 280–289.
[35] Price, S D, *J. Chem. Soc.–Faraday Trans.* **1997**, *93*, 2451–2460.
[36] Olson, R E, Smith, F T and Bauer, E, *Appl. Optics* **1971**, *10*, 1848–&.
[37] Braga, J P, Knowles, D B and Murrell, J N, *Mol. Phys.* **1986**, *57*, 665–674.
[38] Harper, S M, Hu, S W P and Price, S D, *J. Chem. Phys.* **2004**, *120*, 7245–7248.
[39] Harper, S M, Hu, W P and Price, S D, *J. Phys. B* **2002**, *35*, 4409–4423.

Chapter 4: N_2^{2+} + H_2

4.1 Introduction

N_2^{2+} has been implicated in the chemistry of the upper atmosphere of both Earth and Titan[1,2]. In fact modelling indicates that optical emission from N_2^{2+} should be observable in Titan's ionosphere[2]. The density of N_2^{2+} in the atmosphere of Titan has been predicted to have a maximum of 10^{-2} cm^{-3} at altitudes of 1000–1200 km, which is greater than the density for several key monocations such as CH^+, CN^+ and C_2H^+[2]. Indeed, the presence of dications in Titan's ionosphere is supported by the tentative assignment of N^{2+} in the ion abundances recorded by Cassini[3]. The principal loss mechanisms for ionospheric molecular dications have been identified as electron recombination and reaction with neutral species[2]. Thus, along with the fact that dicationic chemistry has been proposed as a mechanism for the synthesis of larger hydrocarbons[4-6], it is pertinent to understand the reactivity of N_2^{2+} with abundant components in Titan's atmosphere to gain a full understanding this environment's intriguing evolution.

This chapter reports a study of the reactivity of N_2^{2+} with H_2, since both experiments and models indicate that H_2 is the third most abundant molecular species in Titan's atmosphere[7]. Thus, the result of reactive events such as those between N_2^{2+} and H_2 could have consequences for the fate of N_2^{2+} in Titan's ionosphere. In particular, recent computational studies have investigated the structure of N_2H^{2+}[8,9]. These calculations showed that the ground state of N_2H^{2+} is metastable and, in addition, that many of the excited N_2H^{2+} electronic states also possess metastable minima. Results of this computational study suggested that interactions between N_2^{2+} and H_2 may provide a source of N_2H^{2+} in Titan's ionosphere. It has been shown experimentally that the interaction of singly charged molecular nitrogen, N_2^+, with molecular hydrogen predominantly results in the formation of N_2H^+. The rate constant for this process has been measured to be around 2.0×10^{-9} $molecule^{-1}cm^3s^{-1}$ at 300K. It is interesting to compare the difference between singly– and doubly–charged ion reactions and also the different rates of such reactions. Stimulated by the relevance to

Titan's ionosphere, and the intriguing possibility of the formation of N_2H^{2+}, this chapter reports our experimental study of the reactivity of N_2^{2+} with $H_2(D_2)$.

4.2 Results

Five bimolecular reactions are clearly observed in the PSCO spectrum, Figure 4.1, recorded following collisions of N_2^{2+} with D_2 at CM collision energy of 1.8 eV. The reaction of N_2^{2+} was studied with both H_2 and D_2, for reasons described below. These two collision systems exhibit the same five reaction channels, thus, only the pairs spectrum collected with D_2 is shown in Figure 4.1. The details of these reactions are given in Table 4.1.

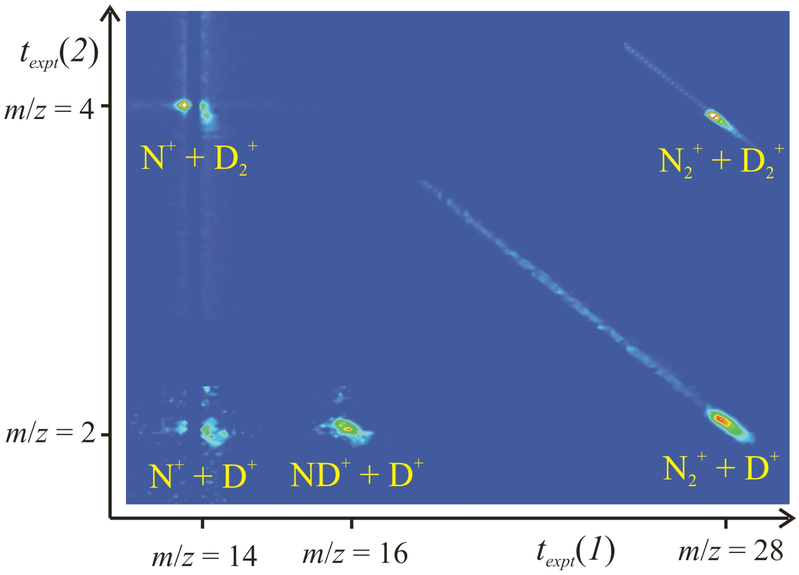

Figure 4.1 The pairs spectrum recorded following the collisions of N_2^{2+} with D_2 at E_{CM} = 1.8 eV. The peaks involving coincidences with N^+ have a "split" shape due to the exclusion of a strip of false coincidences resulting from the N^+ ions present in the reactant ion beam. See text for details.

Initial measurements with H_2 as the neutral collision partner showed a peak in the coincidence spectrum at *m/z* of 15 and *m/z* of 1. There are two possible explanations for such a reaction channel: it is either due to a reaction of an isotopically substituted reactant $^{15}N^{14}N^{2+}$ reacting *via* dissociative SET to yield $^{15}N^+$ + H^+, or due to a chemical channel yielding NH^+ + H^+. The tuning of the Wein filter determined the proportion of isotopically substituted reactants which were transmitted to the reaction region; however, this was unlikely to be more than the natural abundance. In the case of N_2, the relative isotopic ratio for $^{14}N_2$:$^{15}N_2$ is 99.63:0.37. Thus, given the branching into the dissociative SET channel yielding $^{14}N+ + H^+$ of 3.4 %, we predict a maximum branching into this ambiguous channel of 0.006 %. The experimentally determined branching into the $m/z = 15 + m/z = 1$ channel is around 1.7 %, clearly much greater than predicted using the standard isotopic abundances as a guide, thus implying the channel is of chemical origin.

There is, however, only one way to be certain of the products of this channel, which is using D_2 as the reactant neutral. With D_2 as the reactant, the former scenario would result in the peak appearing at $m/z = 15$ ($^{15}N^+$) and $m/z = 2$ (D^+), whereas if the peak is indeed due to a bond–forming channel, then we would expect the arrival times of the products to be consistent with $m/z = 16$ (ND^+) and $m/z = 2$ (D^+). As is clear from the spectrum recorded following interaction of N_2^{2+} with D_2, Figure 4.1, there is evidently a peak at m/z of 16 and 2, thereby explicitly clarifying the origin of the products as from a bond–forming channel. The relative numbers of ion–counts in each peak in the coincidence spectrum yields the branching ratios R into the separate reaction channels shown in Table 4.1.

Table 4.1 The bimolecular reactions observed between N_2^{2+} and H_2 (E_{CM} = 0.9 eV) and D_2 (E_{CM} = 1.8 eV). The table also gives the branching ratio R for each channel in the different collision systems.

Chan.	Reaction	R / % ($N_2^{2+} + H_2$)	R / % ($N_2^{2+} + D_2$)
(4.1)	$N_2^{2+} + H_2 \rightarrow N_2^+ + H_2^+$	52.8	61.1
(4.1a)	$^{15}N^{14}N^{2+} + H_2 \rightarrow {}^{14}N^{15}N^+ + H_2^+$	0.3	0.10
(4.2)	$N_2^{2+} + H_2 \rightarrow N_2^+ + H^+ + H$	10.3	12.1
(4.3)	$N_2^{2+} + H_2 \rightarrow N^+ + H_2^+ + N$	31.5[a]	23.6[a]
(4.4)	$N_2^{2+} + H_2 \rightarrow N^+ + H^+ + (N + H)$	3.4[a]	1.6[a]
(4.5)	$N_2^{2+} + H_2 \rightarrow NH^+ + H^+ + N$	1.7	1.5

[a] Counts corrected for losses in the excluded zone of the pairs spectrum. See text for details.

In the ion–pairs spectrum we exclude a strip of TOFs that are close to that of the reactant, in this case for m/z = 14, as detection of ions in this TOF range would result in a large number of false coincidences. Unfortunately, this ‘exclusion zone’ sometimes coincides with the unperturbed TOF for a product ion. In this case, reactions that form N^+ products result in peaks that lie around the excluded zone. As a consequence, these peaks have a "split" shape as is clear in Figure 4.1, and as such, we need to correct for the counts that are missing from these peaks.

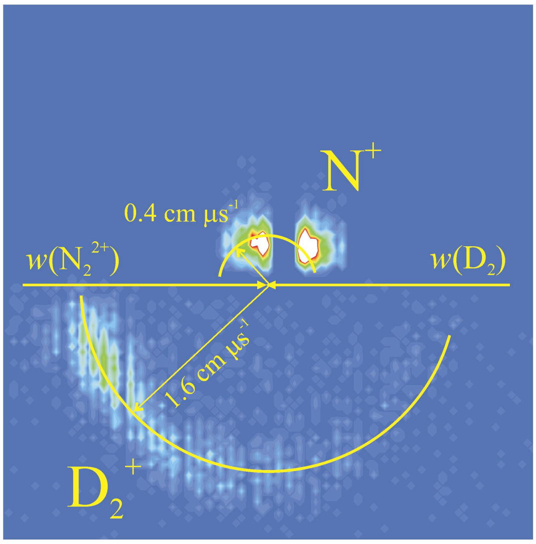

Figure 4.2 CM frame scattering diagram for channel (4.3) yielding N^+ + D_2^+ + N. The directions of the reactants prior to the interaction are shown by the full-headed arrows. The split shape of the scattering due to the 'exclusion zone' is clearly visible in the scattering of the N^+ products.

There are two reaction channels that are affected by this "exclusion zone", these are channels (4.3) and (4.4) forming N^+ in coincidence with $H_2^+(D_2^+)$ and $H^+(D^+)$ respectively. It is clear from the CM frame scattering diagram for channel (4.3) (Figure 4.2) constructed following collisions of N_2^{2+} with D_2, that N^+ products scattered to a particular range of angles near 90° are not recorded due to the excluded TOF zone. Plotting a histogram of the scattering angles of the N^+ product allows us to correct for the missing counts in two simple ways. The first of these corrections (method 1) involves fitting the scattering angle distribution with a Gaussian curve, Figure 4.3, the second (method 2) is to estimate, by eye, the shape of the distribution where no ions are detected, Figure 4.4.

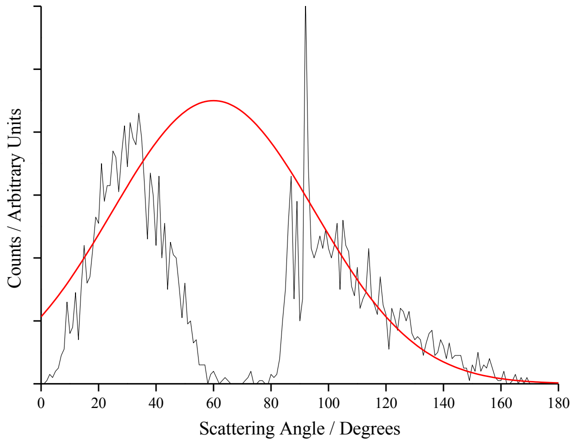

Figure 4.3 Black line – histogram of scattering angles recorded for the N^+ product arising from channel (4.3), which yields $N^+ + D_2^+ + N$. Red line – Gaussian curve used to model the distribution to correct for losses due to the "exclusion zone".

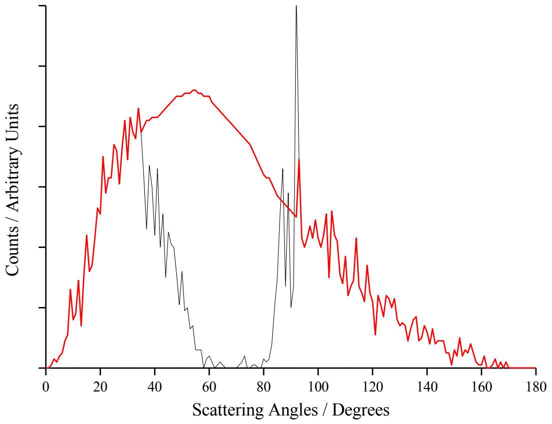

Figure 4.4 Black line – histogram of scattering angles recorded for the N^+ product arising from channel (4.3), which yields $N^+ + D_2^+ + N$. Red line – estimate of the distribution made by eye, over the range of angles that are not recorded, to correct for losses due to the "exclusion zone".

By integration of the curves generated by correction methods 1 and 2 we obtain a better estimate of the number of pairs in the reaction channel. This correction is executed for both channels (4.3) and (4.4), which involve production of N^+ ions; the results can be seen in Table 4.2. The branching ratios presented in Table 4.1 are calculated using the number of pairs generated employing correction method 2, as this was deemed the more accurate of the two methods. Clearly, equivalent corrections were carried out for the N_2^{2+} – H_2 data.

Table 4.2 Counts for channels forming N^+ products corrected *via* methods 1 and 2 compared to the original number of detected counts.

Method for Correction	Number of Pairs in Peak	
	$N^+ + D_2^+ + N$	$N^+ + D^+ + N + D$
No Correction	4241	384
1	7626	577
2	7439	518

We see no signals due to N_2D^{2+} or N_2H^{2+} in the mass spectra we collect in parallel with the PSCO data. In any case, the bond-forming reaction we detect, that forms $NH^+ + H^+ + N$, clearly cannot proceed *via* a N_2H^{2+} intermediate which requires the accompanying formation of an H atom. In principle, it is possible that there is a contribution to channels (4.2) and (4.4) from decay of an N_2H^{2+} intermediate, however, we see little evidence of this, as discussed below.

4.3 Bond-Forming

The dynamics and mechanism of the bond-forming reaction which generates $NH^+ + H^+$ have been revealed by the PSCO experiments. We present hereafter the data for the $N_2^{2+} + D_2$ collision system, which displays identical correlations to those we observe for the $N_2^{2+} + H_2$ collision system.

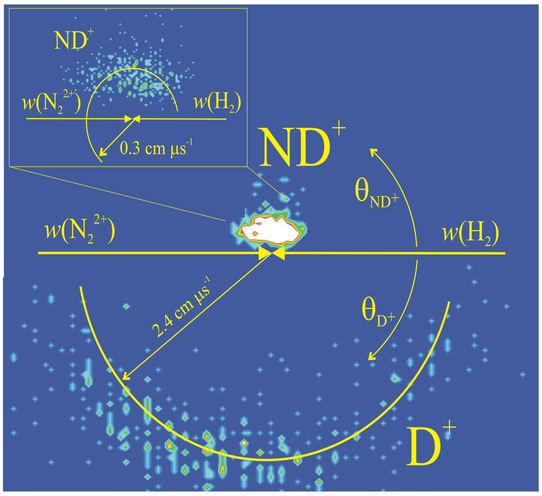

Figure 4.5 The CM frame scattering diagram for the reaction $N_2^{2+} + D_2$ $ND^+ + D^+ + N$, showing the scattering of ND^+ and D^+, relative to the direction of the reactant dication velocity $w(N_2^{2+})$, derived from PSCO data recorded at E_{CM} = 1.8 eV. The inset shows the scattering of the ND^+ fragment on a larger scale. See text for details.

Figure 4.5 shows the CM frame scattering diagram for the ND^+ and D^+ ions generated by channel (4.5). The data in Figure 4.5 shows that there is little correlation between the velocities of the products of channel (4.5) with the velocity of the reactant N_2^{2+}. This lack of correlation is a clear indication that a collision complex is involved in the reaction pathway, before the formation of any of the products[10]. If the collision complex lives for at least a few rotational periods then the products have no "memory" of the original direction of the reactant N_2^{2+} ion, as we observe experimentally.

To probe the mechanism of channel (4.5) in more detail we examine the mutual correlation between the product velocities in the internal frame. Figure 4.6 (a) shows the scattering of $w(ND^+)$ and $w(N)$ with respect to the direction of $w(D^+)$. Figure 4.6 (b) and (c) show internal frame scattering diagrams with reference to the velocities of N and ND^+ respectively.

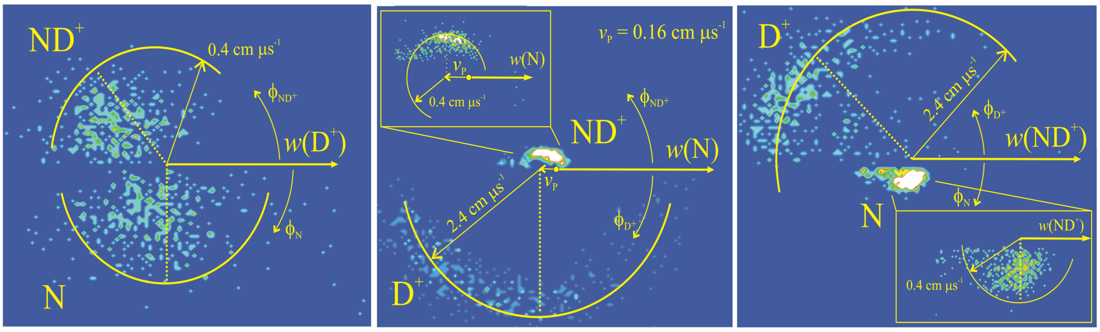

(a) **(b)** **(c)**

Figure 4.6 The internal frame scattering diagrams from channel (4.5) in the $N_2^{2+} + D_2$ collision system at E_{CM} = 1.8 eV. (a) shows the scattering of ND^+ and N relative to $w(D^+)$, (b) shows the scattering of the ND^+ and D^+ relative to $w(N)$ and (c) shows the scattering of D^+ and N relative to $w(ND^+)$. The insets in (b) and (c) show the scattering of the ND^+ and N fragments respectively on a larger scale.

There are four possible mechanisms (4.6)–(4.9) for the formation of $ND^+ + D^+ + N$, given that, as discussed above, the CM scattering data (Figure 4.5) shows that the first step in this mechanism is the formation of a collision complex:

$$N_2^{2+} + D_2 \rightarrow [N_2D_2]^{2+} \rightarrow ND^+ + N + D^+ \tag{4.6}$$

$$N_2^{2+} + D_2 \rightarrow [N_2D_2]^{2+} \rightarrow ND^+ + ND^+ \text{ then } ND^+ \rightarrow N + D^+ \tag{4.7}$$

$$N_2^{2+} + D_2 \rightarrow [N_2D_2]^{2+} \rightarrow N_2D^+ + D^+ \text{ then } N_2D^+ \rightarrow ND^+ + N \tag{4.8}$$

$$N_2^{2+} + D_2 \rightarrow [N_2D_2]^{2+} \rightarrow ND_2^{2+} + N \text{ then } ND_2^{2+} \rightarrow ND^+ + D^+ \tag{4.9}$$

The form of Figure 4.6 immediately allows us to discount the concerted fragmentation of the collision complex (4.6). Such concerted reactions have been shown[11] to yield internal frame scattering diagrams where there are fixed relationships between the velocity vectors of the products, relationships reflecting the structure of the dicationic complex, exactly as for the concerted decay of a molecular dication[12]. The scattering diagrams in Figure 4.6 clearly do not show such fixed relationships between the product velocity vectors.

From inspection of Figure 4.6, the sequential mechanism (4.7) can also readily be discounted. Charge separation of the $[N_2H_2]^{2+}$ collision complex to form two ND^+ ions would form these primary products with significant velocities, A typical dication charge separation involves an energy release of approximately 6 eV, which would give the ND^+ velocities of the order 0.6 cm μs^{-1}. Extraction of the CM velocity distributions of the product ions from our data (Figure 4.7) shows that the average value of $w(ND^+)$ is markedly lower than the expected value of 0.6 cm μs^{-1}. Furthermore, in the secondary fragmentation of one of the ND^+ ions, the heavier N fragments velocity will remain close to that of the precursor ND^+ due to conservation of momentum and energy. Thus mechanism (4.7) would predict ND^+ to have a significant velocity which will be strongly anti–correlated with $w(N)$ and the scattering of the D^+ should be centred about a precursor velocity equal and opposite to that of $w(ND^+)$. None of these predicted features are apparent in Figure 4.6.

Mechanism (4.8) involves charge separation of the initial collision complex and then subsequent secondary fragmentation of the N_2D^+ monocationic product of this initial decay. If this mechanism is operating we can determine the average value of $w(N_2D^+)$ to be 0.18 cm μs^{-1} *via* conservation of momentum from the measured modal value of $w(D^+)$ = 2.75 cm μs^{-1} (Figure 4.7). We would then expect the velocities of ND^+ and N to be isotropically distributed about $w(N_2D^+)$, the velocity of the precursor ion, as we have observed before for such secondary fragmentations[13]. Figure 4.6 (a) clearly does not show such a characteristic distribution for the N atom. In addition, the secondary fragmentation of N_2D^+ should not involve a significant kinetic energy release, in comparison to the large kinetic energy released upon the charge separation of the doubly charged collision complex. Thus, we would expect the average value of $w(ND^+)$ to be similar to that of the precursor ion $w(N_2D^+)$ = 0.18 cm μs^{-1}. As shown in Figure 4.7, the average value of *w*(ND^+) is almost twice this value. Hence, the observed scattering is not in accord with mechanism (4.8).

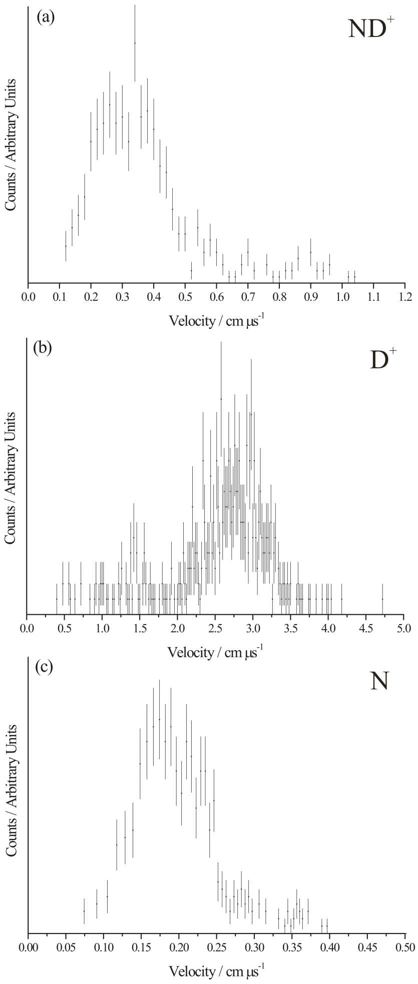

Figure 4.7 Velocity distributions of the ND^+, D^+ and N products of channel (4.5) in the CM frame.

In mechanism (4.9) the collision complex first loses an N atom to form NH_2^{2+} and this daughter dication then undergoes a two–body charge separation to form the observed products. For this mechanism we would expect *w*(N) to be broadly anti–correlated with *w*(D^+) and *w*(ND^+), as we observe in Figure 4.6 (b). From the average value of *w*(N) of 0.2 cm μs^{-1} we can estimate the average value of *w*(ND_2^{2+}) to be 0.16 cm μs^{-1} by conservation of momentum. The scattering of ND^+ and D^+ should then be centred about *w*(ND_2^{2+}) , as is also clearly visible in Figure 4.6 (b) where *w*(ND_2^{2+}) is marked as v_p. Thus, the only reaction mechanism in full accord with the PSCO data is (4.9). It seems apparent that the formation of NH^+ + H^+ + N following collisions of N_2^{2+} with H_2 proceeds *via* initial formation of a collision complex $[N_2H_2]^{2+}$ which lives for several rotational lifetimes before losing an N atom to form NH_2^{2+}. This daughter dication also lives for several rotational periods before decaying to NH^+ + H.

4.3.1 Estimating the Reaction Cross–Section and Rate Constant

The relative intensities of the different reactions in the pairs spectrum (Figure 4.1), when corrected for any ion losses due to the exclusion of the false coincidences, give the branching ratio between the different reaction channels. However, this relative measurement does not place the rates of these reactions on an absolute scale and such absolute measurements are those of real value to ionospheric modelling. To obtain estimates of the rate coefficient for the formation of NH^+ +H^+ from the ion signals in the pairs spectra two different approaches have been adopted. Firstly we have extrapolated the absolute measurements of the cross–section for forming N_2^+ from reactions between N_2^{2+} and H_2 of Agee *et al.*[14], studied at N_2^{2+} kinetic energies between 2 and 6 keV, to our collision energy and then used our measured relative intensity of the channels forming N_2^+ and NH^+ to estimate the absolute cross–section for forming NH^+ under our experimental conditions to be 1.0×10^{-17} cm^2. To estimate the corresponding thermal rate constant for this reaction from this cross–section we assume the limiting $E_{CM}^{-½}$ dependence of an ion–molecule reaction cross–section and perform the standard integration over a Boltzmann distribution[15]. This procedure yields an estimated rate coefficient k_5 for the formation of NH^+ at 300 K of 1.0×10^{-11} molecule^{-1} cm^3 s^{-1}. This estimate is likely to be a lower limit as the linear decrease with collision energy we assume in the data of Agee *et al.*[14] probably results in an underestimate of the cross section for N_2^+ formation at our collision energies, giving a consequent underestimate of k_5.

The second approach to provide an estimate of k_5 is to assume the dication–neutral interactions occur at the Langevin rate, which is defined by the classical Langevin rate constant[16]:

$$k_L = 2\pi q\sqrt{\frac{\alpha}{\mu}} \tag{4.10}$$

where q is the charge on the ion, α is the polarisability of the molecule and μ is the reduced mass of the system. The Langevin rate is calculated for the N_2^{2+} – H_2 collision system. We then partition this rate between the various channels in proportion to our measured branching ratios. This calculation results in an estimate of $k_5 = 5.4 \times 10^{-11}$ molecule^{-1}cm^{3}s^{-1}, a value independent of temperature and in good accord with our first estimate of k_5 given the approximations involved. Note that the incident dictions, which are produced by electron ionisation, cannot be considered to be equilibrated to a thermal temperature. Thus, as is always the case with ion beam experiments, the rate coefficients we derive should be considered to be merely indicative of a thermalised rate coefficient for N_2^{2+} ions.

4.4 Computational Investigations

To lend further support to the above mechanistic conclusions we have investigated the stationary points on the $N_2^{2+} + H_2$ PES using Gaussian98[17]. Stationary points were located by B3LYP/aug–ccVTZ optimization and their energies characterized by CCSD(T)/aug–ccVTZ single point calculations. B3LYP frequency analysis was used to identify minima and transition states, and the connectivity of the transition states was confirmed by the Internal Reaction Coordinate (IRC) methodology and inspection of imaginary frequencies. Of course, the geometries of several of the reactant and product species have been determined before either theoretically or experimentally[18-22]. In these cases our calculated geometries agree well with literature values. The energy of any excited states of atomic products were determined by adding spectroscopic excitation energies[23] to the calculated energies of the relevant ground states. This procedure generates a reaction exothermicity of –2.8 eV (Figure 4.8) for channel (4.5), which on the singlet PES forms NH^+ and N in doublet states, in excellent agreement with literature thermodynamics (–2.8 eV)[18,24].

4.4.1 Singlet Surface

We initially restricted our calculations to the singlet potential energy surface, as experiments have indicated that the majority of dications in N_2^{2+} beams are in the ground $X^1\Sigma_g^+$ state[25,26]. Figure 4.8 reveals two pathways from $N_2^{2+}(X^1\Sigma_g^+) + H_2$ on the singlet $[N_2H_2]^{2+}$ surface to reach pairs of monocations with new chemical connectivity; one of these pathways leads to the formation of the experimentally observed products $NH^+ + H^+ + N$ (channel (4.5)). Both pathways proceed *via* the formation of a collision complex (**1**). We have also located a low lying H–NN–H^{2+} minimum ($E = -13.6$ eV, r(HN) = 1.104 Å, *r*(NN) = 1.073 Å) on the singlet PES, of $D_{\infty h}$ symmetry, but this minimum does not appear to readily connect to the observed products.

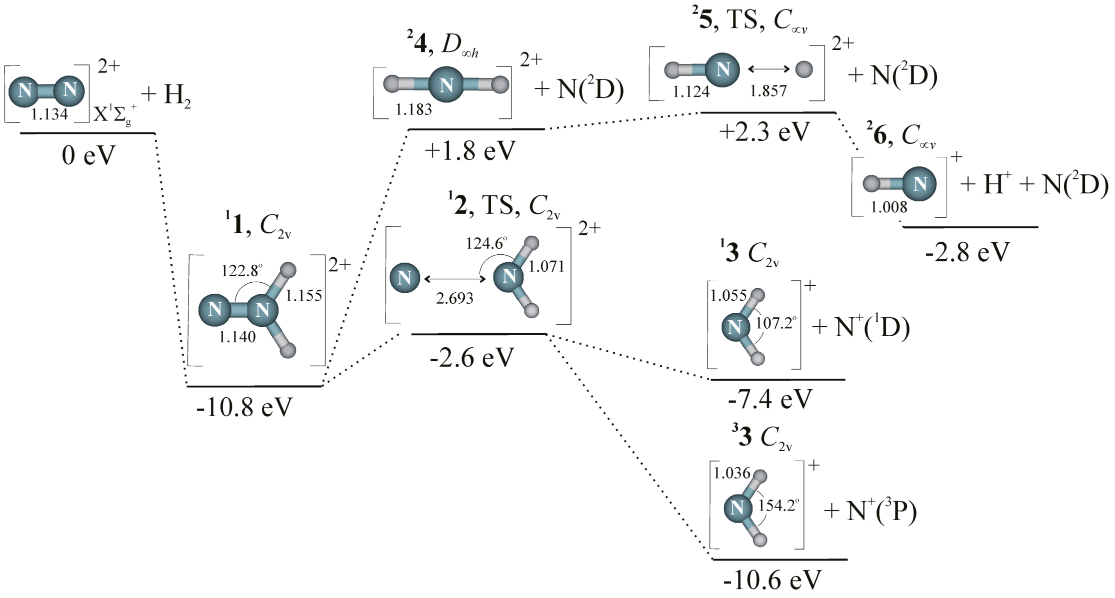

Figure 4.8 Stationary points on the singlet $[N_2H_2]^{2+}$ potential energy surface. All energies include estimated zero point energies and are expressed relative to the infinitely separated reactants. The levels labelled TS are transition states with a critical vibration shown by the double headed arrow. All bond lengths are in Angstroms and angles in degrees.

The lowest energy reaction pathway involves charge–separating decay of **1,** *via* a transition state **2,** to form NH_2^+ (**3**) + N^+. Spin conservation means that **3** can be formed in either a singlet or triplet state as illustrated in Figure 4.8. Interestingly, we observe no evidence of the products of this pathway, N^+ + NH_2^+ or even N^+ + NH^+, in our PSCO spectra. The second reactive pathway revealed by our calculations (Figure 4.8) corresponds exactly to the experimentally determined mechanism (4.9) for forming the observed NH^+ + H^+ + N products. Specifically, the theoretical pathway involves the loss of a nitrogen atom from **1** to yield an NH_2^{2+}dication (**4**) in a doublet state. This loss of an N atom appears not to involve a transition state. The NH_2^{2+} ion (**4**) then decays *via* a transition state (**5**) to yield the experimentally observed products. However, the energetics revealed in Figure 4.8 indicate that pathway (4.9), the mechanism revealed to be operating by our PSCO spectra, proceeds *via* stationary points (**4** and **5**) which are energetically inaccessible for reactants in their ground vibrational levels, even allowing for the contribution of the CM collision energy (E_{CM} = 0.9 eV for H_2). The $N_2^{2+}(X^1\Sigma_g^+)$ ions in our reactant beam are not necessarily in their ground vibrational states. However, experimental investigations of the population of the ground electronic state of N_2^{2+} following photoionisation clearly show only the population of the three lowest vibrational levels is favoured, giving a maximum vibrational energy of 0.5 eV[24]. Thus, if the vibrational distribution of the N_2^{2+} reactant ions in our beam is similar to that formed by photoionisation, then the $N_2^{2+}(^1\Sigma_g^+)$ + H_2 collision system should not be able to energetically access the observed products *via* structures **4** and **5**.

4.4.2 Triplet Surface

To resolve the inconsistencies between the calculated energetics on the singlet surface of $[N_2H_2]^{2+}$ and the experimental observation of channel (4.5) we note that it is well established that beams of N_2^{2+} ions contain a small proportion of ions in the metastable $c^3\Sigma_u^+$ state[25,26]. This state lies 1.5 eV above $N_2^{2+}(X^1\Sigma_g^+, v = 0)$[20,27]. Thus, given the difficulties in explaining the observation of the formation of NH^+ +H^+ *via* a singlet PES we have also calculated stationary points on the $^3[N_2H_2]^{2+}$ surface (Figure 4.9).

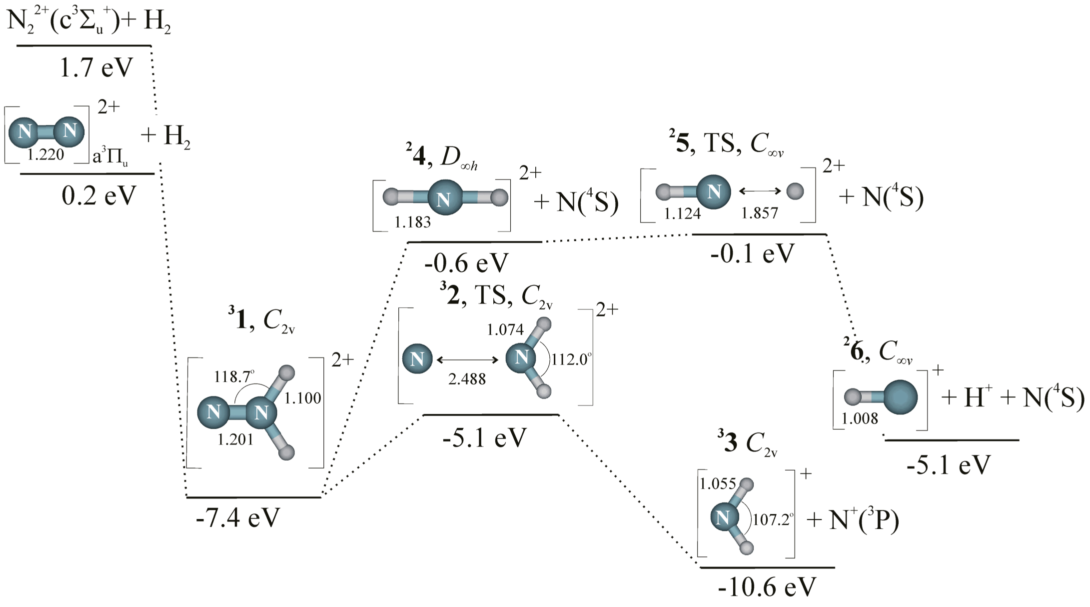

Figure 4.9 Stationary points on the triplet $[N_2H_2]^{2+}$ potential energy surface. All energies include estimated zero point energies and are expressed relative to the infinitely separated singlet reactants. The levels labelled TS are transition states with a critical vibration shown by the double headed arrow. All bond lengths are in Angstroms and angles in degrees.

For easy comparison between the singlet and triplet PESs the energies of the stationary points on the triplet surface (Figure 4.9) are relative to the reactant asymptote of the singlet surface. The lowest triplet state of N_2^{2+}has been shown[19] to lie less than 0.1 eV above the ground singlet state of the dication, an energy difference determined as 0.15 eV by our lower–level calculations in reasonable agreement with the higher level study. The general form of the triplet surface (Figure 4.9) is qualitatively similar to that of the singlet surface (Figure 4.8) with the same two series of stationary points leading to NH^+ + H^+ + N and NH_2^+ + N^+. In addition, again as for the singlet surface, we also find a global $[H–NN–H]^{2+}$ minimum, this time of C_{2h} geometry [r(H–N) = 1.108 Å, r(N–N) = 1.280 Å, ∠(HNN) = 125.7°, E = –7.1 eV], but again this minimum does not seem to lie on a pathway to the observed monocationic products.

Inspection of the triplet surface (Figure 4.9) reveals that the stationary points on the pathway to form NH^+ + H^+ + N(^{4}S) all lie at energies below the $N_2^{2+}(c^3\Sigma_u^+)$ asymptote. Thus our computational results strongly indicate the observed products of channel (4.5) are formed by the reaction of the excited metastable triplet N_2^{2+} ions in our dication beam. No quantitative evaluation of the relative abundances of the X and c states of N_2^{2+} ion dication beams is available. Previous investigations of the electron transfer reactivity of N_2^{2+} with the rare gases show that reactions of the ground electronic state of the dication dominate the ion yield when such channels are accessible. Hence, it seems likely that the $N_2^{2+}(c^3\Sigma_u^+)$ are a minority species in our dication beam, and thus the small yield of NH^+ + H^+ in our experiments is indicative of a significant reaction cross section for NH^+ formation from the $N_2^{2+}(c^3\Sigma_u^+)$ state. If, for example, less than 10% of the N_2^{2+} ions in our ion beam are in the $c^3\Sigma_u^+$ state then the state–resolved cross section for NH^+ formation from this excited state would be close to the collisional value. Thus, it seems clear that state–resolved investigation of the reactivity of N_2^{2+} ions is required. With regard to the ionospheric chemistry of Titan, clearly improved models need to differentiate the X and c electronic states of N_2^{2+}. If a considerable fraction of the N_2^{2+} ions present in Titan's ionosphere are formed in the $c^3\Sigma_u^+$ state, this would have profound consequences for NH^+ ion abundances and therefore the chemical evolution of this fascinating atmosphere.

4.5 Electron–Transfer

4.5.1 Non–Dissociative Electron–Transfer

We now consider the mechanisms of the SET reactions that are observed following collisions of N_2^{2+} with $H_2(D_2)$. The figures presented here are for the N_2^{2+} – D_2 collision system, however, identical dynamics are also observed for the N_2^{2+} – H_2 system.

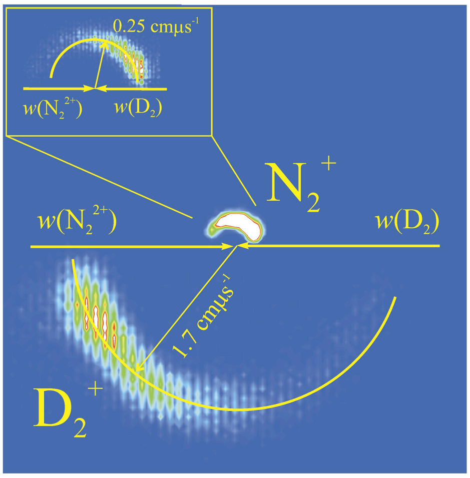

Figure 4.10 Scattering diagram showing the velocities of the products of non-dissociative SET between N_2^{2+} and D_2, in the CM frame, relative to the directions of the reactants prior to the collision (full-headed arrows). The inset shows the scattering of the N_2^+ ion on a larger scale.

The detailed dynamics of dicationic electron transfer reactions at low collision energies (below E_{CM} = 10 eV) have been extensively investigated in recent years[13,28-32]. Experimental work shows that in this low energy regime dicationic electron-transfer commonly involves strong forward scattering; the origin of this characteristic scattering has been described in detail in Chapter 2. Such forward scattering is indeed observed for the non-dissociative SET (channel (4.1)), Figure 4.10, implying that the ET occurred at a large interspecies separation.

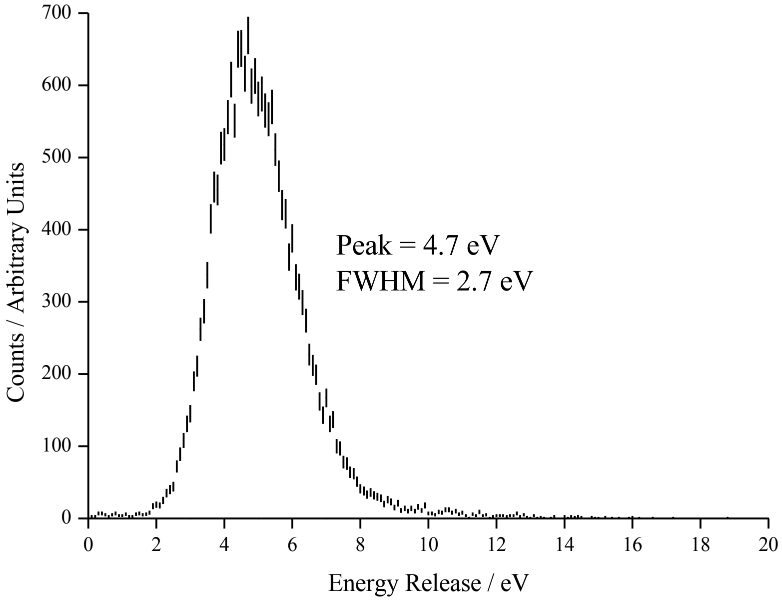

Figure 4.11 Energy release distribution for channel (4.1), the non-dissociative SET reaction. The CM energy has been subtracted yielding the exothermicity of the reaction. Error bars are given by Poissonian statistics.

As described in Chapter 2, the magnitudes of the product velocity vectors give us the KER of a reactive event, and consequently, subtracting the CM velocity from these KERs gives us an exothermicity distribution for the channel. Shown in Figure 4.11, the exothermicity distribution of channel (4.1) is peaked at 4.7 eV with a spread from approximately 2 –10 eV.

The first metastable excited electronic state of H_2^+ is the $B^2\Sigma_g^+$ state that lies 11.63 eV higher in energy than the ground $X^2\Sigma_g^+$ (v = 0)[33,34]. A reaction involving ground state reactants and forming ground state $N_2^+(X^2\Sigma_g^+)$ in conjunction with $H_2^+(B^2\Sigma_g^+)$ would be endothermic by 0.2 eV. Thus, given the measured exothermicity for channel (4.1) of around 4.7 eV, it seems very unlikely that H_2^+ is formed in the $B^2\Sigma_g^+$ state. Therefore, in the non–dissociative SET reaction between N_2^{2+} and H_2, the H_2^+ must be formed in its ground electronic state $X^2\Sigma_g^+$, probably with some degree of rovibrational excitation. Consideration of the electronic states of the N_2^{2+} reactant and N_2^+ product that are involved in channel (4.1) is somewhat more complex. There are two possible bound states of the reactant N_2^{2+} that could be present in the beam; these are the $X^1\Sigma_g^+$ and $c^3\Sigma_u^+$ states[25]. There are also at least five possible states of the product N_2^+ that could be formed; these are the $X^2\Sigma_g^+$, $A^2\Pi_u$, $B^2\Sigma_u^+$, $a^4\Sigma_u^+$ and $D^2\Pi_g$ states[25,34,35]. Thus, there are ten distinct combinations of reactant and product electronic states that could result in an exothermicity of the reaction within the experimentally measured range. Moreover, given that $N_2^+(X^2\Sigma_g^+)$ can support approximately 8 eV of internal excitation[25] and $H_2^+(X^2\Sigma_g^+)$ around 1.8 eV, no further deductions can be made as to the electronic states participating in the reaction.

4.5.2 Dissociative Electron–Transfer

Dissociative SET occurs in the N_2^{2+} – H_2 reactive system resulting in $N_2^+ + H^+ + H$ (channel (4.2)), $N^+ + H_2^+ + N$ (channel (4.3)) and $N^+ + H^+ + N + H$ (channel (4.4)) products. Identical channels and scattering are observed following dissociative SET between N_2^{2+} and D_2, thus all the scattering diagrams presented are for this latter system. The CM frame scattering diagram for channel (4.3) has already been presented (Figure 4.2), in the context of corrections made to the number of pairs, and shows fairly strong forward scattering.

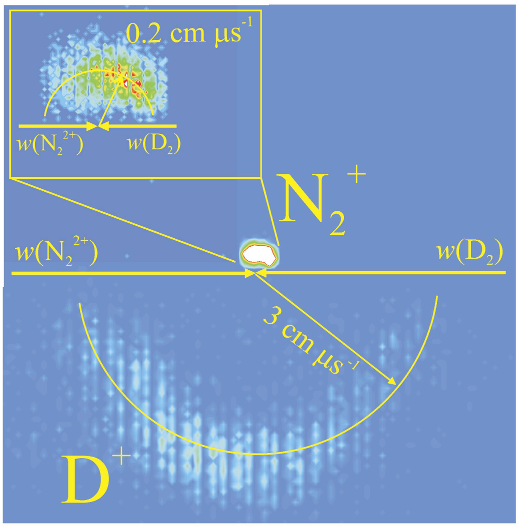

Figure 4.12 CM frame scattering diagram for dissociative SET channel (4.2) that yields N_2^+ + D^+ + D. The inset shows the scattering of the N_2^+ on a larger scale. Directions of the reactants prior to the collision are indicated by the full-headed arrows.

The CM frame scattering for channel (4.2), Figure 4.12, again exhibits forward scattering, although in this case the scattering angles of the D^+ product appear to be more widely spread than for the D_2^+ of channel (4.3). The obvious conclusion of forward scattering in the CM frame diagrams is that the first step of the reaction is electron transfer at significant interspecies separation, which is followed by fragmentation of either the nascent N_2^+ or D_2^+ ions, according to Reaction 4.11. The broadened distribution of D^+ scattering angles seen in Figure 4.12 can be readily explained as due to the energy release associated with the dissociation of D_2^+ into D^+ + D.

$$N_2^{2+} + D_2 \rightarrow N_2^+ + D_2^+ \text{ then } N_2^+ \rightarrow N^+ + N \text{ or } D_2^+ \rightarrow D^+ + D \qquad (4.11)$$

The internal frame scattering diagrams, Figure 4.13 and Figure 4.14, corroborate the mechanistic deductions drawn from the CM scattering diagrams for channels (4.2) and (4.3), as will be explained below.

As described in Chapter 2, internal frame scattering diagrams show the scattering of each of the products in the frame defined by the products themselves. The three internal frame scattering diagrams that have been constructed for channels (4.3) and (4.2) are shown in Figure 4.13 and Figure 4.14. Figure 4.13 (b) and Figure 4.14 (b) are the most significant of the six diagrams constructed and they show the scattering of N^+ and N relative to D_2^+, and D^+ and D relative to N_2^+, respectively. Significantly, in both of these diagrams, it seems that the scattering centre of both the atomic ion and its related neutral (N^+ and N or D^+ and D) is displaced away from the CM. This displacement is indicative that the N^+ and N or D^+ and D have arisen from dissociation of a metastable N_2^{+*} or D_2^{+*}, respectively. The short-lived N_2^{+*} or D_2^{+*} intermediate has separated from the nascent partner ion (D_2^+ or N_2^+), resulting in the observed displacement of the scattering centers from the CM, as discussed above.

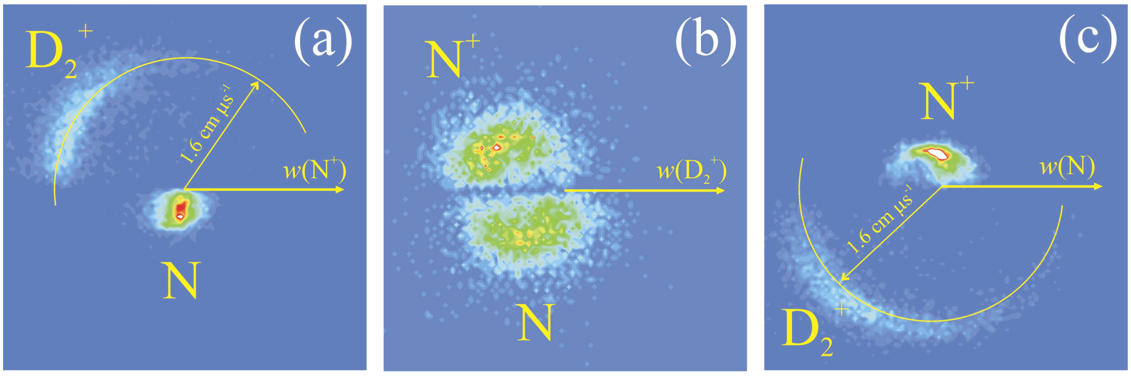

Figure 4.13 Internal frame scattering diagrams for the dissociative SET channel (4.3) forming $N^+ + D_2^+ + N$. (a) Scattering of D_2^+ and N relative to the direction of the N^+, (b) scattering of N^+ and N relative to the direction of D_2^+, (c) scattering of N^+ and D_2^+ relative to the direction of N.

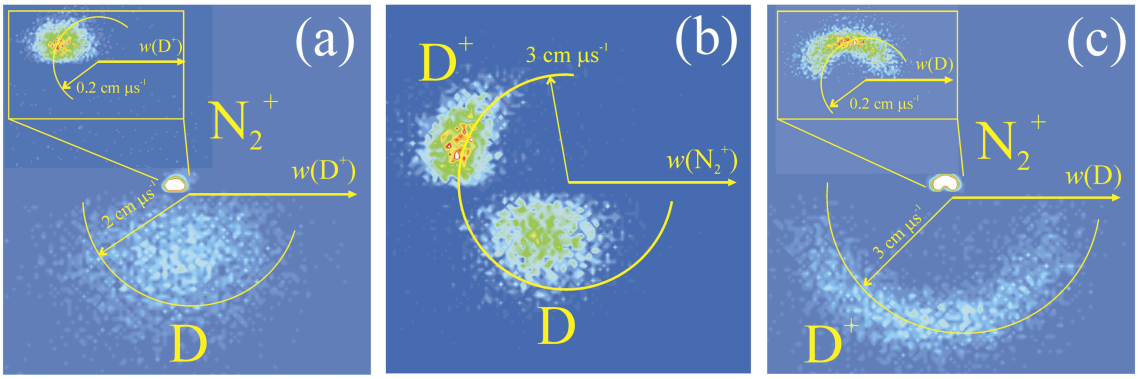

Figure 4.14 Internal frame scattering diagrams for the dissociative SET channel (4.2) forming $N_2^+ + D^+ + D$. (a) Scattering of N_2^+ and D relative to the direction of the D^+, (b) scattering of D^+ and D relative to the direction of N_2^+, (c) scattering of N_2^+ and D^+ relative to the direction of D. Insets show the scattering of N_2^+ on a larger scale.

What is more, from Figure 4.13 and Figure 4.14 ((a) and (b)) we can deduce by the anti-correlation of the ionic products' directions, that the dissociation of the nascent N_2^{+*} or D_2^{+*} takes place while the metastable ion is still strongly within the Coulomb field of the partner ion. Such an effect is much more obvious for the light D^+ (Figure 4.14 (b)) than for the heavier N^+ (Figure 4.13 (b)).

Unfortunately, in spite of the rather convincing evidence for the dissociative SET reaction mechanism described above, we cannot definitively establish the step–wise processes that occur to form the products of channel (4.2). This uncertainty is primarily due to the disparity in the mass between the reactants, and consequently products. More precisely, changes in the scattering directions of the light product (D_2^+, D^+) are greatly amplified in comparison with changes in the directions of the heavier product (N_2^+, N^+), which are negligible. As a consequence, there is another possible mechanisms for the dissociative SET channels (4.2) that cannot be completely discounted, Equations (4.12).

$$N_2^{2+} + D_2 \rightarrow N_2D^+ + D^+ \text{ then } N_2D^+ \rightarrow N_2^+ + D \qquad (4.12)$$

Complementary experimental or computational techniques could be employed to distinguish between the possible mechanisms for channel (4.2), specifically, Reaction (4.11) or (4.12).

Despite the obvious advantage of the PSCO technique to calculate the momentum of a third neutral product of a reaction, if more than one neutral atom is generated by a reaction we can no longer use conservation of momentum to calculate their velocities. Channel (4.4) corresponds to formation of $N^+ + D^+ + N + D$. However, the PSCO methodology does not allow us to directly determine if the neutrals are bound as ND. In this case, the only way to determine if these neutrals are in atomic or molecular form is by comparing the measured energy release with literature values. Unfortunately, this comparison is not possible for channel (4.4) due to the low number of counts, a problem exacerbated by the “exclusion zone” as described earlier. Therefore, we do not postulate further on the reaction dynamics or energetics of channel (4.4.).

4.6 Conclusion

We have investigated the chemical reactions forming pairs of monocations following collisions of the N_2^{2+} dication with H_2(D_2) at a centre–of–mass collision energy of 0.9(1.8) eV. These experiments reveal, in addition to single electron transfer reactions, a bond–forming pathway forming $NH^+ + H^+ + N$ and allow us to estimate of the reaction cross section for NH^+ formation and a rate coefficient for this reaction. Correlations between the velocities of the products of this bond–forming channel show that NH^+ is formed *via* N atom loss from a primary encounter complex $[N_2H_2]^{2+}$ to form NH_2^{2+}, with this triatomic dication fragmenting to yield NH^+ + H^+. No strong evidence of the proposed involvement of an N_2H^{2+} ion is observed. A computational investigation of stationary points on the singlet and triplet $[N_2H_2]^{2+}$ potential energy surfaces confirms the mechanistic deductions from the experiments and indicates that the formation of NH^+ occurs solely, and efficiently, from the reaction of the $c^3\Sigma_u^+$ excited electronic state of N_2^{2+} with H_2. The formation of NH^+ from reactions of $N_2^{2+}(c^3\Sigma_u^+)$ probably proceeds close to the collisional rate, with significant ramifications for the ionospheric chemistry of Titan. In particular, it is now important to identify the relative abundances of the metastable electronic states of N_2^{2+} that are present in Titan's ionosphere.

4.7 References

[1] Simon, C, Lilensten, J, Dutuit, O, Thissen, R, Witasse, O, Alcaraz, C and Soldi-Lose, H, *Ann. Geophys.* **2005**, *23*, 781-797.

[2] Lilensten, J, Witasse, O, Simon, C, Solidi-Lose, H, Dutuit, O, Thissen, R and Alcaraz, C, *Geophys. Res. Lett.* **2005**, *32*, L03203.

[3] Cravens, T E, Robertson, I P, Clark, J, Wahlund, J E, Waite, J H, Ledvina, S A, Niemann, H B, Yelle, R V, Kasprzak, W T, Luhmann, J G, McNutt, R L, Ip, W H, De La Haye, V, Muller-Wodarg, I, Young, D T and Coates, A J, *Geophys. Res. Lett.* **2005**, *32*,

[4] Roithova, J, Ricketts, C L and Schroder, D, *Int. J. Mass Spectrom.* **2009**, *280*, 32-37.

[5] Ricketts, C L, Schroder, D, Alcaraz, C and Roithova, J, *Chem.-Eur. J.* **2008**, *14*, 4779-4783.

[6] Ascenzi, D, Roithova, J, Schroder, D, Zins, E L and Alcaraz, C, *J. Phys. Chem. A* **2009**, *113*, 11204-11210.

[7] Cravens, T E, Robertson, I P, Waite, J H, Yelle, R V, Vuitton, V, Coates, A J, Wahlund, J E, Agren, K, Richard, M S, La Haye, V, Wellbrock, A and Neubauer, F M, *Icarus* **2009**, *199*, 174-188.

[8] Brites, V and Hochlaf, M, *J. Phys. Chem. A* **2009**, *113*, 11107-11111.

[9] Brites, V and Hochlaf, M, *Chem. Phys. Lett.* **2009**, *477*, 48-51.

[10] Levine, R D and Bernstein, R B *Molecular Reaction Dynamics and Chemical Reactivity*; Oxford University Press: Oxford, **1987**,

[11] Harper, S M, Hu, S W P and Price, S D, *J. Chem. Phys.* **2004**, *120*, 7245-7248.

[12] Hsieh, S and Eland, J H D, *Journal of Physics B-atomic Molecular and Optical Physics* **1997**, *30*, 4515-4534.

[13] Hu, W P, Harper, S M and Price, S D, *Mol. Phys.* **2005**, *103*, 1809-1819.

[14] Agee, J H, Wilcox, J B, Abbey, L E and Moran, T F, *Chemical Physics* **1981**, *61*, 171-179.

[15] Lin, S H and Eyring, H, *Proc. Natl. Acad. Sci. U. S. A.* **1971**, *68*, 402-&.

[16] Gioumousis, G and Stevenson, D P, *J. Chem. Phys.* **1958**, *29*, 294-299.

[17] Frisch, M J, Trucks, G W, Schlegel, H B, Scuseria, G E, Robb, M A, Cheeseman, J R, Zakrzewski, V G, Jr., J A M, Stratmann, R E, Burant, J C, Dapprich, S, Millam, J M, Daniels, A D, Kudin, K N, Strain, M C, Farkas, O, Tomasi, J, Barone, V, Cossi, M, Cammi, R, Mennucci, B, Pomelli, C, Adamo, C, Clifford, S, Ochterski, J, Petersson, G A, Ayala, P Y, Cui, Q, Morokuma, K, Malick, D K, Rabuck, A D, Raghavachari, K, Foresman, J B, Cioslowski, J, Ortiz, J V, Baboul, A G, Stefanov, B B, Liu, G, Liashenko, A, Piskorz, P, Komaromi, I, Gomperts, R, Martin, R L, Fox, D J, Keith, T, Al-Laham, M A, Peng, C Y, Nanayakkara, A, Challacombe, M, Gill, P M W, Johnson, B, Chen, W, Wong, M W, Andres, J L, Gonzalez, C, Head-Gordon, M, Replogle, E S and Pople, J A, *Gaussian, Inc*, Pittsburgh PA, **1998**

[18] *NIST Chemistry WebBook, NIST Standard Reference Database Number 69*; National Institute of Standards and Technology, Gaithersburg MD, 20899 (http://webbook.nist.gov): **2003**,

[19] Taylor, P R and Partridge, H, *J. Phys. Chem.* **1987**, *91*, 6148-6151.

[20] Wetmore, R W and Boyd, R K, *J. Phys. Chem.* **1986**, *90*, 5540-5551.

[21] Olsson, B J, Kindvall, G and Larsson, M, *J. Chem. Phys.* **1988**, *88*, 7501-7507.

[22] Cossart, D, Launay, F, Robbe, J M and Gandara, G, *J. Mol. Spectrosc.* **1985**, *113*, 142-158.

[23] Martin, W C, Fuhr, J R, Kelleher, D E, Musgrove, A, Podobedova, L, Reader, J, Saloman, E B, Sansonetti, C J, Wiese, W L, Mohr, P J and Olsen, K *NIST Atomic Spectra Database 2.0* (http://physics.nist.gov/asd); National Institute of Standards and Technology: Gaithersburg, MD., **2002**,

[24] Eland, J H D, **2003**, *294*, 171-186.

[25] Koslowski, H R, Lebius, H, Staemmler, V, Fink, R, Wiesemann, K and Huber, B A, *Journal of Physics B-atomic Molecular and Optical Physics* **1991**, *24*, 5023-5034.

[26] Kamber, E Y, Akgungor, K, Safvan, C P and Mathur, D, *Chemical Physics Letters* **1996**, *258*, 336-341.

[27] Lundqvist, M, Edvardsson, D, Baltzer, P and Wannberg, B, *Journal of Physics B-atomic Molecular and Optical Physics* **1996**, *29*, 1489-1499.

[28] Ricketts, C L, Schroder, D, Roithova, J, Schwarz, H, Thissen, R, Dutuit, O, Zabka, J, Herman, Z and Price, S D, *Phys. Chem. Chem. Phys.* **2008**, *10*, 5135-5143.

[29] Harper, S M, Hu, W-P and Price, S D, **2002**, *35*, 4409-4423.

[30] Mrazek, L, Zabka, J, Dolejsek, Z, Hrusak, J and Herman, Z, *J. Phys. Chem. A* **2000**, *104*, 7294-7303.

[31] Herman, Z, Zabka, J, Dolejsek, Z and Farnik, M, *International Journal of Mass Spectrometry* **1999**, *192*, 191-203.

[32] Lockyear, J F, Parkes, M A and Price, S D, **2009**, *42*, 145201.

[33] Bishop, D M, Shih, S K, Beckel, C L, Wu, F M and Peek, J M, *J. Chem. Phys.* **1975**, *63*, 4836-4841.

[34] Huber, K, Herzberg, G and (data prepared by J.W. Gallagher and R.D. Johnson, I, *"Constants of Diatomic Molecules"* **in NIST Chemistry WebBook, NIST Standard Reference Database Number 69**, , *Eds. P.J. Linstrom and W.G. Mallard, National Institute of Standards and Technology, Gaithersburg MD, 20899,* http://webbook.nist.gov, *(retrieved February 8, 2011)*,

[35] Colbourn, E A and Douglas, A E, *J. Mol. Spectrosc.* **1977**, *65*, 332-333.

Chapter 5: Reactivity of SF_4^{2+} with Neutrals

5.1 Introduction

Reactions of fluorinated sulphur compounds are significant in the chemistry of many natural and technological environments, these compounds are particularly important as industrial gasses[1]. More specifically, SF_6 is used extensively in plasma etching[2-4], as it is a good source of F^+ ions, and as an insulating dielectric[5]. Due to fluorine's high electronegativity, fluorination can have a dramatic effect on molecular properties. Nowhere is this perturbation more important than for organic compounds, where fluorination can impart substantial metabolic stability to prospective pharmaceutically active species[6-8]. However, due to their stability and inertness[8,9], facile synthesis of C–F bonds still provides a considerable challenge for chemists[6,10-14]. Gozzo *et al* have shown that gas–phase SF_3^+ ions donate F^+ to heteroaromatics[15] and F_2^+ has been observed to fluorinate some molecules[16]. In contrast, fluorination by gaseous molecular dications has never been specifically investigated, despite the current interest in bond–forming reactivity of these species[17,18]. This finding implies that further research is needed into the potential of SF_x^{n+} ions to fluorinate organic species. Gas–phase reactions monitored in a mass spectrometer provide a unique environment to study such chemical reactivity, free from the effects of solvents or counter ions[19,20].

Fluorinated sulphur compounds are also potentially significant global warming agents partly due to their long atmospheric lifetimes; significantly, SF_6 is one of the six greenhouse gases that the Kyoto protocol hopes to control as it has a global warming potential of around 22,200 relative to CO_2[1,21]. In 2000, Sturges *et al* reported the detection of the greenhouse gas SF_5CF_3, which has the largest radiative forcing of any individual gas molecule detected in the atmosphere to date[21]. SF_6 is not naturally occurring, but since its discovery in the early 1950s, and first industrial use in 1953, it has been heavily relied upon by many industries[1,22] resulting in atmospheric concentrations of both SF_6 and SF_5CF_3 growing steadily by about 6% per year from near zero in the late 1960s[21]. Molecules such as SF_6 and SF_5CF_3 are so stable that they will only be removed from the atmosphere by lightning or ion–molecule reactions in the ionosphere[23]. SF_6^{2+} is a thermodynamically and kinetically unstable dication and breaks down either by charge separation or by loss of neutral F atoms to give, amongst other ions, SF_4^{2+}. For a full understanding of ionospheric chemistry it is clearly important to study the reactions of such ions with neutral species. Indeed, our research has shown that bond–forming reactions of SF_4^{2+} proceed very readily, with potential consequences for ionospheric chemical evolution.

To our knowledge, there have only been two previous studies of the bimolecular gas–phase reactivity of SF_4^{2+} with molecular neutrals, firstly that carried out by Price *et al*[24] employing crossed–beam mass spectrometry, where predominantly SET and collision induced neutral loss were observed. However, in this study Price *et al* did observe one chemical channel between SF_4^{2+} and CO forming OCF^+. The second study was undertaken by Sparrapan *et al*[25] employing a quadrupole mass spectrometer and only products due to SET were observed. A heterogeneous study of gaseous SF_4^{2+} reacting with a hydrocarbon covered stainless steel surface was also carried out by Feketeova *et al*; the authors observed mainly SET products and also small but significant amounts of the bond–forming products $SF_2CH_3^+$, $SFCH_2^+$ and SCH^+[26].

Dication–neutral interactions have been observed to result in products due to SET, DET and bond–forming reactions. However, the rates of these bond–forming reactions are usually much lower than those for SET between the dication and neutral (for example CH_4, Reaction 5.1). In contrast to this weak dicationic bond–forming reactivity, we report in this chapter a series of very fast and efficient reactions involving the fluorination of a variety of neutral species (for example H_2, Reaction 5.2) following collisions with SF_4^{2+}.

$$SF_4^{2+} + CH_4 \rightarrow SF_4^+ + CH_4^+ \text{ then } SF_4^+ \rightarrow SF_3^+ + F \tag{5.1}$$

$$SF_4^{2+} + H_2 \rightarrow SF_3^+ + H_2F^+ \tag{5.2}$$

5.2 Results

We have employed the PSCO technique to detect the pairs of ions formed following collisions of SF_4^{2+} with Ar, H_2, D_2, CO, CO_2, N_2, H_2O, H_2S, NH_3, CH_4, C_2H_4, C_2H_6, CH_3OH and CHF_3. Rather remarkably, in ten of the fourteen collision systems investigated we observe fluorination channels (Table 5.1) many of which compete very effectively with single electron transfer[27]. Of special note are those reactions of SF_4^{2+} with hydrocarbons which exhibit the facile formation of C–F bonds.

Table 5.1 Products of the bond forming reactions of SF_4^{2+} that we observe, along with the relative branching into each channel as a percentage of the total reactivity for that collision system that forms a pair of monocations. The collision energy E_{CM} for each system is also shown.

Neutral Reactant	**Products**	E_{CM} / **eV**	**Branching Ratio / %**
Ar	$SF_3^+ + ArF^+$	3.0	13
H_2	$SF_3^+ + H_2F^+$	0.2	24
D_2	$SF_3^+ + D_2F^+$	0.4	29
CO	$SF_3^+ + FCO^+$ (or COF^+)	2.5	8
N_2	$SF_3^+ + N_2F^+$	2.5	9
H_2O	$SF_3^+ + H_2OF^+$	1.7	3
NH_3	$SF_3^+ + NH_3F^+$	1.5	0.4
CH_4	$SF_3^+ + CH_2F^+ + 2H$	1.0	19
C_2H_4	$SF_3^+ + C_2H_2F^+ + 2H$	2.5	3
	$SF_3^+ + C_2H_3F^+ + H$	2.5	1
C_2H_6	$SF_3^+ + C_2H_3F^+ + 3H$	2.6	2

Two representative coincidence spectra that were collected following interactions of SF_4^{2+} with (a) H_2 and (b) CH_4 are shown in Figure 5.1. These spectra clearly show the intense peaks due to detection of SF_3^+ in coincidence with the monocation formed by fluorination of the neutral. Following the reaction of SF_4^{2+} with the organic molecules CH_4, C_2H_4 and C_2H_6, the corresponding, directly fluorinated species were not detected, rather, the nascent CH_4F, C_2H_4F and C_2H_6F ions exhibit some degree of fragmentation yielding CH_2F^+, $C_2H_3F^+$ and $C_2H_2F^+$, and $C_2H_3F^+$ respectively. Dissociation of these nascent ions is likely to be due to the small bond–dissociation energy of the C–H bonds in these types of ions (around 1.7 eV for dissociation of CH_4^+ into CH_3^+ + H), along with the large energy releases associated with dication–neutral reactions.

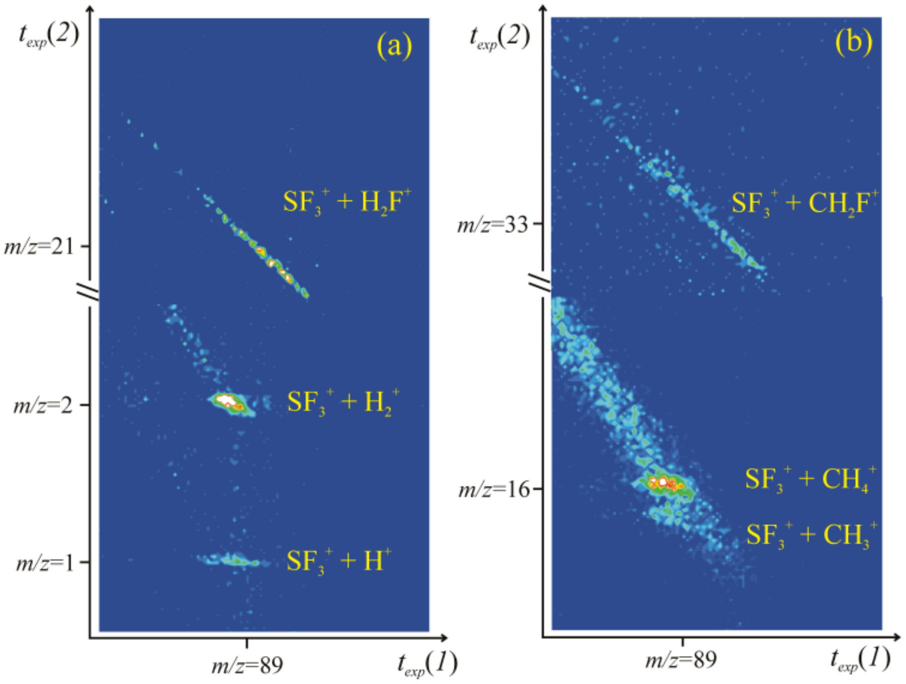

Figure 5.1 Two-dimensional mass spectra showing the ion pairs formed following collisions of SF_4^{2+} with (a) H_2 and (b) CH_4. From ref. [28].

The branching ratios we observe for some of these fluorination reactions, particularly those with Ar, H_2/D_2 and CH_4, are extremely high compared to the branching ratios for bond-formation in dication-neutral reactions that are generally observed. Recent reports of bond-forming chemistry between dications and neutrals include the observation of OCF^+ following collisions of CF_2^{2+} with H_2O[29], $ArCF_2^{2+}$ following collisions of CF_3^{2+} with Ar[30], ArC^+ following collisions of Ar^{2+} with C_2H_2[31] and NH^+ following collisions of N_2^{2+} with H_2[32]. The branching ratios into the OCF^+, $ArCF_2^{2+}$, ArC^+ and NH^+ bond-forming channels in these collision-systems are 0.3 %, 1.0 %, 1.0 % and 1.6 % respectively, which is consistent with bond-formation occurring on no more than around 1 in 100 reactive events at E_{CM} of a few eV. In contrast, following collisions of SF_4^{2+} with D_2, as presented here, bond-formation occurs on almost 1 in 3 reactive events, an exceptionally high proportion. It is particularly interesting to note that in collisions of SF_4^{2+} with CH_4, bond-formation yielding CH_2F^+ occurs on around 1 in 5 reactive events. Such an observation could have profound consequences for the vast field of fluorochemistry, which includes industries such as pharmaceuticals and agrochemicals among many others, as discussed in detail in the introduction to this chapter. Carbon-fluorine bonds are vital for such industries, yet their formation still provides chemists with huge challenges. Here we present a study of gas-phase reactants that exhibit facile formation of C–F bonds; the next challenge will be to transfer this finding to solution to enable the interesting properties of the SF_4^{2+} dication to be exploited effectively for fluorocarbon synthesis.

Price *et al* have studied the reactions of SF_4^{2+} with Xe, D_2, O_2, N_2, NO and CO using crossed–beam TOF spectrometry[24]. Our results corroborate their finding that bond–formation, yielding FCO^+ (or COF^+), is observed between SF_4^{2+} and CO. However, Price and co–workers did not observe bond–formation with any of the other neutral collision partners that they studied, whereas we observe formation of D_2F^+ and N_2F^+ with significant branching ratios. This apparent inconsistency could be explained by several factors. Primarily, the contrasting observations of our work with that of Price *et al* almost certainly arise due to differing collision energies in the two experiments; our experiment used laboratory frame collision energies of roughly 8 eV and that of Price *et al* between 30 and 50 eV. As has been observed before, the cross–sections for chemical channels in bimolecular ion–molecule reactions often decrease rapidly with increasing collision energy and are peaked near zero collision energy[30,33,34].

Sparrapan *et al* have studied the bimolecular reactions occurring following the interaction of SF_4^{2+} with H_2O, CO, CO_2, O_2 and N_2O, although, unlike our study and the experiments of Price *et al*, these interactions were at near zero collision energy[25]. Sparrapan *et al* observed only dissociative SET to form $SF_3^+ + F + X^+$, where X is the neutral collision partner[25]. Rather surprisingly, considering the large branching ratios that we observe, these experiments showed no signal due to any bond–forming processes, whereas we detect H_2OF^+ and FCO^+ products. Such an incongruity cannot be easily explained, apart from by low SF_4^{2+} signals in the quadrupole experiment or, uncharacteristically, cross–sections for the bond–forming channels that decrease dramatically at near zero collision energy. Cross–sections for chemical channels that peak at non–zero collision energy have been observed for both singly–[35] and doubly–charged[36] ion reactions, although this sort of energy dependence is rare.

We have constructed CM frame scattering diagrams for all of the bond–forming reactions detected. Figure 5.2 shows a representative diagram for the SF_3^+ and ArF^+ products from a reaction of SF_4^{2+} with Ar. The scattering diagram in Figure 5.2 clearly shows that the product scattering directions from the bond–forming reactions are isotropic; meaning that the reaction has proceeded via formation of a complex that survives for several rotations. As will be seen later, this is quite different behaviour to the SET reactions. In previous experiments we have observed chemical channels that do not occur *via* formation of a long–lived complex and instead involve a direct "stripping" of a fragment of one of the reactants by the other. Direct transfer of a proton H^+ or a hydride H^- has been observed in several reactions, but we have also seen direct transfer of heavier fragments such as CH^- by both Ar^{2+} and O_2^{2+} in the Ar^{2+} – C_2H_2 and O_2^{2+} – C_2H_2 collision systems respectively. The heaviest fragment that we have observed to be transferred *via* a direct mechanism is O^+, which is rapidly transferred between O_2^{2+} and CO to form O^+ and CO_2^+. The net effect of all of the bond–forming reactions is transfer of an F^+ ion, which is only three atomic mass units heavier than O^+, however, clearly direct transfer of an F^+ would be highly energetically unfavourable. Therefore, it seems that the complexation between the reactants is crucial to allow this reaction pathway to occur.

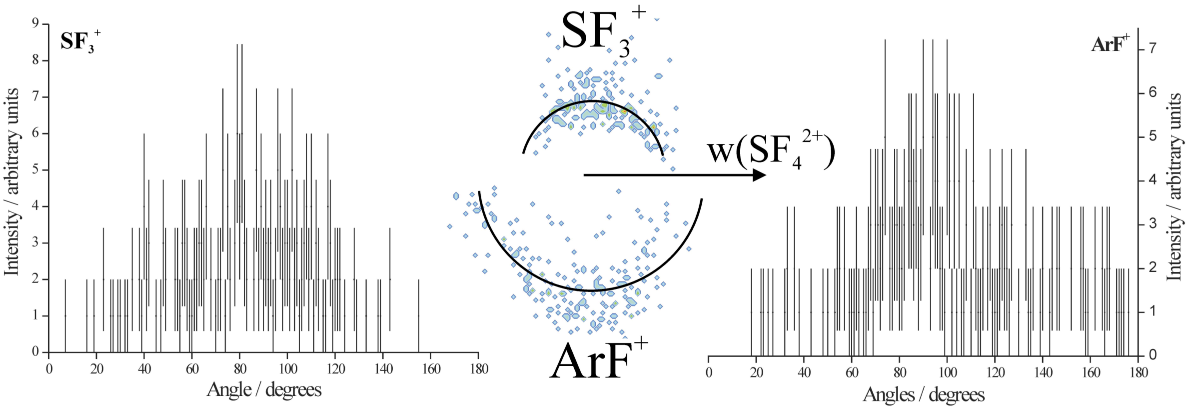

Figure 5.2 CM scattering diagram for the bond–forming channel resulting in SF_3^+ + ArF^+ products, following interaction of SF_4^{2+} with Ar. Also shown are the histograms of scattering angles of the product ions. The vector $w(SF_4^{2+})$ represents the direction of the dication velocity prior to the collision; 0° scattering angle.

5.2.1 Structure Optimisations of the SF_4^{2+} Dication

To try to rationalise the tendency of SF_4^{2+} to form complexes and understand its high propensity to fluorinate neutrals, we have probed the structure of SF_4^{2+} computationally. Stationary points and ionization energies were determined using the Coupled–Cluster method that fully includes singles and doubles, and triples are calculated with a perturbation theory CCSD(T) methodology with an augmented–ccVTZ basis set. We have identified three low lying stable geometries of SF_4^{2+}, the ground singlet state and two metastable excited triplet states as shown in Figure 5.3 along with their double IEs.

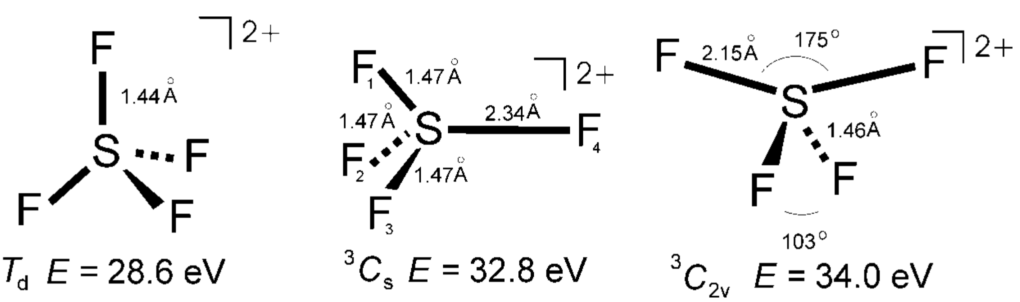

Figure 5.3 Calculated geometries of SF_4^{2+}. The point group of each structure, and their energy relative to the ground state of SF_4, are shown. For the ^3C_s state the bond angles are: $\angle F_1F_2=\angle F_1F_3=\angle F_2F_3=108^\circ$, $\angle F_2F_4=\angle F_3F_4=109^\circ$, $\angle F_1F_4=112^\circ$. From ref. [28].

Our calculations show the electronic ground state of SF_4^{2+} simply has T_d symmetry, but there are two higher lying triplet states that have more unusual geometries of C_s and C_{2v} symmetry. The ^3C_s state lying 32.8 eV higher than ground state SF_4 has one elongated and presumably weaker S–F bond. The fact the SF_4^{2+} dications in our beam readily donate F^+ ions strongly hints that the ^3C_s structure is responsible for fluorination. Indeed the calculations show that the distinct F atom in the ^3C_s structure bears a considerably higher charge (+0.37*e*) than the other fluorine atoms (+0.05*e*). Further to these qualitative arguments, as explained below, the energetics revealed by our experiments strongly point to the ^3C_s state of SF_4^{2+} being the fluorinating agent and a major species in our dication beam.

From the velocities of products of reactions, we derive the energy release of a given reactive process[17]. We detect a reaction between SF_4^{2+} and Ar that forms SF_3^+ +F + Ar^+ and which should involve minimal product vibrational excitation, as two of the products are atoms. The enthalpies of formation ΔH_f of the SF_3^+, Ar^+ and F products are known and the ΔH_f of the reactant Ar is by definition zero. We measure a modal energy release for this dissociative SET process to be 4.6 eV. Thus according to Equation (5.1), we can estimate a ΔH_f for the SF_4^{2+} reactant. The ΔH_f of neutral SF_4 is around –7.96 eV, giving the double IE of our SF_4^{2+} reactants as 32.9 eV, in excellent agreement with the calculated double IE for the ^3C_s state of SF_4^{2+} at 32.8 eV.

$$\Delta H_f\,(\mathrm{SF_4}^{2+}) = \Delta H_f\,(\mathrm{SF_3}^{+}) + \Delta H_f\,(\mathrm{Ar}^{+}) + \Delta H_f\,(\mathrm{F}) - \Delta E_{exp}(-4.6\ \mathrm{eV}) \qquad (5.1)$$
$$= 24.9\ \mathrm{eV}$$

Consequently, there are several pieces of evidence that point towards the excited triplet SF_4^{2+} with a C_s structure being the dominant species in our dication beam. This highly unusual structure with an elongated bond and high partial charge on the distinct F atoms could be a principle reason for the intense fluorination channels we observe with a variety of neutrals. Therefore, unusual structures such as these, and the SF_4^{2+} dication in particular, deserve further investigation in order to explore their potential as fluorinating agents in organic chemistry.

In addition to the chemical channels, each of the fourteen collision–systems that we have studied exhibits at least one dissociative SET channel. Specifically, an electron is transferred from the neutral to the SF_4^{2+}, forming a nascent SF_4^{+}, which fragments into SF_3^{+} + F before reaching the detector. Fisher *et al* have measured the dissociation energy of the SF_3^{+}–F bond to be extremely small, specifically 0.36 ± 0.05 eV[37]. In agreement with the experimental study of Fisher *et al*, several computational studies have also predicted this value to be less than 0.5 eV[38,39]. Thus SF_4^{+} only exists in a very shallow potential well and readily breaks down into SF_3^{+} and F, hence explaining why we observe no SF_4^{+} products following SET with neutrals.

The monocation formed from the neutral dissociates following SET in many of the systems, exceptions are the CO^{+}, CO_2^{+}, N_2^{+}, H_2O^{+} and NH_3^{+} monocations, which do not exhibit any fragmentation. The reason that these monocations, formed by removal of an electron from the neutral collision partner, do not dissociate is related to the bond–dissociation energies for each of these species. These dissociation energies are sufficiently high that breaking a bond of the molecular ion is endothermic for ground state reactants and therefore not within the reaction window for excited triplet state reactants. An exception is fragmentation of the H_2^{+}/D_2^{+} monocation formed by SET with SF_4^{2+}. In these cases, despite the fact that dissociation of the nascent H_2^{+}/D_2^{+} following SET reaction between H_2/D_2 and ground state SF_4^{2+} is endothermic by 2 eV, we still detect H^{+}/D^{+} products following these collisions. The obvious conclusion is that these reactions arise from excited state SF_4^{2+} reactants, most likely the excited triplet state with C_s symmetry that has been proposed as the dominant species in our dication beam.

Collisions with H_2S, NH_3, C_2H_4, C_2H_6 and CH_3OH result in SF_2^+ products from further fragmentation of the nascent SF_4^+. Unfortunately, we cannot measure directly whether the two F atoms produced in addition to SF_2^+ in these dissociative SET reactions are bound as F_2 or in atomic form. However, energetic arguments can help to resolve this uncertainty. Table 5.2 lists the calculated literature exothermicity of the reactions of ground state reactants forming ground state $SF_2^+ + F_2 + X^+$ products (where X = neutral collision partner). From Table 5.2 it is clear that the $SF_2^+ + F_2 + X^+$ channel becomes exothermic by 0.9 eV for $X = H_2O$. However this exothermicity of 0.9 eV is outside the Landau–Zener reaction window of 2–6 eV for which SET is likely. Thus, the Landau–Zener reaction window theory explains why we do not observe SF_2^+ products following SET with H_2O. As the reaction exothermicity increases with decreasing ionisation energy of the neutral, up to $X = NH_3$, the exothermicity moves into the reaction window, explaining why we see SF_2^+ products with $X = C_2H_6$, CH_3OH, C_2H_4, H_2S and NH_3. The Landau–Zener reaction window theory thus readily explains why we observe the branching ratio into this dissociative SET channel to increase with increasing exothermicity. Clearly, this simple explanation for ground state reactants seems to fit well with our experimental data, but we recall that there is evidence that the excited triplet state with double IE of 32.8 eV is the dominant species in our beam. If this were true then it is still possible that the reaction exothermicities for the dissociative SET reactions we observe lie within the reaction window. Specifically, it is expected, and has been shown, that many SET reactions between dications and neutrals generate products with considerable amounts of internal energy. We therefore expect it is highly unlikely that the SF_2^+ product is formed in its ground state; instead we expect there to be a degree of internal energy. This product internal energy effectively “cancels out” the additional energy of the reactants meaning the reaction exothermicity remains within the reaction window. Thus, the SET reactions that are observed between SF_4^{2+} and neutrals also seem to be consistent with a predominantly excited triplet state reactant SF_4^{2+} beam.

Table 5.2 Exothermicity of the reaction $SF_4^{2+} + X \rightarrow SF_2^+ + F_2 + X^+$ for ground state reactants and products. In brackets is shown the branching into the detailed reaction channel as a percentage of all reactivity for that collision system that results in a pair of monocations.

Neutral Species, X	Exothermicity of Reaction Forming Ground State SF_2^+ + F_2 + X^+ / eV (Branching into this channel)	Neutral Species, X	Exothermicity of Reaction forming Ground State SF_2^+ + F_2 + X^+ / eV (Branching into this channel)
Ar	+2.3 (0)	H_2O	–0.9 (0)
N_2	+2.1 (0)	CH_4	–0.9 (0)
D_2	+1.9 (0)	C_2H_6	–2.0 (9.6)
H_2	+1.9 (0)	CH_3OH	–2.7 (11.9)
CO	+0.5 (0)	C_2H_4	–3.0 (26.3)
CHF_3	+0.4 (0)	H_2S	–3.1 (29.5)
CO_2	+0.3 (0)	NH_3	–3.4 (25.8)

Scattering diagrams in the CM frame have been constructed for the dissociative SET reactions forming SF_3^+ + F + X^+ for each collision system. A representative selection of these diagrams, along with a histogram of the scattering angles of each product ion, can be seen in Figure 5.4. The vector $w(SF_4^{2+})$ indicates the direction of travel of the reactant dication in the CM frame prior to the collision; the neutral is moving in the opposite direction to the dication. For contrast, Figure 5.4 also shows the CM frame scattering diagram and integrated angular histograms for the dissociative single electron–transfer between O_2^{2+} and CO_2 to form O_2^+ (from addition of an electron to the dication) + CO^+ + O. The O_2^+ and CO^+ products from the ET reaction between O_2^{2+} and CO_2 exhibit very strong forward scattering, to very low and high angles respectively. Such scattering implies that the SET occurred at a large interspecies separation and more importantly that little or no complexation between the reactants has occurred. As is clear from Figure 5.4, this strong forward scattering is clearly not observed in dissociative SET reactions of SF_4^{2+} with neutrals. The scattering directions of both the SF_3^+ and the X^+ are weakly peaked in the directions of their respective precursors. However, there is a strong component of the scattering of both ionic products that extends more evenly over a wider range of scattering angles.

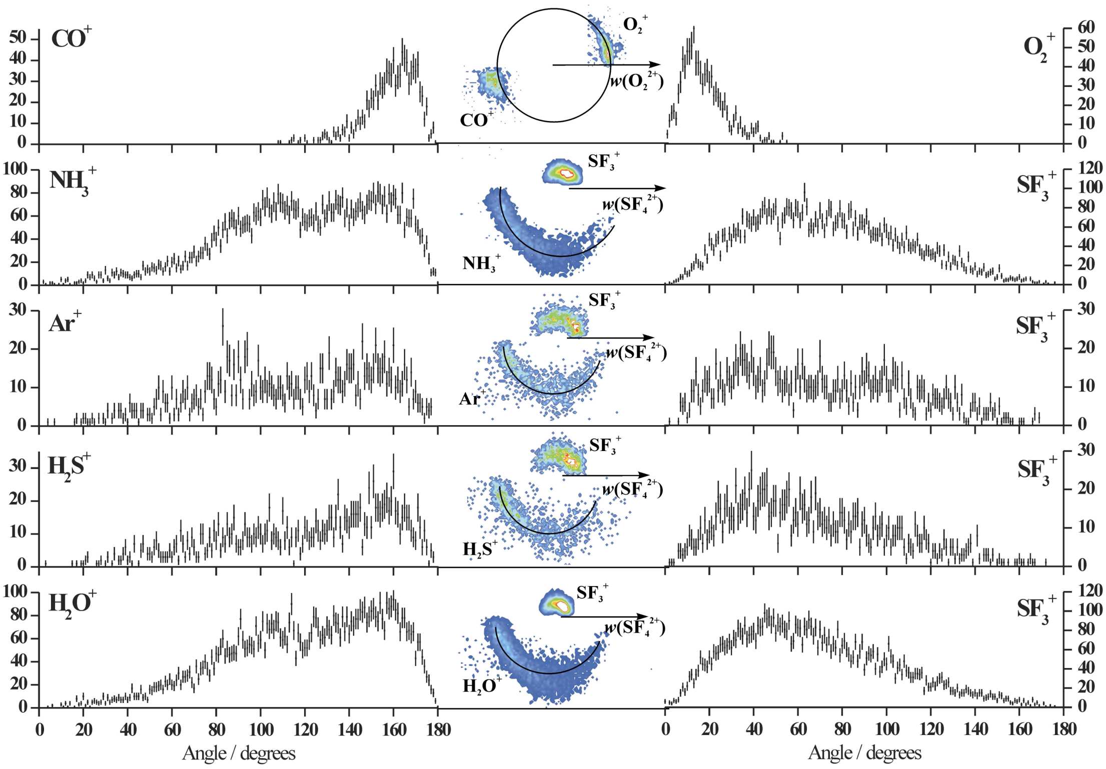

Figure 5.4 The lower four panels show the CM scattering for the dissociative single electron-transfer reactions forming SF_3^+ + F + X^+. The vector $w(SF_4^{2+})$ shows the direction of the reactant dication prior to the collision, in the CM frame. For comparison, the topmost panel shows the CM scattering of the O_2^+ and CO^+ products of dissociative single electron-transfer between O_2^{2+} and CO_2, where the vector $w(O_2^{2+})$ shows the direction of the reactant dication prior to the collision (see text for details). Alongside each CM frame scattering diagram are histograms of the scattering angles of each product ion, where scattering towards 0° is in the same direction as the reactant dication prior to the collision, in the CM frame. Scattering towards 180° is in the direction of the reactant neutral prior to the collision, in the CM frame.

The SF_3^+ product scattering angles that are *weakly* peaked in the direction of the reactants prior to the collision, such as those in Figure 5.4, imply that the dissociative SET reactions of SF_4^{2+} with neutral species proceed *via* the formation of a short-lived complex between the reactants. We conclude that the complex is very short-lived as it is formed and then dissociates to the detected products before several complete rotations can take place. The result of this rapid fragmentation of the encounter complex is that there is still a degree of correlation between the scattering directions of the products with the direction of their respective reactant precursors prior to the collision, in the CM frame. Such a mechanism is unusual as this class of reaction generally exhibit strong forward scattering[17,27,31,40–43]. The same broad scattering angles of the ionic products are observed in the reactions forming SF_3^+ + F + X^+ for every X studied, thus implying it is a property of the SF_4^{2+} which contributes most strongly to the lifetime of the encounter complex. As is evident from the scattering of the products seen in Figure 5.2 and Figure 5.4, the complex formed between the SF_4^{2+} and neutral that results in net "F^+ transfer" survives longer than the complex formed resulting in net electron transfer. Tautologically, the different reactivity may be due to the different lifetimes of the complex, that is, if the encounter complex only lives for less than a rotational period then there is only sufficient time to transfer an electron and not an F^+. Conversely, if the complex survives longer than a rotation, then the net result of the interaction will be F^+ transfer. It also seems clear that SF_4^{2+} readily forms an encounter complex with almost any neutral reactant.

5.3 Conclusion

A study of the reactivity of the SF_4^{2+} ion with Ar, H_2, D_2, CO, CO_2, N_2, H_2O, H_2S, NH_3, CH_4, C_2H_4, C_2H_6, CH_3OH and CHF_3 has been carried out at low collision energies in the CM frame. We observe both SET and chemical reactive channels, the former dominate the chemistry; however, the bond–forming channels have unprecedented high branching ratios. Indeed, the D_2F^+ forming channel that we observe following the interaction of SF_4^{2+} and D_2 is formed on nearly 1 in 3 collisions that result in a pair of monocations. Our methodology allows us to determine the scattering dynamics of each reaction channel and hence determine that the electron–transfer channel proceeds *via* the formation of a very short–lived complex. The chemical channels proceed *via* a reaction complex that has a lifetime longer than several of its rotational periods. These reactions of SF_4^{2+} that we have recorded, and the branching rations into each channel, will extend our understanding of dication–neutral reactivity. In addition, fast and efficient formation of C–F bonds is demonstrated, suggesting that dications or at least an analogue of SF_4^{2+} in solution could be used in synthesis of fluorocarbons. Computational methods have been employed to identify three low lying metastable electronic states of SF_4^{2+}. It is proposed that the triplet state of C_s symmetry may be the principle state in our beam and is responsible for the high fluorination propensity of the SF_4^{2+} dication.

5.4 References

[1] Christophorou, L G, Olthoff, J K and VanBrunt, R J *IEEE Electr. Insul. Mag.* **1997**, *13*, 20–24.

[2] Tessier, P Y, Chevolleau, T, Cardinaud, C and Grolleau, B *Nucl. Instrum. Methods Phys. Res. Sect. B–Beam Interact. Mater. Atoms* **1999**, *155*, 280–288.

[3] Bjornsen, G, Henriksen, L, Ulvensoen, J H and Roots, J *Microelectron. Eng. 87*, 67–71.

[4] Kokkoris, G, Panagiotopoulos, A, Goodyear, A, Cooke, M and Gogolides, E *J. Phys. D–Appl. Phys.* **2009**, *42*, 15.

[5] Tarnovsky, V, Deutsch, H, Martus, K E and Becker, K *J. Chem. Phys.* **1998**, *109*, 6596–6600.

[6] Pihko, P M *Angew. Chem.–Int. Edit.* **2006**, *45*, 544–547.

[7] Muller, K, Faeh, C and Diederich, F *Science* **2007**, *317*, 1881–1886.

[8] Park, B K, Kitteringham, N R and O'Neill, P M *Annu. Rev. Pharmacol. Toxicol.* **2001**, *41*, 443–470.

[9] Jeschke, P *ChemBioChem* **2004**, *5*, 570–589.

[10] Brunet, V A and O'Hagan, D *Angew. Chem.–Int. Edit.* **2008**, *47*, 1179–1182.

[11] Sun, H and DiMagno, S G *Angew. Chem.–Int. Edit.* **2006**, *45*, 2720–2725.

[12] Steiner, D D, Mase, N and Barbas, C F *Angew. Chem.–Int. Edit.* **2005**, *44*, 3706-3710.

[13] Shimizu, M and Hiyama, T *Angew. Chem.–Int. Edit.* **2005**, *44*, 214–231.

[14] Rozen, S *Acc. Chem.Res.* **1996**, *29*, 243–248.

[15] Gozzo, F C, Ifa, D R and Eberlin, M N *J. Org. Chem.* **2000**, *65*, 3920–3925.

[16] Cipollini, R, Crestoni, M E and Fornarini, S *J. Am. Chem. Soc.* **1997**, *119*, 9499–9503.

[17] Price, S D *Int. J. Mass Spec.* **2007**, *260*, 1–19.

[18] Schröder, D and Schwarz, H *Journal of Physical Chemistry A* **1999**, *103*, 7385-7394.

[19] Dietl, N, Engeser, M and Schwarz, H *Angew. Chem. Int. Ed.* **2009**, *48*, 4861-4863.

[20] Roithová, J and Schröder, D **2009**, *48*, 8788–8790.

[21] Sturges, W T, Wallington, T J, Hurley, M D, Shine, K P, Sihra, K, Engel, A, Oram, D E, Penkett, S A, Mulvaney, R and Brenninkmeijer, C A M *Science* **2000**, *289*, 611–613.

[22] Maiss, M and Brenninkmeijer, C A M *Environ. Sci. Technol.* **1998**, *32*, 3077-3086.

[23] Huang, L, Shen, Y, Dong, W B, Zhang, R X, Zhang, J L and Hou, H Q *J. Hazard. Mater.* **2008**, *151*, 323–330.

[24] Price, S D, Manning, M and Leone, S R *J. Am. Chem. Soc.* **1994**, *116*, 8673-8680.

[25] Sparrapan, R, Mendes, M A, Ferreira, I P P, Eberlin, M N, Santos, C and Nogueira, J C *J. Phys. Chem. A* **1998**, *102*, 5189–5195.

[26] Feketeova, L, Grill, V, Zappa, F, Endstrasser, N, Rasul, B, Herman, Z, Scheier, P and Mark, T D *Int. J. Mass Spectrom.* **2008**, *276*, 37–42.

[27] Mrazek, L, Zabka, J, Dolejsek, Z, Hrusak, J and Herman, Z *J. Phys. Chem. A* **2000**, *104*, 7294–7303.

[28] Lockyear, J F, Parkes, M A and Price, S D *Angew. Chem.–Int. Edit.* **2011**, *50*, 1322–1324.

[29] Harper, S M, Hu, S W P and Price, S D *J. Chem. Phys.* **2004**, *121*, 3507–3514.

[30] Lockyear, J F, Douglas, K, Price, S D, Karwowska, M, Fijalkowski, K J, Grochala, W, Remes, M, Roithova, J and Schroder, D *J. Phys. Chem. Lett.* **2010**, *1*, 358-362.

[31] Parkes, M A, Lockyear, J F and Price, S D *Int. J. Mass Spectrom.* **2009**, *280*, 85-92.

[32] Lockyear, J F, Ricketts, C L, Parkes, M A and Price, S D *Chem. Sci. 2*, 150–156.

[33] Roithova, J, Ricketts, C L, Schroeder, D and Price, S D *Ange. Chem.–Int. Ed.* **2007**, *46*, 9316–9319.

[34] Ascenzi, D, Tosi, P, Roithova, J, Ricketts, C L, Schroeder, D, Lockyear, J F, Parkes, M A and Price, S D *Phys. Chem. Chem. Phys.* **2008**, *10*, 7121–7128.

[35] Di Stefano, M, Rosi, M, Sgamellotti, A, Ascenzi, D, Bassi, D, Franceschi, P and Tosi, P *J. Chem. Phys.* **2003**, *119*, 1978–1985.

[36] Ascenzi, D, Franceschi, P, Tosi, P, Bassi, D, Kaczorowska, M and Harvey, J N *J. Chem. Phys.* **2003**, *118*, 2159–2163.

[37] Fisher, E R, Kickel, B L and Armentrout, P B *J. Chem. Phys.* **1992**, *97*, 4859-4870.

[38] Irikura, K K *J. Chem. Phys.* **1995**, *102*, 5357–5367.

[39] Bauschlicher, C W and Ricca, A *J. Phys. Chem. A* **1998**, *102*, 4722–4727.

[40] Herman, Z *Int. Rev. Phys. Chem.* **1996**, *15*, 299–324.

[41] Harper, S M, Hu, W P and Price, S D *J. Phys. B* **2002**, *35*, 4409–4423.

[42] Hu, W P, Harper, S M and Price, S D *Mol. Phys.* **2005**, *103*, 1809–1819.

[43] Jasik, J, Roithova, J, Zabka, J, Thissen, R, Ipolyi, I and Herman, Z *Int. J. Mass Spectrom.* **2006**, *255*, 150–163.

Chapter 6: $C_2H_2^{2+}$ + Ar and Ar^{2+} + C_2H_2

6.1 Introduction

In 1990, *ab initio* calculations were reported by Frenking *et al* in which they predicted the existence of a series of novel compounds of the rare–gases (Rg)[1]. Some of these "exotic species" are based upon acetylenic subunits. Specifically, $Rg{-}C{\equiv}C{-}H^+$ as well as $Rg{-}C{\equiv}C{-}Rg^{2+}$ are predicted to exist as stable or metastable species in the gas phase, even for Rg = He, despite the inertness of the lightest rare gas. Compounds of xenon with unsaturated hydrocarbons, including acetylene, have been prepared as neutral species by low–temperature photolysis of hydrocarbon–doped rare–gas matrices. Using this methodology, the organo–xenon derivatives HXeC≡CH, HXeCC, and HXeC≡CXeH have been synthesized[2-4]. Similar techniques have been employed to produce insertion compounds of acetylene, diacetylene, and cyanoacetylene with xenon and krypton, specifically HKrC≡CH[5], HRgC≡C–C≡CH (Rg = Kr, Xe)[6] and HRgC≡C–CN (Rg = Kr, Xe)[7]. Synthesis of HXeC≡CH has even been achieved in the gas phase by photolysis of an acetylene molecule on a xenon cluster[8]. In this gas–phase study by Poterya *et al*, it is noted that they did not detect the corresponding acetylene argon compound. Due to their lower polarisability, the lighter rare gases argon, neon and helium are less prone to form chemical bonds than krypton or xenon. Nonetheless, theoretical investigations[9,10] have predicted the existence of a whole series of organo–argon compounds such as FArCCH[11,12] and $HArC_4H$[13]. Despite these theoretical predictions, to the best of our knowledge, none of these rare–gas acetylene compounds has been detected before for the lighter noble gases (He, Ne, and Ar)[14,15]. Recently, however, the fluoro–organo–argon dication $ArCF_2^{2+}$ was detected following thermal collisions of CF_3^{2+} with Ar in a quadrupole MS experiment[16]. Interestingly, it was found that among the rare gases it was only following interaction of CF_3^{2+} with argon that this chemical channel was observed. The lighter rare gases, neon and helium, exhibited no reaction and the only products following collisions with the heavier rare gases were due to SET.

Gas–phase ion–molecule reactions offer a unique environment for formation of this unusual class of acetylenic–rare–gas compounds. Dications are highly energetic and also can be easily manipulated using electrostatic lenses, thus allowing access to hyperthermal collision energies. Also, the low pressures maintained in mass spectrometers decrease the propensity for secondary reactions, such that even energetic species will survive for relatively long times, provided they exist in a sufficiently deep potential–energy minimum. Of course the generation of a novel reaction product in the gas phase does not necessarily mean it will be possible to isolate a similar compound in the condensed phase.

In light of the above, and motivated by the intriguing possibility of the formation of new argon–acetylene compounds, investigations of the reactivity of $C_2H_2^{2+}$ with Ar and the inverted case of Ar^{2+} with C_2H_2 were undertaken. It has been proposed that the exchange of the double charge from one reactant to the other should essentially make no difference to the reactivity as the doubly charged $[Ar – C_2H_2]^{2+}$ encounter intermediate should be the same. Therefore, one of our motivations is to experimentally investigate this hypothesis. It is interesting to ascertain whether formation of new chemical bonds, and ultimately these organo–rare–gas ions, in dication–neutral collisions is dependent on the charged state of the reactants. The $C_2H_2^{2+}$ + Ar collision system was studied employing the PSCO technique and also by the complementary techniques of octopole–quadrupole–octopole–quadrupole (OQOQ) spectrometry and using a TSQ mass spectrometer that has a QOQ configuration. These latter two experiments were carried out by collaborators at laboratories in Italy and the Czech Republic, respectively. For completeness this chapter will briefly describe the results our collaborators have obtained using the OQOQ and TSQ spectrometers for the $C_2H_2^{2+}$ – Ar collision system, followed by a more detailed description of results obtained for both the $C_2H_2^{2+}$ – Ar and Ar^{2+} – C_2H_2 systems employing the PSCO MS at UCL.

6.2 $C_2H_2^{2+}$ + Ar

The $C_2H_2^{2+}$ – Ar system was studied employing three different, complimentary, techniques including using the PSCO, as described above. A brief description of the OQOQ and TSQ mass spectrometers will now be given.

6.2.1 Octopole–Quadrupole–Octopole–Quadrupole

The OQOQ in Trento, Italy, is a home–built guided–ion beam mass spectrometer with an OQOQ configuration[17]. Reactant $C_2H_2^{2+}$ ions were generated by electron ionization of acetylene at energies of 70 – 100 eV. The first octopole O1 is operated as an ion guide. The quadrupole Q1 acts as a mass filter to select the parent dication $C_2H_2^{2+}$ at m/z = 13.0, together with the isobaric monocation CH^+. Parent ions are injected into O2 which is surrounded by a scattering cell filled with the desired neutral reactant. The kinetic energy of the ion–beam, which determines the collision energy between the parent ions and rare gas atoms, can be varied from about 0 to 100 eV by changing the bias potential of O2. Product ions are mass analyzed by Q2 and detected by an electron multiplier.

6.2.2 TSQ Mass Spectrometer (Quadrupole–Octopole–Quadrupole)

The TSQ mass spectrometer in Prague, Czech Republic, is a commercial machine with an exchangeable ion source and a QOQ configuration[18]. The precursor dications C_2HD^{2+} were generated by electron ionisation of HCCD, and mass–selected using Q1 at a mass resolution sufficient to separate C_2HD^{2+} (m/z = 13.5) from $CH^+/C_2H_2^{2+}$ (m/z = 13.0) and $CD^+/CH_2^+/C_2D_2^{2+}/N^+$ (m/z = 14.0). The C_2HD^{2+} ions were then allowed to interact with argon at variable collision energies in the octopole collision cell under predominantly single–collision conditions. The product masses were then scanned using Q2.

6.2.3 Summary of Results from OQOQ and TSQ Experiments[19]

As for most molecular dications, we expect the reactions of $C_2H_2^{2+}$ with a neutral to be dominated by SET[16,20-32]. Furthermore, the hydrogen–containing molecular dication $C_2H_2^{2+}$ is likely to undergo efficient proton transfer to neutral reagents. Thus, depending on their thermochemical properties, reactions (6.1) – (6.3) are expected to occur with rare gases Rg:

$$C_2H_2^{2+} + Rg \rightarrow C_2H_2^{+} + Rg^{+} \qquad (6.1)$$

$$C_2H_2^{2+} + Rg \rightarrow C_2H^{+} + H + Rg^{+} \qquad (6.2)$$

$$C_2H_2^{2+} + Rg \rightarrow C_2H^{+} + RgH^{+} \qquad (6.3)$$

Where reaction (6.1) is non–dissociative SET, reaction (6.2) is dissociative SET and reaction (6.3) is proton transfer (PT). Indeed, reactions (6.1) – (6.3) were detected in the OQOQ and TSQ experiments[19]. A mass spectrum collected following collisions of $C_2H_2^{2+}$ with Ar at E_{CM} of 4.5 eV employing the OQOQ apparatus is shown in Figure 6.1.

A mass spectrum recorded following collisions of C_2HD^{2+} with Ar using the TSQ apparatus at E_{CM} of 4.0 eV is shown in Figure 6.2.

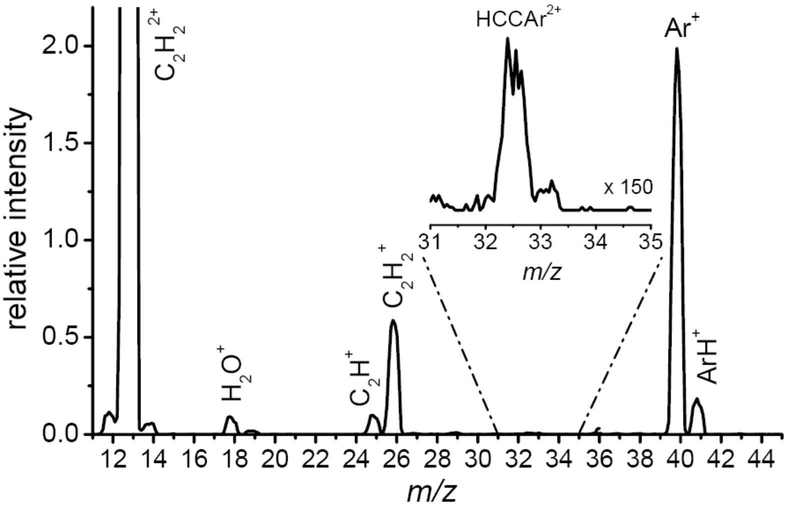

Figure 6.1 Mass spectrum recorded following $C_2H_2^{2+}$ – Ar interactions at E_{CM} of 4.5 eV, recorded on the OQOQ apparatus. From ref. [19].

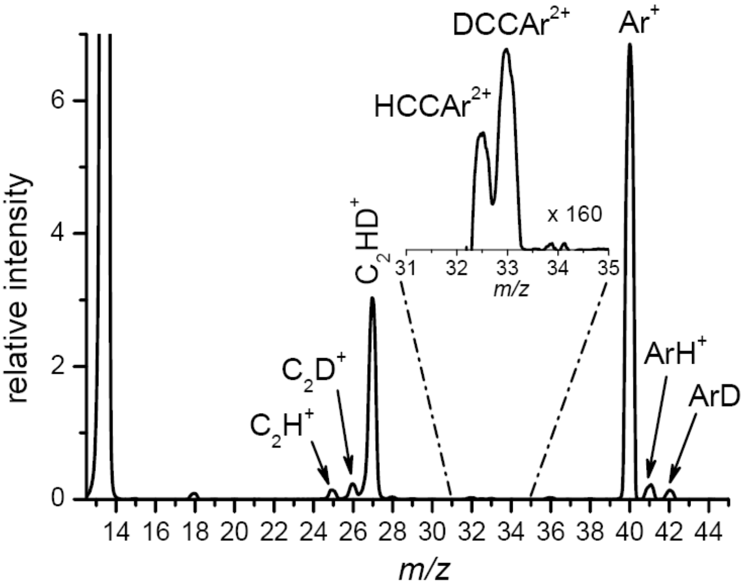

Figure 6.2 Mass spectrum recorded following C_2HD^{2+} – Ar interactions at E_{CM} of 4.0 eV, recorded on the TSQ spectrometer. From ref. [19].

As is clear from the mass spectra shown in Figure 6.1 and Figure 6.2, $C_2H_2^{2+}$ reacts with Ar to give $HCCAr^{2+}$ and C_2HD^{2+} with Ar to give $HCCAr^{2+}$ and $DCCAr^{2+}$ products. These product dications are due to a chemical reaction with maintenance of the two–fold charge, reaction (6.4).

$$C_2H_2^{2+} + Ar \rightarrow HCCAr^{2+} + H \qquad (6.4)$$

Note that the C_2H^+ products detected in the OQOQ and TSQ experiments can arise from both dissociative SET and proton transfer. The simple one–dimensional spectra recorded employing the OQOQ and TSQ spectrometers cannot unambiguously distinguish the products from these channels. Relative ion abundances of C_2H^+ and ArH^+ can give a fairly accurate indication of the branching into the dissociative SET and proton transfer channels. Thus, an estimation of the branching ratio can be made at each E_{CM} measured (between 0 eV and approximately 9 eV). At E_{CM} of 4.5 eV the branching into the SET, dissociative SET and proton transfer relative to the SET channel is 100 : 6 : 10.

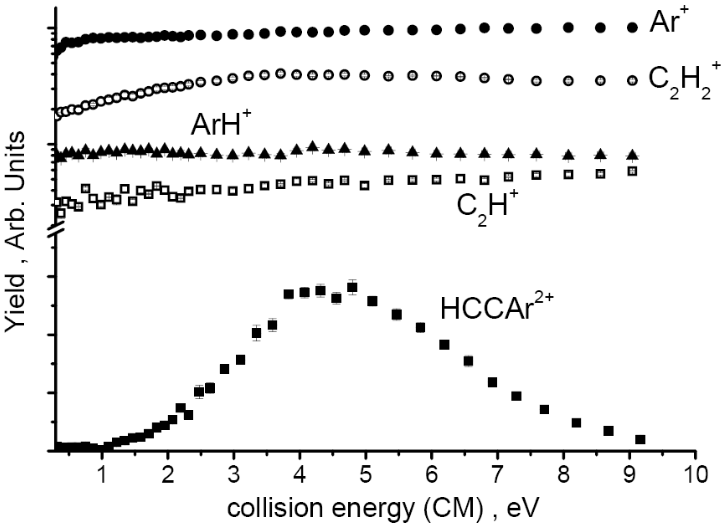

Figure 6.3 Ion yields of all of the observed product ions following interaction of $C_2H_2^{2+}$ with Ar at a range of E_{CM} between 0 and 9 eV. From ref. [19].

The ion yields from SET, dissociative SET, and proton transfer are almost independent of the collision energy, see Figure 6.3. However, the ion yield from the bond–forming reaction (6.4) shows a maximum at E_{CM} = 4.5 eV. Figure 6.3 also shows an apparent threshold of 1.4 ± 0.4 eV associated with the bond–forming process, indicating that this is an endothermic reaction pathway. Due to the fact that the experimental method makes no attempt to control the internal energy content of the acetylene dication, we refrain from a more detailed analysis of the threshold behaviour.

6.2.4 Results from experiments with the PSCO

The next section will describe the results we obtained when the $C_2H_2^{2+}$ – Ar collision system was investigated using PSCO MS. As the PSCO methodology employs coincidence detection, the $HCCAr^{2+}$ product that was detected in the OQOQ and TSQ experiments will not produce a peak in our pairs spectra following interactions of $C_2H_2^{2+}$ with Ar. However, the PSCO technique is complementary to the quadrupole studies, as alluded to before, as ion yield contributions from the dissociative SET and proton transfer channels can be separated. Moreover, our capability to disentangle the dynamics of dication–neutral reactions means we can deduce whether any of the reaction channels proceed *via* formation, and dissociation, of a dicationic complex; a candidate for such a complex could be the $HCCAr^{2+}$ dication. The distinct peaks in the PSCO pairs spectra allow us to examine the branching into each reaction channel, along with the dynamics, independently. What is more, reactions of the isobaric CH^+ ion, which is transmitted to the reaction region along with the $C_2H_2^{2+}$, will not result in pairs of ions and so will not affect the $C_2H_2^{2+}$ – Ar data.

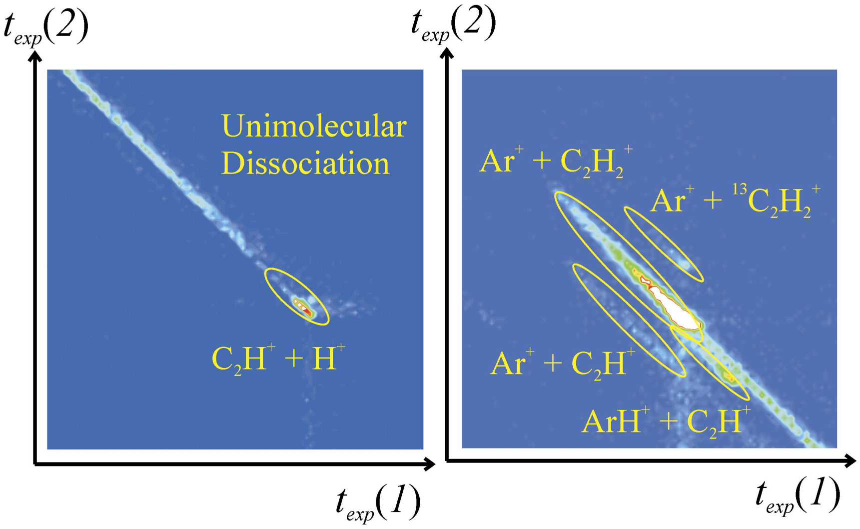

Figure 6.4 Insets from the pairs spectrum collected following interaction of $C_2H_2^{2+}$ with Ar at E_{CM} of 8.5 eV; these sections clearly show the five peaks we observe in the pairs spectrum. 300 V was applied to the repeller plate.

The reaction of the acetylene dication with argon has been studied using the PSCO spectrometer at a range of collision energies between 1.45 and 10 eV. Figure 6.4 shows a representative pairs spectrum collected following interaction of $C_2H_2^{2+}$ with Ar at E_{CM} of 8.5 eV. As is clear from Figure 6.4, we identify five peaks in the spectrum, these are due to reactions (6.1) – (6.3) in addition to an isotopically substituted SET channel (Equation (6.5)) and a unimolecular dissociation (Equation (6.6)).

$$^{13}CH^{12}CH^{2+} + Ar \rightarrow {}^{13}CH^{12}CH^{+} + Ar^{+} \tag{6.5}$$

$$C_2H_2^{2+} \rightarrow C_2H^{+} + H^{+} \tag{6.6}$$

By collection of a data set where no Ar was introduced to the reaction region, we have verified that reaction (6.6) is indeed due to unimolecular dissociation, as opposed to collision–induced dissociation. For collisions at E_{CM} of 4.2 eV, we measure a ratio between the SET, dissociative SET and proton transfer channels of 100 : 4.6 : 10 respectively. Such branching is consistent with that measured using the OQOQ experiment of 100 : 6 : 10 at E_{CM} of 4.5 eV.

In Figure 6.5 we present the intensity of reactions (6.2) and (6.3) relative to the intensity of reaction (6.1) over the range of E_{CM} studied. The intensity of the SET channel is set to 100 for each data set collected and is off the scale in Figure 6.5. The relative intensity of the proton transfer channel remains fairly constant at around 10 relative to reaction (6.1) over the range of E_{CM} studied, although there may be a slight decrease in the branching into this channel at higher collision energy. However, it seems fairly clear that the relative intensity of the dissociative SET channel increases with increasing E_{CM}. Patently, at higher E_{CM} the SET process populates one or a cluster of states of $C_2H_2^{+*}$ that may be either directly repulsive or pre–dissociated. A more detailed discussion of the specific states that are implicated is included in the discussion of the exothermicity that we calculate for this channel.

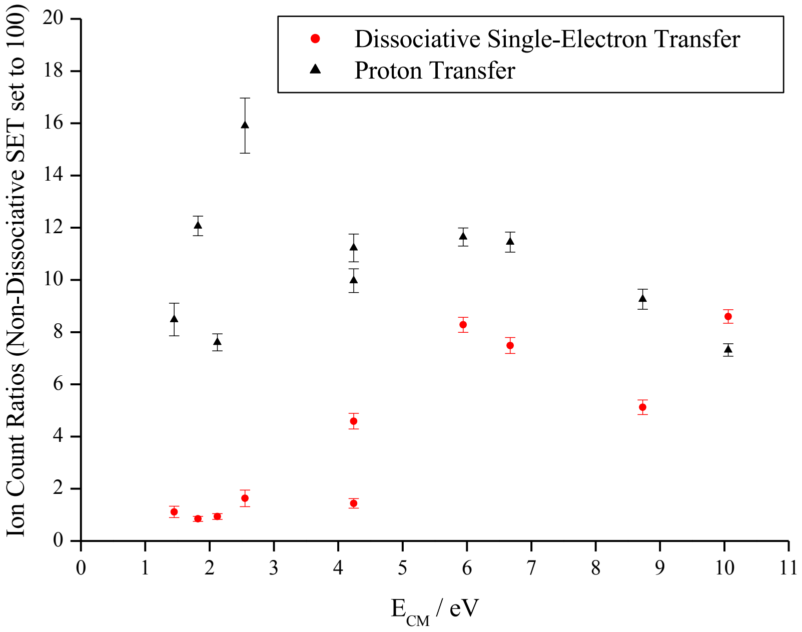

Figure 6.5 Branching ratios into each of the single electron transfer (SET), dissociative SET and proton transfer channels as a percentage of the sum of the pairs in all three channels.

6.2.4.1 Dynamics of the SET, Dissociative SET and Proton Transfer Channels

Figure 6.6 shows representative scattering diagrams derived from the PSCO experiments for reactions (6.1) – (6.3). As typically observed for dication SET reactions, the PSCO data in Figure 6.6 (a) reveal a marked anisotropy of the scattering directions of the $C_2H_2^+$ and Ar^+ products, this is typical of a direct process with strong forward-scattering. The corresponding diagrams for reactions (6.2) and (6.3), shown in Figure 6.6 (b) and (c), also exhibit this strong forward scattering. Hence, it appears that for both of these channels a direct mechanism is taking place with little complexation of the reactants. In the case of reaction (6.2), the scattering can be interpreted as due to a two-step reaction mechanism consisting of SET followed by the dissociation of $C_2H_2^{+*}$. This conclusion is confirmed by the scattering relationships revealed in the internal frame scattering diagrams for reaction (6.2). For reaction (6.3), there is a single reaction step, which is the "stripping" of a proton H^+ by the Ar at significant interspecies separation.

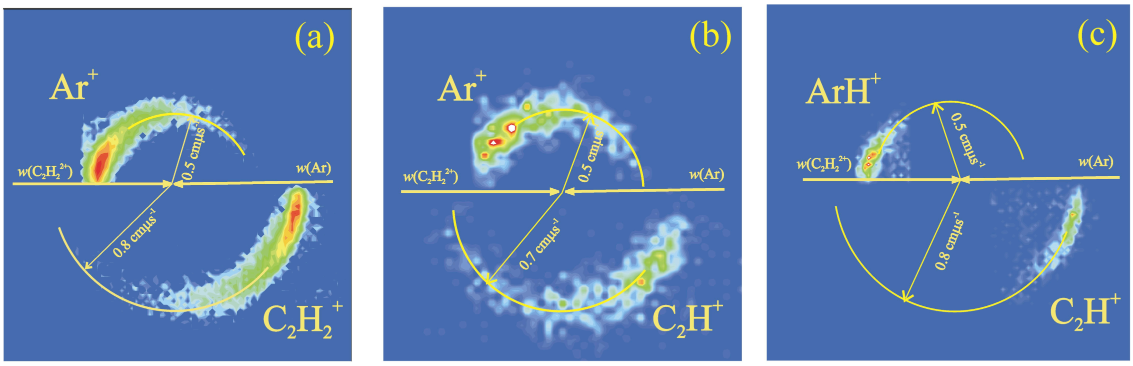

Figure 6.6 Representative scattering diagrams for the (a) single electron transfer (SET) (b) dissociative SET and (c) proton transfer channels following interaction of $C_2H_2^{2+}$ with Ar at E_{CM} of 10 eV. All of these data were collected using a high repeller plate voltage of 300 V. The directions of the reactant $C_2H_2^{2+}$ and Ar prior to the collision are indicated by the full-headed arrows.

The characteristic forward scattering for all the of reaction channels (6.1) – (6.3), Figure 6.6, confirms that the C_2H^+, Ar^+ and ArH^+ produced in reactions (6.2) and (6.3) are not formed by dissociation of the $HCCAr^{2+}$ dicationic complex that was detected in the quadrupole studies. If these product ions were formed by fragmentation of an $HCCAr^{2+}$ intermediate, we would expect the scattering angles of the products to be isotropic with respect to the directions of the reactants prior to the collision, as has been observed before[27,33-35]. Consequently, using the PSCO we can disentangle the contribution to the ion yields from the different reactions (6.1) – (6.4) and conclude that the C_2H^+, Ar^+ or ArH^+ product ions do not arise from fragmentation of a 'long–lived' complex such as $HCCAr^{2+}$.

6.2.4.2 Exothermicities of Reactions (6.1) – (6.3)

Further analysis of the coincidence data for the individual channels allows the determination of the KERs and thus translational exothermicities associated with reactions (6.1) – (6.3) from the product's velocities. For reactions (6.1) – (6.3), these experimental exothermicity distributions are peaked at −4.4, −4.5 and −4.3 eV with widths of 2, 7 and 3 eV, respectively. Literature values for the ground state exothermicities $\Delta_r H$ for reactions (6.1) – (6.3) are −4.6 eV, +1.4 and −4.6 eV[36-38]. Therefore, due to the close agreement of the experimental and literature exothermicities, it is clear that in the SET reaction the product ions are formed in their ground electronic states. The discrepancy of 0.2 eV between the experimental and literature values for reaction (6.1) can easily be accommodated as rovibrational excitation in the $C_2H_2^+$ ion. We can exclude the possibility of forming the first excited electronic state of $C_2H_2^+$ as this would result in an exothermicity of approximately +0.6 eV from ground state reactants[39]. Similarly, the close agreement of the experimental and literature exothermicities for the proton transfer channel shows that the product ions are formed in their ground electronic states. Excited electronic states of the C_2H^+ and ArH^+ lie significantly higher in energy and so are not formed in the PT reaction[40].

The widths of the experimental exothermicity distributions result, predominantly, from the range of internal excitation of both the reactant dications and the product ions. The observed widths of 2 – 3 eV for reactions (6.1) and (6.3) indicate that the reactant dications may contain up to 1.5 eV of internal energy. Such a level of excitation, in principle, allows for the presence of the first electronically excited state of $C_2H_2^{2+}$ in the beam[41]. However, since the modal exothermicity corresponds to a reaction of the ground electronic state, this first excited dication state is clearly a minor component of the reactant beam. Higher electronically excited states which do not take part in the SET or proton transfer reactions may still be present in the dication beam, as discussed below. The widths of the experimental exothermicity distributions further indicate that the extent of rovibrational excitation of the molecular products of reactions (6.1) and (6.3) is low, and certainly less than 2 eV.

The dissociative SET channel is nominally endothermic for ground–state species by 1.4 eV. However, experimentally we measure that the events comprising the reaction (6.2) channel are on average exothermic by 4.5 eV. Assuming that the reaction forms ground–state products, the experimental exothermicity thus indicates the involvement of an electronically excited state of $C_2H_2^{2+}$ lying around 5 eV higher in energy than the $X^3\Sigma^-_g$ ground state[41]. This energy corresponds well with a group of excited electronic states of $C_2H_2^{2+}$, several of which have potential–energy minima[42]. Thus, it seems clear that reaction (6.2), unlike (6.1) and (6.3), is due to the reaction of electronically excited $C_2H_2^{2+}$ present in our dication beam. This excited dication state does not react with Ar to form ground state products in the SET channel because the large (9–10 eV) exothermicity for this process places the relevant curve crossing outside the Landau–Zener reaction window[31,43,44]. It is likely that the initial SET reaction populates a bound state of the product $C_2H_2^+$ that is pre–dissociated by a crossing with a purely repulsive state. In particular, we suggest that the pre–dissociated $A^2\Sigma_g^+$ state of $C_2H_2^+$ is formed, as this state is known to dissociate to C_2H^+ and H[45].

6.3 $Ar^{2+} + C_2H_2$

In order to investigate if the arrangement of the double charges makes a difference to the reactivity, we have studied the Ar^{2+} – C_2H_2 collision system, so the dicationic reactant is now the argon. In contrast to the $C_2H_2^{2+}$ – Ar system, the Ar^{2+} – C_2H_2 system has only been studied employing the PSCO methodology[46] and at a range of E_{CM} from 1.2 to 7.1 eV. An overview of the results from these experiments will be given in this section. Fifteen different reaction channels generating pairs of monocations have been observed, these channels arise from double–electron transfer, single–electron transfer and chemical reactions; a representative pairs spectrum is shown in Figure 6.7. Preliminary inspection of these spectra clearly reveals that reacting Ar^{2+} with C_2H_2 results in very different chemistry to the reaction of $C_2H_2^{2+}$ with Ar.

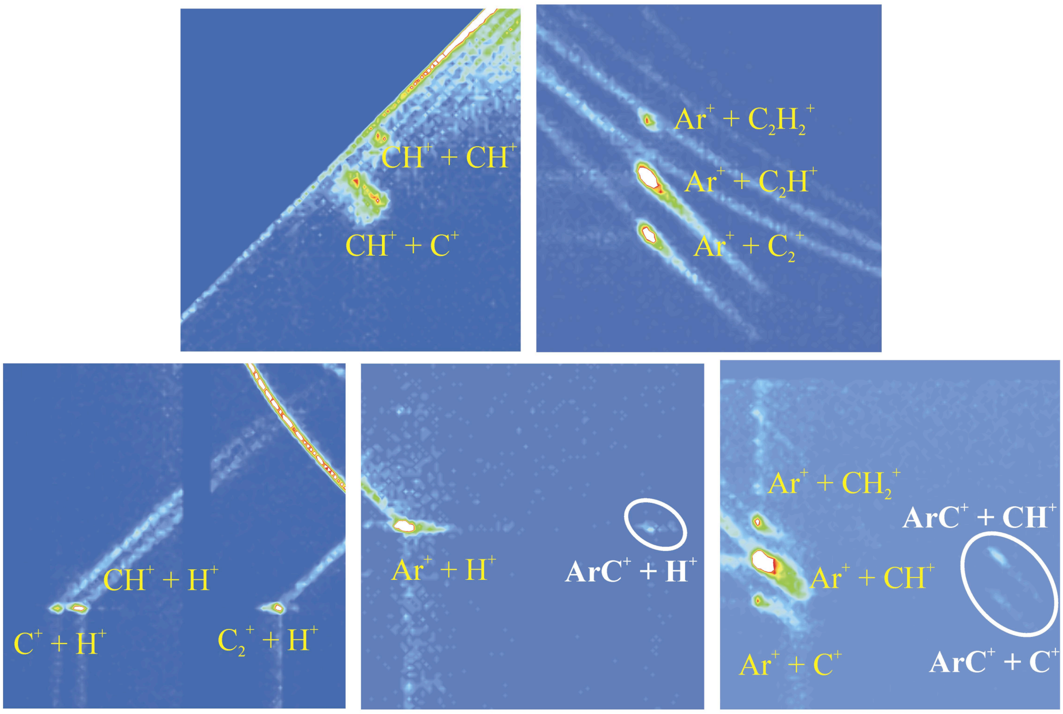

Figure 6.7 Sections of a representative pairs spectrum collected following collisions of Ar^{2+} with C_2H_2 at E_{CM} of 5.5 eV. These sections clearly show the fifteen different peaks we detect and the chemical channels are highlighted in white.

The fifteen different channels detected are detailed in reactions (6.7) – (6.21); reactions (6.7) – (6.11) are double electron–transfer (DET), (6.12) – (6.18) comprise SET and **(6.19)** – **(6.21)** are chemical channels (henceforth in this thesis, bond–forming channels will be indicated in bold). Clearly, the higher double ionisation energy of Ar, compared to that of C_2H_2, means that many more reaction channels are accessible to the Ar^{2+} – C_2H_2 reactants than when the double charge is on the reactant acetylene.

$$Ar^{2+} + C_2H_2 \rightarrow C_2H_2^{2+} \text{ then } C_2H_2^{2+} \rightarrow CH^+ + CH^+ \tag{6.7}$$

$$Ar^{2+} + C_2H_2 \rightarrow C_2H_2^{2+} \text{ then } C_2H_2^{2+} \rightarrow CH^+ + C^+ + H \tag{6.8}$$

$$Ar^{2+} + C_2H_2 \rightarrow C_2H_2^{2+} \text{ then } C_2H_2^{2+} \rightarrow C_2^+ + H^+ + H \tag{6.9}$$

$$Ar^{2+} + C_2H_2 \rightarrow C_2H_2^{2+} \text{ then } C_2H_2^{2+} \rightarrow CH^+ + H^+ + C \tag{6.10}$$

$$Ar^{2+} + C_2H_2 \rightarrow C_2H_2^{2+} \text{ then } C_2H_2^{2+} \rightarrow C^+ + H^+ + [C + H] \tag{6.11}$$

$$Ar^{2+} + C_2H_2 \rightarrow Ar^+ + C_2H_2^+ \tag{6.12}$$

$$Ar^{2+} + C_2H_2 \rightarrow Ar^+ + C_2H^+ + H \tag{6.13}$$

$$Ar^{2+} + C_2H_2 \rightarrow Ar^+ + C_2^+ + [2H] \tag{6.14}$$

$$Ar^{2+} + C_2H_2 \rightarrow Ar^+ + CH_2^+ + C \tag{6.15}$$

$$\mathrm{Ar^{2+} + C_2H_2 \rightarrow Ar^{+} + CH^{+} + [C + H]} \tag{6.16}$$

$$\mathrm{Ar^{2+} + C_2H_2 \rightarrow Ar^{+} + C^{+} + [C + 2H]} \tag{6.17}$$

$$\mathrm{Ar^{2+} + C_2H_2 \rightarrow Ar^{+} + H^{+} + [2C + H]} \tag{6.18}$$

$$\mathbf{Ar^{2+} + C_2H_2 \rightarrow ArC^{+} + CH^{+} + H} \tag{6.19}$$

$$\mathbf{Ar^{2+} + C_2H_2 \rightarrow ArC^{+} + C^{+} + [2H]} \tag{6.20}$$

$$\mathbf{Ar^{2+} + C_2H_2 \rightarrow ArC^{+} + H^{+} + [C + H]} \tag{6.21}$$

The most intense channel that is observed is the dissociative SET reaction (6.13) that yields Ar^{+} + C_2H^{+} + H; this channel accounts for around 30 – 34% of all reactive events detected that produce a pair of ions. Events where two electrons are transferred from C_2H_2 to Ar^{2+} account for around 14 – 16 % of reactivity that produces a pair of ions and chemical channels account for around 1 %. As can be seen in Figure 6.8, the relative branching into the DET, SET and chemical channels remains remarkably constant over the range of collision energies studied. This E_{CM}–independent behaviour of the chemical channels is in stark contrast to the strong energy dependence exhibited by the $HCCAr^{2+}$ forming channel revealed by the quadrupole studies.

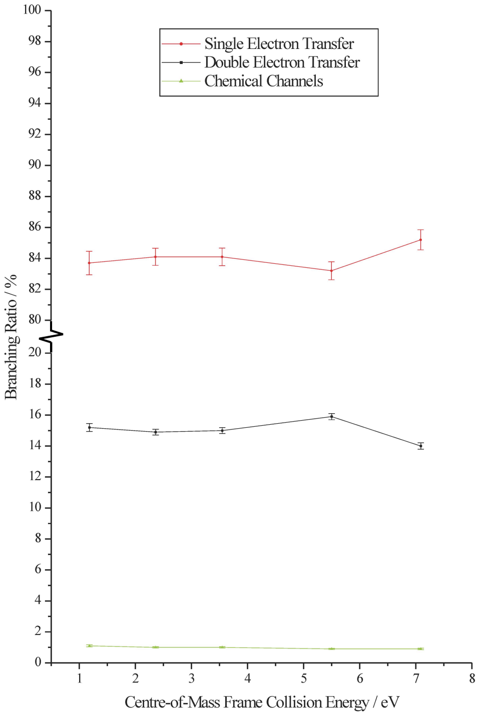

Figure 6.8 Sum of the branching ratios into the chemical and single- and double-electron transfer channels following collisions of Ar^{2+} with C_2H_2 at a range of E_{CM} from 1.2 – 7.1 eV. At each E_{CM} the branching into the three types of reactivity sum to 100 %. Errors given are purely for the counting uncertainties and are based on Poissonian statistics.

4.3.1 Double Electron–Transfer

In all of the DET reactions that we detect (reactions (6.7) – (6.11)) the scattering of both the product ions in the CM frame is uncorrelated with the motion of the reactants prior to the collision. Moreover, the centre of this "isotropic" scattering is displaced away from the CM. We can calculate, from the known velocity of the Ar^{2+} in the laboratory frame, that this displacement from the CM is equivalent to the velocity of a $C_2H_2^{2+}$ intermediate. In principle, there are three mechanisms by which a DET reaction can occur. Specifically, one possible pathway is *via* a $[Ar–C_2H_2]^{2+}$ intermediate which involves a longer term association of the reactants. If such complexation was the dominant pathway, we would not expect the fragment scattering to be centred on $w(C_2H_2^{2+})$, thus, the CM frame scattering diagrams rule out this mechanism. The other two possible DET mechanisms involve transfer of two electrons at relatively large interspecies separation, which is the obvious conclusion from the observed scattering, forming neutral Ar and an excited $C_2H_2^{2+*}$. After these two nascent products have separated from each other, the metastable $C_2H_2^{2+*}$ undergoes Coulomb explosion to the observed fragment ions. There is no correlation between the original reactant directions and the product directions as the $C_2H_2^{2+*}$ rotates several times before it breaks up.

Within the remit of a direct process, there are two possible mechanisms for DET that involve either rapid transfer of electrons at a single crossing of the reactant and product PES (concerted), or alternatively, at two separate crossings (sequential). The former scenario involves the coupling of the Ar^{2+} – C_2H_2 PEC with that for Ar – $C_2H_2^{2+}$ interaction, Figure 6.9 (a). In a one–dimensional model, the only difference between the attractive part of these two PECs arises from the different polarisabilities of the neutral species. Thus, the concerted mechanism requires that the energy separation between the Ar^{2+} + C_2H_2 asymptote and the asymptote accessed by the DET (ΔE_{DET}) is small, ideally less than 1 eV, to place the curve crossing within the reaction window. Alternatively, the electrons could be transferred in two steps, initially from the reactant PES onto the repulsive Ar^+ + $C_2H_2^+$ surface, which then is coupled in a second step to the product PES, Figure 6.9 (b). This latter, sequential, mechanism allows for a wider range of ΔE_{DET} for the DET reaction to be efficient compared to the concerted mechanism.

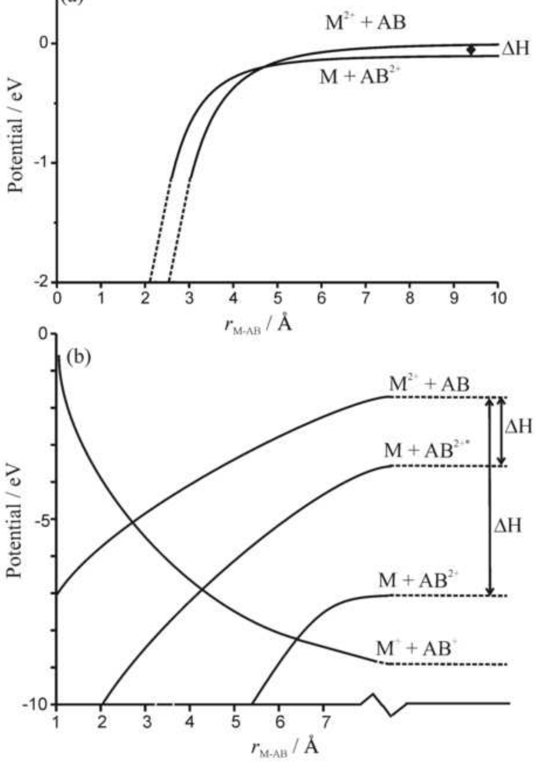

Figure 6.9 Schematic potential energy curves for (a) concerted and (b) sequential double–electron transfer following the reaction of M^{2+} with AB. (a) ΔH indicates the small reaction enthalpy which is required for the curve crossing to lie in the reaction window for the concerted mechanism. (b) The sequential mechanism involves an initial single–electron transfer to the repulsive potential corresponding to a pair of monocations. The system may then remain on this potential, resulting in single electron–transfer, or cross again to reach an M + AB^{2+} asymptote. Both ΔH schematically indicate the limiting reaction exothermicities for which this pair of curve crossings will lie in the reaction window, a markedly larger range of exothermicities than for the concerted mechanism illustrated in (a). From ref. [46].

To determine the energy of the $C_2H_2^{2+*}$ ions that are formed by the primary DET process we examine the KER into the fragment ions formed by the $C_2H_2^{2+*}$ dissociation, these values are shown in Table 6.1. Subsequently, this measured KER, for dissociation of $C_2H_2^{2+*}$ into two monocations, is subtracted from the literature value for the exothermicity between the Ar^{2+} + C_2H_2 reactants and the final products. Any remaining energy approximately equates to ΔE_{DET}. This procedure is illustrated in Figure 6.10 for reaction (6.8) forming CH^+ + C^+ + H, which turns out to exhibit a ΔE_{DET} of 1.0 eV. This calculation of ΔE_{DET} is made for all DET channels (6.7) – (6.11) and the values are shown in Table 6.1.

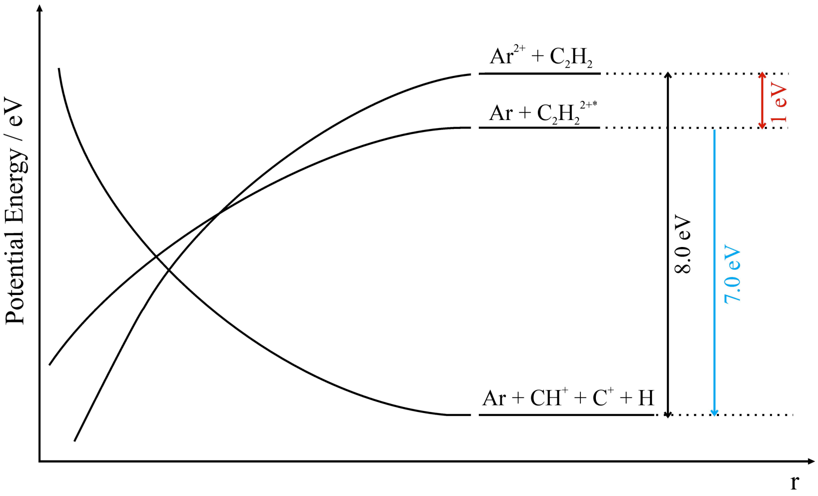

Figure 6.10 Schematic (not on an absolute scale) illustrating how the initial double-electron transfer exothermicity ΔE_{DET} is calculated. The ground state literature exothermicity for the reaction between Ar^{2+} and C_2H_2 forming Ar + CH^+ + C^+ + H is 8.0 eV (black arrow) and the kinetic energy release for the fragmentation of $C_2H_2^{2+*}$ into CH^+ + C^+ + H is measured to be 7.0 eV (blue arrow). Thus, the ΔE_{DET} is 1.0 eV.

Clearly, the values of the energy separation between the Ar^{2+} – C_2H_2 and $C_2H_2^{2+*}$ – Ar PECs (ΔE_{DET}) shown in Table 6.1 are only an estimate and take no account of rovibrational excitation of the products, yet it is clear that the majority of these values are small. An exception is the value of ΔE_{DET} that we derive for reaction (6.7) that forms CH^+ + CH^+ + Ar, which is calculated to be 4.9 eV.

Table 6.1 Measured kinetic energy releases into the monocationic products of dissociation of $C_2H_2^{2+*}$ that is formed in DET reactions with Ar^{2+}. Also shown are the exothermicities of the initial double-electron transfer for each reaction channel ΔE_{DET}.

Reaction No.	Products of $C_2H_2^{2+*}$ Dissociation	Experimental Kinetic Energy Release / eV	ΔE_{DET} / eV
(6.7)	$CH^+ + CH^+$	7.2	4.9
(6.8)	$CH^+ + C^+ + H$	7.0	1.0
(6.9)	$C_2^+ + H^+ + H$	6.5	1.0
(6.10)	$CH^+ + H^+ + C$	5.6	0.0
(6.11)	$C^+ + H^+ + CH$	5.7	-0.7

In the case of CH^+ + CH^+ formation, the larger value of ΔE_{DET} could arise if these molecular products were formed in rovibrationally excited states. As described earlier, the concerted DET mechanism is only likely to occur when ΔE_{DET} is small and preferably less than 1 eV. Therefore, these small ΔE_{DET} that we have determined are consistent with a concerted mechanism for the DET process. Consequently we conclude that this is the much more likely mechanism for DET reactions occurring between Ar^{2+} and C_2H_2.

Further evidence in favour of the concerted mechanism may be extracted from the relative branching ratios into the dissociative DET channels that we measure. These branching ratios may be influenced by the separation between the PECs in the DET step. Detected numbers of pairs for each DET channel, averaged over all E_{CM}, give the branching ratio relation: reaction (6.8) > (6.7) > (6.9) = (6.10) > (6.11). In contrast, photoionisation experiments have shown that the dominant dissociation channel leads to C_2H^+ + H^+ products[42], which we do not detect with any statistically significant branching ratio. Employing photoionisation, the second most intense fragmentation channel of $C_2H_2^{2+}$ leads to CH^+ + CH^+, followed by C_2^+ + H^+ + H production[42]. Evidently, the dissociation of $C_2H_2^{2+}$ that occurs following DET to Ar^{2+} is very different to the analogous dissociation of isolated $C_2H_2^{2+}$ formed by photoionisation. Therefore it seems that the branching into the different dissociation channels is being influenced by the constraint on ΔE_{DET}, which, for formation of CH^+ + CH^+ is not within the correct "window", thus explaining why we see a diminished probability for forming these ions relative to CH^+ + C^+ formation.

6.3.2 Single Electron–Transfer

A representative CM frame scattering diagram for the dissociative SET process yielding Ar^+ + C_2H^+ + H is shown in Figure 6.11. Clearly, the strong anisotropic scattering seen in Figure 6.11 shows that reaction (6.13) takes place *via* rapid SET at large interspecies separation; there is little short range interaction of the reactants.

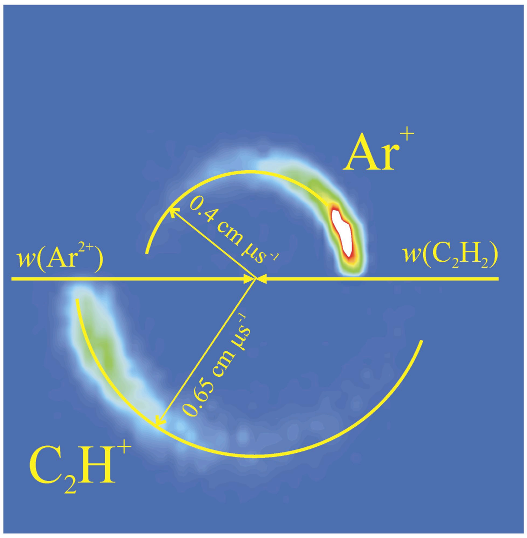

Figure 6.11 Scattering of the Ar^+ and C_2H^+ products of reaction (6.13) in the CM frame, recorded at E_{CM} of 3.55 eV. Directions of the reactant Ar^{2+} and C_2H_2 prior to the collision are shown by the full-headed arrows.

Similar scattering is observed for all of the SET reaction channels, both non-dissociative and dissociative. The implication of such forward scattering is that in every case the reaction proceeds *via* rapid transfer of the electron, followed by a dissociation of the nascent $C_2H_2^{+*}$ some time later when the monocations have begun to fly apart. Internal frame scattering diagrams imply that this dissociation takes place while the $C_2H_2^{+*}$ ion is still well within the Coulomb field of the Ar^+ ion. What is clear in these scattering diagrams is the effective “kick” that the ionic fragment feels from the proximity of the Ar^+, which is ineffectual on the neutral fragment. Thus, we can conclude that the pairs of ions detected that correspond to reactions (6.12) – (6.18) do not arise from fragmentation of any metastable complex between the reactants such as $HCCAr^{2+}$.

6.3.3 Chemical Reactions

Although the formation of new chemical bonds in dication collisions with rare gas atoms is not wholly surprising, for the chemical reactions detected following interaction of Ar^{2+} with C_2H_2 we observe an unusual reaction mechanism. The CM frame scattering diagram for reaction (6.19) that yields ArC^+ + CH^+ + H, recorded at E_{CM} of 2.36 eV is shown in Figure 6.12.

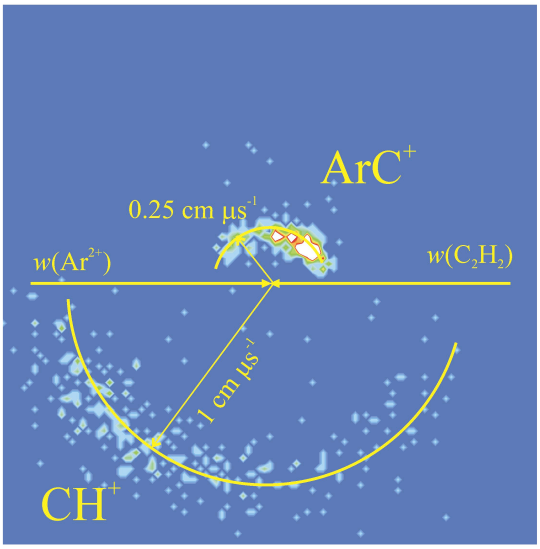

Figure 6.12 Scattering of the ArC$^+$ and CH$^+$ products of reaction (6.19) in the CM frame, recorded at E_{CM} of 2.36 eV. Directions of the reactant Ar^{2+} and C_2H_2 prior to the collision are shown by the full-headed arrows.

What is clear from Figure 6.12 is that there is still a reasonable degree of anisotropy in the scattering of the product ions with respect to the directions of the reactants prior to the reaction. The ArC$^+$ product has scattering peaked in alignment with the direction of the Ar^{2+} prior to the collision, and conversely for the CH$^+$ product, the scattering is aligned with the C_2H_2 direction. Similar anisotropic scattering is seen at every E_{CM} and for all the chemical reactions (6.19) – (6.21).

In order that the ArC$^+$ direction maintains a correlation with the Ar^{2+} direction, this ion must be formed very rapidly in a “stripping” type reaction. Recall that the proton transfer channel occurring following interaction of $C_2H_2^{2+}$ with Ar, described in section 6.2.4.1, also exhibits this anisotropic scattering indicative of a direct mechanism. We have consequently suggested a mechanism for the chemical reactions that involves the stripping of a CH$^-$ group from the C_2H_2 to form ArCH$^+$ and CH$^+$ with little perturbation of the product directions. The nascent ions can then fragment in a series of ways to yield the observed product ions of reactions (6.19) – (6.21). Clearly, in each of these channels, the ArCH$^+$ always breaks up into ArC$^+$ + H, probably due to the large amount of internal energy imparted to the ion. More fuel to this mechanistic flame is found in the internal frame scattering diagrams, where the directions of the neutral H formed in reaction (6.19) is broadly correlated with that of the ArC$^+$ ion.

So, once again, we have detected a bond–forming reaction channel that appears not to be brought about by fragmentation of a "long–lived" complex such as $HCCAr^{2+}$. Thus, we can only conclude that if such an ion were to be formed in Ar^{2+} – C_2H_2 interactions, either it does not dissociate on a timescale shorter than the time the reactant and product ions spend in the interaction region, thus we do not see a peak in the pairs spectra. Alternatively, the $HCCAr^{2+}$ formation cross–section is so small that any pairs detected arising from its dissociation will not produce a statistically significant peak in our pairs spectra.

6.4 Conclusion

Reactions of acetylene dications $C_2H_2^{2+}$ with Ar lead to the rare–gas compound $HCCAr^{2+}$, which has been detected for the first time by employing quadrupole mass–spectrometry. The experimental observation of this species confirms previous theoretical predictions about the stabilities of rare–gas acetylides. The absolute yields of the $HCCRg^{2+}$ remain quite low, however, which can be attributed partly to the pronounced competition with electron– and proton–transfer channels. Studies of the $C_2H_2^{2+}$ – Ar collision system with the PSCO mass–spectrometer have revealed that the Ar^+, C_2H^+ and ArH^+ ions arise from direct reaction mechanisms and not due to fragmentation of the $HCCAr^{2+}$ ion, owing to the strong forward scattering we observe. The branching ratios into the non–dissociative and proton transfer channels remain fairly constant over the E_{CM} range investigated, but the branching into the dissociative SET channel increases with increasing E_{CM}.

Conversely, the reaction of Ar^{2+} with C_2H_2 has been investigated with the PSCO technique, which has revealed an interesting chemical channel yielding ArC^+. The dynamics of this chemical process involve CH^- stripping from the C_2H_2. In the case of the Ar^{2+} – C_2H_2 collision system, the bond–forming chemistry accounts for approximately 1% of reactive events detected that form a pair of ions; the double– and single–electron transfer reactivity account for around 15 % and 84 % respectively. What is interesting is that the reactivity we detect following Ar^{2+} collisions with C_2H_2 is completely different to that detected employing the PSCO following $C_2H_2^{2+}$ collisions with Ar. The $[Ar–C_2H_2]^{2+}$ PES is clearly accessed at a different point that leads to the differing reactivity.

6.5 References

[1] Frenking, G, Koch, W, Reichel, F and Cremer, D, *J. Am. Chem. Soc.* **1990**, *112*, 4240-4256.

[2] Tanskanen, H, Khriachtchev, L, Lundell, J and Rasanen, M, *J. Chem. Phys.* **2006**, *125*, 10.

[3] Khriachtchev, L, Tanskanen, H, Lundell, J, Pettersson, M, Kiljunen, H and Rasanen, M, *J. Am. Chem. Soc.* **2003**, *125*, 4696-4697.

[4] Feldman, V I, Sukhov, F F, Orlov, A Y and Tyulpina, I V, *J. Am. Chem. Soc.* **2003**, *125*, 4698-4699.

[5] Khriachtchev, L, Tanskanen, H, Cohen, A, Gerber, R B, Lundell, J, Pettersson, M, Kiljunen, H and Rasanen, M, *J. Am. Chem. Soc.* **2003**, *125*, 6876-6877.

[6] Tanskanen, H, Khriachtchev, L, Lundell, J, Kiljunen, H and Rasanen, M, *J. Am. Chem. Soc.* **2003**, *125*, 16361-16366.

[7] Khriachtchev, L, Lignell, A, Tanskanen, H, Lundell, J, Kiljunen, H and Rasanen, M, *J. Phys. Chem. A* **2006**, *110*, 11876-11885.

[8] Poterya, V, Votava, O, Farnik, M, Oncak, M, Slavicek, P, Buck, U and Friedrich, B, *J. Chem. Phys.* **2008**, *128*, 10.

[9] McDowell, S A C, *J. Chem. Phys.* **2004**, *120*, 9077-9079.

[10] Jayasekharan, T and Ghanty, T K, *J. Chem. Phys.* **2008**, *129*, 8.

[11] McDowell, S A C, *Mol. Phys.* **2004**, *102*, 1441-1446.

[12] Cheng, J B, Wang, Y L, Li, Q Z, Liu, Z B, Li, W Z and Gong, B A, *J. Phys. Chem. A* **2009**, *113*, 5235-5239.

[13] Sheng, L, Cohen, A and Gerber, R B, *J. Am. Chem. Soc.* **2006**, *128*, 7156-7157.

[14] Grochala, W, *Chem. Soc. Rev.* **2007**, *36*, 1632-1655.

[15] McDowell, S A C, *Curr. Org. Chem.* **2006**, *10*, 791-803.

[16] Lockyear, J F, Douglas, K, Price, S D, Karwowska, M, Fijalkowski, K J, Grochala, W, Remes, M, Roithova, J and Schroder, D, *J. Phys. Chem. Lett.* **2010**, *1*, 358-362.

[17] Ascenzi, D, Aysina, J, Tosi, P, Maranzana, A and Tonachini, G, *J. Chem. Phys.* **2010**, *133*, 9.

[18] Roithova, J, Schroeder, D, Misek, J, Stara, I G and Stary, I, *J. Mass Spectrom.* **2007**, *42*, 1233-1237.

[19] Ascenzi, D, Tosi, P, Roithova, J, Ricketts, C L, Schroeder, D, Lockyear, J F, Parkes, M A and Price, S D, *Phys. Chem. Chem. Phys.* **2008**, *10*, 7121-7128.

[20] Ascenzi, D, Franceschi, P, Tosi, P, Bassi, D, Kaczorowska, M and Harvey, J N, *J. Chem. Phys.* **2003**, *118*, 2159-2163.

[21] Burnside, P W and Price, S D, *Int. J. Mass Spectrom.* **2006**, *249*, 279-288.

[22] Burnside, P W and Price, S D, *Phys. Chem. Chem. Phys.* **2007**, *9*, 3902-3913.

[23] Harper, S M, Hu, S W P and Price, S D, *J. Chem. Phys.* **2004**, *121*, 3507-3514.

[24] Hu, W P, Harper, S M and Price, S D, *Mol. Phys.* **2005**, *103*, 1809-1819.

[25] Jasik, J, Roithova, J, Zabka, J, Thissen, R, Ipolyi, I and Herman, Z, *Int. J. Mass Spectrom.* **2006**, *255*, 150-163.

[26] Kearney, D and Price, S D, *Phys. Chem. Chem. Phys.* **2003**, *5*, 1575-1583.

[27] Lockyear, J F, Ricketts, C L, Parkes, M A and Price, S D, *Chem. Sci.* **2011**, *2*, 150-156.

[28] Manning, M, Price, S D, Rogers, S A and Leone, S R, *Abstracts of Papers of the American Chemical Society* **1993**, *205*, 198-phys.

[29] Newson, K A, Tafadar, N and Price, S D, *J. Chem. Soc.-Faraday Trans.* **1998**, *94*, 2735-2740.

[30] Parkes, M A, Lockyear, J F, Price, S D, Schroder, D, Roithova, J and Herman, Z, *Phys. Chem. Chem. Phys.* **2010**, *12*, 6233-6243.

[31] Price, S D, *J. Chem. Soc.-Faraday Trans.* **1997**, *93*, 2451-2460.

[32] Ricketts, C L, Schroder, D, Roithova, J, Schwarz, H, Thissen, R, Dutuit, O, Zabka, J, Herman, Z and Price, S D, *Phys. Chem. Chem. Phys.* **2008**, *10*, 5135-5143.

[33] Ricketts, C L, Harper, S M, Hu, S W P and Price, S D, *J. Chem. Phys.* **2005**, *123*,

[34] Price, S D, *Int. J. Mass Spec.* **2007**, *260*, 1-19.

[35] Lockyear, J F, Parkes, M A and Price, S D, *Angew. Chem.-Int. Edit.* **2011**, *50*, 1322-1324.

[36] Schroeder, D and Schwarz, H, *Journal of Physical Chemistry A* **1999**, *103*, 7385-7394.

[37] Ralchenko, Y, Kramida, A E and Reader, J, **2010**, *NIST Atomic Spectra Database (ver. 4.0.1),* http://physics.nist.gov/asd, *2011 February 15*, National Institute of Standards and Technology Gaithersburg, MD

[38] Lias, S G, Bartmess, J E, Leibman, J F, Holmes, J L, Levin, R D and Mallard, W G, *J. Phys. Chem. Ref. Data* **1988**, *17*, Supplement No. 1.

[39] Avaldi, L, Dawber, G, Hall, R I, King, G C, McConkey, A G, Macdonald, M A and Stefani, G, *J. Elec. Spec. Rel. Phen.* **1995**, *71*, 93-105.

[40] Stolyarov, A V and Child, M S, *Phys. Chem. Chem. Phys.* **2005**, *7*, 2259-2265.

[41] Kinugawa, T, Lablanquie, P, Penent, F, Palaudoux, J and Eland, J H D, *J. Elec. Spec. Rel. Phen.* **2004**, *141*, 143-148.

[42] Thissen, R, Delwiche, J, Robbe, J M, Duflot, D, Flament, J P and Eland, J H D, *J. Chem. Phys.* **1993**, *99*, 6590-6599.

[43] Rogers, S A, Price, S D and Leone, S R, *J. Chem. Phys.* **1993**, *98*, 280-289.

[44] Herman, Z, *Int. Rev. Phys. Chem.* **1996**, *15*, 299-324.

[45] Hochlaf, M, Taylor, S and Eland, J H D, *J. Chem. Phys.* **2006**, *125*,

[46] Parkes, M A, Lockyear, J F and Price, S D, *Int. J. Mass Spectrom.* **2009**, *280*, 85-92.

Chapter 7: The Oxygen Dication Part I – Reactions of O_2^{2+} with Small Neutral Organic Molecules

7.1 Introduction to the O_2^{2+} Dication

The oxygen dication was first observed in 1963 by Dorman and Morrison using electron ionisation mass spectrometry[1]. Many molecular dications have shallow potential energy wells, which result in their rapid Coulomb explosion. However, the oxygen dication has an unusually deep ground state potential well of approximately 4 eV, which has been shown to support up to nineteen vibrational levels[2-7]. Larsson *et al* have reported some computationally derived PECs, by the CASSCF/MRCCI method, for the low lying electronic states of O_2^{2+} (Figure 7.1)[3], in which the deep ground state potential well is obvious.

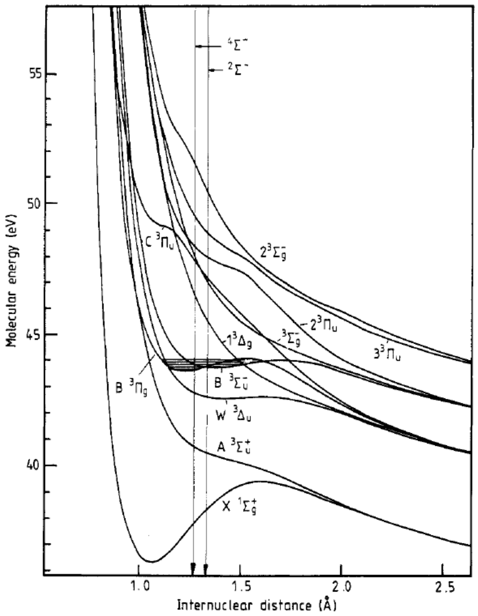

Figure 7.1 Potential energy curves for the oxygen dication derived from CASSCF/MRCCI calculations. Note the particularly deep potential well for the ground electronic state. From ref. [3].

The deep $O_2^{2+}(X^1\Sigma_g^+)$ potential well allows the dication to survive for long periods and lifetimes of several seconds have been measured in ion–storage rings experiments. In fact, in these experiments, the dication is sufficiently long–lived that the measurements become limited by collisions with background gas resulting in artificially short lifetimes;

theoretically, the ground state of O_2^{2+} survives for an almost infinitely long time[3]. The very long lifetime of O_2^{2+} enables us to study its reactions with neutrals using the PSCO methodology.

Almost all the excited electronic states of O_2^{2+} have been shown to be repulsive or pre–dissociated. For example, the $A^3\Sigma_u^+$ first excited state has been revealed as repulsive in several studies[3,4,8,9]. As has been shown by Lundqvist *et al*, there is a cluster of states around 7 – 10 eV higher in energy than O_2^{2+} ($X^1\Sigma_g^+$, $v = 0$) that have wells deep enough to support vibrational levels but which are pre–dissociated by repulsive states[5]. The repulsive state which is likely to be the culprit for this pre–dissociation is the $1^5\Sigma_g^+$ state that crosses all of these electronic states that have potential minima ($W^3\Delta_u$, $B^3\Sigma_u^-$, $1^1\Sigma_u^-$ and $1^1\Delta_u$). Therefore, in the context of our experiment, we expect our O_2^{2+} reactant beam to overwhelmingly consist of ground electronic state dications.

The O_2^{2+} dication has a much smaller equilibrium inter–nuclear separation than neutral O_2, meaning the Frank–Condon region for formation of O_2^{2+} from O_2 is not centred around the lowest vibrational levels of the dication[6,7]. Thus, we expect that the ground electronic state dications in our beam which are formed *via* electron ionisation will have some degree of vibrational excitation. In a study of the reactions of O_2^{2+} using a selected–ion drift–tube, Chatterjee and Johnsen attempted to estimate the vibrational states of O_2^{2+} which were populated in their beam[10]. From the SET reaction of O_2^{2+} with Ne they were able to estimate that the population distribution of O_2^{2+} dications had a maximum in the $v = 5$ or 6 states[10]. Additionally, supporting the findings of Chatterjee and Johnsen, Hall *et al.* have employed threshold photoelectron coincidence spectroscopy (TPESCO)[2] to show that when O_2^{2+} is formed *via* photoabsorption the most populous vibrational levels are the $v = 4$ and 5 states. Feifel *et al* have also studied the photoionisation of O_2, employing a TOF PEPECO technique, and found that the $v = 3$, 4 and 5 levels are the most abundantly populated at photon energies of 40.814 eV and 48.372 eV[11]. Using the vibrational constants measured by Hall *et al*[2] the $v = 4$, 5 and 6 states have been calculated to lie 1.2, 1.40 and 1.63 eV ± 0.01 eV above the $v = 0$ state of O_2^{2+} ($X^1\Sigma_g^+$). Hence, we can estimate that the O_2^{2+} reactants in our beam will have a distribution of vibrational energy centred about 1.4 eV, and generally have no more than 2 eV of internal energy. Like Chatterjee and Johnsen we have studied the SET reaction between O_2^{2+} and Ne and so an extended discussion of the vibrational distribution of the reactant O_2^{2+} ions in our beam is presented in the results section of Chapter 8.

The oxygen dication has been predicted to exist in the terrestrial ionosphere[12] and is likely to be present in other interstellar environments. In terms of the terrestrial ionosphere, the major dicationic species predicted to exist are N_2^{2+}, O_2^{2+} and O^{2+}[12]. Furthermore, observations from Earth based experiments and probes such as the MS aboard the Cassini-Huygens spacecraft have revealed that O^+, O_2^+, O, OH and H_2O are present in the Saturnian system[13]. Titan is known to have significant densities of the oxygen containing molecules CO, CO_2 and H_2O in its atmosphere[14-17]. However, there is an inherent difficulty in detecting homonuclear doubly charged ions using mass spectrometry since these homonuclear species are isobaric with the associated atomic monocation. For example, both O_2^{2+} and O^+ have m/z of 16. Thus, although their existence has been predicted, O_2^{2+} has not been unambiguously detected in any of these ionised environments. Nevertheless, there is clearly an oxygen-containing chemistry cycle occurring in the ionosphere of both Earth and Titan and for a better understanding of these environments it is valuable to understand the reactions of O_2^{2+} with a variety of neutral species.

Previous investigations into O_2^{2+} reactivity were initiated in 1978 by Glosik *et al*, who studied reactions of O_2^{2+} with N_2 and CO in a selected-ion flow-tube (SIFT) experiment[18]. In part due to their analytical methodology, these authors only observed products due to SET. In 1989 Chatterjee and Johnsen reported results of a study of the reactivity of O_2^{2+} with N_2, O_2, CO_2, NO and Ne employing a selected-ion drift-tube (SIDT) apparatus[10]. Employing this SIDT technique, SET was observed to occur between O_2^{2+} and O_2, N_2, CO_2 and Ne. Of greater interest, perhaps, is the fact that in these experiments Chatterjee and Johnsen detected NO_2^+ ions following interaction of O_2^{2+} with NO; bond-formation in a dication-neutral reaction was observed for the first time. In 2005 Simon *et al* reported the rate coefficients for removal of N_2^{2+}, O_2^{2+} and O^{2+} in the presence of the atmospherically significant neutrals N_2, O_2, N and O[12]. To the best of our knowledge, there have been no other studies of the reactivity of O_2^{2+} towards neutrals reported in the literature.

In light of the above, we have investigated the reactions, that form pairs of ions, between O_2^{2+} and many different neutrals using the PSCO methodology. This methodology allows us to determine not only the products of such reactions but also the dynamics. The reactions of O_2^{2+} that have been studied employing the PSCO technique will be reported in two separate chapters; the first of these will discuss the extensive chemical reactivity that has been observed following collisions with small organic neutrals and the second will discuss the predominantly ET reactivity that is observed in collisions with a variety of other neutral species. More specifically, Chapter 7 reports the reactions of O_2^{2+} with CH_4, C_2H_2, C_2H_4 and C_6H_6. Chapter 8 reports, more briefly, the reactivity of O_2^{2+} with Ne, Ar, N_2, NO, N_2O, NH_3, CO, CO_2, OCS, CS_2, H_2O and H_2S.

7.2 Results

7.2.1 O_2^{2+} + CH_4

The reactions of the oxygen dication with neutral methane, which produce a pair of product monocations, have been studied using the PSCO mass spectrometer at E_{CM} = 4.7 eV. In these PSCO spectra we have observed seventeen different reaction channels, of which seven are SET channels, three are DET channels and seven are bond–forming channels. The products formed in these seventeen reactions and their respective branching ratios, experimental translational exothermicities ΔE_T and literature enthalpies of reaction ΔH_{lit} are shown in Table 7.1. The overall branching ratios for the SET, DET and bond–forming classes of reaction are also shown in Table 7.1. From Table 7.1, it is clear that the vast majority of reactive events involve SET, with 50 % of reactive encounters forming O_2^+ + CH_3^+ + H. The overall branching ratios for DET and for bond–forming reactivity are comparable.

As can be seen from Table 7.1, several of the observed reactions involve the formation of a neutral atomic product, which accompanies the pair of product ions (Channels (7.2), (7.13) and (7.14)). As described in Chapter 2, for these reactions the PSCO methodology allows us to derive the nascent momentum of the neutral species. Table 7.1 also indicates that for many of the reactions there are several possibilities for the connectivity of the neutral species formed. For example in channel (7.3), the neutral products could be bound as H_2 or unbound as 2H. However, comparison of the average ΔE_T for the channel with literature values often allows the bonding of the neutral products to be determined. These assignments are discussed in detail below.

Table 7.1 Products and branching ratios for the seventeen reaction channels observed following the interaction of O_2^{2+} with CH_4 at E_{CM} = 4.7 eV. Also shown are the experimental translational exothermicity of the reaction (ΔE_T) and the ground state literature enthalpy of reaction (ΔH_{lit}). Where more than a single atomic neutral product is formed, the various energetically possible fragmentation pathways of these neutrals have also been specified along with their respective enthalpies of reaction.

Channel	Products	Branching Ratio / %	ΔE_T/ eV	ΔH_{lit} / eV
	Single ET	**83.7**		
7.1	$O_2^+ + CH_4^+$	9.8	–4.83	–11.5
7.2	$O_2^+ + CH_3^+ + H$	50.1	–6.13	–9.7
7.3	$O_2^+ + CH_2^+ + H_2$	20.7	–[a]	–8.9
	$+ H + H$			–4.4
7.4	$O_2^+ + CH^+ + H_2 + H$	1.6	–[a]	–4.2
	$+ H + H + H$			+0.3
7.5	$O_2^+ + H^+ + CH_3$	1.2	–[a]	–5.9
	$+ CH_2 + H$			–1.2
	$+ CH + H_2$			–1.3
	$+ C + H_2 + H$			+2.3
	$+ CH + H + H$			+3.2
7.6	$O_2^+ + C^+ + H_2 + H_2$	0.18	–[a]	–4.6
	$+ H_2 + H + H$			–0.1
7.7	$O_2^+ + H_2^+ + CH_2$	0.17	–[a]	–3.8
	$+ C + H_2$			–0.4
	$+ CH + H$			+0.6
	$+ C + H + H$			+4.1
	Double ET	**8.8**		
7.8	$CH_3^+ + H^+ + O_2$	7.1	–6.0	–8.1
7.9	$CH_2^+ + H_2^+ + O_2$	1.1	–5.2	–5.6
7.10	$CH_2^+ + H^+ + H + O_2$	0.57	–4.0	–2.9
	Bond Forming	**7.5**		
7.11[b]	$HCO^+ + H^+ + H_2O$	3.3	–[a]	–13.4
	$+ H_2 + O$			–8.3
	$+ OH + H$			–8.3
	$+ O + H + H$			–3.8
7.12[b]	$HCO^+ + H_2^+ + OH$	2.4	–[a]	–10.9
	$+ O + H$			–6.5
7.13[b]	$HCO^+ + H_3^+ + O$	0.13	–5.33	–12.7
7.14	$HO_2^+ + CH_2^+ + H$	1.2	–6.73	–7.3
7.15	$HO_2^+ + CH^+ + H_2$	0.25	–[a]	–7.1
	$+ H + H$			–2.6

7.16	$CO_2^+ + H^+ + H_2 + H$	0.14	–[a]	–7.5
	$+ H + H + H$			–3.0
7.17	$CO_2^+ + H_2^+ + H_2$	0.09	–[a]	–10.2
	$+ H + H$			–5.7

[a] For these reactions where more than a single atomic neutral is formed, we cannot calculate a translational exothermicity as the velocity of the neutral cannot be calculated by conservation of momentum with the ionic products.

[b] Our technique only allows for the determination of the mass-to-charge ratio of a product. Hence HCO^+ may alternatively be bound as COH^+. However, we assume that the HCO^+ structure is formed since this isomer is lower in energy than the COH^+ structure by 1.63 eV[19].

7.2.1.1 Non-dissociative Single Electron-Transfer

Channel (7.1) corresponds to non-dissociative SET, where an electron is ejected from CH_4 and transferred to the O_2^{2+} ion. The CM scattering diagram for this reaction channel, derived from the PSCO dataset, is shown in Figure 7.2 and reveals strong forward scattering. Thus, the majority of reactive events involve approximate conservation of the direction of the reactant velocities meaning a direct reaction mechanism operates in this channel.

From the PSCO data we determine an average ΔE_T of 4.8 eV for channel (7.1) with a full width at half maximum of 2 eV, whereas the ΔH_{lit} for this reaction is 11.5 eV. As has been discussed in section 7.1, we expect that there is on average 1.4 eV of vibrational excitation in the reactant O_2^{2+} dications. Thus, the modal internal energy of the products will be around 8.1 eV. Accommodating this large amount of internal energy in internal modes of the O_2^+ and CH_4^+ ions is not, in principle, a problem as the dissociation limit of the ground electronic state of O_2^+ is 6.7 eV[20,21] and experiments show that the threshold for fragmentation of the ground electronic state of CH_4^+ is 1.65 eV[22]. Therefore, due to the close match between the internal energy we expect in the products (8.1 eV) and the sum of their dissociation energies (8.35 eV), which only differ by 0.25 eV, we can infer that the O_2^+ and CH_4^+ formed in channel (7.1) will be highly internally excited. It seems clear that the large ground state exothermicity for the non-dissociative SET process, which is well outside the Landau-Zener reaction window, and the consequent formation of highly excited products, accounts for the low branching ratio we observe for the non-dissociative SET channel.

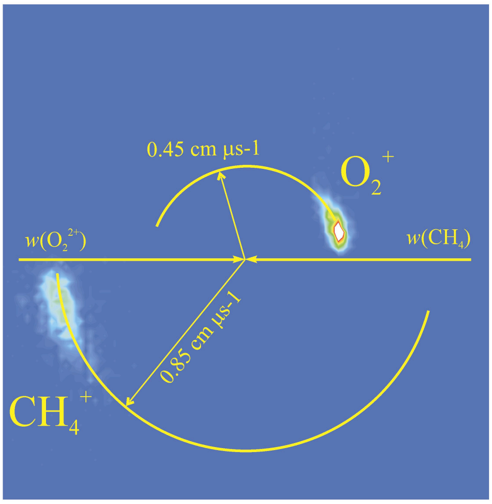

Figure 7.2 The CM frame scattering diagram for the SET reaction between neutral methane and the oxygen dication at E_{CM} of 4.7 eV. The vectors $w(O_2^{2+})$ and $w(CH_4)$ denote the orientation of the velocities of the reactants, in the CM frame, prior to the collision. Subsequent to the electron transfer, the O_2^+ product ion continues travelling predominantly in the direction of $w(O_2^{2+})$ and the CH_4^+ product ion continues travelling predominantly in the direction of $w(CH_4)$.

We conclude, in the previous paragraph, that the product O_2^+ and CH_4^+ ions formed in channel (7.1) are, on average, close to their dissociation limits in electronic and/or rovibrationally excited states. In the non–dissociative SET channel, the CH_4^+ must be in the ground electronic state as the first electronically excited state, the A^2A_1 state which lies 9.8 eV higher than the ground state, is completely repulsive[23,24]. Conversely, the O_2^+ products could be formed in four different electronic states that have all been shown to support vibrational levels. Specifically these are the $X^2\Pi_g$, $a^4\Pi_u$, $A^2\Pi_u$ and $b^4\Sigma_g^-$ states. In order to help predict which of these states may be populated in the SET reactions we have simulated a kinetic energy release spectrum to compare with the measured ΔE_T distribution for channel (1). This calculation involves determining the Franck–Condon overlap between the reactant vibrational states of O_2^{2+} with the product vibrational states of O_2^+ in all of the possible electronic states of the monocation that may be populated. This calculation is made more complex by the fact that our O_2^{2+} reactant ions are formed, *via* electron ionisation, in a distribution of vibrational levels in the ground electronic state, as discussed in section 7.1. The simulated energy release spectrum is calculated by integrating a series of Gaussian functions, which represent the instrument function, placed at the energy releases for the population of each vibrational level of the possible O_2^+ electronic states from the various vibrational levels of O_2^{2+}. To calculate each energy release we also account for the ionisation energy of CH_4 and allow 1 eV of internal energy in the product CH_4^+ (recall that the dissociation limit of CH_4^+ is only 1.65 eV). We assume that CH_4^+ is formed with 1 eV of internal energy as the Franck–Condon zone for single ionisation of neutral ground state CH_4 suggests that CH_4^+ is formed in vibrational levels near the top of the potential well[25]. The intensity ω of each Gaussian function is given by the product of the Franck–Condon–Factors for transitions from O_2^{2+} ($X^1\Sigma_g^+$) to the four possible (n = 1 – 4) electronic product states $F(n, v^+, v^{++})$ with the Franck–Condon–Factors for producing the reactant vibrational states of O_2^{2+} from neutral O_2 ($X^3\Sigma_g^-$) $F(v^{++}, v)$ as described by Equation (7.1). The latter term is very important for correctly representing the vibrational distribution of the O_2^{2+} reactant. Indeed, our Franck–Condon calculations indicate that the most populated level of the reactant O_2^{2+} should be $v^{++} = 4$, as has been determined experimentally[11]. Thus, the calculations include the Franck–Condon overlap of each initial vibrational level of O_2^{2+} ($X^1\Sigma_g^+$) with each possible final vibrational level of O_2^+ in each of the $X^2\Pi_g$, $a^4\Pi_u$, $A^2\Pi_u$ and $b^4\Sigma_g^-$ states.

$$\omega = \sum_{v^{++}=0}^{v^{++}=9} \sum_{v^{+}=0}^{v^{+}_{\max}} \sum_{n=1}^{n=4} F(n, v^+, v^{++}) F(v, v^{++}) \tag{7.1}$$

The simulated and experimentally determined exothermicity spectra can be seen in Figure 7.3. As is patently clear from Figure 7.3, the $X^2\Pi_g$ state of O_2^+ is not populated in the non-dissociative SET reaction between O_2^{2+} and CH_4. However, the curves representing population of O_2^+ ($a^4\Pi_u$, $A^2\Pi_u$ and $b^4\Sigma_g^-$) all have some degree of overlap with the experimentally determined energy release. Therefore, we deduce that one or a combination of these states is populated in channel (7.1). An interesting observation is that in the O_2^{2+} – CH_4 collision system the O_2^+ product is never observed to fragment to O^+ + O, whereas the CH_4^+ is seen to break down into many fragment ions. The observation that O_2^+ does not fragment gives us some indication as to which electronic states are populated in the SET reactions. The $a^4\Pi_u$, $A^2\Pi_u$ and $b^4\Sigma_g^-$ states of O_2^+ all have minima that lie below the first dissociation limit, but only v = 0–3 of the $b^4\Sigma_g^-$ state are stable. Vibrational levels of the $b^4\Sigma_g^-$ state higher than and including v = 4 are pre-dissociated. Hence, we would expect to see fragmentation of the nascent O_2^+ if the $b^4\Sigma_g^-$

state is populated to any significant degree. Thus, it seems unlikely that appreciable amounts of O_2^+ ($b^4\Sigma_g^-$) are formed and most O_2^+ products are in the $a^4\Pi_u$ or $A^2\Pi_u$ states.

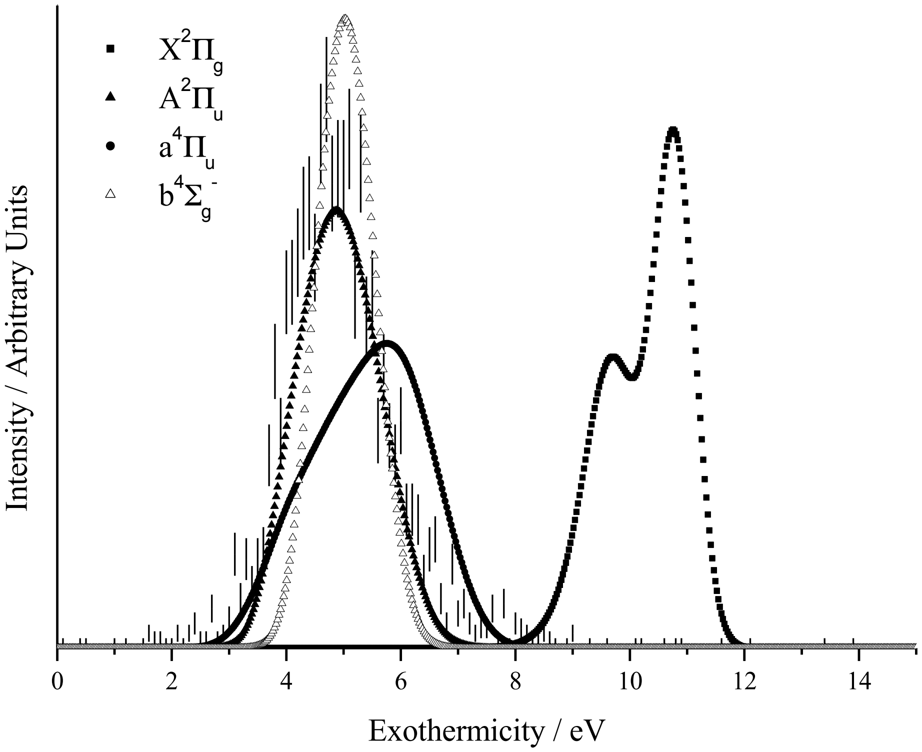

Figure 7.3 The experimental exothermicity spectrum for the non-dissociative single electron-transfer reaction between O_2^{2+} and CH_4 at E_{CM} of 4.7 eV is represented by error bars of length 2σ. Also shown are the results of the simulations for population of the $X^2\Pi_g$, $a^4\Pi_u$, $A^2\Pi_u$ and $b^4\Sigma_g^-$ states of O_2^+ from a distribution of vibrational states of $O_2^{2+}(X^3\Sigma_g^+)$ as calculated from the relevant Franck-Condon factors and explained in the text. The internal energy of the product CH_4^+ ion assumed in the simulation was 1 eV.

7.2.1.3 Dissociative Single Electron-Transfer

Channels (7.2-7.7) are dissociative SET reactions. Here, we detect O_2^+ in conjunction with an ion that arises from dissociation of CH_4^+. As expected, and similarly to channel (7.1), the dissociative SET channels all exhibit strong forward scattering implying that a direct mechanism takes place with fragmentation of the nascent CH_4^+ taking place *after* the SET step. Internal frame scattering diagrams can help us to pin down these finer points of the reaction dynamics. For example, Figure 7.4 shows that for channel (7.2), forming O_2^+ + CH_3^+ + H, the scattering of the H atom is isotropic and centred about the velocity of the CH_3^+. Such scattering clearly shows that CH_4^{+*} was formed by the SET step, which subsequently became well separated from the nascent O_2^+ before dissociating into CH_3^+ + H.

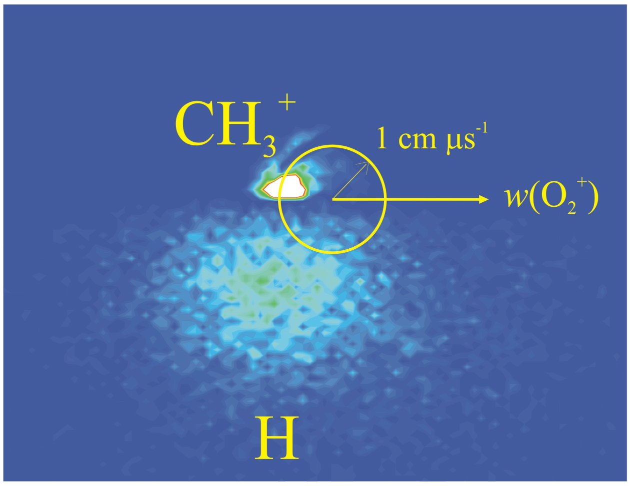

Figure 7.4 Internal frame scattering diagram showing the direction of scattering of the CH_3^+ and H products with respect to the direction of the O_2^+ product, $w(O_2^+)$.

Neutral methane (T_d) has an $(1a_1)^2(2a_1)^2(1t_2)^6$ electronic configuration[23,24,26]. Removal of an electron from the $1t_2$ molecular orbital, whilst maintaining the T_d geometry, leads to the X^2T_2 ground electronic state of the monocation which is unstable to Jahn-Teller distortion and rapidly adopts a C_{2v} symmetry with an X^2B_1 ground electronic state[23,24,26]. The adiabatic ionisation potential of methane has been determined by monochromatic electron ionisation to be 12.63 eV[27] and by photoionisation studies to be 12.615 eV[28]. Removal of an electron from the $2a_1$ orbital gives rise to the A^2A_1 first electronic excited state that lies around 9.8 eV higher in energy than the electronic ground state of CH_4^+; formation of the A state of CH_4^+ always results in dissociation[23,24]. The next dicationic state, the core ionised $(1a_1)^{-1}$ state of CH_4, lies 290.7 eV above the neutral ground state and so there is insufficient energy in this collision system for this core ionised species to be formed[23]. Photo-fragmentation[22,24,29] and electron impact[27] studies have shown that the X^2B_1 and A^2A_1 electronic states of CH_4^+ dissociate *via* several pathways leading to a variety of ionic products. These studies help us determine which states of CH_4^+ are populated in the dissociative SET reactions and provide an explanation for the observed products and their branching ratios.

Our experiments show that in channels (7.2-7.7) the CH_4^{+*} goes on to fragment into CH_3^+, CH_2^+, CH^+, H^+, C^+ and H_2^+ ions and associated neutrals. Photoionisation coincidence studies carried out by Field and Eland show that $CH_4^+(X^2B_1)$ predominantly fragments into CH_3^+ + H when formed with internal energy greater than 1.65 eV above $v = 0$[22]. Field and Eland also found that as the internal energy of the X^2B_1 state is increased from 2.5 to 4.1 eV there is a small amount of CH_2^+ formed in addition to CH_3^+. In agreement with Field and Eland, other studies find that population of the X^2B_1 state of CH_4^+ above the dissociation limit produces chiefly CH_3^+ and less than 3% CH_2^+[24,29–32]. In contrast, various photo–fragmentation studies have shown that CH_2^+ is the major fragment, accompanied by traces of CH_3^+, following population of the A^2A_1 state of CH_4^+[22,24,26,32]. Hence, it seems clear that channel (7.2) (forming CH_3^+ + H) is principally due to population of $CH_4^+(X^2B_1)$ with internal energy greater than 1.65 eV. Whereas, it appears that channel (3) (forming CH_2^+ + 2H) principally arises due to population of $CH_4^+(A^2A_1)$, but there could be a small contribution from population of $CH_4^+(X^2B_1)$ with more than 2.5 eV of internal energy.

Fragmentation of $CH_4^+(A^2A_1)$ into CH^+ has also been observed, although with a smaller branching ratio than for formation of CH_2^+. Field and Eland determined that the branching ratios for formation of CH_2^+ and CH^+ following photoexcitation to $CH_4^+(A^2A_1)$ are around 80% and 20% respectively, along with traces of CH_3^+, and remain roughly constant over the photon energy range from 22.0 – 24.5 eV[22]. Samson *et al* also measured the photo–fragmentation cross–sections for CH_4 and give a CH_2^+:CH^+ fragment ratio, following formation of $CH_4^+(A^2A_1)$, between 10:1 and 6:1[32]. Our experimentally determined branching ratios for channels (7.3) and (7.4) result in a CH_2^+:CH^+ product ratio of 13:1, slightly higher than that measured using photo–fragmentation. From the literature we can draw the conclusion that CH^+ is being formed from population of $CH_4^+(A^2A_1)$ and that the ratio of CH_2^+:CH^+ that we measure is broadly consistent with those determined by photoionisation.

Our data show that channel (7.5), forming O_2^+ + H^+, has a similar branching ratio to channel (7.4), forming CH^+. Samson *et al* have measured the cross–sections for formation of the CH^+ and H^+ fragments over a range of photon energies and found that these ions clearly arise following population of the A^2A_1 state of CH_4^+ with high internal energy[32]. Similarly to our results, the cross–sections for CH^+ and H^+ production measured by Samson *et al* are largely the same upon formation of the A^2A_1 state[32].

We shall now consider the bonding of the C and 3H neutral species that must be produced in conjunction with H^+ in channel (7.5); this is something that we cannot directly determine using the PSCO technique. We can rule out the production of C + 3H, in conjunction with the detected ions, as this asymptote lies too high in energy to be accessed in our experiments. From Table 7.1, we see that formation of C + H_2 + H and CH + H + H in conjunction with the ionic products of channel (7.5) are also endothermic by 2.3 eV and 3.2 eV, respectively, meaning these are not likely outcomes of the dissociation of CH_4^{+*}. The thermodynamic threshold for H^+ + CH_3 production lies at 18.01 eV relative to neutral ground state CH_4[32]. However, the threshold for H^+ detection from photo–fragmentation of CH_4^{+*} was measured by Samson *et al* as 22.4 eV. This experimental threshold energy corresponds closely to the *thermodynamic* thresholds for formation of H^+ + CH_2 + H at 22.5 eV and of H^+ + CH + H_2 at 22.8 eV. Consequently, in dissociative SET between O_2^{2+} and CH_4, it is probable that H^+ + CH_2 + H or H^+ + CH + H_2 are formed.

Channel (7.6), yielding O_2^+ + C^+, has a very small branching ratio compared to channels (7.2–7.5) (Table 7.1). Nevertheless, the observation of C^+ is somewhat more difficult to explain using the results from photo–fragmentation experiments. Field and Eland[22], Samson *et al*[32] and Dutuit *et al*[24] do not observe C^+ formation following population of $CH_4^+(A^2A_1)$ at energies near the thermodynamic threshold of C^+ + $2H_2$ at 19.36 eV[22,24,32]. However, at a photon energy of 28.5 eV, which corresponds to the thermodynamic threshold for formation of C^+ + 4H, Field and Eland detected C^+ ions from breakdown of CH_4^{+*}[22]. Samson *et al* measured the onset for production of C^+ ions at a photon energy of 24.8 eV[32], which is comparable to the thermodynamic threshold for production of C^+ + H_2 + 2H at 24.0 eV. Dutuit *et al*[24] measured the appearance potential of the C^+ fragment to be 25.0 ± 0.5 eV, in good agreement with Samson *et al*[32]. However, highly sensitive monochromatic electron impact ionisation experiments of Plessis *et al*[27] determined the appearance energy of the C^+ fragment to be 19.56 ± 0.2 eV, very close to the thermodynamic threshold of C^+ + $2H_2$. Thus, it seems that although it is possible to form C^+ + $2H_2$ fragments from ionisation of CH_4^+ at energies close to the thermodynamic threshold, this has a very small cross–section, in accord with our observation. In a SET reaction with O_2^{2+} at E_{CM} of 4.7 eV, formation of O_2^+ + C^+ + $2H_2$ is exothermic by 4.6 eV, whereas the formation of O_2^+ + C^+ + H_2 + 2H is only exothermic by 0.1 eV. Formation of 4H in this reaction channel is endothermic by 4.4 eV and so seems unlikely at our collision energy of 4.7 eV as collision energy does not couple well with the potential energy in reactive collisions, particularly those that are direct and do not involve formation of a complex. Consequently, given the thresholds reported in the literature and the small branching ratio we detect for channel (7.6), it is hard to say whether channel (7.6) yields $O_2^+ + C^+ + 2H_2$ or $O_2^+ + C^+ + H_2 + 2H$.

Similarly to channel (7.6), channel (7.7), which corresponds to the formation of O_2^+ and H_2^+, has a very small branching ratio. The dissociative photoionisation cross-section for formation of H_2^+ from CH_4, obtained by Samson *et al*, is very low and is always around an order of magnitude less than for formation of H^+ over the range of photon energies from 28 – 51 eV[32]. This observation is consistent with our results from dissociative SET as we detect that H_2^+ formation is around 7 times less likely than formation of H^+. Furthermore, in accord with our observation that the branching ratios for channels (7.6) and (7.7) are similar, Samson *et al* show the cross-section for formation of H_2^+ is similar to that of C^+ over their range of photon energies[32]. The neutrals formed in this reaction are C and 2H that may be bound as CH_2, $C + H_2$ or $CH + H$, or the neutrals may all be in atomic form. In the photo-fragmentation experiments of Samson *et al*[32], the observed onset for H_2^+ formation was found to be 28.2 eV, which coincides with the thermodynamic threshold for formation of $H_2^+ + C + H + H$. Such a reaction outcome for the O_2^{2+} – CH_4 system is endothermic by 4.1 eV. As mentioned before, collision energy does not couple well with potential energy in direct reactions, thus the low branching ratio we detect for channel (7.7) may be due to the endothermic nature of the channel.

To determine which states of the product O_2^+ are populated in conjunction with the (A^2A_1) state of CH_4^{+*} we have again used the methodology described above that convolutes the Franck-Condon factors for the double ionisation process with those for a transition from O_2^{2+} $(X^1\Sigma_g^+)$ $F(v^{++})$ to O_2^+ (n, v^+). Using this simulation, and on energetic grounds, it was found that when $CH_4^+(A^2A_1)$ is formed as a primary product in the dissociative SET channels, then the partner O_2^+ product must be formed exclusively in the $X^2\Pi_g$ state. This conclusion is unsurprising in the context of the Landau-Zener reaction window as the exothermicity of the reaction must lie between 2 and 6 eV for the reaction to be probable.

7.2.1.4 Double Electron-Transfer

Channels (7.8–7.10) are dissociative DET reactions that involve the formation of a pair of monocations. These three channels yield ionic fragments arising from the dissociation of the CH_4^{2+} dication, which is formed when two electrons are transferred from CH_4 to O_2^{2+}. Dissociation into CH_3^+ + H^+ is the dominant channel; the CM scattering diagram for this channel (7.8) is shown in Figure 7.5. Figure 7.5 clearly shows the isotropic distribution of the scattered CH_3^+ and H^+ fragments about a point that is displaced away from the CM. Prior to the collision, the neutral CH_4 is travelling in the opposite direction to the reactant O_2^{2+} in the CM frame. After the DET, which occurs in a direct manner, the direction of travel of the CH_4^{2+} is unperturbed from that of the CH_4 prior to the collision. Some time after the DET, which is long enough for several rotations of the dication, the CH_4^{2+} dissociates into the observed fragments. Rotation of the CH_4^{2+} scrambles any correlation between the velocities of the fragment ions with respect to the direction of travel of the CH_4 prior to the collision; isotropic scattering is observed.

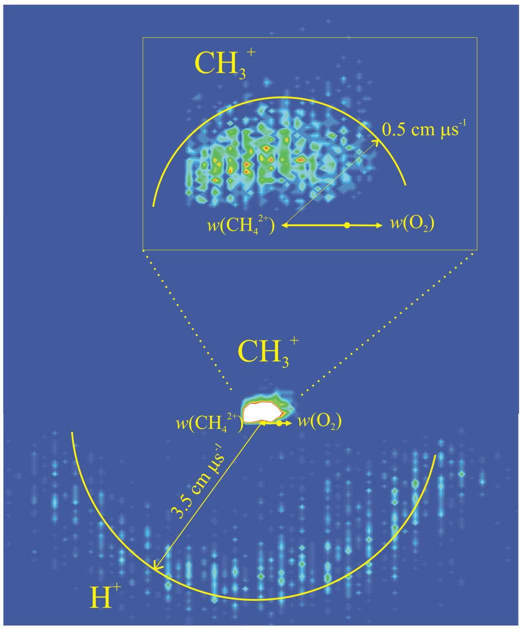

Figure 7.5 The CM frame scattering diagram for the CH_3^+ and H^+ ionic fragments arising from dissociative DET from CH_4 to O_2^{2+} at E_{COM} = 4.7 eV. The vector $w(O_2)$ denotes the velocity of the O_2 neutral, formed following the DET, in the CM frame. The vector $w(CH_4^{2+})$ denotes the velocity of the nascent methane dication formed following the DET, in the CM frame. The inset shows the scattering of the CH_3^+ fragment on a larger scale. Both the CH_3^+ and H^+ ions are scattered isotropically about the velocity of the CH_4^{2+} dication.

The CM frame scattering diagrams show that double ionisation of CH_4 *via* transfer to two electrons to O_2^{2+} can be considered as a vertical transition obeying the Born–Oppenheimer approximation. Therefore, we can compare our measured KERs upon fragmentation of the CH_4^{2+*}, in the frame of the nascent dication, with those in the literature that are measured following photoionisation. We measure peaks in the KER distributions for channels (7.8), (7.9) and (7.10) at 6.0 eV, 5.2 eV and 4.0 eV, with full-widths at half-maximum of approximately 4.5 eV, 3.5 eV and 3.5 eV, respectively. The first of these KERs, for channel (7.8) which yields CH_3^+ + H^+, has a modal value of 6.0 eV, in perfect agreement with the energy release of 6 eV for this dissociation as determined by Fournier *et al* using the photoion–photoion coincidence (PIPICO) technique[33]. For channels (7.9) and (7.10) we measure modal KERs of 5.2 eV and 4.0 eV respectively, whereas those determined by Fournier *et al* are 6 eV and 5.1 eV with an error of 0.4 eV[33]; thus, in broad agreement with our values within the stated error. Dujardin *et al* also used the PIPICO technique to measure the KER for the dissociation of CH_4^{2+} into CH_3^+ + H^+, CH_2^+ + H^+ and CH_2^+ + H_2^+ as 5.3 eV, 5 eV and 5.3 eV, respectively[34]. Hence, on the whole, our experimental KERs agree well with those measured in previous studies. However, we note that the branching ratios that we record for the dissociative DET reactions are markedly different to the branching ratios for these fragmentation channels determined by Fournier *et al.* Fournier *et al* measure relative ion abundances for the reactions forming CH_3^+ + H^+, CH_2^+ + H_2^+ and CH_2^+ + H^+ that indicate a ratio of 100 : 27 : 65[34]. Whereas the branching ratios we measure for channels (7.8) : (7.9) : (7.10) are in a ratio of 100 : 15 : 8, clearly very different to the ratio measured employing photo-fragmentation.

Neutral methane has the electronic configuration $(1a_1)^2(2a_1)^2(1t_2)^6$[33-36] with T_d symmetry. Double ionisation of methane *via* removal of two electrons from the $1t_2$ orbital gives rise to a multiplet of states: X^1T_2, $\tilde{a}^1E$, b^1T_2 and c^1A_1[33-37]. Doubly ionised methane rearranges to a planar structure of D_{4h} symmetry[34]. Several studies have shown that the vertical double IE of methane lies at approximately 35.0 eV[34,38]. Dujardin *et al* note that stable or metastable CH_4^{2+} dications formed *via* vertical ionisation have never been observed. Although, metastable CH_4^{2+} has been formed by charge stripping from CH_4^+ yielding an adiabatic double IE of 30.6 eV[34,36,39,40]. Hence, given that the direct nature of the DET from CH_4 to O_2^{2+} yielding CH_4^{2+}, we can approximate this as a vertical double ionisation process and conclude that all CH_4^{2+} dications formed in our experiment will fragment into monocations.

The studies of the double ionisation and fragmentation of CH_4^{2+} that have been carried out by Dujardin *et al*[34] and Fournier *et al*[33] can help us to elucidate the electronic states of CH_4^{2+} that are populated in the initial DET, which then dissociate into the fragments we observe. The PIPICO studies of both Fournier *et al*[33] and Dujardin *et al*[34] revealed that population of $CH_4^{2+}(X^3T_1)$ *via* vertical double ionisation at an energy of 35.0 eV results in fragmentation into $CH_3^+(X^1A_1')$ + H^+ monocations. Hence, it seems clear that the CH_3^+ + H^+ fragments detected in the PSCO experiment following DET from CH_4 to O_2^{2+} arise from population of the X^3T_1 state of CH_4^{2+}. Channels (7.9) and (7.10), which yield CH_2^+ + H_2^+ and CH_2^+ + H^+ + H, respectively, can also be adequately explained by the studies of Dujardin *et al*[34]. We also invoke the results of another study of CH_4 photo–fragmentation by Hatherly *et al*[36], which employed the photoelectron–photo–ion–photo–ion–coincidence (PEPIPICO) methodology. Dujardin *et al* determined that population of the $\tilde{a}^1E$ state of CH_4^{2+} at an energy of 38.5 eV resulted in dissociation to $CH_2^+(X^1A_1)$ + H^+ + H fragments. The PEPIPICO studies of Hatherly *et al* also reveal a similar fragmentation pathway to $CH_2^+(X^1A_1)$ + H^+ + H upon initial formation of $CH_4^{2+}(\tilde{a}^1E)$ with an onset at 38.1 eV, in general agreement with Dujardin *et al*. With regards to channel (7.9), which yields CH_2^+ + H_2^+, the above studies have shown that these fragments can also be attributed to population of $CH_4^{2+}(\tilde{a}^1E)$ at an identical onset energy of 38.1 eV as for formation of $CH_2^+(X^1A_1)$ + H^+ + H. In accord with our results from the fragmentation of CH_4^{2+*}, formed by DET with O_2^{2+}, other fragmentation channels such as formation of H^+ + H^+, H_2^+ + H_2^+ and CH^+ + H_3^+ are not seen in the PEPIPICO studies of Hatherly *et al* and they have therefore determined an upper limit for the intensity of these channels as 1% of that of the major channel.

As specified in Chapter 4 and reported by Parkes *et al*[41], a common feature of dication–neutral systems where DET occurs with appreciable branching ratio seems to be that the asymptotes of the reactant PEC and primary product PEC are typically separated by less than a few eV. Indeed, the ground state asymptote for O_2^{2+} + CH_4 is 1.1 eV higher than that for ground state O_2 + CH_4^{2+}. Such a small separation between the asymptotes brings the PEC crossing within the Landau–Zener reaction window and allows the two electrons to "hop" from the neutral to the dication in a concerted manner, rather than *via* two separate curve-crossings.

7.2.1.5 Bond-Forming Reactions

The PSCO data reveals seven distinct bond-forming reaction channels following the interaction of O_2^{2+} and CH_4. Three products are observed which involve the formation of a new chemical bond, specifically, the HO_2^+, HCO^+ and CO_2^+ monocations.

7.2.1.5.1 Formation of HO_2^+

Channels (7.14) and (7.15) involve the formation of HO_2^+ in conjunction with CH_2^+ and CH^+ as the partner ion, respectively. The CM scattering diagram for channel (7.14), that yields $HO_2^+ + CH_2^+ + H$, can be seen in Figure 7.6 and it clearly shows the anisotropic nature of the scattering of the ionic fragments.

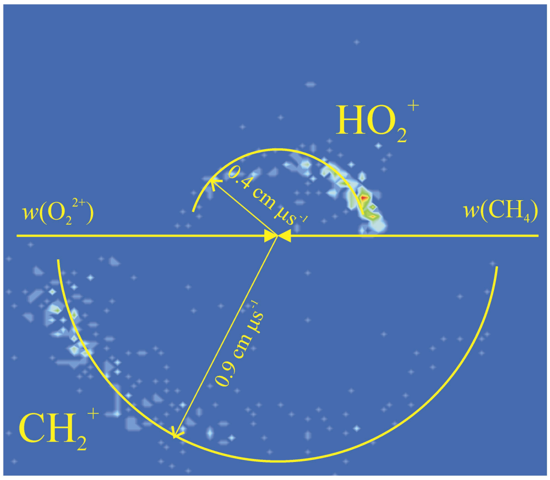

Figure 7.6 CM frame scattering diagram showing the directions of the HO_2^+ and CH_2^+ product ions following the interaction of O_2^{2+} and CH_4 at E_{CM} = 4.7 eV. Velocities of the reactants prior to the collision are indicated by the full-headed arrows. The HO_2^+ velocity is predominantly oriented in the same direction as that of the O_2^{2+} prior to the collision. The CH_2^+ velocity is anti-correlated with that of the O_2^{2+} reactant and predominantly in the direction of the CH_4 prior to the collision.

As is clear in Figure 7.6, the HO_2^+ velocity is strongly correlated with the velocity of the reactant O_2^{2+}, whereas, the CH_2^+ is anti-correlated with the velocity of the O_2^{2+} prior to the collision. Thus, we conclude that the reaction mechanism unambiguously involves "stripping" of H^- from the CH_4 by the O_2^{2+} reactant. This stripping is a direct process that does not perturb the directions of the products from those of the reactants. The nascent metastable CH_3^{+*} formed by removal of the H^- subsequently breaks down into CH_2^+ + H. We have confirmed this mechanistic conclusion by constructing internal frame scattering diagrams that reveal that the velocity of the neutral H species is anti–correlated with the velocity of the HO_2^+ ion. Moreover, the H scattering is isotropically centred about the velocity of the CH_2^+ ion. Hence, it seems clear that the nascent CH_3^{+*}, formed upon H^- transfer, later fragments into CH_2^+ + H. Analogous scattering dynamics are seen in the CM frame scattering diagram for channel (7.15), which yields HO_2^+ + CH^+ + [H + H]. Unfortunately, without making the assumption that the two H atoms formed are bound as H_2, we cannot construct internal frame scattering diagrams for this channel. Nevertheless, from the CM frame diagram alone, it seems extremely likely that an analogous mechanism to that for channel (7.14) operates, namely, direct transfer of a hydride H^- followed by fragmentation of the nascent CH_3^{+*}.

A peak in the ΔE_T spectrum is measured at 6.7 eV for channel (7.14), while the literature ground state exoergicity is 7.3 eV. Given the expected vibrational excitation of the reactant O_2^{2+} of 1.4 eV, we expect the modal internal energy of the HO_2^+ and CH_2^+ products to be around 2 eV. In channel (7.14), the product HO_2^+ may be formed in three energetically accessible electronic states, the ground X^3A'' state and the first and second excited A^1A' and B^1A'' states that lie 0.2 eV and 1.1 eV higher in energy than the ground state[42,43]. In addition, allowing for inclusion of the E_{CM} of 4.7 eV, there is a higher lying electronic state of HO_2^+ that may be accessible, specifically the $^1A'$ state that lies 2.7 eV higher than the ground state[43]. Thus, for channel (7.14) there are several electronic states of the product HO_2^+ that may be populated, but we can conclude that the molecular products of this channel will, on average, be formed with little rovibrational energy.

Channel (7.15) yields HO_2^+ + CH^+ + [2H]. For this channel we cannot unambiguously determine a ΔE_T distribution as we cannot be sure that the 2H formed are bound as H_2. However, the HO_2^+ product could again be formed in a range of electronic states since formation of HO_2^+ in the X^3A'', A^1A', B^1A'' or $^1A'$ states is exothermic if the neutral is bound as an H_2 molecule. If, however, the neutral is formed as two hydrogen atoms, then formation of the highest lying of these states, the $^1A'$ state of HO_2^+, is endothermic by 0.1 eV thereby seeming slightly less likely that it will be formed.

However, we cannot draw any further conclusions regarding the product electronic states formed in channel (7.15).

7.2.1.5.2 Formation of HCO^+

Channels (7.11), (7.12) and (7.13) involve the formation of HCO^+ in conjunction with H^+, H_2^+ and H_3^+, respectively. The CM scattering diagram for channel (7.11), Figure 7.7, shows that the velocities of the HCO^+ and H^+ ionic fragments are clearly evenly distributed over all scattering angles; analogous CM scattering is observed for channels (7.12) and (7.13). The isotropic nature of the scattering of the ionic species in the reactions forming HCO^+ suggests that the reaction mechanism proceeds *via* formation of an encounter complex between O_2^{2+} and CH_4. This $[O_2CH_4]^{2+}$ complex rotates several times, rearrangement of the constituent atoms takes place, and it then breaks down into the product ions we detect.

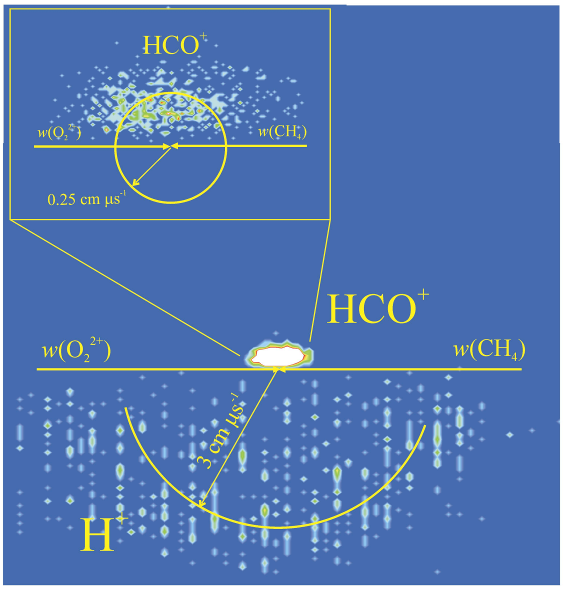

Figure 7.7 The CM scattering diagram for the production of HCO^+ and H^+ following the interaction of O_2^{2+} with CH_4 at E_{CM} = 4.7 eV. The scattering of both ionic species is isotropic with respect to the direction of the CM velocity. The vector $w(O_2^{2+})$ indicates the direction of travel of the O_2^{2+} dication prior to the collision with the neutral methane molecule.

In the case of channel (7.11), which forms $HCO^+ + H^+ + [O + 2H]$, the neutral fragments could be bound as H_2O, $H_2 + O$, $OH + H$, or they may all be in atomic form. In contrast, channel (7.13) corresponds to formation of $HCO^+ + H_3^+ + O$, where there is no doubt as to how the neutrals are bound. Hence, for channel (7.13) it was possible to construct internal frame scattering diagrams, Figure 7.8. An inherent limitation in the interpretation of these scattering diagrams is the small number of pairs that were detected for channel (7.13). However, the dynamics of this bond–forming channel can still be identified fairly reliably. Figure 7.8 (a) shows the velocities of H_3^+ and O with respect to that of the HCO^+ ion. The scattering of the H_3^+ ion is clearly anisotropic and anti–correlated with the direction of the HCO^+ velocity, unsurprising given the Coulomb repulsion between the two ions. The scattering of the neutral O is also slightly anti–correlated with the direction of the HCO^+ velocity. Figure 7.8 (b) shows the velocities of HCO^+ and H_3^+ in relation to the direction of the velocity of the neutral O. Here the scattering of the HCO^+ ion is anisotropic and anti–correlated with the velocity of the O. Unfortunately, the scattering of the H_3^+ is ambiguous in Figure 7.8 (b) but appears to be isotropic and largely not related to the direction of the velocity of the neutral O. Lastly, Figure 7.8 (c) shows the velocities of HCO^+ and O in relation to that of the H_3^+. Figure 7.8 (c) indicates that the scattering of both the HCO^+ and O is isotropic about a point centred away from the CM. Such scattering, as seen in Figure 7.8 (a–c), implies that the first step of the reaction mechanism is a fragmentation of the encounter complex into HCO_2^{+*} and H_3^+ and then a very short time later a secondary fragmentation of the intermediate HCO_2^{+*} occurs. This conclusion is drawn since the HCO^+ and O products have velocities that are slightly anti–correlated, as would arise from the fragmentation of HCO_2^{+*} with a relatively small energy release. This anti–correlation of the HCO^+ and O appears to be more pronounced than it might be in another analogous reaction that forms ionic products with more comparable masses. The vastly different masses of the HCO^+ and H_3^+ product mean that the change in the velocity of the HCO_2^+ due to the dissociation of the initial complex is very small and that of the H_3^+ is very large slightly skewing the apparent directions of the HCO^+ and O products of a secondary dissociation. Significantly, the scattering directions of the HCO^+ and O with respect to the H_3^+ direction are clearly centred away from the CM, indicating that these two products have resulted from a single, and secondary, dissociation. As mentioned above, we expect to see an obvious anti–correlation of the H_3^+ velocity with that of the HCO^+ due to the Coulomb repulsion between these ions, particularly if the second dissociation occurs in rapid succession of the first meaning that the ionic fragments are still well within the Coulombic field of each other. This interpretation is by no means exhaustive, and particularly due to the low count rate we hesitate to say it is concrete. The dynamics of the other channels forming the HCO^+ ion, channels (7.11) and (7.12), cannot be determined by construction of internal frame scattering diagrams. However, it is probable that the initial step of the reaction after complex formation may be the same in all three channels, specifically, fragmentation into HCO_2^+ and H_3^+. The nascent H_3^+ then fragments into H^+ and H_2^+ in channels (7.11) and (7.12) respectively. As discussed later, we have carried out complementary computational investigations of the $[O_2CH_4]^{2+}$ PES that may expose further details of the reaction dynamics.

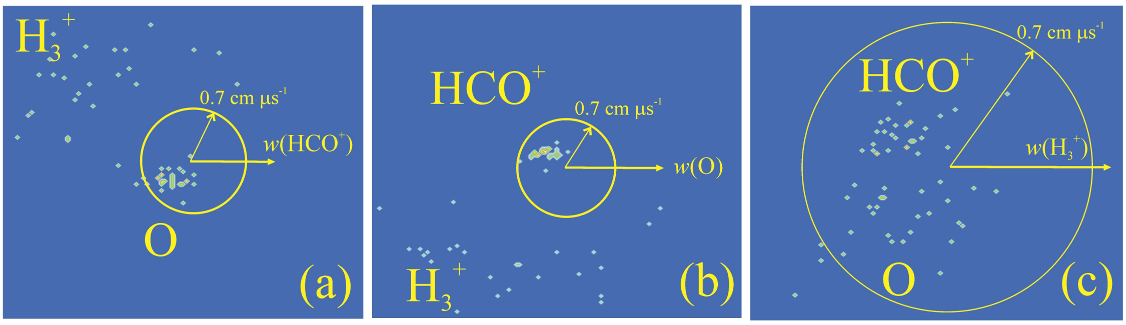

Figure 7.8 Internal frame scattering diagrams for channel (7.13), forming HCO^+ + H_3^+ + O. (a) The scattering of the H_3^+ and O fragments relative to the direction of the velocity of the HCO^+ product, indicated by the vector $w(HCO^+)$. (b) The scattering of the HCO^+ and H_3^+ product ions relative to the direction of the velocity of the O neutral species, indicated by the vector $w(O)$. (c) The scattering of the HCO^+ and O fragments relative to the direction of the velocity of the H_3^+ ion, indicated by $w(H_3^+)$.

For channel (7.11), the reactive mechanism outlined above, that leads to HCO^+ + H^+ formation, means the neutrals formed in conjunction with the ions are unlikely to be bound as H_2O or OH + H. More likely would be the formation of O + H_2 or O + H + H, giving the reaction a literature ground state exothermicity of 8.3 eV and 3.8 eV, respectively. Given their exothermic nature, both of these reaction pathways are feasible for the O_2^{2+} – CH_4 collision system. Under the mechanistic supposition described above, channel (7.12) would correspond to formation of HCO^+ + H_2^+ + O + H, which has a literature ground state exothermicity of 6.5 eV. Therefore, from a thermochemical perspective, these reaction products could also be readily formed following O_2^{2+} – CH_4 interactions.

For channel (7.13), which yields HCO^+ + H_3^+ + O products, we can construct a ΔE_T spectrum. Tentatively, due to the very low number of pairs detected, we can say that there is a peak in this ΔE_T spectrum at 5.3 eV. The ground state literature exoergicity of the reaction is 12.7 eV. For ground vibronic state reactants this would mean that the products must have, on average, 7.4 eV of internal energy between them. The dissociation energy of the HCO^+ is around 6.1 eV meaning that the H_3^+ must have at least 1.3 eV of rovibrational energy. The lowest dissociation limit of the H_3^+ molecule, to H_2 + H^+, has been calculated to lay around 4.61 eV higher than the potential well minimum[44,45], meaning 1.3 eV of internal energy can easily be accommodated.

7.2.1.5.3 Formation of CO_2^+

Following interactions of O_2^{2+} with CH_4 we detect CO_2^+ products in conjunction with H^+ (channel (7.16)) and H_2^+ (channel (7.17)). Formation of $O{=}C{=}O^+$ from O_2^{2+} + CH_4 reactants is somewhat surprising due to the large atomic rearrangement that must take place. The branching ratio for reactions forming CO_2^+ is only 3% of all the bond–forming channels and only 0.23% of all the detected reactions, so CO_2^+ is certainly a minor product of the interaction of O_2^{2+} with CH_4. Construction of the CM scattering diagram for channel (7.16), which yields the products CO_2^+ + H^+ + 3H, reveals that the scattering of both the CO_2^+ and H^+ product ions is isotropic in the CM frame. Therefore, unsurprisingly given the large amount of atomic rearrangement required the reaction proceeds *via* formation of a 'long–lived' encounter complex. Despite the very low numbers of pairs detected, the CM frame scattering for channel (7.17) also seems to show isotropic scattering of the product ions. We have already determined that the HCO^+ products we detect arise from fragmentation of an encounter complex that survives long enough for several rotations. Clearly, the formation of CO_2^+ from such a complex results from a different journey across the PES. The O_2^{2+} – CH_4 PES has been probed employing computational methods, as described in the next section.

7.2.1.6 Computational Investigations of the Reaction Dynamics

We have carried out a preliminary *ab initio* study into the O_2^{2+} – CH_4 potential energy surface using the Gaussian '98 suite[46] and employing Møller–Plesset Theory (MP2). This investigation has revealed several potential minima for complexes formed between the two reactant species and also other possible intermediates on the route to the detected products. Minima were found using the correlation–consistent polarized VDZ basis set and assigned as real minima or transition states by frequency analysis. To check the accuracy of the MP2 calculations, equivalent optimisations and energy calculations were done using density functional theory using the Becke, three–parameter, Lee–Yang–

Parr (B3LYP) exchange–correlation functional and good general agreement was found. The collision system under investigation has seven atoms and as such there are many degrees of freedom on the PES. Indeed it was found that there are many minima that involve skeletal rearrangement that can be accessed when O_2^{2+} and CH_4 interact, these can be seen in Figure 7.9 and Figure 7.10. The oxygen dication has a singlet ground state and so the entry channel refers to a singlet potential energy surface.

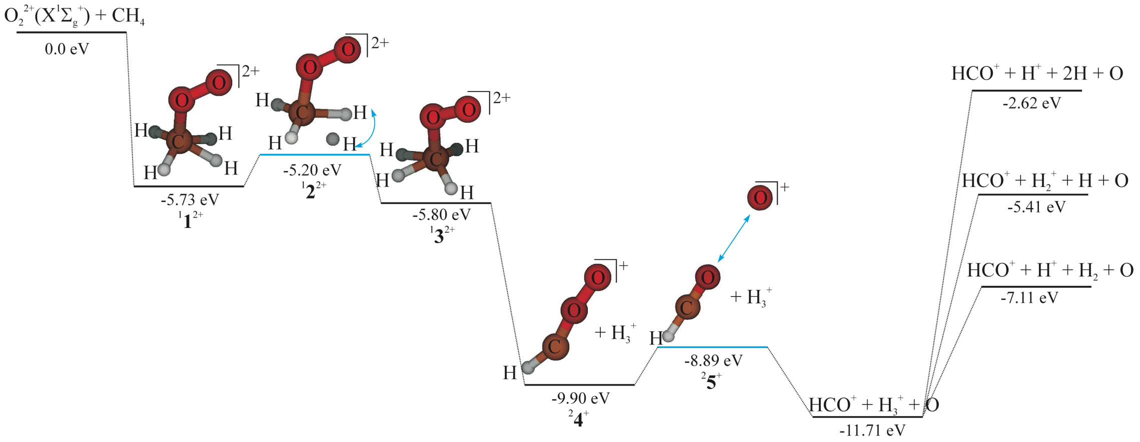

Figure 7.9 Minima on the $[O_2–CH_4]^{2+}$ potential energy surface found using MP2 theory and a cc-pVDZ basis set. The minima found connect the reactant asymptote with the HCO+ product channels. Blue lines indicate transition states and the blue arrows indicate the imaginary frequency.

Experiments show that following interactions of O_2^{2+} with CH_4 two products are formed *via* a "long-lived" complex, these are the HCO^+ and CO_2^+ ions. From our calculations, formation of HCO^+ has been attributed to the passage across the PES that is linked by the minima shown in Figure 7.9, whereas formation of CO_2^+ has been attributed to the passage across the PES that is linked by the minima shown in Figure 7.10. In Figure 7.9, formation of the encounter complex $^1\mathbf{1}^{2+}$ is exothermic by 5.73 eV. This initial complex can isomerise *via* a transition state $^1\mathbf{2}^{2+}$ to a slightly lower energy form, $^1\mathbf{3}^{2+}$. Loss of an H_3^+ molecule from the encounter complex results in $^2\mathbf{4}^+$. This HCO_2^+ minimum can be linked to the observed products by a transition state, $^2\mathbf{5}^+$. These calculations predict that formation of HCO^+ in conjunction with H_3^+ and O is exothermic by 11.71 eV, whereas, the literature ground state value for this exothermicity is 12.7 eV. Thus, given the rather small basis set used in our calculations, a satisfactory agreement is obtained between our theory and the literature value. Clearly, a better agreement could be achieved by using a larger basis set or more accurate computational methodology.

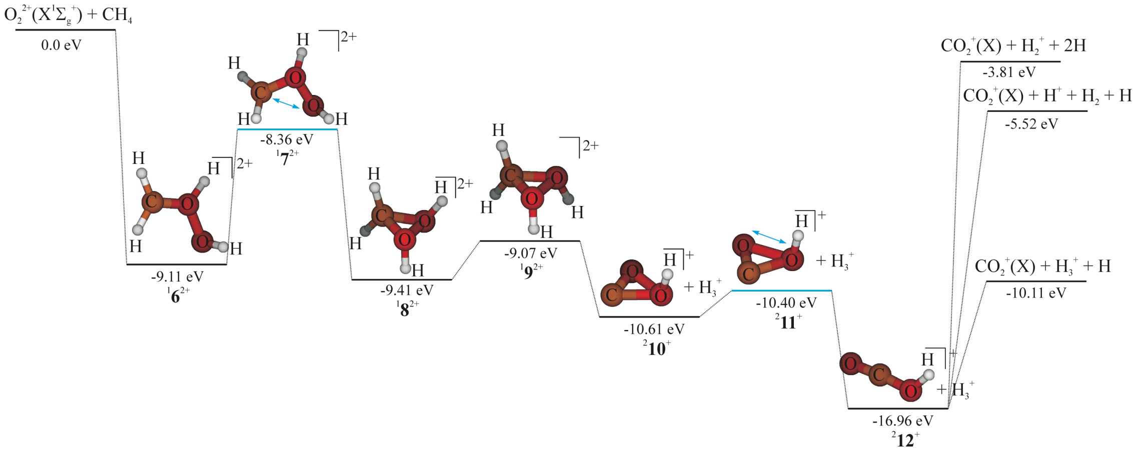

Figure 7.10 Minima on the $[O_2–CH_4]^{2+}$ potential energy surface found using MP2 theory and a cc-pVDZ basis set. The minima found connect the reactant asymptote with the CO_2+ product channels. Blue lines indicate transition states and the blue arrows indicate the imaginary frequency.

Shown in Figure 7.10, formation of a different encounter complex $^1\mathbf{6}^{2+}$ is exothermic by 9.11 eV. The O–O–C ring is closed to form $^1\mathbf{8}^{2+}$ or $^1\mathbf{9}^{2+}$ *via* a transition state, $^1\mathbf{7}^{2+}$. Loss of an H_3^+ molecule leads to another cyclic compound $^2\mathbf{10}^+$, which can then be linked *via* a ring-opening transition state, $^2\mathbf{11}^+$, to an O–C–O–H^+ monocation, $^2\mathbf{12}^+$. Our calculations predict that formation of this HCO_2^+ in conjunction with an H_3^+ ion is exothermic by 16.96 eV. So clearly, there is a huge energetic impetus for chemical channels to occur.

7.2.1.7 Conclusion

The reactions that form a pair of ions, which occur between O_2^{2+} and CH_4 at E_{CM} of 4.7 eV have been investigated employing the PSCO technique. The chemistry between these two species is very rich and seventeen different reaction channels have been detected. The majority of reactive events (around 84 %) result in SET, DET occurs in around 9 % and chemical channels in around 8 %. This branching ratio for bond-forming chemistry is comparatively high compared to previous systems where bond-formation is observed after dication-neutral interactions[47–56]. Interestingly, the connectivity of the reactant atoms is dramatically altered in some of the product ions, particularly in the formation of CO_2^+. We also detect HCO^+ (or COH^+) and HO_2^+ products that involve formation of new chemical bonds. The CM frame scattering diagrams we can construct show that formation of HO_2^+ occurs by a direct process of stripping an H^- from the CH_4. Conversely, formation of HCO^+ and CO_2^+ occur *via* formation of a complex between the reactants that is relatively 'long–lived' as it survives for several rotations. In order to understand the nature of this complex and try to explain how it falls apart to give the observed ions, a computational investigation was carried out. Stationary points were found on the O_2^{2+}–CH_4 PES that can be linked in such a way that largely agrees with our proposed reaction mechanism for the bond–forming channels.

Several interesting features of the SET reactivity have also been determined. The non–dissociative SET has been shown to form the ground electronic state CH_4^+ but the O_2^+ must be formed in either the $a^4\Pi_u$, $A^2\Pi_u$ or $b^4\Sigma_g^-$ excited electronic states. The electronic states involved in all of the separate dissociative SET channels, of which there are six, have been determined and the majority of these dissociations can be accounted for by population of the unbound A^2A_1 state of CH_4^+. When the primary product of electron transfer is $CH_4^+(A^2A_1)$, then the partner O_2^+ must be formed in the ground $X^2\Pi_g$ state, in contrast to the non–dissociative SET reactions.

7.2.2 Reactions of O_2^{2+} with C_2H_2, C_2H_4 and C_6H_6

Reactions between O_2^{2+} and C_2H_2, C_2H_4 and C_6H_6 have been investigated employing the PSCO methodology. Only a brief overview of the observed reactivity will be given here. Table 7.2 shows the reactions occurring between O_2^{2+} and C_2H_2, which form a pair of ions, at E_{CM} of 4.5 eV. Like the O_2^{2+} – CH_4 collision system described earlier, a very rich and complex chemistry is observed and we detect seventeen distinct reaction channels (coincidentally the same number as for the O_2^{2+} – CH_4 system). Again, similarly to the results from the O_2^{2+} – CH_4 collisions, our data reveal that SET, DET and chemical processes occur following O_2^{2+} – C_2H_2 interactions. Compared to the O_2^{2+} – CH_4 collision system, in the O_2^{2+} – C_2H_2 system approximately the same proportion of events involve SET, whereas a much smaller proportion involve DET and we detect a slightly greater branching ratio for bond–forming chemistry. What is striking from Table 7.2 are the large array, and intriguing nature, of product ions formed that involve formation of new bonds. Specifically, we detect HCO^+, CO^+, C_2OH^+ and C_2O^+ ions, and the former two are formed in conjunction with several different partner ions.

Table 7.2 Reaction channels that form a pair of ions that are detected following interactions of O_2^{2+} with C_2H_2 at E_{CM} of 4.5 eV. Also shown is the branching ratio, which is the percentage the pairs in that channel represent of the sum of the number of pairs in all channels. Where possible we present the measured modal energy release for the reaction channel ΔE_T in addition to a ground state literature value ΔH_{lit}. If more than one neutral atom is formed in the reaction, then the bonding of these neutrals has been assumed on the basis of scattering diagrams and/or structural reasons, see text for details.

Channel	**Products**	**Branching Ratio / %**	**ΔE_T/ eV**	**ΔH_{lit} / eV**
	Single ET	**87.5**		
7.18	$O_2^+ + C_2H_2^+$	12.4	–5.7	–12.7
7.19	$O_2^+ + C_2H^+ + H$	38.0	–8.0	–7.6
7.20	$O_2^+ + C_2^+ + 2H$	0.9	–[a]	–1.8
7.21	$O_2^+ + CH_2^+ + C$	0.4	–[a]	–4.6
7.22	$O_2^+ + CH^+ + CH$	0.4	–[a]	–3.4
7.23	$O_2^+ + H^+ + C_2H$	0.3	–[a]	–5.6
7.24	$O^+ + O + C_2H_2^+$	35.1	–5.7	–17.4
	Double ET	**2.6**		
7.25	$C_2H^+ + H^+ + O_2$	1.0	–[a]	–6.1
7.26	$CH^+ + H^+ + C + O_2$	1.6	–[a]	+1.6
	Bond Forming	**9.95**		
7.27[b]	$HCO^+ + CH^+ + O$	5.5	–4.5	–10.5
7.28[b]	$HCO^+ + C^+ + O + H$	0.6	–[a]	–6.4
7.29	$CO^+ + H^+ + CH + O$	0.4	–[a]	–1.0
7.30	$CO^+ + CH_2^+ + O$	1.3	–5.4	–8.7
7.31	$CO^+ + CH^+ + O + H$	1.7	–[a]	–4.0
7.32	$CO^+ + C^+ + O + 2H$	0.3	–[a]	+0.2
7.33	$C_2OH^+ + H^+ + O$	0.05	–[a]	–[c]
7.34	$C_2O^+ + H^+ + O + H$	0.1	–[a]	–[c]

[a] For these reactions where more than a single atomic neutral is formed, we cannot calculate a translational exothermicity as the velocity of the neutral cannot be calculated by conservation of momentum with the ionic products.

[b] Our technique only allows for the determination of the mass–to–charge ratio of a product. Hence HCO^+ may alternatively be bound as COH^+. However, we assume that the HCO^+ structure is formed since this isomer is lower in energy than the COH^+ structure by 1.63 eV[19].

[c] Literature values for the enthalpy of formation of C_2OH^+ and C_2O^+ are not available and so ΔH_{lit} cannot be calculated for these channels.

The large literature value for the exoergicity of the non–dissociative SET reaction (channel (7.18)), compared to the value of 5.7 eV that we measure, leads us to conclude that these products are electronically and/or rovibrationally excited by around 8.4 eV between them. The ground state literature exothermicity for channel (7.24), which yields O^+ in coincidence with $C_2H_2^+$, is also very large at 17.4 eV. So, when this large literature exothermicity is compared to our measured value, we conclude that in channel (7.24) there is a lot of electronic and/or rovibrational excitation of the products. It is interesting to note that for the O_2^{2+} – CH_4 collision system we do not detect the equivalent of channel (7.24) of the O_2^{2+} – C_2H_2 system, that is, dissociative SET where the nascent O_2^+ breaks down rather than the ion formed from the neutral. We can only suppose that this subtle difference is due to the lower IE of C_2H_2 than CH_4. Channels (7.20), (7.22) and (7.23) involve formation of more than one atomic neutral species. We propose, based on the structure of acetylene monocations, that dissociation of the $C_2H_2^{+*}$ to form C_2^+ (channel (7.20)) will be more likely to also form two H atoms rather than an H_2 molecule. When ground state O_2^{2+} and C_2H_2 react to form O_2^+ + CH^+ + C + H, this process is endothermic by 0.1 eV. Thus, we propose that in channel (7.22), the neutrals remain bound as a CH molecule. In terms of channel (7.23), if the neutral is formed as 2C + H, C_2 + H or CH + C, then the reaction becomes endothermic for ground state reactants. Thus, is seems more likely that in channel (7.23) the neutral remains bound as C_2H. Very strong forward scattering is observed in the CM frame scattering diagrams for all of the SET channels. Therefore, SET between O_2^{2+} and C_2H_2 is a direct process with little or no longer–term interaction of the reactants.

Channels (7.25) and (7.26) correspond to dissociative DET. Channel (7.25) is exothermic for ground state reactants, but channel (7.26) is endothermic by 1.6 eV. Therefore it is somewhat surprising that we detect the CH^+ + H^+ products of channel (7.26) in coincidence. However, the O_2^{2+} dications in out beam will generally not be in their ground vibrational level and levels up to v = 6 are expected to be appreciably populated. The v = 6 level of O_2^{2+} lies 1.63 eV higher than v = 0, meaning channel (7.26) would be very slightly exothermic for $O_2^{2+}(X^1\Sigma_g^+, v = 6)$ reactants. Moreover, we introduce around 4.5 eV of energy to this reactive system in the form of the CM collision energy.

The CM frame scattering diagrams for the DET channels leads us to conclude that the process is direct and there is little long term interaction of the reactants.

What is most interesting about the O_2^{2+} – C_2H_2 collision system are the large number of chemical channels that are detected. None of the chemical channels has a huge branching ratio but the overall fraction of reactive events that lead to bond-forming chemistry is quite high at nearly 10 %. HCO^+ and CO^+ products are formed in conjunction with several different partner ions, specifically CH^+ and C^+ with HCO^+, and H^+, CH_2^+, CH^+ and C^+ with CO^+. We also detect the unusual ions C_2OH^+ and C_2O^+ following interactions of O_2^{2+} with C_2H_2, however, these channels have very small branching ratios. The CM frame scattering diagram for channel (7.27), yielding HCO^+ + CH^+ + O, is shown in Figure 7.11.

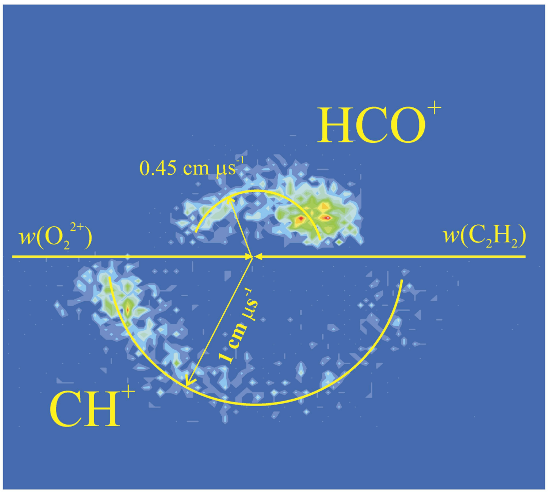

Figure 7.11 CM frame scattering of the HCO^+ and CH^+ products resulting from O_2^{2+} – C_2H_2 interactions at E_{CM} of 4.5 eV. Directions of the reactants prior to the collision are indicated by the full-headed arrows.

What is clear from Figure 7.11 is that the general scattering directions of the ionic products are still somewhat similar to the directions of the reactants prior to the collision; isotropic scattering is *not* observed. Such scattering associated with bond-forming chemistry has been observed before between Ar^{2+} and C_2H_2, where ArC^+ is formed by a rapid stripping of CH^- by the Ar^{2+} dication from C_2H_2. This CH^- stripping initially forms $ArCH^+$, yet in both reaction channels where this mechanism is observed, there is a secondary dissociation leading to the detected ArC^+ ion (see Chapter 4 or reference [41]). Consequently, it seems clear that an analogous reaction mechanism is operating here, forming HCO^+ from O_2^{2+} – C_2H_2 interactions. As the O_2^{2+} flies past the C_2H_2, it strips a

CH^- fragment from the neutral forming O_2CH^+ ions. These metastable O_2CH^+ ions then fragment to the detected HCO^+ product and a neutral O. The cleavage of the C–C bond of acetylene leaves a CH^+ fragment behind that we detect in coincidence with HCO^+ in channel (7.27), but this CH^+ can also fragment to C^+ resulting in channel (7.28). It is for this reason that we assume that the H and O formed in channel (7.28) are not bound as OH as they are formed as the result of two separate dissociations. The large ground state literature exothermicity for channel (7.27) and the relatively small energy release we measure clearly indicate that the $HCO^+ + CH^+ + O$ products of channel (7.27) are highly electronically or rovibrationally excited. Ultimately, such highly excited products could go on to react with other neutrals in reactions that have an activation energy barrier, or that would be endothermic for ground state species. Thus, excited species such as these products of O_2^{2+} – C_2H_2 reactions could influence the chemistry of trace species in environments such as the ionosphere of Titan or Earth.

The CM frame scattering diagrams for channels (7.29) – (7.32), channels that yield CO^+ products, are somewhat ambiguous as the scattering of the products is more isotropic than for the HCO^+ products, but in some cases there also appears to be a weak anisotropy. Therefore, we do not propose a reaction mechanism for the formation of CO^+ following interaction of O_2^{2+} with C_2H_2. Both channels (7.33) and (7.34) are extremely weak, but the CM frame scattering seems to suggest that C_2OH^+ and C_2O^+ are created *via* the formation of a relatively long–lived complex between the reactants. Clearly, further work needs to be carried out to understand this intriguing O_2^{2+} – C_2H_2 PES in more detail; computational methods could be employed to model the rich reactivity between these species.

The PSCO methodology has also been used to study the reactions occurring, that form a pair of ions, between O_2^{2+} and C_2H_4 and C_6H_6. In both of these systems chemical channels have been detected; in the former, these yield HCO^+ and $C_2OH_2^+$ and in the latter the only bond–forming product is HCO^+. Although, following interaction of O_2^{2+} with C_6H_6, the percentage of events that yield HCO^+ products is fairly high at 14 %. Clearly, O_2^{2+} reacts in a number of interesting ways with organic molecules and there is a rich chemistry that deserved to be investigated further.

7.3 Conclusion

An extensive analysis of the energetics and dynamics of the seventeen reaction channels that occur between O_2^{2+} and CH_4, that form a pair of ions, has been carried out. There have been no prior studies of the reactivity in the collision systems presented in this chapter, so the information presented in this chapter is entirely novel and reveals that extensive chemistry, both electron–transfer and bond–forming, occurs between O_2^{2+} dications and small organic molecules. Clearly, the reactions occurring between O_2^{2+} and C_2H_2, C_2H_4 and C_6H_6, where extensive bond–forming chemistry is detected, have not been analysed as fully as for the O_2^{2+} – CH_4 system and this is an obvious extension to this work. A further extension to this work would be to complete the investigation into the complicated PES and many stable complexes that can be formed between O_2^{2+} and CH_4. We have shown, using the PSCO technique, that O_2^{2+} reactions with small organic species, such as those found in the ionosphere of Titan or Earth, readily lead to C–O bond–formation. Given that the only oxygen containing species detected on Titan thus far include CO and CO_2, it is clearly important to understand how these C–O bonds were formed and reactions of O_2^{2+} with basic organic molecules may be one possibility.

7.4 References

[1] F. H. Dorman and J. D. Morrison, **1963**, *39*, 1906–&

[2] R. I. Hall, G. Dawber, A. McConkey, M. A. Macdonald and G. C. King, *Phys. Rev. Lett.* **1992**, *68*, 2751–2754

[3] M. Larsson, P. Baltzer, S. Svensson, B. Wannberg, N. Martensson, A. N. Debrito, N. Correia, M. P. Keane, M. Carlssongothe and L. Karlsson, *J. Phys. B* **1990**, *23*, 1175–1195

[4] L. G. M. Pettersson and M. Larsson, *J. Chem. Phys.* **1991**, *94*, 818–819

[5] M. Lundqvist, D. Edvardsson, P. Baltzer, M. Larsson and B. Wannberg, *J. Phys. B–At. Mol. Opt. Phys.* **1996**, *29*, 499–514

[6] A. C. Hurley, *J. Mol. Spectrosc.* **1962**, *9*, 18–&

[7] A. C. Hurley and V. W. Maslen, *J. Chem. Phys.* **1961**, *34*, 1919–&

[8] S. D. Price and J. H. D. Eland, *J. Phys. B* **1991**, *24*, 4379–4389

[9] M. W. Wong, R. H. Nobes, W. J. Bouma and L. Radom, *J. Chem. Phys.* **1989**, *91*, 2971–2979

[10] B. K. Chatterjee and R. Johnsen, *J. Chem. Phys.* **1989**, *91*, 1378–1379

[11] R. Feifel, J. H. D. Eland and D. Edvardsson, *J. Chem. Phys.* **2005**, *122*, 10

[12] C. Simon, J. Lilensten, O. Dutuit, R. Thissen, O. Witasse, C. Alcaraz and H. Soldi–Lose, *Ann. Geophys.* **2005**, *23*, 781–797

[13] L. W. Esposito, J. E. Colwell, K. Larsen, W. E. McClintock, A. I. F. Stewart, J. T. Hallett, D. E. Shemansky, J. M. Ajello, C. J. Hansen, A. R. Hendrix, R. A. West, H. U. Keller, A. Korth, W. R. Pryor, R. Reulke and Y. L. Yung, *Science* **2005**, *307*, 1251–1255

[14] R. I. Kaiser, P. Maksyutenko, C. Ennis, F. T. Zhang, X. B. Gu, S. P. Krishtal, A. M. Mebel, O. Kostko and M. Ahmed, *Faraday Discuss.* *147*, 429–478

[15] R. E. Samuelson, W. C. Maguire, R. A. Hanel, V. G. Kunde, D. E. Jennings, Y. L. Yung and A. C. Aikin, *J. Geophys. Res–Space Phys.* **1983**, *88*, 8709–8715

[16] B. L. Lutz, C. Debergh and T. Owen, *Science* **1983**, *220*, 1374–1375

[17] A. Coustenis, A. Salama, E. Lellouch, T. Encrenaz, G. L. Bjoraker, R. E. Samuelson, T. de Graauw, H. Feuchtgruber and M. F. Kessler, *Astron. Astrophys.* **1998**, *336*, L85–L89

[18] J. Glosik, A. B. Rakshit, N. D. Twiddy, N. G. Adams and D. Smith, *J. Phys. B–At. Mol. Opt. Phys.* **1978**, *11*, 3365–3379

[19] Y. Yamaguchi, C. A. Richards and H. F. Schaefer, *J. Chem. Phys.* **1994**, *101*, 8945–8954

[20] J. A. R. Samson and J. L. Gardner, *J. Chem. Phys.* **1977**, *67*, 755–758

[21] N. H. F. Beebe, E. W. Thulstrup and A. Andersen, *J. Chem. Phys.* **1976**, *64*, 2080–2093

[22] T. A. Field and J. H. D. Eland, *J. Elec. Spec. Rel. Phen.* **1995**, *73*, 209–216

[23] M. C. Gothe, B. Wannberg, L. Karlsson, S. Svensson, P. Baltzer, F. T. Chau and M. Y. Adam, *J. Chem. Phys.* **1991**, *94*, 2536–2542

[24] O. Dutuit, M. Aitkaci, J. Lemaire and M. Richardviard, *9th International Conference on Vacuum Ultraviolet Radiation Physics (Vuv 9)*, **1989,** Honolulu (Hawaii), 223–226

[25] K. Lammertsma, P. V. Schleyer and H. Schwarz, *Angew. Chem.–Int. Edit. Engl.* **1989**, *28*, 1321–1341

[26] X. M. Liu and D. E. Shemansky, *J. Geophys. Res–Space Phys.* **2006**, *111*, 17

[27] P. Plessis, P. Marmet and R. Dutil, *J. Phys. B–At. Mol. Opt. Phys.* **1983**, *16*, 1283-1294

[28] W. A. Chupka and J. Berkowit, *J. Chem. Phys.* **1971**, *54*, 4256

[29] Stockbau.R, *J. Chem. Phys.* **1973**, *58*, 3800–3815

[30] C. Backx and M. J. Vanderwiel, *J. Phys. B–At. Mol. Opt. Phys.* **1975**, *8*, 3020–3033

[31] C. J. Latimer, R. A. Mackie, A. M. Sands, N. Kouchi and K. F. Dunn, *J. Phys. B–At. Mol. Opt. Phys.* **1999**, *32*, 2667–2676

[32] J. A. R. Samson, G. N. Haddad, T. Masuoka, P. N. Pareek and D. A. L. Kilcoyne, *J. Chem. Phys.* **1989**, *90*, 6925–6932

[33] P. G. Fournier, J. Fournier, F. Salama, P. J. Richardson and J. H. D. Eland, *J. Chem. Phys.* **1985**, *83*, 241–246

[34] G. Dujardin, D. Winkoun and S. Leach, *Phys. Rev. A* **1985**, *31*, 3027–3038

[35] E. Kukk, G. Prumper, R. Sankari, M. Hoshino, C. Makochekanwa, M. Kitajima, H. Tanaka, H. Yoshida, Y. Tamenori, E. Rachlew and K. Ueda, *J. Phys. B–At. Mol. Opt. Phys.* **2007**, *40*, 3677–3692

[36] P. A. Hatherly, M. Stankiewicz, L. J. Frasinski, K. Codling and M. A. Macdonald, *Chem. Phys. Lett.* **1989**, *159*, 355–360

[37] E. M. Siegbahn, *Chem. Phys.* **1982**, *66*, 443–452

[38] J. H. D. Eland, *Chem. Phys.* **2006**, *323*, 391–396

[39] T. Ast, C. J. Porter, C. J. Proctor and J. H. Beynon, *Chem. Phys. Lett.* **1981**, *78*, 439–441

[40] M. Rabrenovic, A. G. Brenton and J. H. Beynon, *Int. J. Mass Spectrom. Ion Process.* **1983**, *52*, 175–182

[41] M. A. Parkes, J. F. Lockyear and S. D. Price, *Int. J. Mass Spectrom.* **2009**, *280*, 85-92

[42] J. M. Robbe, M. Monnerville, G. Chambaud, P. Rosmus and P. J. Knowles, *Chem. Phys.* **2000**, *252*, 9–16

[43] M. L. Senent, *Mol. Phys.* **1999**, *96*, 1587–1594

[44] R. Prosmiti, O. L. Polyansky and J. Tennyson, *Chem. Phys. Lett.* **1997**, *273*, 107-114

[45] R. Rohse, W. Kutzelnigg, R. Jaquet and W. Klopper, *J. Chem. Phys.* **1994**, *101*, 2231–2243

[46] M. J. Frisch, G. W. Trucks, H. B. Schlegel, G. E. Scuseria, M. A. Robb, J. R. Cheeseman, V. G. Zakrzewski, J. A. M. Jr., R. E. Stratmann, J. C. Burant, S. Dapprich, J. M. Millam, A. D. Daniels, K. N. Kudin, M. C. Strain, O. Farkas, J. Tomasi, V. Barone, M. Cossi, R. Cammi, B. Mennucci, C. Pomelli, C. Adamo, S. Clifford, J. Ochterski, G. A. Petersson, P. Y. Ayala, Q. Cui, K. Morokuma, D. K. Malick, A. D. Rabuck, K. Raghavachari, J. B. Foresman, J. Cioslowski, J. V. Ortiz, A. G. Baboul, B. B. Stefanov, G. Liu, A. Liashenko, P. Piskorz, I. Komaromi, R. Gomperts, R. L. Martin, D. J. Fox, T. Keith, M. A. Al–Laham, C. Y. Peng, A. Nanayakkara, M. Challacombe, P. M. W. Gill, B. Johnson, W. Chen, M. W. Wong, J. L. Andres, C. Gonzalez, M. Head–Gordon, E. S. Replogle and J. A. Pople, *Gaussian, Inc,* Pittsburgh PA, **1998**

[47] D. Ascenzi, P. Franceschi, P. Tosi, D. Bassi, M. Kaczorowska and J. N. Harvey, *J. Chem. Phys.* **2003**, *118*, 2159–2163

[48] P. W. Burnside and S. D. Price, *Int. J. Mass Spectrom.* **2006**, *249*, 279–288

[49] P. W. Burnside and S. D. Price, *Phys. Chem. Chem. Phys.* **2007**, *9*, 3902–3913

[50] S. M. Harper, S. W. P. Hu and S. D. Price, *J. Chem. Phys.* **2004**, *121*, 3507–3514

[51] D. Kearney and S. D. Price, *Phys. Chem. Chem. Phys.* **2003**, *5*, 1575–1583

[52] N. Lambert, D. Kearney, N. Kaltsoyannis and S. D. Price, *J. Am. Chem. Soc.* **2004**, *126*, 3658–3663

[53] J. F. Lockyear, C. L. Ricketts, M. A. Parkes and S. D. Price, *Chem. Sci. 2*, 150–156

[54] W. Y. Lu, P. Tosi and D. Bassi, *J. Chem. Phys.* **2000**, *112*, 4648–4651

[55] K. A. Newson and S. D. Price, *Chem. Phys. Lett.* **1998**, *294*, 223–228

[56] K. A. Newson, N. Tafadar and S. D. Price, *J. Chem. Soc.–Faraday Trans.* **1998**, *94*, 2735–2740

Chapter 8: The Oxygen Dication Part II – Selected Reactions of O_2^{2+} with Neutral Species

8.1 Introduction

The previous chapter reported the reactivity of O_2^{2+} with several organic species; it was observed that chemical reactivity has a relatively high branching ratio and complexity in these collision systems. This chapter will report the reactivity we detect following collisions of O_2^{2+} with a variety of neutral atoms and small molecules. More specifically, in Chapter 8 are reported the reactions of O_2^{2+} with Ne, Ar, N_2, NO, N_2O, NH_3, CO, CO_2, OCS, CS_2, H_2O and H_2S. The key feature of the reactivity reported in this chapter is that chemical rearrangement is not prevalent; products from SET or DET dominate.

8.2 Results

8.2.1 O_2^{2+} + Rg (Rg = Ne, Ar)

Reactions of O_2^{2+} with the rare gasses Ne and Ar have been studied employing the PSCO technique. Clearly, in these systems there are very few possible reaction channels, namely SET where the only dissociative channel results in fragmentation of the nascent O_2^+ into O^+ + O. DET is impossible in collisions with Ne due to its very high double IE, which is higher than that of O_2. The double IE of Ar is also higher than that of O_2 and thus DET would be impossible at zero E_{CM}, however, at our E_{CM} of 7.8 eV DET becomes exothermic by a meager 0.5 eV. Therefore, despite the fact that it is not completely energetically inaccessible in the O_2^{2+} – Ar collision system, DET is clearly still rather unlikely. Following interaction of O_2^{2+} with Ne we only observe non–dissociative SET and with Ar we see both non–dissociative and dissociative SET. These reactions are detailed in Table 8.1. In the MS recorded following interactions of O_2^{2+} with Ar we see no evidence of formation of Ar^{2+} products, therefore we can say that in this collision–system DET does not occur with any statistically significant branching ratio.

Table 8.1 Products of the reaction between O_2^{2+} and Ne at E_{CM} of 3.85 eV and Ar at E_{CM} of 7.8 eV. The branching ratio for a channel *R* is given as a percentage of total number of pairs detected for all channels.

Channel	Branching Ratio *R* / %	Reaction No.
$O_2^{2+} + Ne \rightarrow O_2^{+} + Ne^{+}$	100	(8.1)
$O_2^{2+} + Ar \rightarrow O_2^{+} + Ar^{+}$	79.8	(8.2)
$O_2^{2+} + Ar \rightarrow O^{+} + O + Ar^{+}$	20.2	(8.3)

As has been exploited before by Chatterjee and Johnsen[1], the non–dissociative SET reaction between O_2^{2+} and Ne can tell us something about the vibrational distribution in the O_2^{2+} ($X^1\Sigma_g^+$) reactant since there are no internal degrees of freedom in the product Ne^+. We also know that only the ground electronic state of Ne^+ will be produced as the first excited state lies 26.9 eV higher than the ground ^2P state, rendering it energetically inaccessible to the reactants. A plot of the energy release spectrum for the non–dissociative SET reaction between O_2^{2+} and Ne, measured using the PSCO technique, is shown in Figure 8.1. As is clear in Figure 8.1, this energy release is peaked at about 4.2 eV and has a full–width–at–half–maximum (FWHM) of around 2 eV. Also shown in Figure 8.1 are four vertical red lines that represent the literature energy releases for populating, from ground state reactants, the v = 0 level of the $X^4\Pi_g$, $a^2\Pi_u$, $A^4\Pi_u$ and $b^4\Sigma_g^-$ electronic states of O_2^+ in conjunction with $Ne^+(X^2P)$. As seen in Figure 8.1, the formation of O_2^+ in the $a^2\Pi_u$, $A^4\Pi_u$ or $b^4\Sigma_g^-$ states, along with ground state Ne^+, is endothermic by around 2 eV, 3 eV and 3.6 eV respectively. Clearly, from Figure 8.1, these energy releases do not correspond to the measured KER meaning it is highly unlikely that these electronic states are involved in the SET reaction. Thus, we are only left with one possible electronic state of O_2^+ that can be populated, the ground $X^2\Pi_g$ state, which should result in a vibrationless exothermicity of reaction of around 2.5 eV. Clearly, (Figure 8.1) this still does not exactly match our measured modal exothermicity of 4.2 eV.

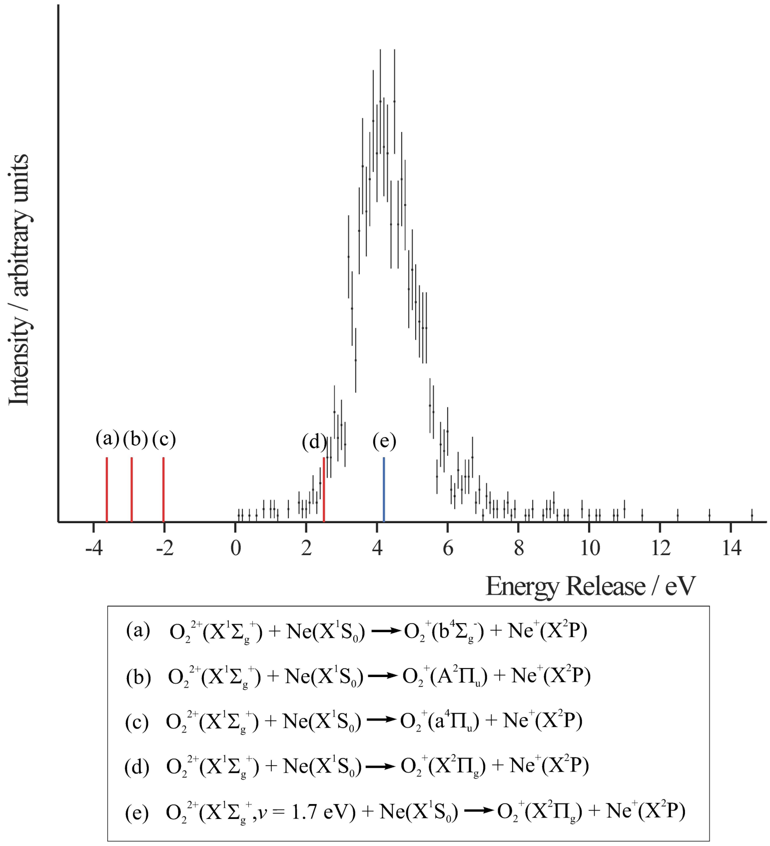

Figure 8.1 Energy release spectrum recorded following SET between O_2^{2+} and Ne to form O_2^+ + Ne^+. Error bars are given by Poissonian statistics. Also shown by the vertical red lines labelled (a) – (d) are ground vibrational state literature exothermicities for the SET reactions forming four different stable states of O_2^+. The blue vertical line shows the literature exothermicity for the SET reaction forming ground state products but from vibrationally excited O_2^{2+} reactants.

As discussed earlier, measurements of the vibrational population distribution of O_2^{2+} formed from O_2 show that the dicationic v = 0 state does not have the strongest Franck–Condon factor and that the v = 4, 5 and 6 levels are more likely to be populated[2,3]. These vibrational levels have energies 1.2, 1.40 and 1.63 eV above v = 0. In fact, if we assume a slightly higher internal energy of 1.7 eV in the reactant O_2^{2+}, reacting to form ground state products, then we exactly reproduce the modal experimental exothermicity for the reaction (8.1). Therefore, we can say with some certainty that the reactant O_2^{2+} ions in our experiments are in their ground electronic states with a degree of internal excitation that peaks between 1.4 and 1.8 eV.

Following interactions of O_2^{2+} with Ar we see dissociative SET (reaction (8.3)) in addition to the non-dissociative process (reaction (8.2)). Figure 8.2 shows the experimental energy release spectrum that we determine for the non–dissociative SET between O_2^{2+} and Ar. The spectrum is peaked at a higher value than that for the Ne interaction, specifically around 5.8 eV, compared to 4.2 eV for Ne. This energy release spectrum for SET between O_2^{2+} and Ar has a FWHM of 2.4 eV, which is also wider than that recorded for the equivalent process with Ne.

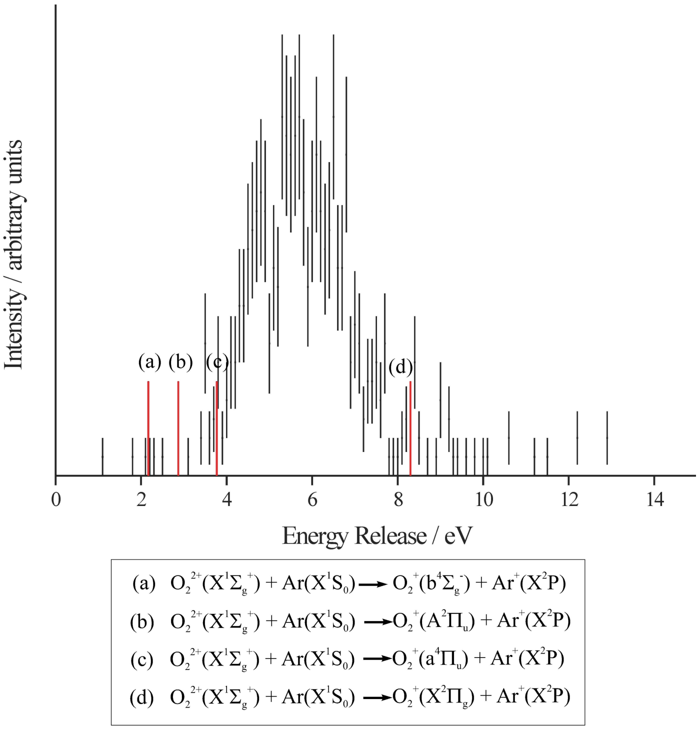

Figure 8.2 Energy release spectrum recorded following SET between O_2^{2+} and Ar to form O_2^+ + Ar^+. Error bars are given by Poissonian statistics. Also shown by the vertical red lines labelled (a) – (d) are ground vibrational state literature exothermicities for the SET reactions forming four different stable states of O_2^+.

Again, in Figure 8.2 are shown four red vertical lines that correspond to the reaction exothermicities from ground state reactants to the $v = 0$ levels of the four stable electronic states of O_2^+, formed along with ground state Ar^+. What is clear from the figure is that none of these particular vibronic states appears to strongly contribute to the peak in our exothermicity spectrum. Evidently there is some internal energy in either the reactant O_2^{2+} or product O_2^+. We have already stated that we expect there to be around 1.6 eV of vibrational energy in the O_2^{2+}, which brings the exothermicity for the reaction forming O_2^+ ($a^4\Pi_u$) products into approximately the correct range of exothermicities that we measure. Therefore, it seems likely that in the SET reaction between O_2^{2+} and Ar, the product O_2^+ is formed in the excited $a^4\Pi_u$ state.

It is interesting to note that the energy release spectrum for the SET reaction between O_2^{2+} and Ne is quite different to that recorded between O_2^{2+} and Ar. The obvious conclusion of this difference is that the SET is not totally independent of the identity of the neutral; the picture we have of an isolated O_2^{2+} receiving an electron in a vertical transition and isolated neutral ejecting an electron is not entirely correct. The ionization energy and polarisability of the neutral influence the degree of complexation between the reactants and consequently the electronic and/or rovibrational levels of both products that are populated. A clue to the degree of reactant complexation can be found in the CM frame scattering diagrams. Although these CM frame diagrams for the SET process following interaction of O_2^{2+} with both Ne and Ar suggest a direct mechanism, the range of scattering angles spanned by the products of SET between O_2^{2+} and Ar is broader that those from the O_2^{2+} – Ne reaction. The larger range of product scattering angles suggests a slightly larger degree of complexation between the O_2^{2+} and Ar reactants occurs than between O_2^{2+} and Ne. This deduction is not surprising since Ar is more polarisable than Ne. In conclusion, the SET reaction between O_2^{2+} and Ar involves marginally more complexation than that between O_2^{2+} and Ne; the result is that the energy releases associated with these reactions differ from each other. Whereas we can determine that the SET between O_2^{2+} and Ne involves ground electronic state reactants and products, with a degree of internal energy in the O_2^{2+}, the SET between O_2^{2+} and Ar is less well defined. In the SET reaction between O_2^{2+} and Ar, we expect that the reactant O_2^{2+} are in their ground electronic state with approximately 1.6 eV of internal energy and our experimental energy release spectrum indicates that the product O_2^+ is most likely to be formed in the $X^4\Pi_g$, $a^2\Pi_u$ or $A^4\Pi_u$ states. In reality there may be a combination of these product electronic states formed with varying degrees of internal excitation.

The CM frame scattering diagrams for the dissociative SET channel between O_2^{2+} and Ar confirm that a direct mechanism is taking place and that little complexation between the reactants occurs. Therefore, the electron is transferred first, forming O_2^{+*} and Ar^+, and the O_2^{+*} dissociates some time later, as confirmed by the internal frame scattering diagrams.

8.2.2 O_2^{2+} + N_2, NO, N_2O and NH_3

In reactions of O_2^{2+} with the nitrogen–based species N_2, NO, N_2O and NH_3 we generally observe only SET, apart from with NH_3 where some very weak bond–forming reactivity is observed. More specifically, we detect products from reactions (8.4) – (8.22), shown in Table 8.2.

Table 8.2 Products of the reactions between O_2^{2+} with N_2, NO, N_2O and NH_3, that form a pair of ions; E_{CM} are 6.5, 5.8, 8.1, 4.9 eV, respectively. The branching ratio for a channel *R* is given as a percentage of total number of pairs detected for all channels.

Channel	Branching Ratio *R* / %	Reaction No.
$O_2^{2+} + N_2 \rightarrow O_2^{+} + N_2^{+}$	94.7	(8.4)
$O_2^{2+} + N_2 \rightarrow O^{+} + O + N_2^{+}$	5.3	(8.5)
$O_2^{2+} + NO \rightarrow O_2^{+} + N^{+} + O$	7.0	(8.6)
$O_2^{2+} + NO \rightarrow O_2^{+} + O^{+} + N$	6.9	(8.7)
$O_2^{2+} + NO \rightarrow O^{+} + O + NO^{+}$	86.1	(8.8)
$O_2^{2+} + N_2O \rightarrow O_2^{+} + N_2O^{+}$	13.3	(8.9)
$O_2^{2+} + N_2O \rightarrow O_2^{+} + N_2^{+} + O$	19.9	(8.10)
$O_2^{2+} + N_2O \rightarrow O_2^{+} + NO^{+} + N$	26.4	(8.11)
$O_2^{2+} + N_2O \rightarrow O_2^{+} + N^{+} + [N + O]$	6.5	(8.12)
$O_2^{2+} + N_2O \rightarrow O_2^{+} + O^{+} + [2N]$	7.0	(8.13)
$O_2^{2+} + N_2O \rightarrow O^{+} + O + N_2O^{+}$	26.9	(8.14)
$O_2^{2+} + NH_3 \rightarrow O_2^{+} + NH_3^{+}$	6.5	(8.15)
$O_2^{2+} + NH_3 \rightarrow O_2^{+} + NH_2^{+} + H$	16.0	(8.16)
$O_2^{2+} + NH_3 \rightarrow O_2^{+} + H_2^{+} + [N + H]$	0.16	(8.17)
$O_2^{2+} + NH_3 \rightarrow O_2^{+} + H^{+} + [N + 2H]$	0.87	(8.18)
$O_2^{2+} + NH_3 \rightarrow O^{+} + O + NH_3^{+}$	75.3	(8.19)
$O_2^{2+} + NH_3 \rightarrow O_2 + NH_2^{+} + H^{+}$	0.59	(8.20)
$O_2^{2+} + NH_3 \rightarrow NO^{+} + H^{+} + [2H + O]$	**0.31**	**(8.21)**
$O_2^{2+} + NH_3 \rightarrow HO_2^{+} + H^{+} + [N + H]$	**0.25**	**(8.22)**

Following the collisions of O_2^{2+} with N_2, the dominant channel is non–dissociative SET (reaction (8.4)), with a small secondary channel in which the nascent O_2^{+*} fragments to O^+ + O (reaction (8.4)). Dissociation of the nascent N_2^{+*} following SET, with the O_2^+ remaining intact, is endothermic by 0.3 eV for ground state reactants and products, hence explaining why we do not observe this channel. The measured exothermicity for reaction (8.4) is 5.1 eV, whereas the literature ground state value is 8.5 eV[4]. Thus, assuming around 1.6 eV internal energy of the reactant O_2^{2+} as explained earlier, there should be on average 5 eV of rovibrational excitation of ground state product monocations. The O_2^+ ($X^2\Pi_g$) ion can support up to around 6.7 eV[5,6] of internal energy and N_2^+ ($X^2\Sigma_g^+$) up to around 8 eV[7], meaning the predicted 5 eV can be easily accommodated between the two products. There are also many low lying metastable electronic states of both the O_2^+ and N_2^+ that, if populated, could result in reaction exothermicity comparable to the measured magnitude.

The CM frame scattering diagrams for reactions (8.4) and (8.5) unambiguously show strong forward scattering, implying that a direct mechanism is taking place with transfer of the electron occurring at significant interspecies separation. For reaction (8.5), such scattering also confirms that the nascent O_2^{+*} does indeed dissociate *after* the SET step.

Following collisions of O_2^{2+} with NO, N_2O and NH_3 the strongest reaction channel is dissociative SET where the nascent O_2^{+*} breaks down to O^+ + O, leaving the NO^+, N_2O^+ or NH_3^+ intact, reactions (8.8), (8.14) and (8.19) respectively. The nascent ion formed by ionization of the neutral species, NO^+, N_2O^+ or NH_3^+, is also observed to fragment in all of these collision systems. Forward scattering is observed for all of the dissociative and non–dissociative SET reactions between O_2^{2+} and nitrogen–based species, thus indicating that a direct mechanism operates in each of these channels.

Only in the O_2^{2+} – NH_3 system do we observe DET and/or chemical reactivity and in this case both are very weak in comparison to SET, comprising only 0.59 % and 0.56 % of reactive events detected that form a pair of ions. The chemical channels that are observed (reactions (8.21) and (8.22)) form NO^+ + H^+ + [2H + O] and HO_2^+ + H^+ + [N + H] with very small branching ratios of 0.31 % and 0.25 %. In reaction (8.21), there are three neutral atoms formed that could be bound as H_2O, as OH + H or as H_2 + O;

alternatively they could all be in atomic form. Similarly, in reaction (8.22) the N and H could be bound as NH or unbound. Thermochemical analysis has been carried out and unfortunately does not indicate how the neutrals are bound in either case. Moreover, due to the extremely low numbers of pairs detected for both chemical channels, the CM frame scattering diagrams do not allow a inference of the reaction dynamics to be made. However, we expect that reaction (8.21), yielding NO^+ + H^+ + [2H + O], will proceed *via* formation of a 'long-lived' encounter complex $[O_2NH_3]^{2+}$, as has been observed before for chemical channels[8-12], due to the large structural rearrangements that are required. Conversely, we expect it is likely that reaction (8.22), yielding HO_2^+ + H^+ + [N + H], proceeds *via* rapid H^- transfer from NH_3 to O_2^{2+} at large interspecies separation, as has been observed before[13].

8.2.2.1 Points of Note on O_2^{2+} + NO and O_2^{2+} + N_2

Employing the drift-tube technique in 1989 Chatterjee and Johnsen were able to report the first example of bond-formation following a dication-neutral reaction. These investigators looked at interactions of O_2^{2+} with N_2 and saw NO_2^+ products[1]. Employing the PSCO technique we do not detect NO_2^+ ions following O_2^{2+} and N_2 interactions. One reason for such a discrepancy could be the differing collision energies that were used in these experiments. Chatterjee and Johnsen used E_{CM} of 0.04 eV and 0.087 eV, whereas in the PSCO experiment our E_{CM} was considerably higher at 5.8 eV. Indeed, Chatterjee and Johnsen comment that at their slightly raised E_{CM} of 0.087 eV, the measured rate coefficient for the formation of NO_2^+ is lower than at E_{CM} of 0.04 eV. Consequently, we suggest that the cross-section of the bond-forming reaction between O_2^{2+} and NO producing NO_2^+ is strongly dependent on collision energy and that it drops off rapidly with increasing E_{CM}.

It is interesting to note that despite the fact that many bond-forming channels between O_2^{2+} and N_2 such as formation of NO^+, N_2O^+ and NO_2^+ are exothermic by several eV, none of these channels appear to be active in this collision system. The reaction of N_2^{2+} with O_2 has been measured in the past employing the PSCO technique, results show that NO^+ products are formed in coincidence with both N^+ and O^+ with intensity about five times less than the SET channels[8]. In both of these bond-forming channels an initial $[N_2O_2]^{2+}$ encounter complex is formed, which later dissociates to the detected products. Clearly, when O_2^{2+} reacts with N_2, as reported here, the formation of this complex is not favourable. Perhaps complexation seems unfavourable because the cross–section for SET is higher in relation to complex formation than when N_2^{2+} reacts with O_2. In any case, it is a valuable observation that the O_2^{2+} + N_2 system is not accessing the same part of the $[N_2O_2]^{2+}$ PES as the N_2^{2+} + O_2 system, resulting in very different reactive behaviour. Such an observation could be significant for the terrestrial ionosphere and suggests that is important to accurately know the relative abundances of N_2^{2+} versus O_2^{2+} as this will have an effect on the chemical evolution of this environment.

8.2.3 O_2^{2+} + CO, CO_2, OCS and CS_2

The reactions of O_2^{2+} with oxygen–based species CO, CO_2 and OCS have been investigated. In addition, we have examined the reactivity of O_2^{2+} with CS_2 to compare with the data for CO_2 and OCS to see how replacing the oxygen with sulphur atoms affects the reactivity with O_2^{2+}. The reaction channels that were observed following these interactions are outlined in Table 8.3 as reactions (8.23) – (8.42).

Table 8.3 Products of the reactions between O_2^{2+} with O_2, CO, CO_2, OCS and CS_2, that form a pair of ions; E_{CM} are 5.1, 8.1, 9.1 and 8.4 eV respectively. The branching ratio for a channel *R* is given as a percentage of total number of pairs detected for all channels.

Channel	Branching Ratio *R* / %	Reaction No.
$O_2^{2+} + CO \rightarrow O_2^{+} + CO^{+}$	78.6	(8.23)
$O_2^{2+} + CO \rightarrow O^{+} + O + CO^{+}$	18.3	(8.24)
$O_2^{2+} + CO \rightarrow O^{+} + CO_2^{+}$	**3.1**	**(8.25)**
$O_2^{2+} + CO_2 \rightarrow O_2^{+} + CO_2^{+}$	42.0	(8.26)
$O_2^{2+} + CO_2 \rightarrow O_2^{+} + O^{+} + CO$	17.8	(8.27)
$O_2^{2+} + CO_2 \rightarrow O_2^{+} + CO^{+} + O$	16.6	(8.28)
$O_2^{2+} + CO_2 \rightarrow O^{+} + O + CO_2^{+}$	23.6	(8.29)
$O_2^{2+} + OCS \rightarrow O_2^{+} + OCS^{+}$	0.6	(8.30)
$O_2^{2+} + OCS \rightarrow O_2^{+} + S^{+} + CO$	25.5	(8.31)
$O_2^{2+} + OCS \rightarrow O_2^{+} + CO^{+} + S$	10.1	(8.32)

$O_2^{2+} + OCS \rightarrow O_2^{+} + CS^{+} + O$	2.8	(8.33)
$O_2^{2+} + OCS \rightarrow O^{+} + O + OCS^{+}$	29.7	(8.34)
$O_2^{2+} + OCS \rightarrow O^{+} + O + S^{+} + [C + O]$	9.5	(8.35)
$O_2^{2+} + OCS \rightarrow O_2 + S^{+} + CO^{+}$	15	(8.36)
$O_2^{2+} + OCS \rightarrow SO^{+} + CO^{+} + O$	**6.8**	**(8.37)**
$O_2^{2+} + CS_2 \rightarrow O_2^{+} + CS_2^{+}$	1.5	(8.38)
$O_2^{2+} + CS_2 \rightarrow O_2^{+} + CS^{+} + S$	13.0	(8.39)
$O_2^{2+} + CS_2 \rightarrow O_2^{+} + S^{+} + CS$	11.0	(8.40)
$O_2^{2+} + CS_2 \rightarrow O^{+} + O + CS_2^{+}$	39.5	(8.41)
$O_2^{2+} + CS_2 \rightarrow O_2 + CS^{+} + S^{+}$	34.9	(8.42)

Firstly, the O_2^{2+} – CO collision system will be discussed. Following collisions of these species we observe non–dissociative SET (reaction (8.23)) and dissociative SET (reaction (8.24)) as expected. The modal exothermicity we measure for the non–dissociative SET process (reaction (8.23)) is 5.1 eV, whereas the ground state literature value is 10.1 eV, leaving around 6.5 eV of internal energy in the product ions. O_2^{+} in its ground electronic state can support up to 6.7 eV of vibrational excitation. Moreover, the dissociation energy of CO^{+} is around 8.41 eV[4]. Clearly, both the O_2^{+} and CO^{+} ions have very deep ground state potential minima, thus explaining why we see a large branching into the non–dissociative SET channel in this system. The small branching into dissociative SET reactions also suggests that the electronic states of O_2^{+} and CO^{+} that are populated in the SET are not strongly pre–dissociated by repulsive PECs or that population of repulsive state in the SET reaction is not facile.

We also observe a rather unusual reaction channel after interactions of O_2^{2+} with CO, specifically, a bond–forming channel that yields CO_2^{+} + O^{+} (reaction (8.25)) with a branching ratio of 3.1 %.

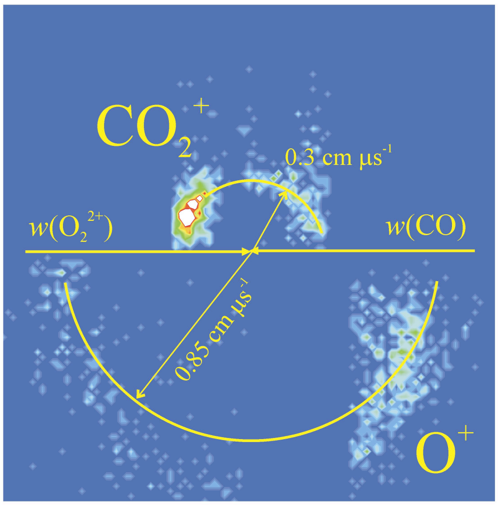

Figure 8.3 Scattering of the CO_2^+ and O^+ products of reaction (8.25) in the CM frame in relation to the directions of the reactants prior to the collision. Reactant directions are shown by the full-headed arrows. The scattering has a split shape due to O^+ arrival times within the 'exclusion zone' used to reduce false coincidences with un-reacted dications.

The CM frame scattering diagram for Reaction number (8.25), shown in Figure 8.3, reveals an interesting reaction mechanism. Unfortunately, as one product of this channel is O^+ that has the same *m/z* as the reactant beam, then some of these ions have arrival times within the exclusion zone meaning the scattering has a "split" shape. However, despite this it is still clear that the scattering is anisotropic, with the CO_2^+ product direction aligned with that of the CO and the O^+ aligned with the O_2^{2+} direction prior to the collision. The implication of this anisotropy is that the CO neutral strips an O^+ from the O_2^{2+}, leaving the direction of the nascent CO_2^+ largely unchanged from that of the CO. The O^+ ion continues traveling in the direction of the O_2^{2+}.

Several examples of chemical channels occurring *via* a rapid "stripping" process have been reported before[13,14]. Specifically, the two examples we have discovered of bond-formation occurring in a manner that maintains the directionality of the products are formation of ArC^+ from Ar^{2+} – C_2H_2 interactions and formation of ArH^+ from $C_2H_2^{2+}$ – Ar interactions. In the former, the Ar^{2+} dication strips an anionic CH^- fragment from the neutral, and in the latter the neutral Ar strips a cationic H^+ fragment from the dication. Formation of CO_2^+ and O^+ from O_2^{2+} + CO interactions is more analogous to the ArH^+ formation as the neutral CO strips a cationic O^+ fragment from the dication, however, the O^+ is far heavier than a proton. As yet, O^+ is the heaviest species we have observed to be transferred rapidly in this way from one reactant to the other without formation of a comparatively long–lived complex.

A striking observation from the branching ratios in Table 8.3 is that following interactions of O_2^{2+} with CO_2 non–dissociative SET is the major channel, whereas for OCS and CS_2 this channel is hugely less favourable than dissociative SET. The single IEs of CO_2, OCS and CS_2 are 13.8 eV, 11.2 eV and 10.1 eV respectively. A fundamental explanation would thus be that the lower IEs of OCS and CS_2 mean that more energy is available to form OCS^+ and CS_2^+ above their dissociation limits. DET reactions following interactions of O_2^{2+} with CO_2, OCS and CS_2 have ground state literature energy releases of +1.21 eV, –5.79 eV and –9.15 eV, respectively[4]; thus readily explaining why we detect no ions due to DET from CO_2, yet we do from OCS and CS_2.

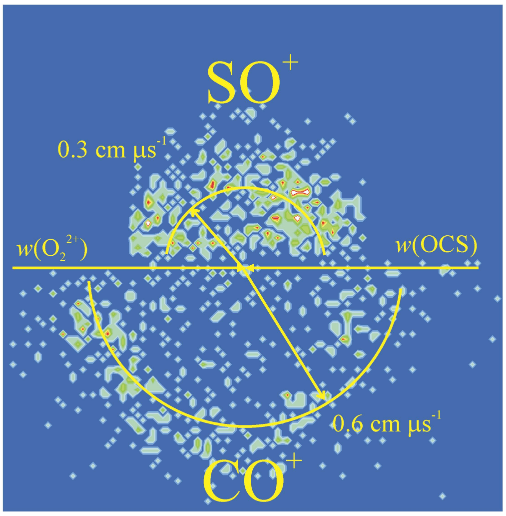

Figure 8.4 Scattering of the SO^+ and CO^+ products of reaction (8.37), in the CM frame, following collisions of O_2^{2+} with OCS. The directions of the reactants prior to the collision are shown by the full–headed arrows $w(O_2^{2+})$ and w(OCS).

A further point of note on the differences between reactions of O_2^{2+} with CO_2, OCS and CS_2 is that only with OCS do we see product ions due to re–arrangement of the reactant atoms, that is, bond–formation. Specifically we see formation of SO^+ in coincidence with CO^+, reaction (8.37). The CM scattering diagram for this channel, seen in Figure 8.4, shows isotropic scattering of the SO^+ and CO^+ with respect to the reactant directions prior to the collision, thereby implying that the reaction proceeds *via* formation of complex.

Although this is a fairly weak channel, the internal frame scattering diagrams hint that after the initial step of formation of $[OCSO_2]^{2+}$, the complex fragments into CO^+ + SO_2^{+*}. A short time later the nascent SO_2^{+*} breaks down further into the SO^+ we detect and O. The formation of ground state SO_2^+ + CO^+ from ground state O_2^{2+} + OCS interactions is exothermic by 12.6 eV[4]. As a result, in all likelihood, at this stage on the reaction pathway there still remains a lot of internal energy in the products. For this reason, the SO_2^{+*} intermediate rapidly dissociates into SO^+ and O. Finally, the ground state literature exothermicity for formation of SO^+ + CO^+ + O from interaction of O_2^{2+} with OCS is still large, at 8.9 eV; therefore we expect the products to be electronically or rovibrationally excited. The analogous reaction channel when O_2^{2+} reacts with CS_2 resulting in formation of SO^+ + CS^+ + O is endothermic by 3.4 eV due to the energetically unfavourable formation of CS^+ compared to CO^+. So, somewhat unsurprisingly when the thermochemistry of the reactions have been considered, we do not detect SO^+ and CS^+ ions in coincidence following interaction of O_2^{2+} with CS_2.

8.2.4 O_2^{2+} + H_2O and H_2S

Table 8.4 Reactions channels observed to occur following collisions of O_2^{2+} with H_2O and H_2S at E_{CM} of 4.3 eV and 7.2 eV respectively.

Channel	Branching Ratio R / %	Reaction No.
$O_2^{2+} + H_2O \rightarrow O_2^+ + H_2O^+$	46.8	(8.44)
$O_2^{2+} + H_2O \rightarrow O_2^+ + OH^+ + H$	28.3	(8.45)
$O_2^{2+} + H_2O \rightarrow O_2^+ + H_2^+ + O$	0.4	(8.46)
$O_2^{2+} + H_2O \rightarrow O_2^+ + H^+ + [O + H]$	15.4	(8.47)
$O_2^{2+} + H_2O \rightarrow O^+ + O + H_2O^+$	9.1	(8.48)
$O_2^{2+} + H_2S \rightarrow O_2^+ + H_2S^+$	1.5	(8.49)
$O_2^{2+} + H_2S \rightarrow O_2^+ + HS^+ + H$	8.4	(8.50)
$O_2^{2+} + H_2S \rightarrow O_2^+ + S^+ + H_2$	4.9	(8.51)
$O_2^{2+} + H_2S \rightarrow O_2^+ + H^+ + HS$	0.7	(8.52)
$O_2^{2+} + H_2S \rightarrow HS^+ + H^+ + O_2$	2.6	(8.53)
$O_2^{2+} + H_2S \rightarrow S^+ + H^+ + H + O_2$	0.9	(8.54)
$O_2^{2+} + H_2S \rightarrow O^+ + O + H_2S^+$	70.0	(8.55)

$O_2^{2+} + H_2S \rightarrow O^+ + O + S^+ + [2H]$	9.2	(8.56)
$O_2^{2+} + H_2S \rightarrow SO^+ + H^+ + [O + H]$	**1.5**	**(8.57)**
$O_2^{2+} + H_2S \rightarrow SO^+ + H_2^+ + O$	**0.3**	**(8.58)**

Finally, in this chapter the reactivity of O_2^{2+} towards H_2O and H_2S will be covered. Water and the related molecule H_2S are important trace constituents of Earth's atmosphere. So to understand the reaction pathways when these species interact with O_2^{2+} is valuable. Using the PSCO we have investigated the O_2^{2+} – H_2O and O_2^{2+} – H_2S collision systems at E_{CM} of 4.3 eV and 7.2 eV respectively. Reaction channels that were observed are shown in Table 8.4.

Clearly, a greater number of dissociative routes are available after SET between O_2^{2+} and H_2S when compared to H_2O. Principally, this is likely due to the lower single IE of H_2S (10.5 eV) than H_2O (12.6 eV)[4]. Moreover, apart from the ground state, all low lying electronic states of H_2S^+ are known to be dissociative apart from the A state which can support up to a maximum of 1 eV of vibration[17]. We do not see DET from H_2O to O_2^{2+} but this channel is open in collisions of H_2S with O_2^{2+}. What is most striking, however, when examining the branching ratios for the two collision systems is that when H_2O is the reactant the nascent O_2^{+*} only dissociates in 9% of events, where a pair of ions are formed, whereas when H_2S is the reactant this channel becomes by far the dominant channel with O_2^{+*} dissociating in 70% of events. We are comparing only relative branching ratios rather than cross–sections on an absolute scale. Therefore, it is difficult to say whether the cross–section for the dissociative SET channel where O_2^{+*} breaks down is in fact increased in collisions with H_2S over H_2O, or whether the all other channels have smaller cross–sections. However, reaction (8.48) is exothermic by 4.7 eV, whereas reaction (8.55) has a larger exothermicity of 6.9 eV. So it seems a reasonable assumption that the absolute cross–section for dissociation of the nascent O_2^{+*} following SET with H_2S is greater than the equivalent process following SET with H_2O. Mechanistically, all of the dissociative and non–dissociative SET channels for both H_2O and H_2S reactants exhibit the strong forward scattering that is typical for this class of reaction.

Following interaction of O_2^{2+} with H_2O we only observe SET, whereas, following interaction of O_2^{2+} with H_2S we also observe two chemical channels. Specifically, these are reactions (8.57) and (8.58) that form $SO^+ + H^+ + [O + H]$ and $SO^+ + H_2^+ + O$ respectively.

The detected number of pairs in both of these channels are rather low and as such the reaction mechanism cannot be determined. Although, the CM frame scattering *suggests* that the products are scattering isotropically which would mean a complex was formed that survived for several rotational periods. Such a mechanism would be unsurprising given the amount of atomic rearrangement required to form these products from the reactants. Reaction (8.58), yielding SO^+ + H_2^+ + O, has a ground state literature exothermicity of 7.6 eV. Given that typical energy releases for dication–neutral reactions are of the order of 5 eV, we expect the products of this reaction (8.58) to be electronically or rovibrationally excited by several electron–volts. The same is true for reaction (8.57), yielding SO^+ + H^+ + [O + H]. If the neutrals are formed as OH, then the literature exothermicity is 9.3 eV and if they are in atomic form as O + H then the literature exothermicity is 4.9 eV[4]. Unfortunately, we have no further means to determine which of these scenarios is happening in this channel, although, modelling of the O_2^{2+} – H_2S PES may help resolve this uncertainty.

8.3 Conclusion

This chapter has presented the numerous reaction channels that form a pair of ions that have been observed to occur between O_2^{2+} and twelve different neutrals. The identity of these neutrals ranges from the rare gases Ne and Ar to larger molecular species such as NH_3 and CS_2. Bond–formation was observed to occur with only four of these neutrals, specifically, NH_3, CO, OCS and H_2S. Following interactions of O_2^{2+} with NH_3 we detect NO^+ products in one channel and HO_2^+ in another. Bond–formation following interactions of O_2^{2+} with NH_3 has an almost negligible relative branching ratio of 0.56 %. The reaction channels forming SO^+ and CO_2^+ following interactions of O_2^{2+} with H_2S and CO, respectively, only have branching ratios of 1.8 % and 3.1 %. The observation of CO_2^+ formation following O_2^{2+} and CO collisions is of note, not only for its atmospheric implications, but also for the unusual reaction kinematics that we have determined. Following interactions of O_2^{2+} with OCS we see SO^+ + CO^+ + O formation with a more appreciable branching ratio of 6.8 %. This reaction channel proceeds *via* the formation of a $[OCSO_2]^{2+}$ complex, which initially fragments to CO^+ and SO_2^{+*}. Collisions of O_2^{2+} with N_2 merely result in SET, whereas collisions of N_2^{2+} with O_2 have been shown to result in bond–formation with a substantial branching ratio. Therefore, it is an interesting finding that the two 'mirror' collision systems are clearly not accessing the same part of the PES.

In sharp contrast to the previous chapter that reports the results of interactions of O_2^{2+} with CH_4, C_2H_2, C_2H_4 and C_6H_6, wherever bond–formation is reported in this chapter it has been shown to have a very low branching ratio. Moreover, the complexity of the atomic rearrangement in bond–forming reactions seen in collisions with NH_3, CO, OCS and H_2S is not great. Following collisions of O_2^{2+} with CH_4 and C_2H_2 we observe, among other bond–forming products, CO_2^+ monocations, which involves rather extensive rearrangement of the reactant species. It seems clear that the cross–section for bond–forming chemistry following interaction of O_2^{2+} with small organic species is greater than for the closed–shell small neutral species examined in this chapter. This observation is hard to explain as the propensity for bond–forming chemistry seems unrelated to the size of the neutral, for example CS_2 has a much larger van der Waals radius than CH_4. It also seems unrelated to the polarisability of the neutral, for example the polarizabilities of N_2, CH_4 and N_2O are 1.7403[18,19], 2.593[20] and 3.03 Å^3[21], respectively. It seems clear that further work is needed to fully understand the chemical reactivity of the oxygen dication with neutral molecules. Computational investigations of the O_2^{2+} – neutral PESs may help in this endeavour.

The majority of these reactive systems have not been investigated before, so this chapter presents new information about the reactivity of O_2^{2+}, the results of which could be valuable for a better understanding of ionospheric chemistry.

8.4 References

[1] B. K. Chatterjee and R. Johnsen, *J. Chem. Phys.* **1989**, *91*, 1378–1379

[2] A. C. Hurley and V. W. Maslen, *J. Chem. Phys.* **1961**, *34*, 1919–&

[3] R. I. Hall, G. Dawber, A. McConkey, M. A. Macdonald and G. C. King, *Phys. Rev. Lett.* **1992**, *68*, 2751–2754

[4] S. G. Lias, J. E. Bartmess, J. F. Leibman, J. L. Holmes, R. D. Levin and W. G. Mallard, *J. Phys. Chem. Ref. Data* **1988**, *17*, Supplement No. 1

[5] J. A. R. Samson and J. L. Gardner, *J. Chem. Phys.* **1977**, *67*, 755–758

[6] N. H. F. Beebe, E. W. Thulstrup and A. Andersen, *J. Chem. Phys.* **1976**, *64*, 2080–2093

[7] H. R. Koslowski, H. Lebius, V. Staemmler, R. Fink, K. Wiesemann and B. A. Huber, *J. Phys. B–At. Mol. Opt. Phys.* **1991**, *24*, 5023–5034

[8] C. L. Ricketts, S. M. Harper, S. W. P. Hu and S. D. Price, *J. Chem. Phys.* **2005**, *123*,

[9] S. D. Price, *Int. J. Mass Spec.* **2007**, *260*, 1–19

[10] S. M. Harper, S. W. P. Hu and S. D. Price, *J. Chem. Phys.* **2004**, *121*, 3507–3514

[11] J. F. Lockyear, C. L. Ricketts, M. A. Parkes and S. D. Price, *Chem. Sci.* *2*, 150–156

[12] J. F. Lockyear, M. A. Parkes and S. D. Price, *Ange. Chem. Int. Ed.* doi: 10.1002/anie.201006486

[13] D. Ascenzi, P. Tosi, J. Roithova, C. L. Ricketts, D. Schroeder, J. F. Lockyear, M. A. Parkes and S. D. Price, *Phys. Chem. Chem. Phys.* **2008**, *10*, 7121–7128

[14] M. A. Parkes, J. F. Lockyear and S. D. Price, *Int. J. Mass Spectrom.* **2009**, *280*, 85–92

[15] W. P. Hu, S. M. Harper and S. D. Price, *Meas. Sci. Techn.* **2002**, *13*, 1512–1522

[16] M. Dantus, R. M. Bowman and A. H. Zewail, *Nature* **1990**, *343*, 737–739

[17] H. B. Chang and M. B. Huang, *Theor. Chem. Acc.* **2009**, *122*, 189–196

[18] A. C. Newell and R. C. Baird, *J. Appl. Phys.* **1965**, *36*, 3751–&

[19] R. H. Orcutt and R. H. Cole, *J. Chem. Phys.* **1967**, *46*, 697–&

[20] T. K. Bose, Sochansk.Js and R. H. Cole, *J. Chem. Phys.* **1972**, *57*, 3592–&

[21] S. Kirouac and T. K. Bose, *J. Chem. Phys.* **1973**, *59*, 3043-3047

Chapter 9: Conclusions and Future Work

9.1 General Conclusions

The PSCO technique has been successfully employed to investigate a range of dication-neutral reactions. Many of these dication-neutral reactions have not been studied before and so have been revealed for the first time employing the PSCO apparatus. Intriguing features of both electron-transfer[1,2] and chemical reactivity[3-5] have been revealed. The coincidence detection employed in the PSCO experiments allows the pairs of monocations formed in dication-neutral reactions to be identified. What is more, the use of a position sensitive detector allows the dynamics of each reaction channel to be determined.

Detailed, state specific, insights into the seemingly simple single electron-transfer reaction between Ar^{2+} and He have been made. The angularly resolved reaction dynamics of unprecedented resolution, determined using the PSCO apparatus, have shown that the Ar^{2+} (^3P) and Ar^{2+} (^1D) states undergo SET with He in very different ways. The scattering directions of the Ar^+ products from the reaction of Ar^{2+} (^3P) are generally towards low angles over the collision energy range investigated (0.4 eV – 1.2 eV). In contrast, the scattering distribution of Ar^+ products from the reaction of Ar^{2+} (^1D) is peaked forwards at E_{CM} of 1.2 eV and backwards at E_{CM} of 0.4 eV. Perhaps the most interesting aspect of the scattering that has been determined, is that a classical model fairly accurately reproduces the experimental scattering angles for reactions of Ar^{2+} (^3P), but fails dramatically for reactions of Ar^{2+} (^1D). Thus, we can conclude that the SET process between dications and neutrals is not fully understood and some new physics of the interaction of Ar^{2+} (^1D) and He has been revealed by these PSCO experiments.

A bond-forming reaction between N_2^{2+} and H_2 that is of astrochemical relevance has also been discovered. It is vital to understand the outcome of interactions of N_2^{2+} with neutrals, since N_2^{2+} is present in the ionosphere of Titan with significant density. The PSCO experiments have revealed that NH^+ is formed following collisions of N_2^{2+} with H_2. These NH^+ products are formed *via* complexation between the reactants and subsequent fragmentation by neutral loss and then charge separation. Computationally derived stationary points on the potential energy surface agree well with the experimentally determined reaction mechanism.

In addition, PSCO experiments have shown that bond-forming chemistry readily occurs between SF_4^{2+} and several neutral species. Our data shows that SF_4^{2+} very rapidly, and efficiently, fluorinates small neutral atoms or molecules. For example, we observe formation of H_2OF^+ in collisions of SF_4^{2+} with H_2O; H_2F^+ in collisions of SF_4^{2+} with H_2 and CH_2F^+ in collisions of SF_4^{2+} with CH_4. Each of these bond-forming products is shown to be generated with an extremely high branching ratio. The observation that SF_4^{2+} readily fluorinates small organic molecules has potential implications for the pharmaceutical and agrochemical industries, where fluorination is key. Thus, it may be extremely valuable to undertake further research into the properties and reactions of SF_4^{2+}.

Generation of a new class of organo-rare gas dications was observed by Schröder *et al* following collisions of $C_2H_2^{2+}$ with Ar and this collision-system was subsequently investigated employing the PSCO technique. The PSCO technique has been employed to show that electron- and proton-transfer channels also occur following interaction of $C_2H_2^{2+}$ with Ar. The PSCO technique can confirm that the electron- and proton-transfer products do not arise from fragmentation of the $HCCAr^{2+}$ dicationic complex that was observed by Schröder *et al.* The $[C_2H_2\text{-}Ar]^{2+}$ potential energy surface was investigated by reversing the charges on the reactants and studying the reactions between Ar^{2+} and C_2H_2 employing the PSCO apparatus. Results show that the system accesses a different part of the PES. Namely, following collisions of Ar^{2+} with C_2H_2 we observe a chemical channel forming ArC^+ *via* a direct mechanism.

Lastly, an extensive investigation of the reactivity of O_2^{2+} with small neutral species has been presented. This dication is predicted to exist in the terrestrial ionosphere and so an understanding of its reactivity towards atmospheric constituents is valuable. In general, our results show that O_2^{2+} undergoes extensive complexation and bond-forming reactivity with small organic species such as CH_4 and C_2H_2, whereas in collisions with many other small closed-shell species the reactivity is dominated by electron-transfer. The origin of this differing reactivity does not seem related to the size or polarisability of the neutral, since in collisions with CS_2, only SET and DET were observed. Computational investigations of the $[O_2\text{-}CH_4]^{2+}$ potential energy surface show that there are many minima corresponding to a variety of complex structures, thus demonstrating the need for further work on this system.

9.2 Modifications to the PSCO Apparatus

In addition to the interesting electron transfer and chemical reactions that have been discovered using the PSCO apparatus, several modifications to the experimental design have been implemented and commissioned. Firstly, a pulsed value and skimmer were installed that allow the neutral reactant to be introduced to the reaction region in the form of a supersonic molecular beam. The angular acceptance of the time-of-flight mass spectrometer has been increased, thereby allowing the detection of ions scattered over a wider range of angles when using low repeller plate voltages.

An interesting observation is that the resolution of the kinetic energy release distributions can be significantly improved by pulsing the first accelerating electrostatic lens in the acceleration region. Pulsing the electrostatic lens at the same time as the repeller plate reduces the magnitude of the penetrating field from the acceleration to the source region. At an intermediate repeller plate voltage of 100 V it was in fact found that the optimum improvement was obtained when the electrostatic lens was set to a positive bias voltage of +36 V when the repeller plate was off. This method reduced the full-width-at-half-maximum of the KER peak from 5 eV (normal operation) to 3 eV.

9.2.1 Further Possible Modifications

The new TOF MS that was installed included an electrostatic lens that was not present in the original design, specifically, a lens that is near the start of the drift tube that can be operated as an Einzel lens. In addition, in contrast to the original design, the voltages applied to each of the ten accelerating guard rings can now be varied independently. This experimental set up means that the Velocity Map Imaging (VMI) technique can be integrated with the existing PSCO methodology. VMI uses inhomogeneous electric fields to focus ions with the same velocity to the same point on the detector[6]. Kinetic energy releases and angular distributions can be obtained from the resulting sets of rings on the detector. VMI experiments have only ever been carried out using photoionisation to generate ions; therefore, to incorporate it with the PSCO technique would be a novel way to study dication-neutral reactions. Investigations into the implementation of VMI have been initiated, although the method of data collection *via* reaction products is too slow to allow "real time" tuning on any feasible time scale. As a consequence, a He I discharge lamp has been installed in order to generate larger fluxes of ions in the source region of the spectrometer, which will allow tuning of the voltages on a more practical time scale. It is expected that the correct electrostatic potentials to focus the product ions by VMI will then be elucidated and the technique implemented for the extended PSCO study of dication-neutral reactions.

It has been proposed that one of the principle sources of broadening in the data analysis arises due to the assumption of a single (x, y) coordinate for the reaction centre. With only two ionic products it is impossible to calculate the (x, y) coordinates of the reaction on an event-by-event basis. However, if three ionic products are formed, as may be the case in trication-neutral reactions, then this (x, y) coordinate can be calculated. What is more, trication-neutral reactions have received negligible attention and there are potentially interesting reaction channels to be revealed. As such, the reaction of Ar^{3+} with OCS has been investigated using the PSCO apparatus. Preliminary analysis of the triples data (for which a new analysis program was written) suggests that the reactions shown in Equations (9.1) – (9.4) occur.

$$Ar^{3+} + OCS \rightarrow Ar^{+} + S^{+} + CO^{+} \tag{9.1}$$

$$Ar^{3+} + OCS \rightarrow Ar^{+} + S^{+} + C^{+} + O \tag{9.2}$$

$$Ar^{3+} + OCS \rightarrow Ar^{+} + S^{+} + O^{+} + C \tag{9.3}$$

$$Ar^{3+} + OCS \rightarrow Ar^{+} + C^{+} + O^{+} + S \tag{9.4}$$

Moreover, a peak in the one-dimensional mass spectrum recorded even suggests that the bond-forming product ArO^{2+} is formed following collisions of Ar^{3+} with OCS. A major difficulty in studying trication reactions with the current technique are the poor trication fluxes obtained. Work is ongoing to try to maximize these counts and use the triples data collected to calculate an individual (x, y) reaction coordinate for each event detected.

9.3 References

[1] J. F. Lockyear, M. A. Parkes and S. D. Price, *J. Phys. B-At. Mol. Opt. Phys.* **2009**, *42*, 9

[2] D. Ascenzi, P. Tosi, J. Roithova, C. L. Ricketts, D. Schroeder, J. F. Lockyear, M. A. Parkes and S. D. Price, *Phys. Chem. Chem. Phys.* **2008**, *10*, 7121-7128

[3] J. F. Lockyear, C. L. Ricketts, M. A. Parkes and S. D. Price, *Chem. Sci. 2*, 150-156

[4] J. F. Lockyear, M. A. Parkes and S. D. Price, *Angew. Chem.-Int. Edit.* **2011**, *50*, 1322-1324

[5] M. A. Parkes, J. F. Lockyear and S. D. Price, *Int. J. Mass Spectrom.* **2009**, *280*, 85-92

[6] A. Eppink and D. H. Parker, *Rev. Sci. Instr.* **1997**, *68*, 3477-3484

Appendix

A schematic of the position-sensitive coincidence two-field time-of-flight mass spectrometer used in this thesis is shown in Figure A.1. The PSCO is based on the classic Wiley-McLaren two-field design[1] with dimensions that allow Eland's second-order focussing conditions[2].

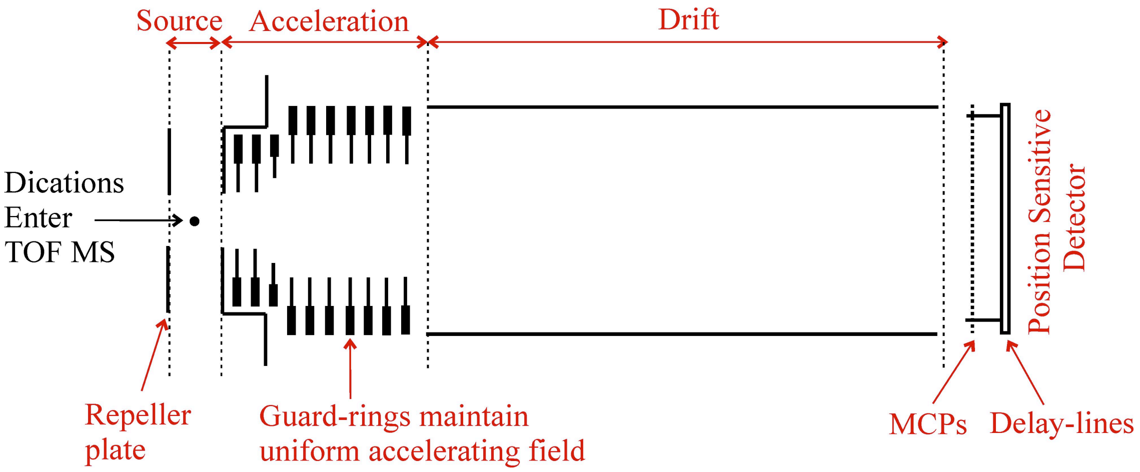

Figure A.1 Schematic of the Wiley-McLaren two-field time-of-flight mass-spectrometer used in this thesis.

The TOF of an ion through this spectrometer is the sum of its TOF through the source t_S, acceleration t_A and drift regions t_D, Equation (A.1).

$$TOF = t_S + t_A + t_D \tag{A.1}$$

The source is defined as having length 2S, thus S is the distance travelled by an ion formed in the centre of the region. The TOF of such as ion can be determined by Newtonian mechanics and is given by Equation (A.2), where v_{si} is the initial velocity of the ion on entering the source region, v_{sf} is the final velocity of the ion as it exits the region and a_s is the acceleration of the ion due to the source field. We will consider ions that have zero initial velocity.

$$t_S = \frac{(v_{sf} - v_{si})}{a_s} \tag{A.2}$$

The final velocity of the ion at the exit of the source can be determined using another equation of motion, Equation (A.3).

$$v_{sf}^2 = v_{si}^2 + 2a_s S \tag{A.3}$$

Therefore, substituting (A.3) into (A.2), we obtain Equation (A.4).

$$t_S = \frac{(v_{si}^2 + 2a_s S)^{1/2} - v_{si}}{a_s} \tag{A.4}$$

The acceleration in the source region a_s can be calculated using Newton's second law, Equation (A.5).

$$F = ma \tag{A.5}$$

The force acting on the ion is given by the product of the electric field in the source region E_s and the charge on the ion q. Therefore we can rearrange (A.5) to give Equation (A.6).

$$a_s = \frac{E_s q}{m} \tag{A.6}$$

Hence, substituting (A.6) into (A.4) we obtain Equation (A.7).

$$t_S = \frac{\left(v_{si}^2 + 2\left(E_s q/m\right)S\right)^{1/2} - v_{si}}{\left(E_s q/m\right)} \tag{A.7}$$

The initial velocity of an ion formed with kinetic energy T_0 is defined as Equation (A.8).

$$v_{si} = \left(\frac{2T_0}{m}\right)^{1/2} \tag{A.8}$$

Thus Equation (A.7) becomes Equation (A.9).

$$t_S = \frac{\left(\left(2T_0/m\right) + 2\left(E_s q/m\right)S\right)^{1/2} - \left(2T_0/m\right)^{1/2}}{\left(E_s q/m\right)} \tag{A.9}$$

The above expression for the TOF of an ion across distance S in the source can be simplified to Equation (A.10).

$$t_S = \frac{\sqrt{2m}}{E_s q}\left[\sqrt{T_0 + E_s qS} - \sqrt{T_0}\right] \tag{A.10}$$

The TOF of an ion through the acceleration region of length A with electric field strength E_A leading to an acceleration a_A is given by Equation (A.15), where v_{Af} is the final velocity of the ion at the end of the acceleration region.

$$t_A = \frac{(v_{Af} - v_{sf})}{a_A} \tag{A.11}$$

Thus it follows that Equation (A.12) is true.

$$t_A = \frac{\left(\left(\frac{2T_0}{m}\right) + 2\left(\frac{E_s q}{m}\right)S + 2\left(\frac{E_A q}{m}\right)A\right)^{\frac{1}{2}} - \left(\left(\frac{2T_0}{m}\right) + 2\left(\frac{E_s q}{m}\right)S\right)}{\left(\frac{E_A q}{m}\right)} \tag{A.12}$$

Equation (A.12) can be simplified to Equation (A.13).

$$t_A = \frac{\sqrt{2m}}{E_A q}\left[\sqrt{T_0 + E_s qS + E_A qA} - \sqrt{T_0} - \sqrt{E_s qS}\right] \tag{A.13}$$

Where T can be defined as the final kinetic energy of the ion as it enters the drift region, and thus the energy of the ion that impacts on the detector, Equation (A.14).

$$T = T_0 + E_s qS + E_A qA \tag{A.14}$$

There is no electrostatic field gradient in the drift region, so the ion is not accelerated further. Thus, the time taken to traverse the drift region t_D is given by Equation (A.15), where D is the drift length.

$$t_D = \frac{D}{v_{Af}} \tag{A.15}$$

Consequently, the drift TOF is given by Equation (A.16), and is again dependent on the square root of m/z.

$$t_D = D\sqrt{\frac{m}{2T}} \tag{A.16}$$

The total TOF of an ion through a two-field TOF MS is thus given by the summation of Equations (A.9), (A.13) and (A.16), giving Equation (A.17).

$$TOF = \sqrt{2m}\left[\left(\frac{\sqrt{T_0 + E_s qS} - \sqrt{T_0}}{E_s q}\right) + \left(\frac{\sqrt{T} - \sqrt{T_0} - \sqrt{E_s qS}}{E_A q}\right) + \left(\frac{D}{2\sqrt{T}}\right)\right] \quad \text{(A.17)}$$

If the electric fields and experimental geometry are kept constant then these terms can all be encompassed in a constant "c". The TOF can then be expressed in terms of the mass *m*, charge on the ion *z* and c, Equation (A.18).

$$TOF = c\sqrt{\frac{m}{z}} \quad \text{(A.18)}$$

Wiley and McLaren calculated the electric fields and source, acceleration and drift lengths required so that the TOF of ions with the same *m/z* is independent of initial source position, termed space-focussing. To first order this condition requires that Equation (A.19) is true.

$$\left(\frac{d(TOF)}{dS}\right)_{S=0} = 0 \quad \text{(A.19)}$$

Wiley and McLaren have shown that the drift length that defines that plane of space focus is given by Equation (A.20).

$$D = 2Sk_0\left(1 - \frac{A}{S\left(k_0 + \sqrt{k_0}\right)}\right) \quad \text{(A.20)}$$

Where k_0 is given by Equation (A.21).

$$k_0 = \frac{E_s S + E_A A}{E_s S} \quad \text{(A.21)}$$

The advantage of a two-field TOF MS is that the fields can be adjusted appropriately to achieve space-focussing conditions. In contrast, in a single-field TOF MS, the length of the drift region must be exactly the same length as the entire source region, or D = 2S[1] (Remember that S equals half of the total source length), which means that construction of the MS must be extremely accurate. Later, Eland discovered that it was in fact possible to achieve experimental conditions that also allows the second differential of the TOF with source position to equal zero, Equation (A.22), termed “second-order” space focussing[2]. Second-order space focussing is employed in the PSCO experiments.

$$\left(\frac{d^2(TOF)}{dS^2}\right)_{S=0} = 0 \tag{A.22}$$

References

[1] Wiley, W C and McLaren, I H, *Rev. Sci. Instr.* **1955**, *26*, 1150-1157.
[2] Eland, J H D, *Meas. Sci. Technol.* **1993**, *4*, 1522-1524.